Elucidating the endogenous distribution, topography, and cells-of-origin of α-synuclein in relation to Parkinson's Disease

By Zoe Fisk

A thesis submitted in partial fulfillment of the requirements for the Master's degree in Neuroscience

Department of Cellular and Molecular Medicine

Faculty of Medicine

University of Ottawa

DEDICATION

This thesis is dedicated to my father, Dr. Aaron Fisk, and my grandfather, Dr. John Fisk. Your passion for your work and contributions to science have inspired me to do great things, and I can’t wait to follow in your footsteps.

ACKNOWLEDGMENTS

I am incredibly lucky to have such an amazing support group around me, and therefore many to acknowledge for their contribution to this thesis.

Firstly, I would like to thank my parents, Aaron and Melissa, for supporting me on my academic journey. Your endless love and support has not gone unnoticed, and I appreciate all of the opportunities you have provided me with. Thanks to my brother, Liam, for providing me with laughs and pictures of Finn and Olive whenever I needed them most.

This endeavor genuinely would not have been possible without the support of Cassis Varlow, both as a friend and a peer. It was such a joy being able to share the triumphs and struggles of graduate school with you by my side (although technically in Toronto), and I can't wait to see you blossom into the amazing scientist you inevitably will become.

I would like to thank my supervisor and mentor, Dr. Maxime Rousseaux, who has provided endless support and excitement for my research. Your knowledge, encouragement and guidance throughout my studies has been instrumental to my success, and I am very grateful to have had a supervisor who is not only passionate about his research and the success of his students but creating dedicated scientists.

I would like to express my deepest gratitude to Haley Geertsma, my lab mentor, for training me and guiding me through graduate school. I wholeheartedly appreciate the training, feedback, and support you've given me throughout my studies, and for not getting annoyed when I ask where

the same antibody is multiple times. Your kind words of encouragement were so integral to my success over the past two years, and I wholeheartedly appreciate it.

Many thanks to the many members of the Rousseaux lab for their support and feedback, particularly Dr. Konrad Ricke for your words of encouragement and Terry Suk for your knowledge and training of molecular techniques. I would like to specifically highlight the help I received from the Rousseaux lab manager Steve Callaghan, whose endless knowledge of laboratory techniques was beyond essential for the progression of my research.

I would like to extend my sincere thanks to the members of my committee, Dr. Greg Silasi and Dr. Michael Schlossmacher, who generously provided me with knowledge, expertise, and words of encouragement throughout my thesis. I would also like to thank Dr. Mathew McDonald for your assistance with ilastik, and Michelle Seguin for building the foundation that my project was based upon.

Words cannot express my gratitude to my friends and support system, in both Ottawa and Toronto. Special thanks to Ana Hamilton for listening to me practice my presentations, emotionally supporting me and letting me spend time with my favorite little stress reliever, Milo. Thanks to Gavin, Jill, Marisa, Ana, Elizabeth, Brent, Emily, and Amelia for making me laugh when my stress levels were at their highest. And finally, my deepest thanks to my partner, Anthony Crawford. Your love and encouragement made this all seem so simple.

FUNDING

I would like to mention and thank my funding sources, **Dave and Jill Hogg** and the **Toth Family**, for providing me the financial backing for my project through the Parkinson's Research Consortium. Your dedication to help and support advancements in Parkinson's research is beyond admirable, and it has been my pleasure being funded by you.

TABLE OF CONTENTS **PAGE NO.**

ABSTRACT

Parkinson's Disease (PD), the second most common neurodegenerative disease worldwide, pathologically presents with the inclusion of Lewy bodies and dopaminergic cell loss in the brain. Lewy bodies are composed of aggregated α-synuclein protein, and although essential to our understanding of PD, not much is known about the native, pre-synaptic state of α-synuclein (α-syn). Due to its mostly synaptic local, immunostaining results in diffuse signal, ultimately providing little insight into the types of α-syn-resident cells. As a result, insight into α-syn expression driven cellular vulnerability has been difficult to ascertain. Using a knockin mouse model that localizes α-syn to the nucleus of cells by insertion of a nuclear localization signal into the α-syn gene locus (*Snca*^{NLS}), we overcome visualization issues and map out the topography and cells-of-origin of α-syn in mice. I performed immunohistochemistry on *Snca*^{NLS} mouse tissue to map out the endogenous distribution of α-synuclein in the brain. Using *ilastik* machine learning analysis, I determined regions with high α-syn expression, which were subsequently co-stained with cell-type specific markers to gain further topographical granularity. α-syn showed high expression in the olfactory bulb, hippocampus, cerebral cortex, substantia nigra and cerebellum. Within these structures, there was a high level of expression of α-syn in granule cells, pyramidal cells, mitral cells, and dopaminergic neurons. Taken together, the *Snca*^{NLS} mouse serves as a tool to define an atlas of α-syn topography, potentially providing insight into cellular vulnerability in PD.

ABBREVIATIONS

α-syn	α-synuclein
aa	amino acid
ABA	Allen Brain Atlas
CB	cerebellum
CP	caudoputamen
CSF	cerebrospinal fluid
CTX	cortex
DA	dopaminergic
DBS	deep brain stimulation
DG	dentate gyrus
FPKM	fragments per kilobase million
GBA	glucocerebrosidase (gene, human)
GCI	glial cytoplasmic inclusions
GI	gastrointestinal
GL	granule layer
Glo	glomeruli
HCF	hippocampus
HDAC6	histone deacetylase 6 (gene, human)
HT	hypothalamus
HY	Hoehn- Yahr
IF	immunofluorescence
IHC	immunohistochemistry
ISH	in situ hybridization
LB	Lewy Body
LBD	Lewy Body Dementia
LN	Lewy Neurite
LKKR2	leucine rich repeat kinase 2 (gene, human)
MC	motor cortex
Mid	midbrain
ML	mitral layer
MO	molecular layer
MSA	Multiple Systems atrophy
NA	noradrenaline
na	numerical aperture
NAC	non-amyloid-β-component
OB	olfactory bulb
OPC	oligodendrocyte precursor cells

OPL	outer plexiform layer
PBS	phosphate buffered saline
PD	Parkinson’s Disease
PFA	paraformaldehyde
PFF	preformed fibril
PL	pyramidal layer
PO	polymorph layer
ROI	Region of interest
S	striatum
SNc	substantia nigra pars compacta
SNCA	a-synuclein (gene, human)
Snca	a-synuclein (gene, mouse)
SNr	substantia nigra pars reticulata
SO	stratum oriens
SR	stratum radiatum
STN	subthalamic nuclei
TH	thalamus
UPDRS	Unified Parkinson's Disease Rating Scale
wt	wild type

List of Figures and Illustrations **Page No.**

List of Tables **Page No.**

1. INTRODUCTION

1.A. PARKINSON 'S DISEASE

1.A.1 History of PD

Parkinson's disease (PD) is a debilitating neurodegenerative disorder that presents with motor and non-motor symptoms. Although first clinically described by James Parkinson in 1817[1] as the "shaking palsy", evidence of PD can be found in ancient Italian and Chinese sources dating back to 1000 BC[2]. Parkinson succinctly described the manifestation of PD to include involuntary motion, which was then elaborated on by the neurologist Jean Martin Charcot to include bradykinesia, dysautonomia and pain[2,3]. Charcot was also the first to describe the disease as "Parkinson's disease"[3] and the first comprehensive description of the disease, including the presence of brainstem lesions, was published in 1953[4]. Since then, PD has been recognized as the most common motor neurodegenerative disease worldwide[5].

1.A.2 Clinical Features of PD

1.A.2.1 Symptoms and Progression

PD presents with a multitude of both motor and non-motor symptoms, leading to complex clinical manifestation, progression, and treatment course. Classical symptoms of PD include stiffness, bradykinesia, tremor and balance issues, however autonomic dysfunction, constipation, cognitive decline, and mood disturbances have also been cited as symptoms of PD[6–9]. Non-motor symptoms typically preface the motor symptoms of PD[10,11], and symptoms such as olfactory dysfunction and REM sleep behavior disorder are considered to be prodromal indicators of PD development[12–14]. The pathological progression of typical PD can be broken into 6 stages, referred to as Braak staging, each with specific pathological hallmarks that can be observed post-mortem[15]. The first Braak stage of PD is marked by pathological α-synuclein (α-syn) aggregates

in the olfactory bulb, dorsal motor nucleus of the vagus nerve in the medulla oblongata and anterior olfactory nucleus causing olfactory dysfunction and other non-motor impairments. In stage 2, pathology spreads to the locus coeruleus (LC), further into the medulla oblongata and the pontine tegmentum, and mild motor impairments occur at this stage. By stage 3, pathology has progressed to the midbrain, particularly the substantia nigra pars compacta (SNc), and forebrain, and loss of balance and bradykinesia ensue. By this stage, the patient is still fully independent, but the disease has made normal functioning difficult. Stage 3 is also when patients typically present to neurologists, as symptoms become too severe to ignore. By stage 4, there is significant degeneration of dopaminergic (DA) neurons in the SNc; and the mesocortex, hippocampus CA1 and thalamus are affected by pathology. In stage 4, movement is very difficult, and patients typically are dependent on assistive care. In stage 5 the disease begins to spread to the neocortex and the frontal, parietal and temporal lobes are pathologically affected. At this stage, cognitive defects occur as pathology spreads into the cortex. Finally, in stage 6, Lewy pathology is found in the primary motor cortex, primary sensory cortex and premotor cortex and the disease is at its most severe. In this stage patients require full assistance, and may be bedridden[15,16].

.

1.A.2.2 Diagnosis

Unfortunately, there is no definitive way to diagnose PD in the clinic. Clinical scales, such as the Hoehn-Yahr (HY)[17] and Unified Parkinson's Disease Rating Scale (UPDRS), are used to assess the severity of symptoms in potential PD patients, however absolute diagnosis cannot be achieved until post-mortem tissue can be analysed for the presence of the two pathological hallmarks, Lewy bodies and DA neuron degeneration in the SNc. The HY scale is used to

diagnose and assess potential PD patient's motor symptoms, assigning them to a category in the 5-step test scale[17]. The first symptom observed in the HY scale is unilateral involvement[17], and the staging typically correlates with pathology, however this scale is weakened by its inability to assess the non-motor symptoms of PD[18]. The UPDRS is a more comprehensive examination and is frequently used in tandem with the HY Scale, where the following four categories are assessed; 1. non-motor aspects of daily living; 2. motor aspects of experiences of daily living; 3. motor examination; and 4. motor complications[19]. By using the HY and UPDRS together, and MRI and PET imaging to rule out other diseases, clinicians can accurately predict the presence of PD in live patients. Additionally, research into potential biomarkers for PD, primarily focused on the presence of aggregated α-syn in the blood and CSF[20,21], has recently become a focus of interest as these could allow for diagnostic clarity in living patients. PD patients are typically diagnosed around age 60, and usually live for 10-20 years after diagnosis of PD[8].

1.A.2.3 Pathology

Two pathological characteristics are necessary for the differential diagnosis of PD *post-mortem*: the degeneration of DA neurons in the SNc and the appearance of Lewy bodies (LBs) and neurites (LNs) throughout the brain[22–24]. When DAs are lost in the SNc, dopamine levels drop in SNc projection area, the striatum. This loss of dopaminergic innervation causes a network imbalance in the basal ganglia, specifically, decreased DA signalling in the indirect pathway of the basal ganglia. In healthy patients, proper functioning of the indirect pathway leads to inhibition of cortical excitability, but in PD, there is a marked reduction in this inhibition, leading to cortical hyperactivity and the characteristic motor impairments and clinical symptoms of PD patients[22,25–27]. LBs are composed primarily of α-syn protein, which becomes toxic when

aggregated[23,28,29]. When these protein aggregates form in the brain, cellular processes and cell survival are impacted, causing pathology and the potential for clinical features to appear.

1.A.3 Epidemiology

PD is the most common motor neurodegenerative disease worldwide, and the second most common neurodegenerative disease next to Alzheimer's. It is estimated that 1% of the population over the age of 60 has PD[30]. PD is two times more common in men, and women with PD typically have a higher age on onset; hypothesized to be caused by neuroprotective effects of estrogens on striatal dopamine levels[31]. PD is rare in people under the age of 50, and typically appears in patients over the age of 60[6]. There is low variance between PD prevalence rates geographically in industrialized countries, however there is some cross-cultural differences in PD incidence, thought to be due to exposure to different environmental toxins and susceptibility genes[32]. Additionally, the prevalence of PD in North American tends to differ depending on race/ethnicity, with the largest PD incidence in Hispanic populations[32]. The number of people with PD has doubled from 1990 to 2015[33], and it is estimated that this will occurring again as the population rises, causing some researcher to refer to PD as a "pandemic"[33].

1.A.4 Causes of PD: Genetic and Sporadic

There is no singular cause for PD, and it is though that many factors contribute to its pathogenesis. The multi-hit hypothesis postulates that several factors, both genetic and environmental, are needed to trigger a disease state[34]. In a subset of cases, mutations in *SNCA, LRRK2, PINK,* and *PRKN,* amongst other genes, cause familial forms of PD[35–39]. However, PD is a complex disease, and no specific gene is completely responsible for all cases. In fact, only an

estimated 10-15% of PD cases account for familial forms of the disease[40], while the remaining cases are idiopathic. Environmental factors can also contribute to disease genesis, including pesticide, heavy metal, and detergent exposure [41–44]. Certain factors have been shown to lower the risk of PD, including appendectomy, cigarette use, non-steroidal inflammatory drug use, and caffeine intake[44–49]. This interplay between genetic and environmental factors leads to a complicated disease milieu, which contributes to the difficulties that arise in treating and curing PD.

1.A.5 Management and treatment

There is currently no cure for PD, and treatments focus on alleviating the symptoms of the disease, not the pathology, to provide some improvement in the quality of life of those with PD. There are two primary courses of disease treatment – pharmaceutical and surgical. There are three types of drugs used to treat PD, the most used of which is Levodopa. Levodopa, or L-dopa, is the precursor to dopamine, and its pharmaceutical replacement can help to alleviate the effects of dopamine loss in PD[50,51]. However, chronic L-dopa use can lead to unwanted side effects, such as dyskinesia, nausea, and desensitization from excessive drug use[52,53]. To combat this loss of efficacy, usually by 3-5 years of drug use, administration of a dopa-decarboxylase inhibitor, carbidopa, is used in tandem with L-dopa to alleviate nausea symptoms and increase the efficacy of L-dopa[54,55]. Other drugs used to treat PD include DA receptor agonists, such as bromocriptine and lisuide, to stimulate D2 receptors and promote DA replacement[56,57] and MAO inhibitors, which work to increase the availability of DA in the synaptic cleft[58]. Additionally, anticholinergic agents may be used to treat PD, as they work to balance DA and acetylcholine levels in the brain which can lead to increased DA in the striatum[56]. Early surgical intervention for PD included ablation therapy[59], however the vast amount of side effects promoted the

development of Deep Brain Stimulation (DBS) surgery to minimize PD symptoms. DBS involves implantation of an electrode in the subthalamic nuclei (STN) and globus pallidus of the brain to inhibit activity of the STN and recover motor symptoms in patients[60,61]. DBS is typically used in patients who have been overexposed to dopamine replacement therapy drugs, and only targets the tremor-based symptoms of the disease[60].

Ultimately, the lack of long-term efficacy, invasiveness and multitude of side effects begs the development of new treatments to prolong the life and quality of life of those with PD. Although DA cell loss is ultimately the end point of PD pathogenesis, a focus on DA neuron loss cannot address all parts of this complicated disease. One window into the pathogenesis of PD is α-syn, as mutations in its gene cause PD and its accumulation into LBs is present in the majority of PD patients[23,36]. Research into α-syn and its involvement in the development of PD may provide the missing piece needed to cure, or better treat this debilitating disease.

1B. THE ROLE OF ALPHA-SYNUCLEIN IN PD

1.B.1 Structure and Function

First discovered in 1993, α-syn is a 140 amino acid (aa) long protein found abundantly throughout the brain[62–65]. It is a member of the synuclein family of proteins, also consisting of β- and γ-synuclein[66]. α-syn is composed of three sections: aa 1-65 comprising the N-terminus in an alpha-helical formation, aa 65-90 comprising the non-amyloid-β-component (NAC), and aa 91-140 comprising the c-terminus[65]. The c-terminal end of α-syn has been found to be involved in its subcellular locale and interactions with protiens[67,68] and the NAC is most implicated its pathological aggregation[64,66,69].

Although α-syn is generally well characterized biochemically, the exact function of the protein remains elusive. α-syn is primarily found in the cytoplasm with a pre-synaptic locale, however it has also been associated with neuronal nuclei, the Golgi apparatus, endoplasmic reticulum, mitochondria and endolysosomes[65,70–74]. Functionally, α-syn is hypothesized to be involved in the synapse, particularly in neurotransmitter release and vesicle trafficking[75,76]. Additionally, α-syn is thought to be involved in the immune system, as gastrointestinal (GI) inflammation and illness promotes the increase of α-syn, which in turn increases the recruitment of immune cells and is necessary for certain immune responses[77–79].

Although there is a strong emphasis on research pertaining to α-syn and more is being learned about the normal and pathological roles of a-syn, there remains a void in our understanding because we do not know the exact cells the α-syn occupies. Attempts to visualize α-syn throughout the brain leave much information to be uncovered, as the cytoplasmic, pre-synaptic locale of the protein causes a diffuse staining pattern using traditional immunostaining methods. This gives the impression that α-syn is expressed uniformly throughout the brain and in all cell

types when RNA in situ hybridization (ISH) experiments have shown otherwise[80]. To fully understand the role of α-syn in PD and normally, we must uncover the exact topography of this elusive protein, throughout the brain.

1.B.2 Lewy Bodies and α-synuclein's implication in disease

The formation of LB and LNs are one of the two hallmarks of PD, which are accompanied by motor and non-motor dysfunction in PD. The main component of LBs and LNs is α-syn which aggregates and can cause toxicity when oligomerized or fibrilized[28,29](Figure 1). Structurally, LBs form in the cytoplasm of cells and consist of a dense core surrounded by a halo of fibrilized protein, primarily α-syn, and LNs are more filamentous aggregates of α-syn[81,82]. Lewy structures also consist of other proteins, such as leucine rich repeat kinase 2 (*LKKR2)* and histone deacetylase 6 (*HDAC6*)[83,84]. When these protein aggregates form in the brain, cellular processes and cell survival are impacted, causing PD and PD-like symptomology. Mutations to certain genes, such as *SNCA* and glucocerebrosidase *(GBA)* have been directly linked to cause LB pathology in hereditary PD[36,85].

1.B.3.Synucleinopathies

α-syn aggregates are also present in MSA and LBD, which are collectively termed synucleinopathies[86,87]. In PD and LBD, LBs form in the neurons on affected cells, however in MSA Lewy structures form in the cytoplasm of oligodendrocytes, are called Glial Cytoplasmic Inclusions (GCIs), leading to differential disease presentation. Beyond the common feature of Lewy body formation in synucleinopathies, these diseases are analogous in having autonomic dysfunction, and neurodegeneration, however the manifestation and severity of these symptoms

differ depending on the disease[88]. Interestingly, REM sleep disorder predates the onset of motor and autonomic dysfunction in all synucleinopathies[89]. Typically, in MSA autonomic dysfunction is more severe, accompanied by extreme bladder dysfunction[88]. PD and LBD typically show parkinsonism and anosmia, where MSA patients do not[88].

1.B.4. Aggregation, misfolding, and spread of α-synuclein

The exact triggers of the aggregation of α-syn are unknown. In 2003, a theory developed by Heiko Braak, Kelly Del Tredici and Eva Braak states that α-syn pathology is initiated by a pathogen entering the body through the nasal cavity and traveling down the vagus nerve to the GI tract, where α-syn is oligomerized[15,90]. α-syn oligomers are then able to spread in a prion like manner where misfolded α-syn can seed, and corrupt, endogenous α-syn, thereby propagating pathology throughout the nervous system. Accordingly, in Braak staging, α-syn spreads outward from the most rostral and caudal parts of the brain, in phases which are associated with PD symptomology [15,90]. This theory accounts for disease progression in about 50% of PD patients[91]. Further evidence for this "prion-like" spreading of α-syn has been shown *in vitro*, as inoculation of healthy neurons with fibrilized exogenous α-syn leads to the production of LB like-inclusions[92,93]. Additionally, *in vivo,* injection of toxic α-syn aggregates, or synthetic pre-formed fibrils (PFFs), into the striatum of *wild type (wt)* mice cause aspects of PD symptomology in mice[94], including Lewy-like pathology, DA neuron loss, and motor deficits, suggesting a further role of the pathological spreading of aggregated α-syn. This spreading occurs only in the presence of endogenous a-syn, as *Snca* heterozygous KO mutants have less spreading than *wt* mice, and homozygous KOs have no PFF induced spreading[92]. In clinical studies, transplantation of healthy grafted nigral neurons into PD patients lead to these neurons eventually developing

LB-like inclusions, suggesting the seeding of toxic α-syn from endogenous neurons into the healthy grafted neurons[95,96]. However, this spread did not occur in people who received growth hormone from PD patients, suggesting some limitations to Braak's hypothesis[97]. Additionally, studies have shown that disease progression does not always match Braak staging, and sometimes symptoms do not line up with pathology[98–101]. Although the Braak hypothesis accounts for the spread of pathology in most cases of PD, more research into α-syn and its role in PD is essential to our understanding of this disease.

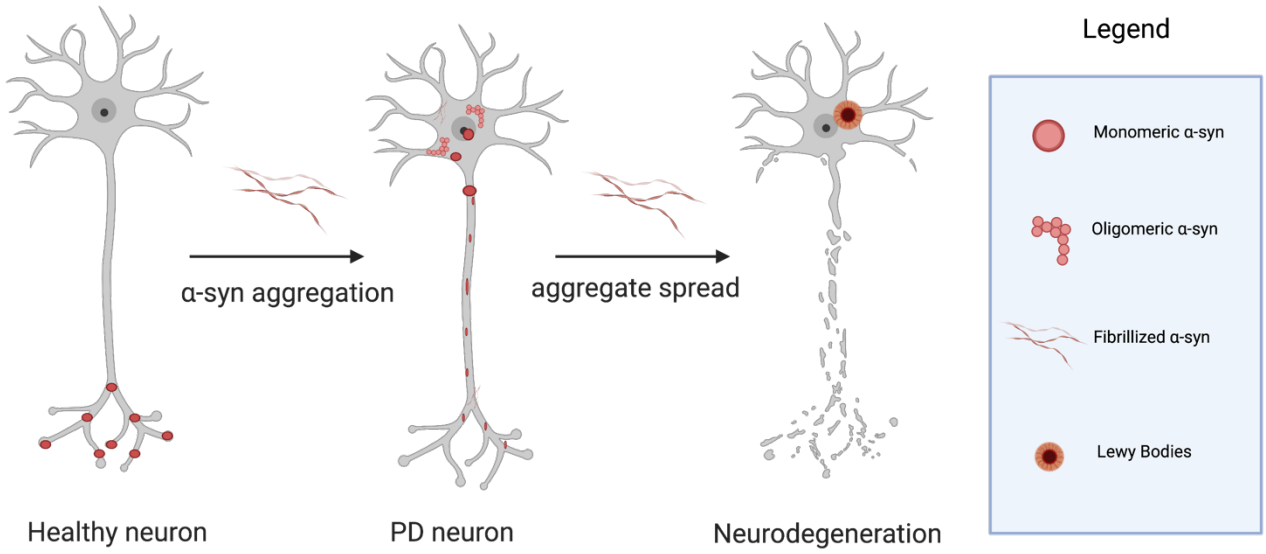

Figure 1: Progression of α-syn toxicity in PD neurons from a healthy neuron. Illustration of α-syn progressing from a healthy, monomeric state to its toxic oligomerized and fibrilized form. Eventually, these aggregates can form an LB and lead to neurodegeneration.

1.B.5 Mouse models of α-synuclein toxicity and PD.

Since PD does not naturally occur in animals, its pathology needs to be artificially induced to study its features in *in vivo* models. PD-like scenarios in rodents can be triggered by genetic manipulation, either by loss of function or gain of function, or by exposure to toxins. Pesticides, such as Paraquat and Rotenone, induce systemic PD-linked synucleinopathy[44,102–105], while focal injection with PFFs cause local pathology that spreads to synaptically connected structures[92–94]. These toxins can induce a variety of the hallmarks of PD including dopaminergic neuron loss and Lewy-like structure formation. Point mutations and other copy number variations in the α-syn gene, *SNCA,* cause PD[106–110]. These mutations can be introduced into mice to recreate some

of the PD-linked features, including decreased striatal dopamine signaling and olfactory dysfunction[111].

1.B.6 Issues in the study of α-synuclein.

Although much is known about α-syn, many aspects of this protein remain elusive. Outside of the lack of definitive function and triggers of α-syn aggregation, the endogenous cell-specific distribution of α-syn remains unknown. While immunostaining for α-syn to visualize the protein is well established, since α-syn is a cytoplasmic protein, staining looks diffuse throughout the brain, giving the impression that α-syn is uniformly present. This is likely not the case, as studies looking at RNA in situ hybridization of *Snca*, and *Snca*-GFP knockin mice show patterns of α-syn expression which are not brain wide[112,113], leaving a major gap in our understanding of this protein. To overcome the diffuse staining pattern elicited from endogenous α-syn, I used a recently developed mouse model, the *Snca*$^{NLS/NLS}$ mouse, as a reporter line to determine the locale of α-syn [114]. These mice, which have α-syn localized to the nucleus by insertion of an NLS tag into the *Snca* gene, show PD like motor deficits at 9 months of age, and cortical neurodegeneration at 18 months, but are also able to clearly show the nuclear presence of α-syn by condensing the protein to the nucleus of cells (Figure 3)[114]. This thesis will expand upon the study of nuclear α-syn with these mice by looking at the endogenous distribution of α-syn, using nuclear α-syn as a reporter to determine the precise location and intensity of α-syn throughout the brain, with the goal of identifying cells with differential levels of α-syn, both in percentage of cells that contain α-syn and the intensity of α-syn in these cell types. Considering the relation of *SNCA* dosage to pathology[39,115,116], it is possible that cells with increased α-syn are most

susceptible to LB pathology, and therefore elucidating these cells as potential targets for treatments and therapeutics is essential in our understanding of PD.

2. HYPOTHESIS

Snca^{NLS} reporter mice will show region and cell-type specific protein levels throughout the brain, giving insight into neuronal circuits and cells most vulnerable to synucleinopathy.

3. AIMS

1. Generate a brain-wide atlas of endogenous α-syn topography, distribution, and cells-of-origin in *Snca*^{NLS} mice.

2. Determine the abundance of α-syn in defined PD-linked regions and cell types in the brain.

4. CONTRIBTIONS TO PROJECT

Generation, characterization, genotyping, and colony maintenance of the *Snca*^{NLS} mice was completed by Haley Geertsma (Ph.D. Candidate, Rousseaux Lab, University of Ottawa). Dr. Konrad Ricke (Post-doc, Rousseaux Lab, University of Ottawa) and Haley Geertsma assisted me in training the machine learning program, ilastik, to detect nuclear α-syn. Haley Geertsma assisted in the generation of Figure 3. All other experiments, data analysis and figure creation were completed by myself.

5. METHODS

5.1 COLLECTION OF MOUSE TISSUE AND SECTIONING

Ten *Snca*$^{NLS/NLS}$ mice were collected and used in all further analysis. Details of the mouse cohort can be found in Table 1. Mice were anesthetized with 30 units of 120 mg/kg Euthanyl (DIN00141704) before being perfused with 10 ml 1x phosphate buffered saline (PBS) and 10 ml 4 % paraformaldehyde (PFA). Brain tissue was collected and stored for 48 hours in 4 % PFA. Brain tissue was then dehydrated in 10, 20 and 30 % sucrose solutions for 48 hours each before being flash frozen in -40ºC isopentane for 1 minute. Tissue was kept at -80ºC until sectioned. Brain tissue was then cryosectioned, both coronally and sagittally, at 20 μm and -21ºC on the Thermo Scientific HM 525 NX at the Louise Pelletier Histology Core at the University of Ottawa, and stored free floating in 1x PBS + 0.02 % NaN_3 in a 24 well plate at 4ºC until use. 12 sections of brain tissue were collected and placed in each well of the 24 well plate to ensure uniform representation of brain structures throughout the mouse brains.

5.2 α-SYN ATLAS GENERATION

5.2.1 IMMUNOHISTOCHEMISTRY

Mouse brain tissue was stained using the Mouse IgG Vectastain ABC kit. Brains and spinal cord tissues were incubated for 1 hour in blocking buffer (1.5 % Triton X-100, 5 % Vectastain Horse serum in 1X PBS), 24 hours in primary antibody (1:1000 BD Biosciences Purified Mouse anti-α-synuclein (Syn1), Cat 610787) in blocking buffer, and 1 hour in secondary antibody (1:500 Alexa Fluor 488) in blocking buffer. Following secondary antibody, sections were exposed to Vectastain ABC solution (1:200 Solution “A”, 1:200 Solution “B”, made 30 minutes before use)

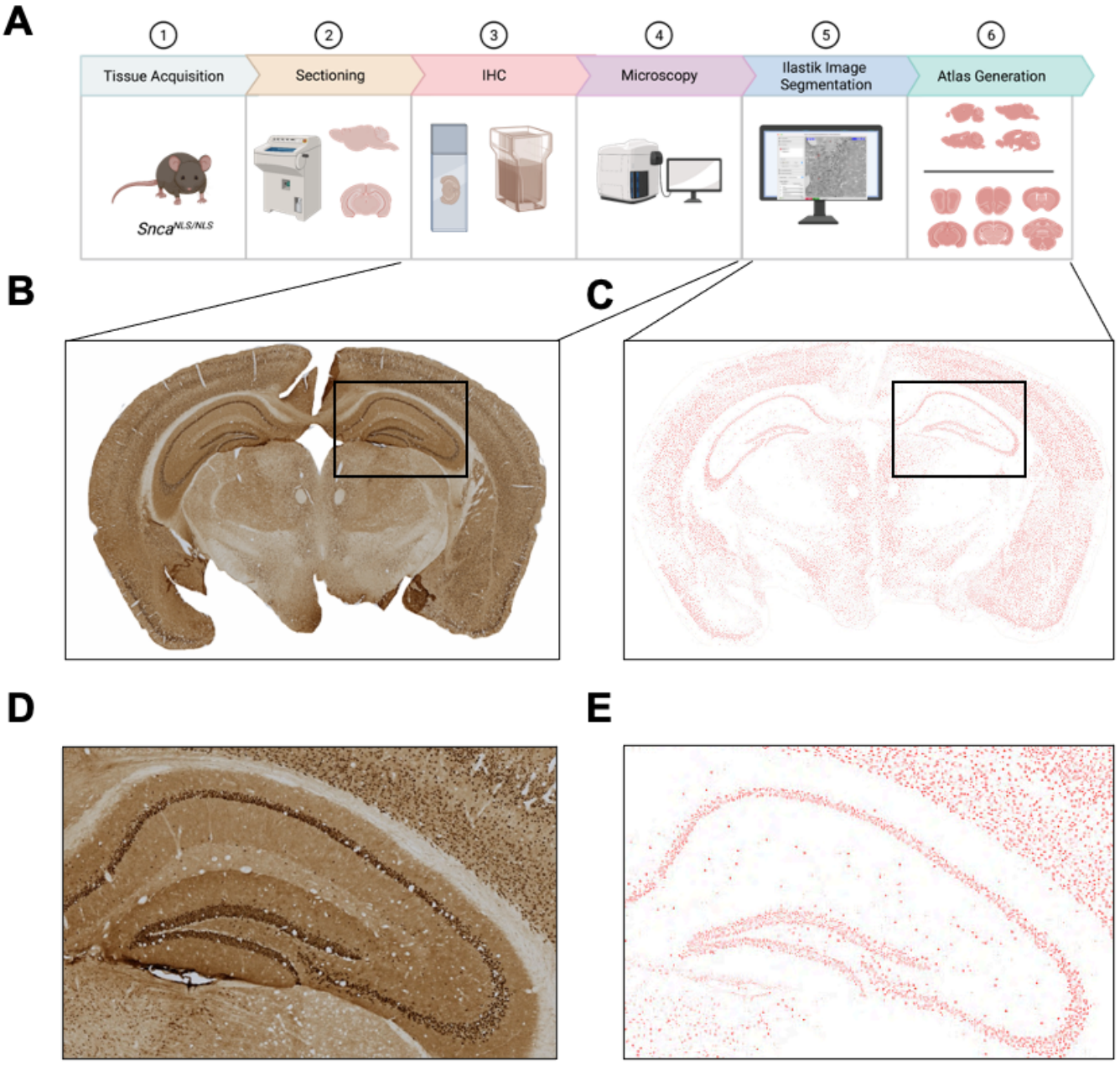

Figure 2 : Pipeline for *Snca*^{NLS} atlas generation. A. Schematic of approach used to generate atlas. B. IHC staining for **α**-syn in *Snca*$^{NLS/NLS}$ tissue. C. ilastik segmentation of IHC stain for **α**-syn. D. Zoomed in IHC staining for **α**-syn in the hippocampus of *Snca*$^{NLS/NLS}$ tissue. E. Zoomed-in ilastik segmentation of IHC staining for **α**-syn.

for 1 hour. Sections were then exposed to DAB KIT for 2 minutes, and excess DAB was washed with 1x PBS. Tissue was washed 5x for 5 minutes in 1x PBS between each treatment and mounted on superfrost slides. Sections were dehydrated in 50% EtOH, 70% EtOH, 95% EtOH and 100% EtOH for 1 minutes each, then finally in 100% Xylenes for 5 minutes. Following dehydration, slides were covered with Permount (Fisher Scientific Cat# SP15-100) and covered with #1.5 coverslips.

5.2.3 IMAGING AND MICROSCOPY

All IHC image acquisition was completed by the Louise Pelletier Histology Core at the University of Ottawa. Images were whole brain slide scanned at 20x magnification on the Axio Scan Z1 Slide Scanner and exported as .czi files for subsequent analysis.

5.2.3 ILASTIK AND ATLAS CONSTRUCTION

IHC images (as .czi files) were imported into FIJI as multichannel "composite" images. The area around the brain sections was selected and background was cleared, then images were exported as .tiff files. For analysis in ilastik, a new project was created under the "Pixel Classification" pipeline. Three images (N=3) were inputted as training files, and features for ilastik to detect were selected (color/intensity, edge, and texture: σ= 0.7, 1.6, 5.0). To eliminate training bias, three students (ZAF, HMG, KR) completed ilastik training to outline positive signal and background on the same image. Classification of positive signal is indicated in red and background in white (Supplementary Figures 1 and 2). Once training was completed to encompass the variance between IHC stains, all .tiff files were inputted into ilastik under the "Batch Process" function and exported as .tiff files.

Export from ilastik was imported into FIJI as “colorized” images, and then LUT “greys” was assigned to the images, followed by the “invert LUT” command. Images were exported as .jpg files from FIJI, then imported into GIMP. To assign the final red color to atlas images, a layer with the final atlas color was added as a screen, and background was set to “color to alpha”. Images were then exported as .jpg files.

To construct the atlas, all serial sections were matched to the Allen Brain Atlas (ABA) and assigned an ABA and Bregma coordinate. 8 representative images from the coronal atlas and 6 from the sagittal atlas, spaced throughout the brain, were chosen for Supplementary Figures 1 and 2 to best represent the distribution of α-syn throughout the brain.

5.3 ATLAS QUANTIFICATION

5.3.1 HEMOTOXYLIN STAINING FOR NUCLEI

Mouse brain tissue (N=3) was stained using the abcam H&E Staining Kit (ab245880). Tissue was previously stored free floating in 1x PBS + 0.02% NaN_3 in a 24 well plate at 4ºC and was washed in 1x PBS for 10 minutes before staining to remove NaN_3. A 24 well plate was used for staining, and one section of tissue was placed in each well. Hematoxylin was placed to cover the tissue in each well and was left to incubate for 5 minutes. Tissue was then washed in two changes of water, and blueing reagent was added for 15 seconds to each piece of tissue, then washed again 2x in distilled water. The eosin portion of the Abcam kit protocol was omitted as only nuclei staining with hemotoxin was necessary. Sections were then dehydrated in 50% EtOH, 70% EtOH, 95% EtOH and 100% EtOH for 1 minutes each, then finally in 100% Xylenes for 5 minutes. Following dehydration, slides were covered with Permount (Fisher Scientific Cat: SP15-100) and covered with #1.5 coverslips.

5.3.2 IMAGING AND ILASTIK

All hematoxylin image acquisition was completed by the Louise Pelletier Histology Core at the University of Ottawa. Images were whole brain slide scanned at 20x magnification on the Axio Scan Z1 Slide Scanner and exported as .czi files for subsequent analysis. .czi files were imported to FIJI and exported as .tiff files, and inputted through the ilastik, FIJI and GIMP pipeline using the same protocol as in Section 5.2.3.

5.3.2 REGIONAL QUANTIFICATION

Hematoxylin staining was matched to the appropriate ABA coordinate, and an N of 3 hematoxylin and α-syn atlas images were used in subsequent analysis at ABA sagittal level 14 (Bregma 1.35). To count the number of nuclei in each brain region of interest, in FIJI a region of interest (ROI) was drawn matching the layers for the brain region according to the ABA (Figure 5). The "analyze particles" function in FIJI was used to count the number of cells over 5 pixels in sizes, corresponding to a single nucleus. The number of nuclei per region in the hematoxylin sections was averaged between the N of 3, and the percentage of α-syn positive nuclei per region was determined as a percentage of the average number of hematoxylin positive nuclei per region. ISH data from the ABA was extracted from *Snca* experiments 79904550 and 990 and averaged, then used in Figure 6 to compare ABA ISH data to α-syn Atlas data[80].

5.4 CELL-TYPE AND REGION-SPECIFIC α-SYN OVERLAP

5.4.1 IMMUNOFLUORSENCE

Brain tissue obtained using the methods from section 5.1 was incubated for 24 hours in blocking buffer (1.5 % Triton X-100, 10 % cosmic calf serum in 1X PBS), 24 hours in primary antibody and 1 hour in secondary antibody with DAPI at 1:1,000 (Millipore Sigma, D9542-1MG). Tissue was washed in 1x PBS 5 times for 5 minutes each between each treatment and mounted on Fisherbrand Superfrost Plus slides. After drying for 24 hours, sections were covered with DAKO mounting medium (Cat: S3023, Lot: 11347938) and #1.5 coverslips. Exact primary antibody concentrations for each experiment as well as corresponding secondary concentrations can be found in Table 2.

5.4.2 IMAGING AND MICROSCOPY

IF images were taken on the Zeiss AxioObserverZ1 LSM800 at the Cell Biology and Image Acquisition core at the University of Ottawa. Images used in CellProfiler analysis were taken at 20x (0.8 numerical aperture [na]) objective with 8bit 1,024 x 1,024 resolution with a Z distance of approximately 0.88 μm per image. Representative images used in all IF figures (Figures 7-10, 12) were taken at 40x (1.3 na) oil objective with 8-bit 1,024 x 1,024 resolution and a Z distance of approximately 0.47 μm per image. Specific multichannel acquisition parameters used to detect signal for each antibody can be found in Table 2.

5.4.3 FIJI ANALYSIS OF IMMUNOFLORESENCE DATA

IF images taken on the LSM800 were analyzed using FIJI. For the analysis on 40x images (Figures 7-10, 12) .CZI files were inputted into FIJI as “colorized” images, then Z-projected at

max intensity. Z-projected images were separated by channel and the brightness was set to identical values for each comparison. Images were then merged and exported as .jpg files. For the analysis on 20x images later used in CellProfiler, .CZI files were inputted into FIJI as "colorized" images, then z projected at average intensity. Images were exported as .tiff files for later use.

5.4.4 CELLPROFILER QUANTIFICATION OF α-SYN INTENSITY AND NUMBER

.tiff files from FIJI were imported into CellProfiler. Image metadata was extracted, and images with "C" matching 0 were assigned as cell type (either neurons, astrocyte, microglia, or oligodendrocytes), 1 were assigned as DAPI, 2 assigned as αSyn. Cell type and αSyn positive cells were counted individually using the "IdentifyPrimaryObjects" feature (pixel size 20-50 for α-syn, neurons, 30-50 for astrocytes and microglia, and 20-50 for oligodendrocytes). For astrocyte signal, since immunostaining is not nuclear, Gfap/Aldh1l signal was assigned to a DAPI positive cell using the "RelativeObjects" function, and the output from this was used in the follow analysis to determine overlap between α-syn and cell types. To determine overlap between α-syn and each cell type, the function "Threshold" and "MaskObject" to isolate cells with α-syn signal over a certain intensity and create a mask of the cell type over the α-syn signal. The "IdentifyPrimaryObjects" function was then used to count the output from the masked threshold analysis, and the "MeasureObjectIntensity" function was used to determine the intensity of α-syn in cell types containing the protein. Data were then exported as a .xls/.pzfx file and analysed in Excel and Prism, respectively.

To determine the percentage of each cell type that α-syn occupies, the total number of α-syn positive cells was divided by the total number of each cell type and multiplied by 100 (Figure 7-10,12). To determine the intensity of α-syn in each cell type, the output of each individual intensity point from cell profiler was inputted into Prism and plotted to visualize the mean and distribution of the intensity of cells. To determine the variance between the means of each group, a one-way ANOVA (post hoc Tukey's multiple comparisons test) was conducted by Prism, and a *p* value below 0.05 was considered as a significant difference in the mean intensity between groups.

6. RESULTS

6.1 *Snca*$^{NLS/NLS}$ mice are a reporter of endogenous α-syn levels.

Although well characterized in structure and function, the topography of α-syn throughout the brain remains elusive. Typical immunostaining results in a diffuse pattern (Figure 3B), making it hard to clearly visualize the cells in which α-syn resides since this protein has a presynaptic cellular locale (Figure 3C). To combat this, the *Snca*$^{NLS/NLS}$ mouse was generated by the Rousseaux Laboratory as a novel mouse line that localizes endogenous cytoplasmic α-syn to the nucleus of neurons[114.] This phenomenon is possible by inserting a nuclear localization signal (NLS), as well as a flag tag, into the C-terminus of the mouse *Snca* gene (Figure 3A), which forces the majority of endogenous cytoplasmic α-syn into the nucleus of the cells (Figure 3C). In turn, α-syn is targeted and concentrated to the cell's nucleus, permitting precise visualization of cells containing α-syn in the brain (Figure 3C). Initially generated to study the toxic effects of nuclear α-syn, this mouse line can also be used as an α-syn reporter, as staining for α-syn results in distinct nuclear signal, instead of the typical diffuse cytoplasmic signal seen in wild-type mice (Figure 3C). We used this model for the rest of our analyses, allowing for the precise visualization and mapping of α-syn throughout the brain.

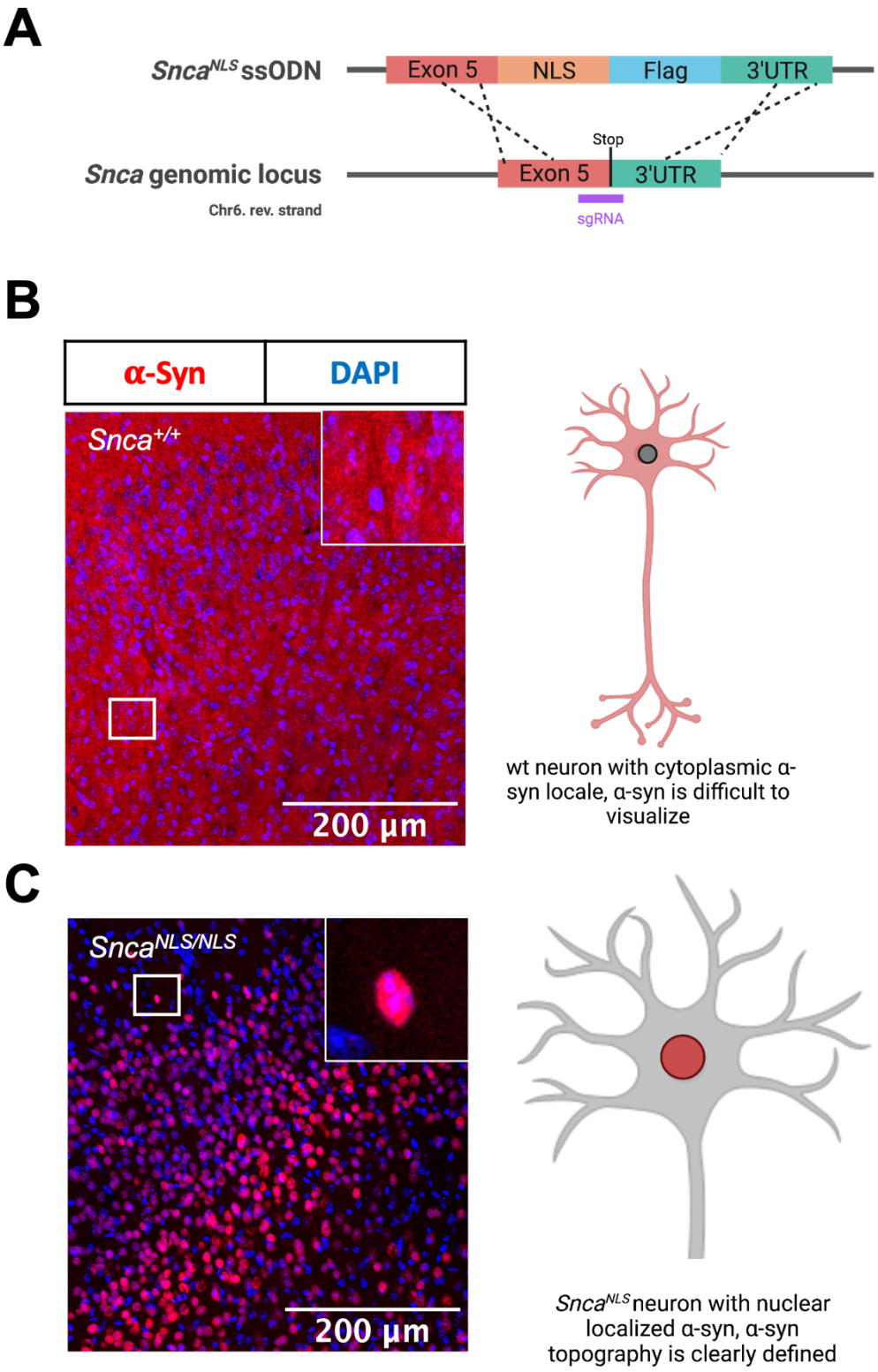

Figure 3: The use of *Snca*$^{NLS/NLS}$ mice as a reporter of α-syn distribution. A. Insertion of an NLS and Flag tag into the 3' of the mouse *Snca* gene. B. Diffuse visualization of α-syn in wt mice and graphical illustration of the distribution of α-syn in a wt neuron. C. Visualization of nuclear α-syn in *Snca*$^{NLS/NLS}$ mice and graphical illustration of the nuclear α-syn in an *Snca*$^{NLS/NLS}$ neuron.

6.2 Visualization of nuclear α-syn throughout the brain allows for construction of an atlas showing the precise distribution of this protein.

To assess the brain wide distribution of α-syn, we stained serial *Snca*$^{NLS/NLS}$ brain sections (both sagittal and coronal) using IHC. We used ilastik to create a machine learning pipeline to identify and distinguish nuclear signal from background and processed all brain sections (approximately 50 per brain, 6 brains total) using this program. Final ilastik output was aligned to the coordinates and sections on the Allen Brain Atlas (ABA)[80], and a brain wide atlas of α-syn distribution was developed, hereby referred to as the *Snca*^{NLS} Atlas (Supplementary Figures 1, 2). To best show the distribution of α-syn in the brain, 4 coronal sections and 1 sagittal section were selected as representative sections and the visual intensity of α-syn per brain region was quantified (Figure 4). This atlas shows clear differences between the amount of α-syn positive cells in differential brain regions at the protein level from the previous developed atlas of ISH data[80], (Figure 4, Supplementary Figures 1, 2). The regions with the highest visual α-syn intensity were the OB glomeruli, mitral layer, and granule layer, cortex layers 4-6, pyramidal layer (PL) of the hippocampal formation (HCF), granule layer of the HCF, SNc, LC, and granule layer of the cerebellum. The regions with the lowest visual α-syn intensity were the cortex layer 1 (CTX1), Thalamus (TH), Caudoputamen (CP), and the *stratum oriens* (SO), *stratum radiatum* (SR), polymorph layer (PO) and molecular layer (MO) of the hippocampus (HCF).

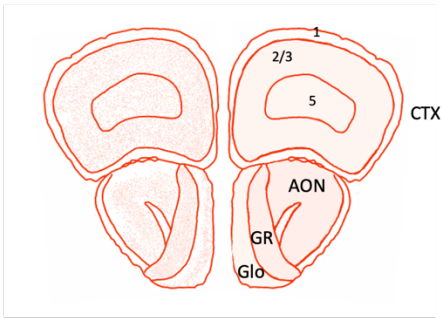

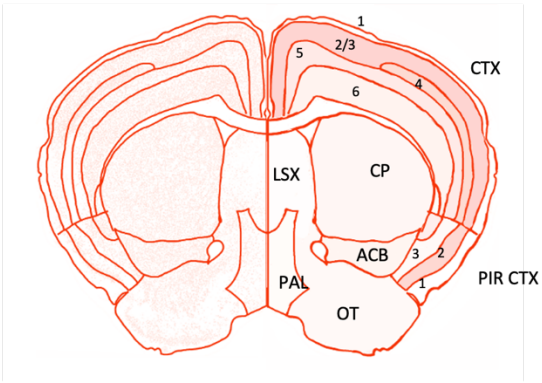

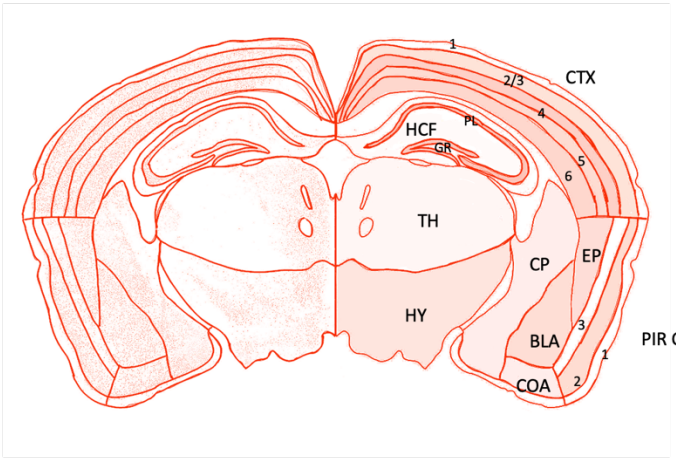

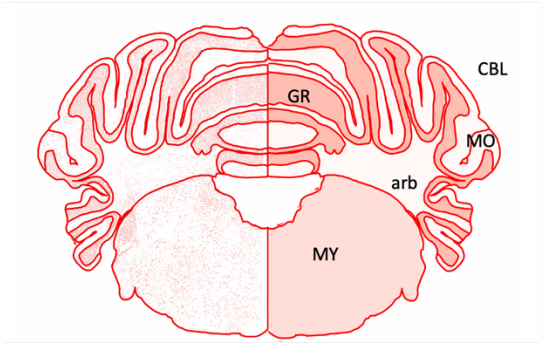

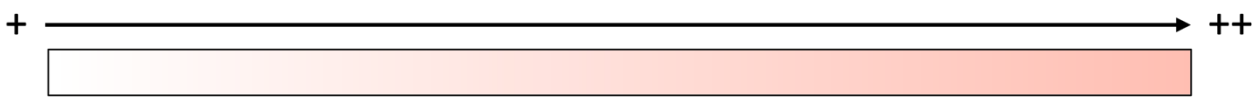

Relative amount of α-syn positive cells per region

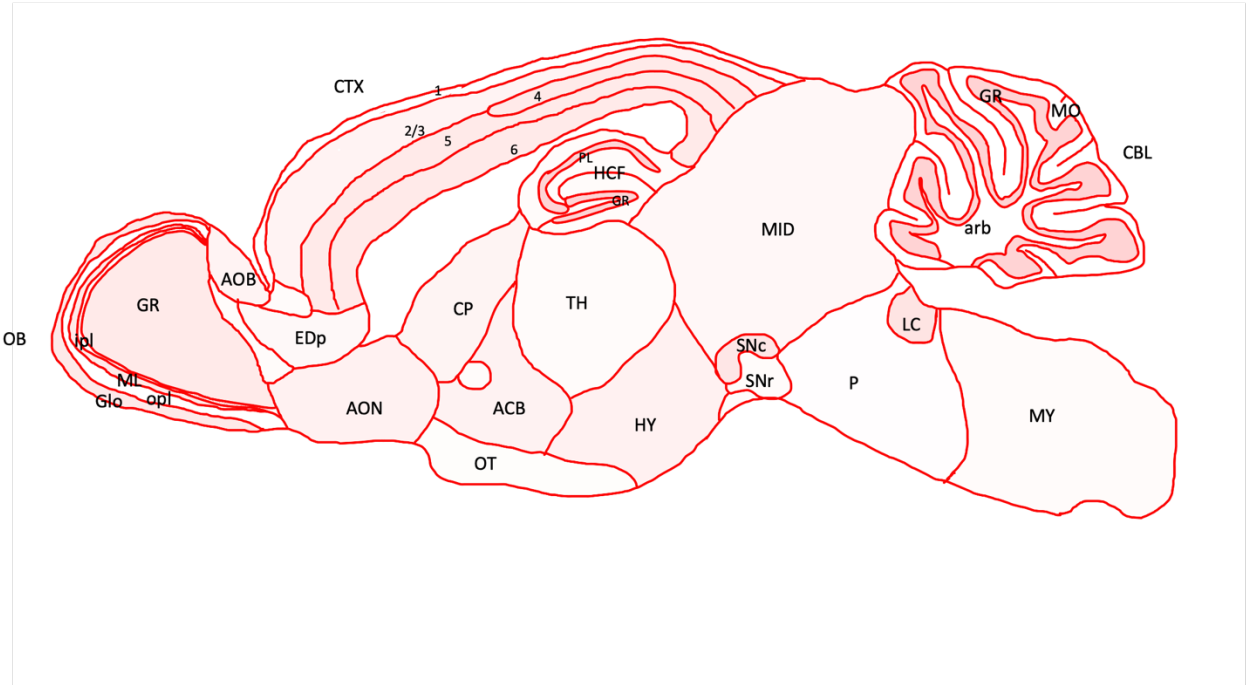

Figure 4: Qualitative analysis of regional α-syn levels. Representative images of ilastik Atlas images detecting nuclear **α**-syn in *Snca*$^{NLS/NLS}$ mice. Brain sections are from the following ABA and bregma coordinates (nm), respectively: Coronal, 25; 2.945, 44; 1.045, 79; -2.48, 114; -6.055, Sagittal, 14; 1.35. Left side of coronal sections represents ilastik output aligned with ABA layers, right side of A-D showed average cellular intensity of α-syn per regions. Abbreviations are listed below. For more information on atlas serial sections, see Supplementary Figures 1 and 2.

Abbreviation Brain Regions (Figure 4)

ACB	Nucleus accumbens	**LSX**	Lateral septal complex
AOB	Accessory olfactory bulb	**MID**	Midbrain
AON	Anterior olfactory nucleus	**ML**	Mitral Layer
arb	Arbor vitae	**MO**	Molecular layer
BLA	Basolateral amygdala	**MY**	Mendulla
CB	Cerebellum	**opl**	Outer plexiform layer
CP	caudoputamen	**OT**	Olfactory tubercle
COA	Cortical amygdalar area	**P**	Pons
CTX	Cortex	**PAL**	Pallidum
EDp	Endo piriform nucleus	**PIR CTX**	Piriform cortex
Glo	Glomeruli	**PL**	Pyramidal layer
GR	Granule Layer	**SNc**	Substantia nigra pars compacta
HCF	Hippocampal Formation	**SNc**	Substantia nigra pars reticulata
ipl	Inner plexiform layer	**TH**	Thalamus
LC	Locus coeruleus	**#**	Layer number

6.3 Normalization of nuclear α-syn counts to total neuronal counts shows regional differences in α-syn expression

To ensure the visual patterns of α-syn expression seen in Figure 4 were consistent with the quantitative data, we normalized the total counts of α-syn to total nuclei counts based on hematoxylin staining. We did this to remove any bias that may occur when qualitatively looking at the levels of α-syn per brain region, as regions with higher cell density could be skewed towards falsely reporting higher amount of α-syn positive cells. All hematoxylin staining was subjected to the same ilastik pipeline as the α-syn IHC data to ensure identical classification of positive cell signal and background (Figure 5). Comparison of identical (according to the ABA) sections allowed for delineation of regions and layers (Figure 5), and by using FIJI to count the cell numbers we were able to determine the percentage of cells per region and layer that contain α-syn. Finally, we compared our data to two different experiments we extracted from the ABA RNA ISH database[80] , averaged these values and normalized the Fragments per kilobase million (FPKM) data to 100 to get a percentage of *Snca* RNA expression per region.

Quantification of the amount of α-syn per region showed that the regions with the highest percentage of α-syn, relative to the total amount of nuclei, are the SNc and the locus coeruleus (LC), both differing from the results from the ABA RNA ISH data (Figure 6). The granule, mitral and glomeruli layers of the OB (OB-Glo, ML and GL), motor cortex (MC) layers 2/3 and 5/6, pyramidal layer of the hippocampus (H - PL) and granule layer of the dentate gyrus (DG – GL), and striatum (S) showed medium-to-high levels of α-syn correlating to the ABA ISH, all with approximately 50-80% of cell containing α-syn (Figure 6B). The TH, midbrain *substantia nigra pars reticulata* (SNr) and cerebellum all showed low levels of α-syn correlating to the

ABA ISH data (Figure 6 B, C) with under 40% of cells expressing α-syn. This cerebellum quantification differs vastly from the visual quantification shown in Figure 4, proving the importance of correcting α-syn cell counts to total nuclei per region. Finally, the outer plexiform layer of the olfactory bulb (OB – OPL), MC layer 1, *stratum oriens* and *stratum radiatum* of the hippocampus (H – SO, SR) and molecular and polymorph layer of the DG (DG – ML, PO) showed striking less α-syn in our *Snca*^{NLS} atlas than in the ABA ISH data (Figure 6C).

6.4 α-synuclein is differentially expressed in number and intensity in different brain cell types and regions

After identifying the brain regions where α-syn is differentially abundant, we next looked at the cell types α-syn occupies in each of these regions. We chose to do an in-depth analysis of α-syn density in neurons, microglia, astrocytes, and oligodendrocytes in the CTX, HCF CA1 and OB. All three regions selected had layers with high amounts of α-syn protein (Figure 6), so we chose to highlight those layers to see if there is a pattern to how α-syn occupies CNS cell types. Firstly, we conducted our analysis to determine the amount of α-syn in neurons (Figure 7). We co-stained for α-syn with NeuN which localizes with the nuclei of neurons. We were able to determine visually the overlap between α-syn and neurons (Figure 6A). We quantified the amount of α-syn positive neurons by counting the number of neuronal nuclei, α-syn nuclei, and the number over overlapping cells (Figure 7A). This quantification of the amount of α-syn in neuronal cells showed that α-syn occupies 80-90% of all neurons in the CTX, HCF CA1 and OB (Figure 7B). Of these three regions, neurons in the hippocampus have the highest proportion of α-syn positive neurons, with an average of 89% of all hippocampal neurons containing α-syn.

To further our understanding how α-syn occupies neurons, we determined the intensity of α-syn in each neuronal cell containing the protein through CellProfiler. One-way ANOVA showed that hippocampal neurons contain significantly higher intensity of α-syn compared to the OB and CTX. The difference in intensity between OB and CTX neurons containing α-syn was non-significant (Figure 7C). We compared our results to *Snca* mouse brain RNA-sequencing (RNA-Seq) data from the Brain-RNA-Seq database[80], and saw that α-syn was mostly expressed in neurons, with a FPKM value of 74.97 ± 9.06. FPKM values are used to normalize RNA-Seq data set values to compare the amount of RNA transcripts from a sample, and a higher FPKM value corresponds to more RNA expression of a gene in a cell type. In the case of *Snca* in mouse tissue, the highest FPKM value in the Brain-RNA-Seq data set was for neuronal populations containing α-syn [80].

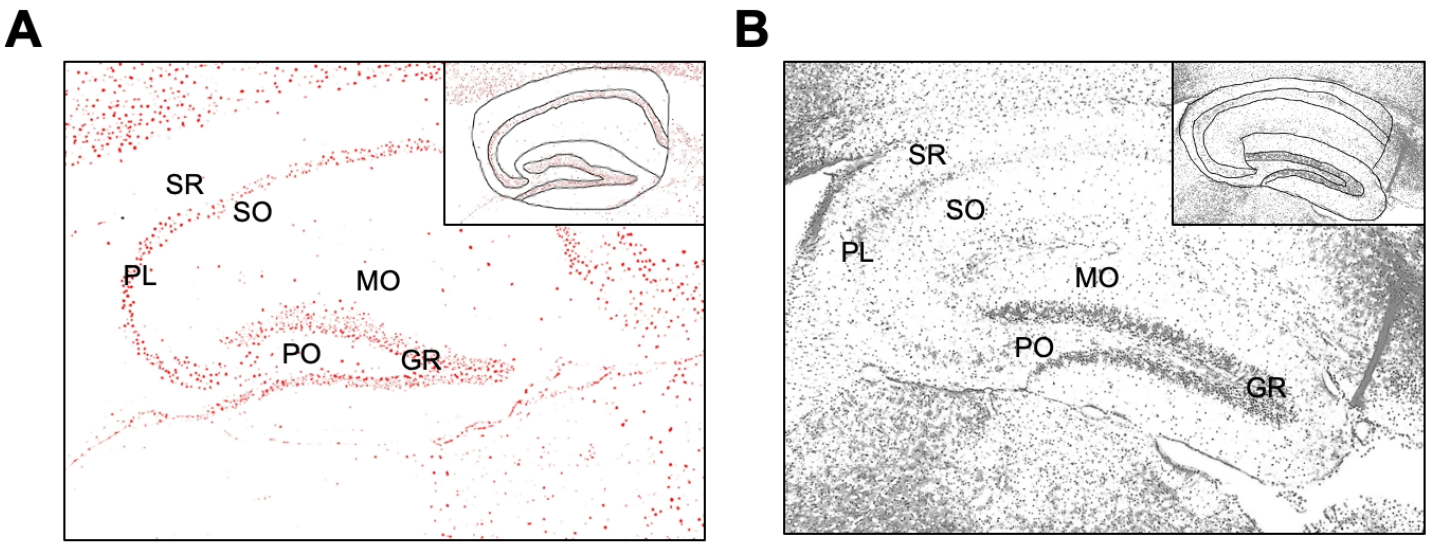

Figure 5: Comparison of nuclei counts to determine differential regional α-syn expression.

Representative images of IHC staining for **α**-syn (A) and hematoxylin (B) analyzed with ilastik. Images are taken at 20x magnification of sagittal *Snca*$^{NLS/NLS}$ mouse brains. Inset represents delineation of hippocampal layers used for subsequent analysis (abbreviations; SR: Stratum Radium, PL: Pyramidal Layer, PO: Polymorph Layer, GR : Granule layer, MO : Molecular layer).

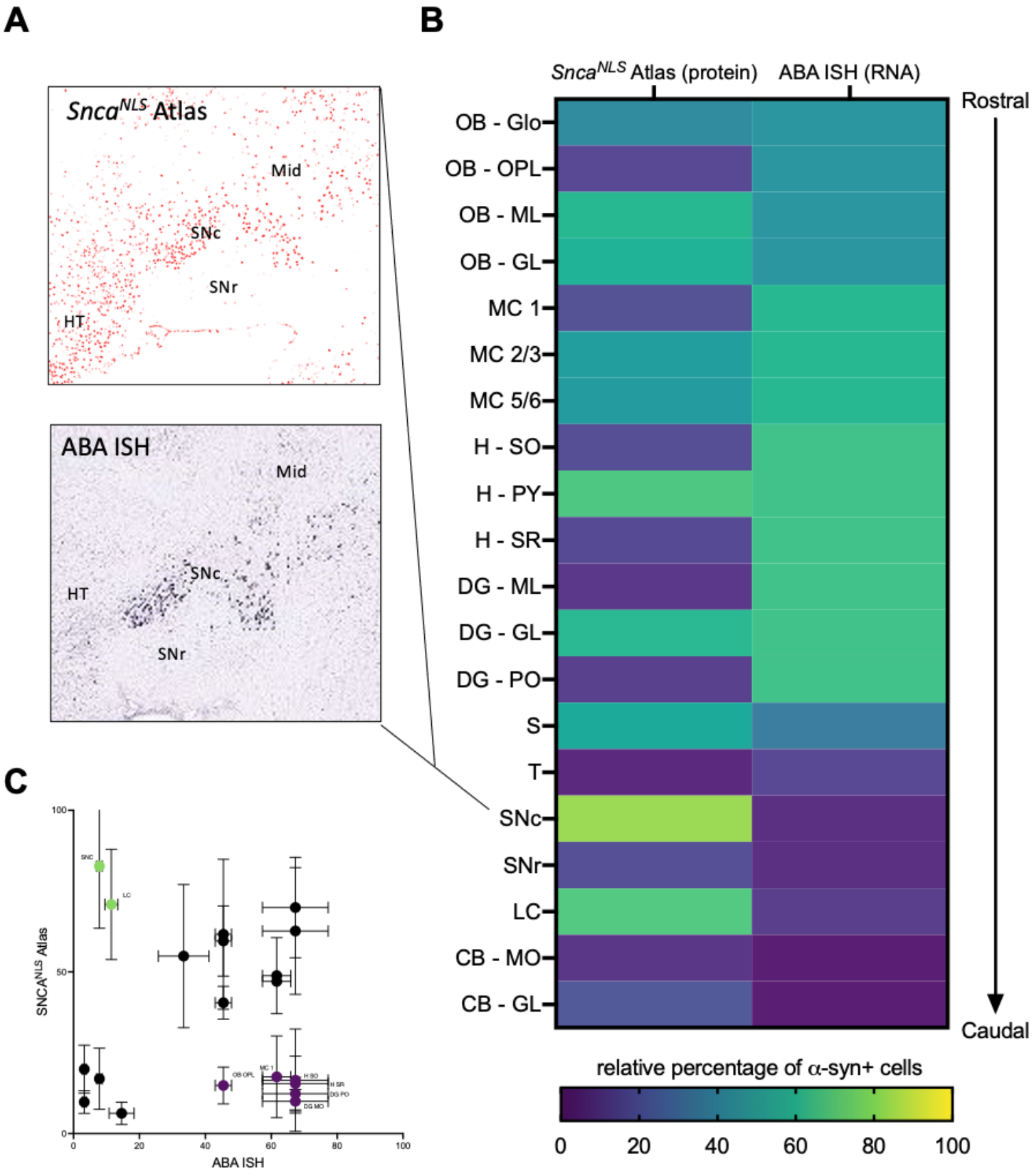
A
Snca^NLS Atlas
Mid
SNc
SNr
HT
ABA ISH
Mid
SNc
HT
SNr
B
Snca^NLS Atlas (protein)
ABA ISH (RNA)
Rostral
OB - Glo
OB - OPL
OB - ML
OB - GL
MC 1
MC 2/3
MC 5/6
H - SO
H - PY
H - SR
DG - ML
DG - GL
DG - PO
S
T
SNc
SNr
LC
CB - MO
CB - GL
Caudal
relative percentage of α-syn+ cells
0
20
40
60
80
100
C
SNCA^NLS Atlas
ABA ISH
0
50
100
0
20
40
60
80
100
SNC
LC
OB OPL
MC 1
H SO
H SR
DG PO
DG MO

Figure 6: Regional quantification of α-syn levels. A. representative images from sagittal sections of the SNc and surrounding areas from the *Snca*^{NLS} Atlas and ABA ISH data. B. Heatmap showing the average percentage of α-syn protein occupancy per region (*Snca*^{NLS} Atlas) compared to the relative RNA expression of *Snca* per region (ABA ISH). C. Correlation plot of the relative α-syn amount per region in the *Snca*^{NLS} Atlas compared to ABA ISH data. Regions with more synuclein in *Snca*^{NLS} Atlas than ABA ISH in green, less synuclein in *Snca*^{NLS} Atlas than ABA ISH in purple. Abbreviations for brain structures: OB Glo – Olfactory bulb glomeruli, OB OPL- Olfactory bulb outer plexiform layer, OB ML – olfactory bulb mitral layer, OB GL – olfactory bulb granule layer, MC1- motor cortex layer 1, MC2/3 – motor cortex layer 2/3, MC 5/6- motor cortex layer 5/6, H SO – hippocampus *stratum oriens*, H PY – hippocampus pyramidal layer, H SR – hippocampus *stratum radiatum*, DG ML – dentate gyrus molecular layer, DG GL – dentate gyrus granule layer, DG PO – dentate gyrus polymorph layer, S – striatum, T – thalamus, HT – hypothalamus, Mid – midbrain, SNc – substantia nigra pars compacta, SNr – substantia nigra pars reticulata, LC – locus coeruleus, CB MO – cerebellum molecular layer, CB GL – cerebellum granule layer.

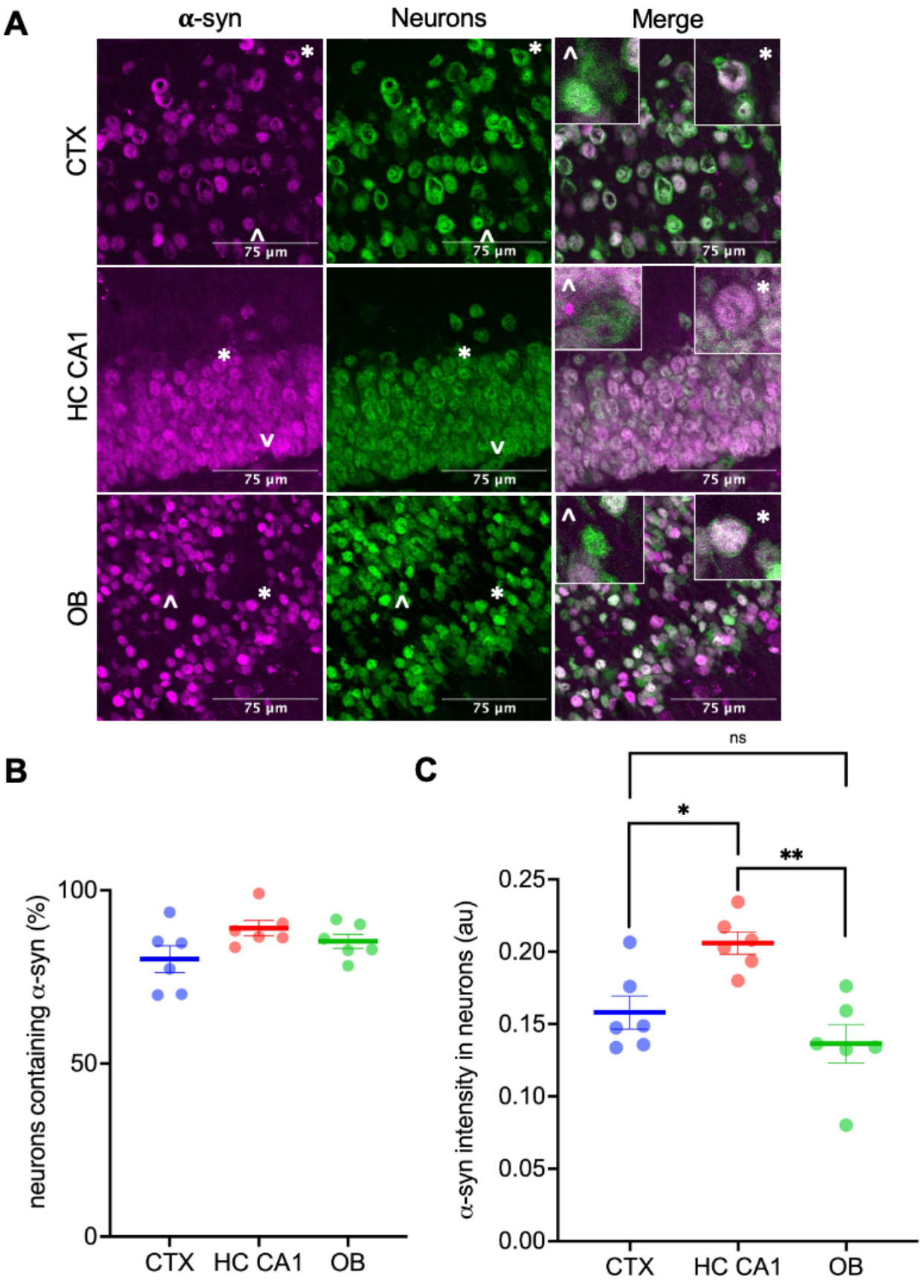
A
α-syn
Neurons
Merge
CTX
HC CA1
OB
75 µm
B
neurons containing α-syn (%)
100
50
0
CTX
HC CA1
OB
C
ns
*
**
α-syn intensity in neurons (au)
0.25
0.20
0.15
0.10
0.05
0.00
CTX
HC CA1
OB

Figure 7: Visual distribution, density, and intensity of α-syn in neuronal cells. A. Comparison of **α**-synuclein (Syn1), neurons (NeuN) and overlap (merge) immunofluorescence staining in the cortex (CTX), hippocampus (HC CA1) and olfactory bulb (OB) of *Snca*$^{NLS/NLS}$ mice. Images taken on the Zeiss LSM800 at 40x magnification (1.3 na). Left inset in merge column represents a neuron without α-syn (^), right inset represents a neuron with α-syn (*). B. percentage of total neurons in the CTX, HC CA1 and OB that contain **α**-synuclein. C. Nested averages of the intensity of α-syn in α-syn + neurons in the CTX, HC CA1, and OB. Differences between groups analyzed using a one-way ANOVA with Tukey's multiple comparisons test (<>0.001 indicated by ****). B and C were analyzed on CellProfiler using 20xmagnification confocal images (0.8 na) an N=6 animals.

Next, we applied our analysis to astrocytes. We used Aldh1l to stain for cortical astrocytes and Gfap to stain for all other astrocytes in the brain and compared this staining to nuclear α-syn IF staining. Visually, we saw that α-syn occupies far fewer numbers of astrocytes (Figure 8A) than neurons, which was unsurprising as the Brain-RNA-Seq FPKM value of expression was 6.03 ± 1.58. Since neither of our astrocyte markers were nuclear, we used CellProfiler to assign each astrocyte to a nucleus by looking at the DAPI co-stain, then determined the presence and intensity of α-syn colocalized with astrocytic DAPI. Quantification of the number of α-syn containing astrocytes showed an average of 5% of cortical astrocytes, 12% of hippocampal astrocytes, and 18% of OB astrocytes containing α-syn (Figure 8B). Interestingly, we saw that while α-syn is present in the smallest number in cortical astrocytes, the intensity of α-syn in these cells was significantly higher than in the OB or hippocampus, suggesting that while α-syn may be present in less cortical astrocytes than other regions of the brain, that these astrocytes contain much more α-syn than other regional astrocytes (Figure 8C). The difference in α-syn intensity of hippocampal and OB astrocytes was non-significant.

We then looked at another glial cell type in the brain, microglia. We co-stained for α-syn with microglia marker Iba1, which labels the nucleus as well as axons of microglial cells (Figure 9A). We saw that an average of 17.2% of cortical microglia, 23.4% of hippocampal microglia, and 23.3% of OB microglia contain α-syn (Figure 9B). This was higher than expected, as the Brain RNA Seq data showed an FPKM value of 5.09 ± 0.68 of *Snca* in microglia. We saw a significant increase in the intensity of α-syn in hippocampal microglia compared to the CTX and OB, suggesting that this region has the highest number of microglial α-syn cells, and the highest levels of α-syn in these cells (Figure 9C).

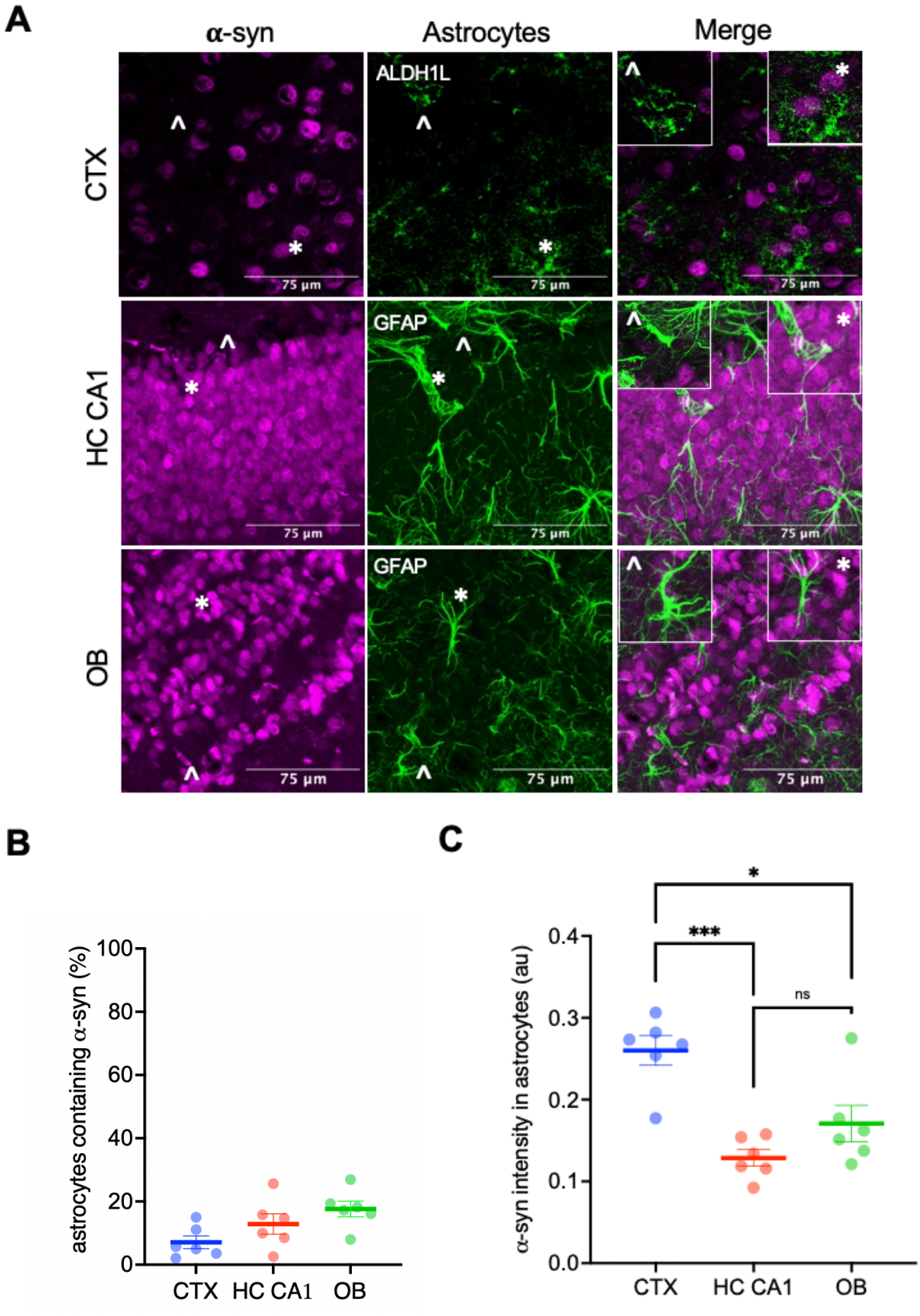
A
α-syn
Astrocytes
Merge
CTX
HC CA1
OB
ALDH1L
GFAP
GFAP
75 µm
B
astrocytes containing α-syn (%)
100
80
60
40
20
0
CTX
HC CA1
OB
C
α-syn intensity in astrocytes (au)
0.4
0.3
0.2
0.1
0.0
*
***
ns
CTX
HC CA1
OB

Figure 8: Visual distribution, density, and intensity of α-syn in astrocytes. A. Comparison of **α**-synuclein (Syn1), astrocytes (Gfap and Aldh1l) and overlap (merge) immunofluorescence staining in the cortex (CTX), hippocampus (HC CA1) and olfactory bulb (OB) of *Snca*$^{NLS/NLS}$ mice. Images taken on the Zeiss LSM800 at 40x magnification (1.3 na). Left inset in merge column represents an astrocyte without α-syn (^), right inset represents an astrocyte with α-syn (*). B. percentage of total astrocytes in the CTX, HC CA1 and OB that contain **α**-synuclein. C. Nested averages of the intensity of α-syn in α-syn + astrocytes in the CTX, HC CA1, and OB. Differences between groups analyzed using a one-way ANOVA with Tukey's multiple comparisons test ($p<0.001$ indicated by ****). B and C were analyzed on CellProfiler using 20x magnification confocal images (0.8 na) an N=6 animals.

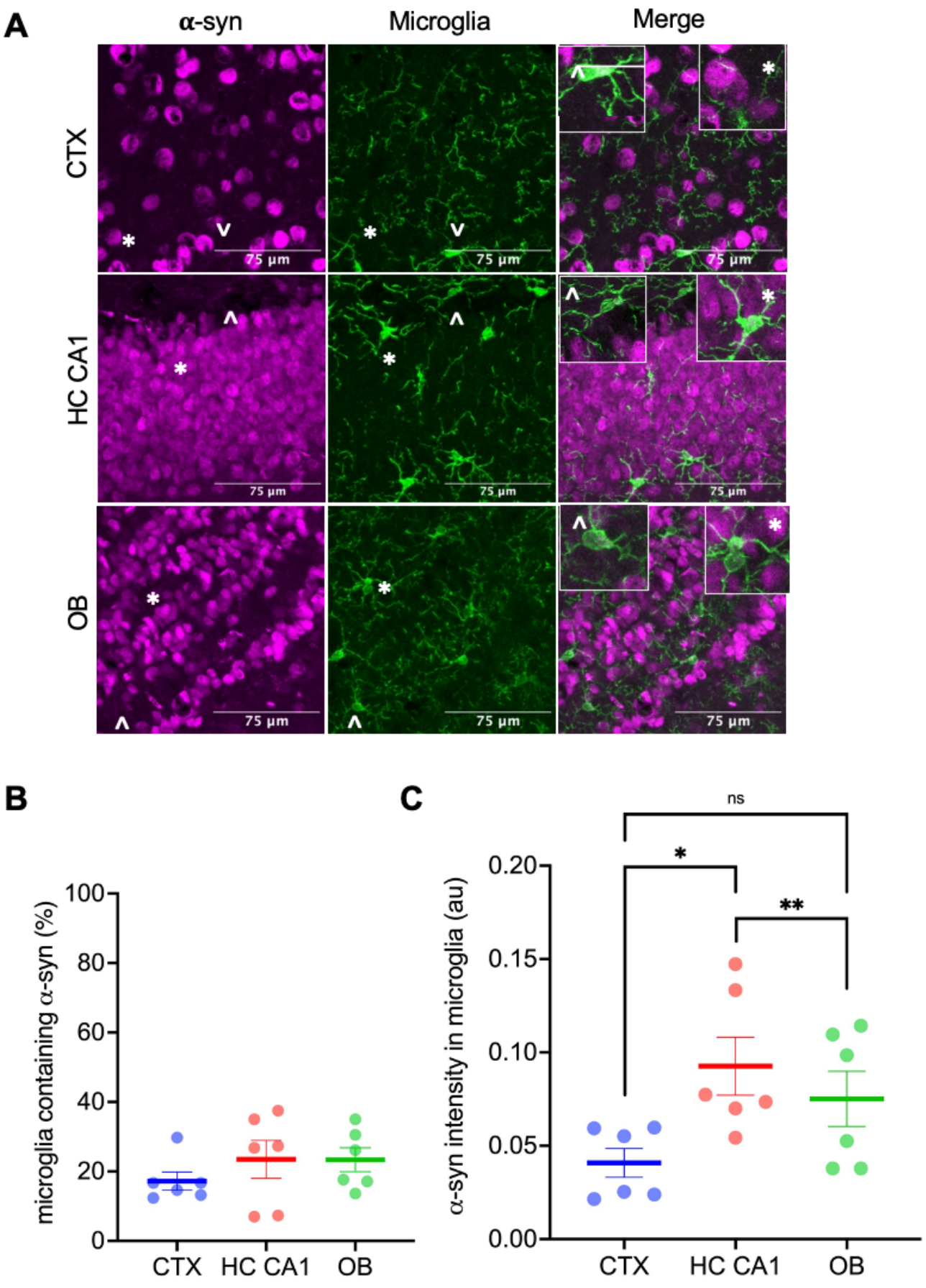
A
α-syn
Microglia
Merge
CTX
HC CA1
OB
75 µm
B
microglia containing α-syn (%)
100
80
60
40
20
0
CTX
HC CA1
OB
C
α-syn intensity in microglia (au)
0.20
0.15
0.10
0.05
0.00
ns
*
**
CTX
HC CA1
OB

Figure 9: Visual distribution, density, and intensity of α-syn in microglia. A. Comparison of **α**-synuclein (Syn1), microglia (Iba1) and overlap (merge) immunofluorescence staining in the cortex (CTX), hippocampus (HC CA1) and olfactory bulb (OB) of *Snca*$^{NLS/NLS}$ mice. Images taken on the Zeiss LSM800 at 40x magnification (1.3 na). Left inset in merge column represents a microglial cell without α-syn (^), right inset represents a microglial cell with α-syn (*). B. percentage of total microglia in the CTX, HC CA1 and OB that contain **α**-synuclein. C. Nested averages of the intensity of α-syn in α-syn + microglia in the CTX, HC CA1, and OB. Differences between groups analyzed using a one-way ANOVA with Tukey's multiple comparisons test ($p<0.001$ indicated by ****). B and C were analyzed on CellProfiler using 20xmagnification confocal images (0.8 na) an N=6 animals.

Finally, we looked at α-syn in oligodendrocytes. We co-stained for α-syn in tandem with Olig2, a nuclear marker for oligodendrocytes (Figure 10A). We saw that on average, 11.3% of cortical oligodendrocytes, 9.8% of hippocampal oligodendrocytes, and 11.6% of OB oligodendrocytes contain α-syn (Figure 10B). This roughly corresponds to the Brain RNA Seq data, which showed a KPMN of 6.16 ± 1.29 in newly formed oligodendrocytes and 10.31 ± 4.56 in myelinating oligodendrocytes. The intensity of α-syn in oligodendrocytes in the hippocampus was significantly higher than that in the CTX and OB (Figure 10C).

Based on our co-staining analysis, α-syn appears to be present mostly in neuronal cells, followed by microglia, astrocytes and then oligodendrocytes. To see the difference in the intensity of α-syn in these four groups per region, we plotted the regional intensity of α-syn and ran a one-way ANOVA (Figure 11). In the cortex, α-syn intensity was significantly higher in astrocytes than in all other cell types. Additionally, the intensity of neuronal α-syn was higher in the cortex than microglial and oligodendrocyte α-syn. There was no significant difference in the intensity of α-syn between microglia and oligodendrocytes (Figure 11). In the hippocampus, neuronal α-syn intensity was higher than in all other cell types (Figure 11). Microglial and astrocytic α-syn was significantly more intense than in oligodendrocytes. The difference in intensity of α-syn in astrocytes and microglia was non-significant in the hippocampus. Lastly, we looked at α-syn intensity in OB cells. In the OB, cortical α-syn intensity was significantly higher than microglial α-syn, but not in astrocytes or oligodendrocytes. Astrocytic α-syn was significantly higher than both microglial and oligodendrocytic α-syn. There were no significantly differences in the intensity of α-syn in oligodendrocytes and microglia.

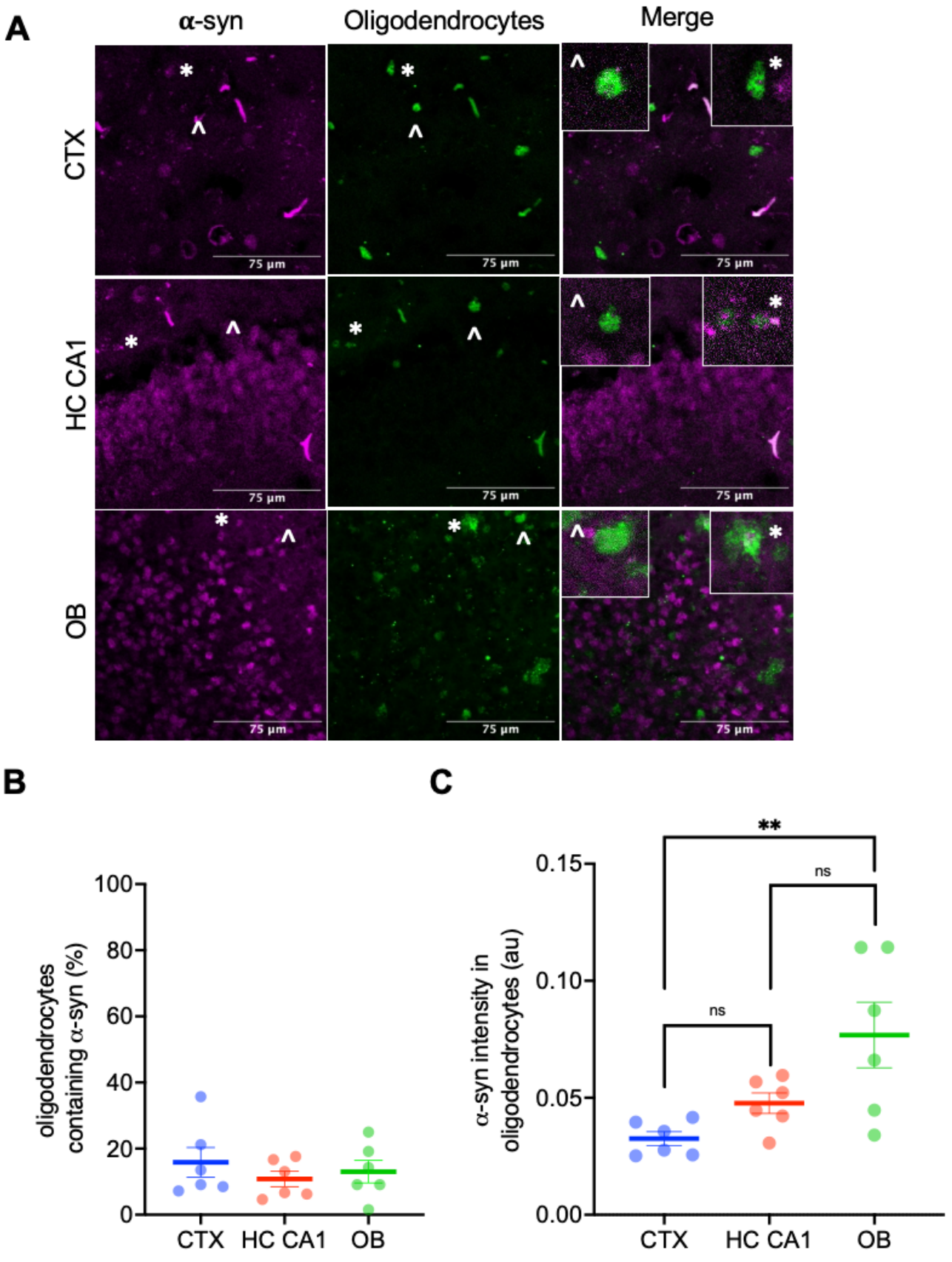
A
α-syn
Oligodendrocytes
Merge
CTX
HC CA1
OB
75 µm
B
oligodendrocytes containing α-syn (%)
100
80
60
40
20
0
CTX
HC CA1
OB
C
α-syn intensity in oligodendrocytes (au)
0.15
0.10
0.05
0.00
**
ns
ns
CTX
HC CA1
OB

Figure 10: Visual distribution, density, and intensity of α-syn in oligodendrocytes. A. Comparison of **α**-synuclein (Syn1), oligodendrocytes (Olig2) and overlap (merge) immunofluorescence staining in the cortex (CTX), hippocampus (HC CA1) and olfactory bulb (OB) of *Snca*$^{NLS/NLS}$ mice. Images taken on the Zeiss LSM800 at 40x magnification (1.3 na). Left inset in merge column represents an oligodendrocyte without α-syn (^), right inset represents an oligodendrocyte with α-syn (*). B. percentage of total oligodendrocytes in the CTX, HC CA1 and OB that contain **α**-synuclein. C. Nested averages of the intensity of α-syn in α-syn + oligodendrocytes in the CTX, HC CA1, and OB. Differences between groups analyzed using a one-way ANOVA with Tukey's multiple comparisons test ($p<0.001$ indicated by ****). B and C were analyzed on CellProfiler using 20x magnification confocal images (0.8 na) an N=6 animals.

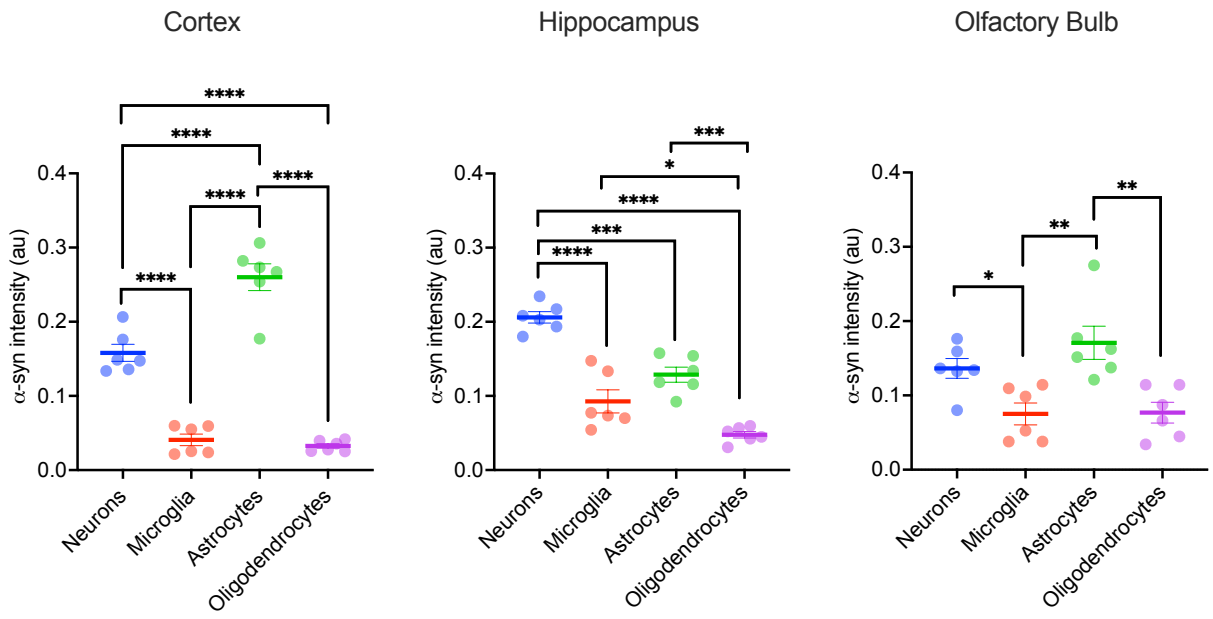

Figure 11: Comparison of cell type intensity of α-syn in the cortex, hippocampus, and olfactory bulb. Intensity is measured using CellProfiler in arbitrary units (au). Differences between groups analyzed using a one-way ANOVA with Tukey's multiple comparisons test ($p<0.001$ indicated by ****, $p<0.01$ indicated by ***, $p<0.05$ indicated by *).

6.5. α-synuclein is preferentially present in catecholaminergic neurons in regions containing highest amounts of the protein.

Finally, we wanted to determine what region-specific cell types contain α-syn in areas of the brain with highest amounts of the protein. Based on our quantification of the percentage of cells containing α-syn per region (Figure 6), we determined that the SNc and LC both contained highest amounts of α-syn and therefore should be further investigated. Both the SNc and LC are affected by pathology in PD and contain primarily catecholaminergic neurons, DA neurons in the SNc and noradrenergic (NA) neurons in the LC. To see the overlap between these neurons and α-syn, we co-stained for α-syn with tyrosine hydroxylase (TH), rate limiting enzyme in the synthesis of both dopamine and norepinephrine (Figure 12A). Interestingly, we saw that 100% of DA neurons in the SNc and NA neurons in the LC contain α-syn, suggesting α-syn might be preferentially present in catecholaminergic neurons (Figure 12B). We saw no significant difference in the intensity of α-syn in these two regions (Figure 12C), suggesting similar protein characteristics in these two populations.

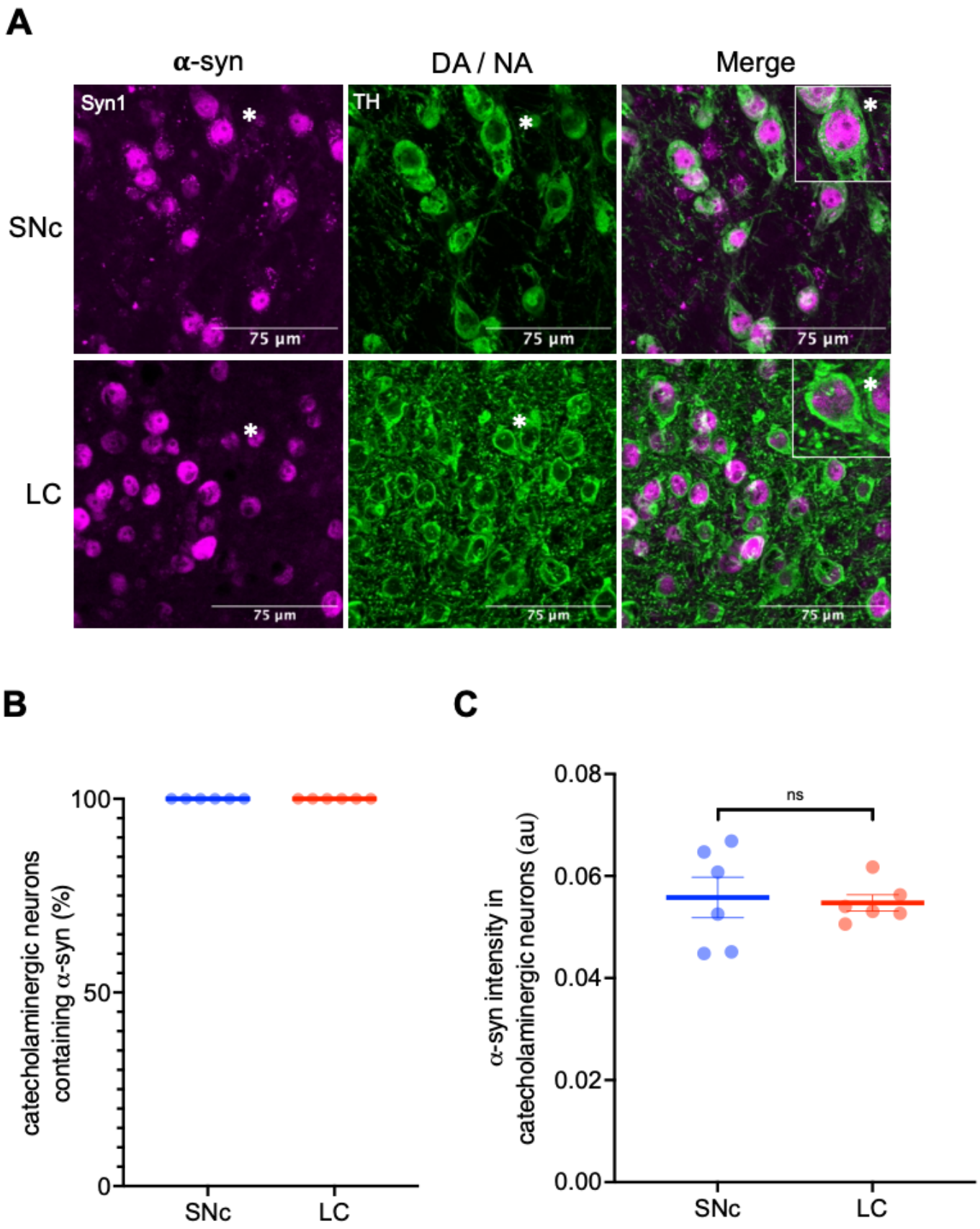
A
α-syn
DA / NA
Merge
Syn1
TH
SNc
LC
75 µm
B
catecholaminergic neurons containing α-syn (%)
100
50
0
SNc
LC
C
α-syn intensity in catecholaminergic neurons (au)
0.08
0.06
0.04
0.02
0.00
ns
SNc
LC

Figure 12: Visual distribution, density, and intensity of α-syn in catecholaminergic neurons. A. Comparison of **α**-synuclein (Syn1), Tyrosine Hydroxylase producing cells (DA and NA neurons, TH) and overlap (merge) immunofluorescence staining in the cortex, hippocampus (HC CA1) and olfactory bulb (OB) of *Snca*$^{NLS/NLS}$ mice. Images taken on the Zeiss LSM800 at 40x magnification (1.3 na). Right inset in merge column represents a neuron with α-syn. B. percentage of total neurons in the cortex, HC CA1 and OB that contain **α**-synuclein. C. Nested averages of the intensity of α-syn in α-syn + neurons in the cortex (CTX), HC CA1, and OB. Differences between groups analyzed using a T-test with Tukey's multiple comparisons test ($p<0.001$ indicated by ****). B and C were analyzed on CellProfiler using 20x magnification confocal images (0.8 na) an N=6 animals.

7. DISCUSSION

Previously, the endogenous topography and distribution of α-syn in the brain has been difficult to pinpoint due to the diffuse staining pattern of α-syn. In this thesis, we describe the generation of an atlas where we pinpoint the localization of cell types expressing α-syn throughout the brain using *Snca*$^{NLS/NLS}$ mice as a reporter of protein topography. By compiling a brain wide atlas of nuclear α-syn distribution, we were able to observe regional variations in α-syn topography and distribution, and hypothesize the relation of these regions to PD. Here, we found five regions with high levels and amounts of α-syn, analyzed both qualitatively (Figure 4) and quantitatively (Figure 6) and saw patterns of α-syn distribution that were consistent in some cases and inconsistent in others with previous ISH data. Below, I explore some of the regions of interest identified in the initial iteration of the atlas and their relationship to PD pathogenesis.

Olfactory Bulb

The OB, primarily associated with olfaction and smelling, is heavily associated with PD. OB dysfunction and anosmia is present in up to 90% of PD patients, and this dysfunction is an early biomarker of PD[13,14,117,118], sometimes present 10 years before the onset of motor dysfunction. We found high amounts of α-syn in the OB, both visually and when quantified. Particularly, we saw the most amount of α-syn in the OB layers containing the glomeruli, mitral cells, and granule cells, which was not indicated in the ABA ISH data, improving on the complexity of previously established data. The glomeruli, mitral and granule cells of the OB are all involved in the GABAergic (inhibitory) and glutamatergic (excitatory) neurotransmitter release that is essential for olfactory sensory processing, solidifying the importance of these cell types in OB function[117]. Therefore, it is likely that the high presence of α-syn in these cell types plays a role

in the olfactory dysfunction present in PD. Also, the first stage in the Braak hypothesis includes the presence of Lewy pathology in the OB[15,90], so the increased levels of α-syn here are likely involved in this pathological response.

Cortex

The cortex is heavily implicated in PD as the site of pathology that induces cognitive and motor symptoms, as well as the final site of Braak staging[15,90]. It is therefore unsurprising we saw large amounts of α-syn in the cortex, particularly in the layers that contain primarily excitatory cells, layers 2-6. It is possible that this large amount of α-syn positive cells is implicated in the prion like spreading of α-syn that occurs in Braak staging. Additionally, when the same mouse model used to create our atlas (*Snca*$^{NLS/NLS}$) was used to study the toxic effects of nuclear α-syn, layer 5/6 cortical neuron loss was observed after 18 months of nuclear expression of α-syn [114]. Therefore, it is possible that the increased amount of α-syn here is involved in this neurodegeneration, showing a clear pathological connection between cortical α-syn and PD.

Hippocampus

Both our *Snca*^{NLS} Atlas and the ABA ISH data showed increased amounts of α-syn in the hippocampus and dentate gyrus, however our analysis showed far larger amounts of α-syn in the pyramidal and granule layers of these regions, with almost no α-syn in the surrounding layers. This is unsurprising as α-syn and LB pathology have been well established in PD, specifically during Stage 4 of the Braak staging system[15,90,119]. In this Braak stage, we see Lewy neurites forming in the hippocampus, which disrupts memory consolidation and leads to cognitive defects[15,90]. Moreover, additional studies have highlighted the importance of the hippocampus,

specifically the CA2 and CA3, in neurodegeneration and cognitive defects in PD and other neurodegenerative diseases[119–121]. It is likely the increased amount of α-syn in this region is involved in its susceptibility to Lewy pathology and PD symptomology.

Midbrain

The midbrain contains the most essential brain structure to the development of PD pathology, the SNc. Therefore, based on our hypothesis that increased levels of α-syn leads to increased susceptibility to pathology, it was surprising that the AHA ISH data suggested the midbrain contained low levels of α-syn. Our *Snca*^{NLS} atlas data conflicted with this, showing that the SNc was one of the brain regions with the highest amount of α-syn (Figure 6). Since midbrain DA neurons signal from the SNc to the striatum, immunostaining for normal, mostly pre-synaptic, α-syn in mouse neurons was diffuse throughout the midbrain as SNc DAs extend into the striatum, incorrectly implying α-syn was mostly diffuse throughout this entire region. Since we were able to localize α-syn into the nucleus of cells, we were able to visualize the high abundance of α-syn in the SNc compared to other midbrain regions. These high levels of α-syn could be explained by the vast spread of the axonal arbors from the SNc DA neurons to the rest of the midbrain and striatum[122]. It is likely that these widespread arbors cause the diffuse staining pattern of α-syn in a normal mouse, but by using the *Snca*$^{NLS/NLS}$ mice as a reporter we are able to see the cellular origin of α-syn in the DA neurons of the SNc. Additionally, it is likely that this increased amount of α-syn is involved with the hallmark DA cell neurodegeneration observed in this region in PD, which has been supported by studies showing overexpression of α-syn in the SNc lead to increased neurodegeneration of DA neurons and decreased dopamine signaling in mice[123].

Pons

We observed high levels of α-syn in the LC of the pons, conflicting with the ABA ISH data that suggested the pons contained low levels of *Snca*. The Braak hypothesis suggests Lewy pathology in this region as early as in Stage 2 of the disease[15], suggesting the importance of this region in the development of Lewy pathology. There is a clear role of the NA neurons in this region in PD, as reduction of the DA transporter, a protein involved in DA reuptake and essential for DA processing throughout the brain, efficiency in LC NA neurons resulted in increased tremor severity in PD pateints[124]. It has also been suggested that increased loss of NAs might contribute to increasing the severity of nigrostriatal damage in PD[125]. Therefore, the increased levels of α-syn in this region likely contribute to this role in PD pathology.

We saw low levels of α-syn in the thalamus and cerebellum, as well as any region of the brain containing primarily inhibitory neurons (Motor CTX Layer 1, HC- SO, H-SR, OB – OPL, DG – PO, DG- PL). This suggests that α-syn is primarily present in excitatory neurons and regions associated with PD, consistent with previous findings in the literature[126]. While the cerebellum and thalamus do show evidence of Lewy pathology in PD and are involved in PD symptomology[127,128], the lack of α-syn in these regions suggests that another factor could be involved in making these cell types susceptible to LB pathology, but these regions are less important in the development of PD pathology. Additionally, in a related study using the *Snca*^{NLS} mice, we saw that decreased levels of α-syn in the thalamus compared to those in the cortex. These anatomical findings correlated with a decreased susceptibility to BLA

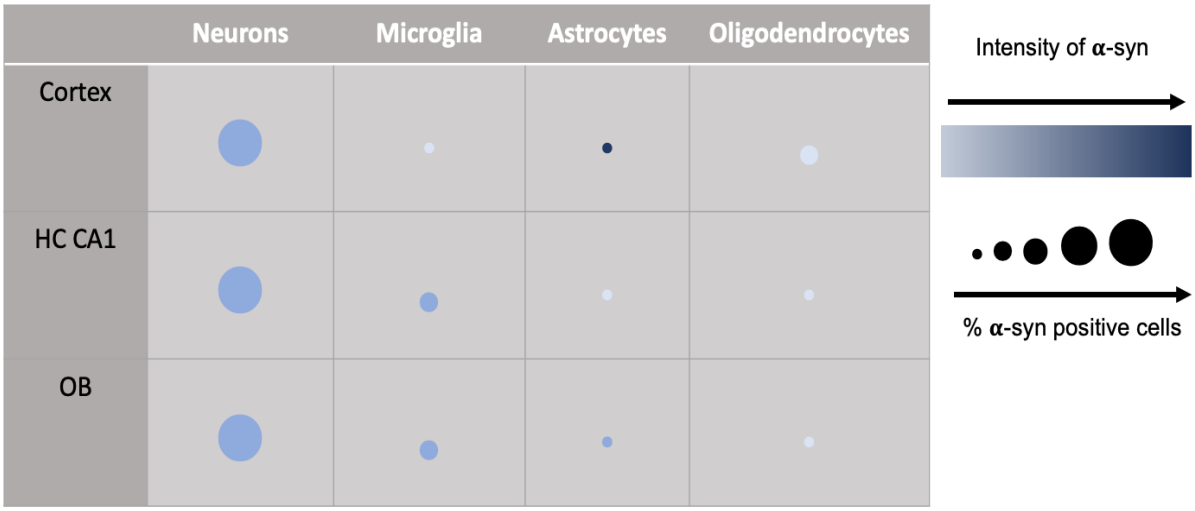

Figure 13: Summary of α-syn cell-type specific characteristics. Percentage occupancy and intensity of α-syn per cell type (neurons, microglia, astrocytes, and oligodendrocytes) in the cortex, hippocampus CA1 (HC CA1) and olfactory bulb (OB).

glutamatergic signaling disruptions due to α-syn aggregation[129], suggesting the lesser involvement of the thalamus in PD pathogenesis, compared to α-syn rich regions, like the cortex.

Beyond the lack of understanding of the cell types that natively express α-syn throughout the brain, there is a lack of understanding in how this protein is dispersed throughout the major cell types in the brain. Since these cell types in the brain have all been implicated in PD pathogenesis, it is important we understand the role of α-syn in these cells. We know that α-syn has been shown to induce a proinflammatory state in glial cells, and that cell to cell spread of α-syn can occur between cell types, so it is important to quantify exactly how α-syn occupies these cell types, and the roles this may play in PD[76,130–132]. Additionally, α-syn is known to cause GCIs in oligodendrocytes, so mapping out this distribution of this protein in healthy cells could have broader implications for other synucleinopathies. According to the sequencing data presented on

brainrnaseq.org[133], *Snca* RNA is present in all the primary cell types in the brain (astrocytes, neurons, OPCs, newly formed and mature oligodendrocytes, microglia, and endothelial cells) however since this data was extracted from the cortex only, we do not know the intricacies of how α-syn occupies these cell types in different regions throughout the brain. To observe if α-syn is present in different cell types depending on the region, we determined the overlap between α-syn and neurons, astrocytes, microglia and oligodendrocytes in the motor cortex, hippocampus CA1, and olfactory bulb. All data on the percentage of α-syn positive cells per cell type and intensity of α-syn in each cell type can been seen summarized in Figure 13.

Neurons

We used IF to stain for neurons and α-syn positive cells and visually observed the amount of overlap between these cells. We saw that in all three regions, α-syn appears to be present in at least 80% of cells, suggesting a heavy presence of neuronal α-syn. This correlated with the brainrnaseq.org data, which showed neurons having the highest expression of *Snca*[133]. This is unsurprising as all three of these regions are implicated in neuronal LB pathology, and the high number of α-syn positive cells in these regions could be contributing to this. Beyond the number of cells containing α-syn, we saw a significant increase in the intensity of α-syn in hippocampal neurons compared to in the OB and cortex. This increase in intensity could perhaps contribute to the regional staging in the Braak hypothesis, perhaps making the hippocampal neurons more susceptible to Lewy pathology in stage 4 before cortical neurons in stages 5 and 6[15,90].

Astrocytes

Astrocytes play a smaller role in the pathogenesis of PD than neurons, which correlates to the levels of α-syn containing astrocytes we observed. Under 20% of all astrocytes in the cortex, hippocampus and OB contain α-syn. We saw the astrocytes in the cortex contain significantly more α-syn than their counterparts in the hippocampus and OB. In PD, astrocytes are involved in dysfunction of the BBB, so the increase in astrocytic α-syn in the cortex could have to do with the increased BBB and vascular innervation in this area[132,134]. Moreover, astrocytes are able to clear some formed of aggregated a-syn, suggesting a beneficial role of astrocytes in clearing pathological α-syn and therefor, incentive for these cells to contain a-syn[131]. Our results correspond to the brainrnaseq.org data, as they also saw a low amount of *Snca* in astrocytes[133].

Microglia

Microglia can have detrimental and helpful roles in neurodegeneration and PD. Microglia are known to participate in the inflammatory response to PD pathology and promoting α-syn aggregation and cell to cell transfer[135–137]. However, microglia can also be neuroprotective and involved in the clearance of aggregated neuronal α-syn [138]. Therefore, we wanted to see the amount of microglia that contained α-syn, and how much α-syn was in each cell. We found microglia contain α-syn in smaller amounts than neurons, and larger percentages than astrocytes. The intensity of microglia α-syn was higher in the hippocampus, suggesting α-syn may play a larger role in the microglia inflammatory response in PD in this region. Our results were similar to the brainrnaseq.org data, which showed low amounts of *Snca* in microglia[133]. Considering the role of microglia in PD and the low number of α-syn positive cells, it is possible that the high

intensity of α-syn we saw in certain microglial populations could be contributing to the involvement of these cell types in PD.

Oligodendrocytes

Oligodendrocytes and oligodendrocyte precursor cells (OPCs) are both clearly involved in the pathogenesis of PD and other synucleinopathies, as dysfunction of these cell types has been linked to increased neurodegeneration[139–141]. For this study, we looked at mature oligodendrocytes and saw a low percentage of cells containing α-syn, and a low intensity of α-syn in these populations. This was surprising, as α-syn aggregation in the cytoplasm of oligodendrocytes is the driving pathological hallmark of MSA, so we expected to see higher levels of α-syn in these cell types. Our data, however, does correspond with the brainrnaseq.org data as oligodendrocytes contained less *Snca* RNA than other cell types, with an FPKM value of 10.31[133].

Finally, since the loss of DA neurons in the SNc is the primary hallmark of PD, we looked at the levels of α-syn in these cells, as well as NA neurons in the LC. We saw that 100% of DA and NA neurons in these regions contained α-syn, solidifying the important role of this protein in PD neurodegeneration. We observed the intensity of α-syn in these neurons were not significantly different, suggesting these two populations of cells behave similarly regarding PD. This would explain the importance of DA loss in the development of PD, and how NA loss in the LC can worsen this neurodegenerative response.

Taken together, in this study, we mapped out the specific regions and cell types in the mouse brain that contain high and low amounts of α-syn. Considering our hypotheses that higher levels of α-syn lead to protein aggregation and eventual toxicity, we have highlighted cell types that are potentially most vulnerable to pathogenesis. Further analysis into the regions and cell types containing high amounts of α-syn could uncover new cell types with an association to PD and solidify the importance of cells known to play a role in PD disease progression. Since α-syn is known to spread pathologically along anatomically connected networks[142], it will be valuable to also interpret this data in the context of network connectivity and see how endogenous α-syn levels are connected to this spread. Alternatively, it is possible that the cell types containing less α-syn could be equally susceptible to PD pathology, as these cells may not have the proper machinery and clearance methods to deal with increased α-syn. Therefore, spread of pathological α-syn into these regions could stress cells to a diseased state, similarly to the in the PFF model[92,94]. Further studies into these cell types with increased or decreased α-syn are needed to fully elucidate the cell type specific role of α-syn in PD, and one potential study for this could include conditional genetic manipulation of α-syn levels, either through knockout or overexpression of *Snca*, in cell types we have shown to have high or low levels to see the phenotypic effect α-syn level has on the body. These cell types of interest could be starting points for the development of PD treatments, as therapies could be developed to target and modify α-syn in vulnerable cell types. Additionally, to confirm the role of these cell types in PD pathogenesis, studies could be conducted to see how α-syn changes in these cell types over time, or when exposed to PD-linked stimuli. Finally, it would be valuable to study the distribution of α-syn in the peripheral nervous system, GI tract and other peripheral organs, since

synucleinopathy has been linked to these regions. In all, this atlas can be used as a tool to elucidate the brain and body-wide location and role of α-syn in PD.

Limitations

Our study and the use of the *Snca*$^{NLS/NLS}$ mice has limitations. Firstly, the *Snca*$^{NLS/NLS}$ reporter mice were used as a reporter of endogenous nuclear α-syn, so it is important to consider that the location of α-syn could potentially be influenced by the nuclear localization of the protein in this mouse line. Second, the amount of α-syn detected in the nucleus and used in the intensity analysis for cell type specific α-syn distribution could be influenced by the physical limitations of forcing the protein into the nucleus. Since the nucleus is smaller in area than the cytoplasm, we see a marked decreased in α-syn levels in the *Snca*$^{NLS/NLS}$ reporter mice[114], so it is possible that α-syn expression might compensate for these physical limitations and produce less synuclein than in its wt state. Finally, there are some observed PD-linked phenotypes in the *Snca*$^{NLS/NLS}$ from the toxic effects of nuclear α-syn expression at 9 and 18 months[114], so there is potential for the toxic effects of nuclear α-syn to impact its distribution. To overcome this, we did all our analysis on mice around the age of 3 months, however it is possible that nuclear α-syn expression could have a neurotoxic effect at this age.

In the context of our cell type specific analysis, some limitations surrounding antibody specificity can complicate data interpretation. For example, the antibody typically used to label astrocytes, Gfap, does not label cortical astrocytes, so we had to use a different antibody, Aldh111 to label these astrocytes[143,144]. Since we used two different markers, there is a potential variance in how α-syn is being detected, and the characteristics of this protein we observed here.

Finally, our analysis covered a large range of sections of the brain and determined the relative expression of α-syn in these regions, however we did not analyze every section and layer of the brain to determine α-syn content. Future studies should expand upon our atlas and selected brain regions to determine an absolute brain wide expression map of α-syn. Additionally, we are in the process of developing a 3D render of nuclear α-syn throughout the brain to accompany our 2D atlas here.

8. CONCLUSIONS

In this thesis, we mapped out the endogenous distribution of α-synuclein in *Snca*$^{NLS/NLS}$ mice. We used ilastik to automate detection of α-syn in IHC stained tissue and generated a whole brain atlas of the distribution of this protein, corresponding to the ABA. We were able to detect differences in the amount of α-syn in different brain types and showed that regions associated with PD and PD symptoms have higher amounts of α-syn, and therefore likely to be more susceptible to its toxicity. We showed that the visual intensity of α-syn per brain region differed from nuclei specific quantification, adding a second layer of information – and complexity – to our analysis. Building on the *Snca*^{NLS} Atlas, we found that α-syn occupies all types of brain cells (neurons, astrocytes, microglia, and oligodendrocytes) in differing amounts and intensities per brain region. Finally, we found that all DA and NA neurons in the SNc and LC contain α-syn. This thesis shows the variability and complexity of the distribution and characteristic of endogenous α-syn throughout the brain. While we were able to elucidate some of the characteristics of this protein, much is left to be uncovered about α-syn and the part it plays in the development of PD.

9. REFERENCES

1. Parkinson, J. *An Essay on the Shaking Palsy*. *J Neuropsychiatry Clin Neurosci* vol. 14 (1817).
2. Goetz, C. G. The history of Parkinson's disease: Early clinical descriptions and neurological therapies. *Cold Spring Harb Perspect Med* **1**, (2011).
3. Charcot JM. *Lectures on the Diseases of the Nervous System*. (1877).
4. Greenfield, J. G. & Bosanquet, F. D. *THE BRAIN-STEM LESIONS IN PARKINSONISM*. *J. Neurol. Neurosurg. Psychiat* (1953).
5. Mhyre, T. R., Boyd, J. T., Hamill, R. W. & Maguire-Zeiss, K. A. Parkinson's disease. *Subcell Biochem* **65**, 389–455 (2012).
6. Parkinson's Disease: Causes, Symptoms, and Treatments. *NIH* (2022).
7. Symptoms - Parkinson's Disease. *NHS* (2019).
8. The Micheal J. Fox Foundation for Parkinson's Research. Symptoms. *https://www.michaeljfox.org/symptoms* https://www.michaeljfox.org/symptoms.
9. American Parkinsons Disease Association. Symptoms of Parkinson's Disease. https://www.apdaparkinson.org/what-is-parkinsons/symptoms/.
10. Hawkes, C. H. The prodromal phase of sporadic Parkinson's disease: Does it exist and if so how long is it? *Movement Disorders* **23**, 1799–1807 (2008).
11. Sauerbier, A., Qamar, M. A., Rajah, T. & Chaudhuri, K. R. New concepts in the pathogenesis and presentation of Parkinson's disease. *Clinical Medicine* **16**, 365–370 (2016).
12. Boeve, B. F. Idiopathic REM sleep behaviour disorder in the development of Parkinson's disease. *Lancet Neurol* **12**, 469–482 (2013).
13. Fullard, M. E., Morley, J. F. & Duda, J. E. Olfactory Dysfunction as an Early Biomarker in Parkinson's Disease. *Neurosci Bull* **33**, 515–525 (2017).
14. Walker, I. M., Fullard, M. E., Morley, J. F. & Duda, J. E. Olfaction as an early marker of Parkinson's disease and Alzheimer's disease. in 317–329 (2021). doi:10.1016/B978-0-12-819973-2.00030-7.
15. Braak, H. *et al.* Staging of brain pathology related to sporadic Parkinson's disease. *Neurobiol Aging* **24**, (2003).
16. Parkinson's Foundation. Staging of Parkinson's.
17. Hoehn, M. M. & Yahr, M. D. Parkinsonism: Onset, progression and mortality. *Neurology* **57**, S11–S26 (2001).
18. Goetz, C. G. *et al.* Movement Disorder Society Task Force report on the Hoehn and Yahr staging scale: Status and recommendations. *Movement Disorders* **19**, 1020–1028 (2004).
19. Goetz, C. G. *et al.* Movement Disorder Society-sponsored revision of the Unified Parkinson's Disease Rating Scale (MDS-UPDRS): Scale presentation and clinimetric testing results. *Movement Disorders* **23**, 2129–2170 (2008).
20. Kluge, A. *et al.* Detection of neuron-derived pathological α-synuclein in blood. *Brain* (2022) doi:10.1093/brain/awac115.
21. Parnetti, L., Cicognola, C., Eusebi, P. & Chiasserini, D. Value of cerebrospinal fluid α-synuclein species as biomarker in Parkinson's diagnosis and prognosis. *Biomark Med* **10**, 35–49 (2016).
22. German, D. C., Manaye, K., Smith, W. K., Woodward, D. J. & Saper, C. B. *Midbrain Dopaminergic Cell Loss in Parkmson's Disease: Computer Visualization*. (1989).

23. Spillantini, M. G., Crowther, R. A., Jakes, R., Hasegawa, M. & Goedert, M. *Synuclein in filamentous inclusions of Lewy bodies from Parkinson's disease and dementia with Lewy bodies (ubiquitinsarkosyl-insoluble filamentsimmunoelectron microscopy)*. *Neurobiology Communicated by Max F. Perutz, Medical Research Council* vol. 95 www.pnas.org. (1998).
24. Kish, S. J., Shannak, K. & Hornykiewicz, O. Uneven Pattern of Dopamine Loss in the Striatum of Patients with Idiopathic Parkinson's Disease. *New England Journal of Medicine* **318**, 876–880 (1988).
25. lo Bianco, C., Ridet, J.-L., Schneider, B. L., Dé, N. & Aebischer, P. *Synucleinopathy and selective dopaminergic neuron loss in a rat lentiviral-based model of Parkinson's disease*. www.pnas.orgcgidoi10.1073pnas.152339799.
26. Surmeier, D. J. Determinants of dopaminergic neuron loss in Parkinson's disease. *FEBS Journal* vol. 285 3657–3668 Preprint at https://doi.org/10.1111/febs.14607 (2018).
27. Obeso, J. A. *et al.* Pathophysiology of the basal ganglia in Parkinson's disease. *Trends Neurosci* **23**, S8–S19 (2000).
28. Conway, K. A. *et al.* Acceleration of oligomerization, not fibrillization, is a shared property of both α-synuclein mutations linked to early-onset Parkinson's disease: Implications for pathogenesis and therapy. *Proceedings of the National Academy of Sciences* **97**, 571–576 (2000).
29. Spillantini, M. G. *et al.* α-Synuclein in Lewy bodies. *Nature* **388**, 839–840 (1997).
30. Tysnes, O.-B. & Storstein, A. Epidemiology of Parkinson's disease. *J Neural Transm* **124**, 901–905 (2017).
31. Haaxma, C. A. *et al.* Gender differences in Parkinson's disease. *Journal of Neurology, Neurosurgery & Psychiatry* **78**, 819–824 (2007).
32. de Lau, L. M. & Breteler, M. M. Epidemiology of Parkinson's disease. *Lancet Neurol* **5**, 525–535 (2006).
33. Dorsey, E. R., Sherer, T., Okun, M. S. & Bloem, B. R. The Emerging Evidence of the Parkinson Pandemic. *J Parkinsons Dis* **8**, S3–S8 (2018).
34. Sulzer, D. Multiple hit hypotheses for dopamine neuron loss in Parkinson's disease. *Trends Neurosci* **30**, 244–250 (2007).
35. Klein, C. & Westenberger, A. Genetics of Parkinson's disease. *Cold Spring Harb Perspect Med* **2**, (2012).
36. Polymeropoulos, M. H. *et al.* Mutation in the α-synuclein gene identified in families with Parkinson's disease. *Science (1979)* **276**, 2045–2047 (1997).
37. Valente, E. M. *et al.* Hereditary Early-Onset Parkinson's Disease Caused by Mutations in *PINK1*. *Science (1979)* **304**, 1158–1160 (2004).
38. Kitada, T. *et al.* Mutations in the parkin gene cause autosomal recessive juvenile parkinsonism. *Nature* **392**, 605–608 (1998).
39. Singleton, A. B. *et al.* α-Synuclein Locus Triplication Causes Parkinson's Disease. *Science (1979)* **302**, 841–841 (2003).
40. Parkinson's Canada. Understanding Parkinson's. https://www.parkinson.org/Understanding-Parkinsons/Statistics.
41. Elbaz, A., Carcaillon, L., Kab, S. & Moisan, F. Epidemiology of Parkinson's disease. *Rev Neurol (Paris)* **172**, 14–26 (2016).
42. Rybicki, B. A., Johnson, C. C., Uman, J. & Gore11, J. M. *Parkinson's Disease Mortality and the Industrial Use of Heavy Metals in Michigan*. *Movement Disorders* vol. 8 (1993).

43. Montgomery, E. B. *Heavy metals and the etiology of Parkinson's disease and other movement disorders*. *Toxicology* vol. 97 (1995).
44. Tanner, C. M. *et al.* Rotenone, paraquat, and Parkinson's disease. *Environ Health Perspect* **119**, 866–872 (2011).
45. Killinger, B. A. *et al.* The vermiform appendix impacts the risk of developing Parkinson's disease. *Sci Transl Med* **10**, (2018).
46. Gao, X., Chen, H., Schwarzschild, M. A. & Ascherio, A. Use of ibuprofen and risk of Parkinson disease. *Neurology* **76**, 863–869 (2011).
47. Mendes, A. *et al.* Appendectomy may delay Parkinson's disease Onset. *Movement Disorders* **30**, 1404–1407 (2015).
48. Thacker, E. L. *et al.* Temporal relationship between cigarette smoking and risk of Parkinson disease. *Neurology* **68**, 764–768 (2007).
49. Kolahdouzan, M. & Hamadeh, M. J. The neuroprotective effects of caffeine in neurodegenerative diseases. *CNS Neurosci Ther* **23**, 272–290 (2017).
50. Cotzias, G. C., van Woert, M. H. & Schiffer, L. M. Aromatic Amino Acids and Modification of Parkinsonism. *New England Journal of Medicine* **276**, 374–379 (1967).
51. Cotzias, G. C., Papavasiliou, P. S. & Gellene, R. Modification of Parkinsonism — Chronic Treatment with L-Dopa. *New England Journal of Medicine* **280**, 337–345 (1969).
52. LeWitt, P. A. Levodopa therapy for Parkinson's disease: Pharmacokinetics and pharmacodynamics. *Movement Disorders* **30**, 64–72 (2015).
53. Marsden, C. D. & Parkes, J. D. SUCCESS AND PROBLEMS OF LONG-TERM LEVODOPA THERAPY IN PARKINSON'S DISEASE. *The Lancet* **309**, 345–349 (1977).
54. Boomsma, F., Meerwaldt, J. D., Man in't Veld, A. J., Hovestadt, A. & Schalekamp, M. A. D. H. Treatment of idiopathic parkinsonism with l-dopa in the absence and presence of decarboxylase inhibitors: effects on plasma levels of l-dopa, dopa decarboxylase, catecholamines and 3-O-methyl-dopa. *J Neurol* **236**, 223–230 (1989).
55. LIEBERMAN, A., GOODGOLD, A., JONAS, S. & LEIBOWITZ, M. Comparison of dopa decarboxylase inhibitor (carbidopa) combined with levodopa and levodopa alone in Parkinson's disease. *Neurology* **25**, 911–911 (1975).
56. Wood, A. J. J. & Calne, D. B. Treatment of Parkinson's Disease. *New England Journal of Medicine* **329**, 1021–1027 (1993).
57. Blandini, F. & Armentero, M.-T. Dopamine receptor agonists for Parkinson's disease. *Expert Opin Investig Drugs* **23**, 387–410 (2014).
58. Riederer, P. & Laux, G. MAO-inhibitors in Parkinson's Disease. *Exp Neurobiol* **20**, 1–17 (2011).
59. Walter, B. L. & Vitek, J. L. Surgical treatment for Parkinson's disease. *Lancet Neurol* **3**, 719–728 (2004).
60. Volkmann, J. Deep Brain Stimulation for the Treatment of Parkinson's Disease. *Journal of Clinical Neurophysiology* **21**, (2004).
61. Benabid, A. L. Deep brain stimulation for Parkinson's disease. *Curr Opin Neurobiol* **13**, 696–706 (2003).
62. Hashimoto, M. *et al.* The Role of NAC in Amyloidogenesis in Alzheimer's Disease. *Am J Pathol* **156**, 734–735 (2000).
63. Jakes, R., Spillantini, M. G. & Goedert, M. Identification of two distinct synucleins from human brain. *FEBS Lett* **345**, 27–32 (1994).

64. Uéda, K. *et al.* Molecular cloning of cDNA encoding an unrecognized component of amyloid in Alzheimer disease. *Proceedings of the National Academy of Sciences* **90**, 11282–11286 (1993).
65. Maroteaux, L., Campanelli, J. & Scheller, R. Synuclein: a neuron-specific protein localized to the nucleus and presynaptic nerve terminal. *The Journal of Neuroscience* **8**, 2804–2815 (1988).
66. Lashuel, H. A., Overk, C. R., Oueslati, A. & Masliah, E. The many faces of α-synuclein: from structure and toxicity to therapeutic target. *Nat Rev Neurosci* **14**, 38–48 (2013).
67. Eliezer, D., Kutluay, E., Bussell, R. & Browne, G. Conformational properties of α-synuclein in its free and lipid-associated states 1 1Edited by P. E. Wright. *J Mol Biol* **307**, 1061–1073 (2001).
68. Ulmer, T. S., Bax, A., Cole, N. B. & Nussbaum, R. L. Structure and Dynamics of Micelle-bound Human α-Synuclein. *Journal of Biological Chemistry* **280**, 9595–9603 (2005).
69. El-Agnaf, O. M. A., Jakes, R., Curran, M. D. & Wallace, A. Effects of the mutations Ala ^{30} to Pro and Ala ^{53} to Thr on the physical and morphological properties of α-synuclein protein implicated in Parkinson's disease. *FEBS Lett* **440**, 67–70 (1998).
70. Bernal-Conde, L. D. *et al.* Alpha-Synuclein Physiology and Pathology: A Perspective on Cellular Structures and Organelles. *Front Neurosci* **13**, (2020).
71. Lee, H.-J. Clearance of -Synuclein Oligomeric Intermediates via the Lysosomal Degradation Pathway. *Journal of Neuroscience* **24**, 1888–1896 (2004).
72. Gosavi, N., Lee, H.-J., Lee, J. S., Patel, S. & Lee, S.-J. Golgi Fragmentation Occurs in the Cells with Prefibrillar α-Synuclein Aggregates and Precedes the Formation of Fibrillar Inclusion. *Journal of Biological Chemistry* **277**, 48984–48992 (2002).
73. Hoozemans, J. J. M. *et al.* Activation of the unfolded protein response in Parkinson's disease. *Biochem Biophys Res Commun* **354**, 707–711 (2007).
74. Liu, M. *et al.* α-synuclein induces apoptosis of astrocytes by causing dysfunction of the endoplasmic reticulum-Golgi compartment. *Mol Med Rep* (2018) doi:10.3892/mmr.2018.9002.
75. Cheng, F., Vivacqua, G. & Yu, S. The role of alpha-synuclein in neurotransmission and synaptic plasticity. *Journal of Chemical Neuroanatomy* vol. 42 242–248 Preprint at https://doi.org/10.1016/j.jchemneu.2010.12.001 (2011).
76. Austin, S. A., Floden, A. M., Murphy, E. J. & Combs, C. K. α-synuclein expression modulates microglial activation phenotype. *Journal of Neuroscience* **26**, 10558–10563 (2006).
77. Stolzenberg, E. *et al.* A Role for Neuronal Alpha-Synuclein in Gastrointestinal Immunity. *J Innate Immun* **9**, 456–463 (2017).
78. Labrie, V. & Brundin, P. Alpha-Synuclein to the Rescue: Immune Cell Recruitment by Alpha-Synuclein during Gastrointestinal Infection. *J Innate Immun* **9**, 437–440 (2017).
79. Kasen, A. *et al.* Upregulation of α-synuclein following immune activation: Possible trigger of Parkinson's disease. *Neurobiol Dis* **166**, 105654 (2022).
80. Allen Institute for Brain Science. Allen Mouse Brain Atlas [dataset]. *Available from mouse.brain-map.org.* (2004).
81. Giráldez-Pérez, R. M., Antolín-Vallespín, M., Muñoz, M. D. & Sánchez-Capelo, A. Models of α-synuclein aggregation in Parkinson's disease. *Acta Neuropathol Commun* **2**, 176 (2014).

82. Forno, L. S. The neuropathology of Parkinson's disease. *Progress in Parkinson research* 11–21 (1988).
83. Miki, Y. *et al.* Accumulation of histone deacetylase 6, an aggresome-related protein, is specific to Lewy bodies and glial cytoplasmic inclusions. *Neuropathology* **31**, 561–568 (2011).
84. Vitte, J. *et al.* Leucine-Rich Repeat Kinase 2 Is Associated With the Endoplasmic Reticulum in Dopaminergic Neurons and Accumulates in the Core of Lewy Bodies in Parkinson Disease. *J Neuropathol Exp Neurol* **69**, 959–972 (2010).
85. Sidransky, E. *et al.* Multicenter Analysis of Glucocerebrosidase Mutations in Parkinson's Disease. *New England Journal of Medicine* **361**, 1651–1661 (2009).
86. Coon, E. A. & Singer, W. Synucleinopathies. *CONTINUUM Lifelong Learning in Neurology* vol. 26 72–92 Preprint at https://doi.org/10.1212/CON.0000000000000819 (2020).
87. Jellinger, K. A. Neuropathological spectrum of synucleinopathies. *Movement Disorders* vol. 18 Preprint at https://doi.org/10.1002/mds.10557 (2003).
88. Coon, E. A. & Singer, W. Synucleinopathies. *CONTINUUM: Lifelong Learning in Neurology* **26**, 72–92 (2020).
89. Boeve, B. F. *et al.* Synucleinopathy pathology and REM sleep behavior disorder plus dementia or parkinsonism. *Neurology* **61**, 40–45 (2003).
90. Braak, H., R□b, U., Gai, W. P. & del Tredici, K. Idiopathic Parkinson's disease: possible routes by which vulnerable neuronal types may be subject to neuroinvasion by an unknown pathogen. *J Neural Transm* **110**, (2003).
91. Rietdijk, C. D., Perez-Pardo, P., Garssen, J., van Wezel, R. J. A. & Kraneveld, A. D. Exploring Braak's Hypothesis of Parkinson's Disease. *Front Neurol* **8**, (2017).
92. Luk, K. C. *et al.* Exogenous α-synuclein fibrils seed the formation of Lewy body-like intracellular inclusions in cultured cells. *Proceedings of the National Academy of Sciences* **106**, 20051–20056 (2009).
93. Volpicelli-Daley, L. A. *et al.* Exogenous α-Synuclein Fibrils Induce Lewy Body Pathology Leading to Synaptic Dysfunction and Neuron Death. *Neuron* **72**, 57–71 (2011).
94. Luk, K. C. *et al.* Pathological α-Synuclein Transmission Initiates Parkinson-like Neurodegeneration in Nontransgenic Mice. *Science (1979)* **338**, (2012).
95. Kordower, J. H., Chu, Y., Hauser, R. A., Freeman, T. B. & Olanow, C. W. Lewy body–like pathology in long-term embryonic nigral transplants in Parkinson's disease. *Nat Med* **14**, 504–506 (2008).
96. Li, J.-Y. *et al.* Lewy bodies in grafted neurons in subjects with Parkinson's disease suggest host-to-graft disease propagation. *Nat Med* **14**, 501–503 (2008).
97. Irwin, D. J. *et al.* Evaluation of Potential Infectivity of Alzheimer and Parkinson Disease Proteins in Recipients of Cadaver-Derived Human Growth Hormone. *JAMA Neurol* **70**, 462 (2013).
98. Parkkinen, L., Pirttilä, T. & Alafuzoff, I. Applicability of current staging/categorization of α-synuclein pathology and their clinical relevance. *Acta Neuropathol* **115**, 399–407 (2008).
99. Zaccai, J., Brayne, C., McKeith, I., Matthews, F. & Ince, P. G. Patterns and stages of -synucleinopathy: Relevance in a population-based cohort. *Neurology* **70**, 1042–1048 (2008).

100. Beach, T. G. *et al.* Multi-organ distribution of phosphorylated α-synuclein histopathology in subjects with Lewy body disorders. *Acta Neuropathol* **119**, 689–702 (2010).
101. Kalaitzakis, M. E., Graeber, M. B., Gentleman, S. M. & Pearce, R. K. B. The dorsal motor nucleus of the vagus is not an obligatory trigger site of Parkinson's disease: a critical analysis of α-synuclein staging. *Neuropathol Appl Neurobiol* **34**, 284–295 (2008).
102. William Langston, J. MPTP and parkinson's disease. *Trends Neurosci* **8**, (1985).
103. Uversky, V. N. Neurotoxicant-induced animal models of Parkinson?s disease: understanding the role of rotenone, maneb and paraquat in neurodegeneration. *Cell Tissue Res* **318**, (2004).
104. Tieu, K. A Guide to Neurotoxic Animal Models of Parkinson's Disease. *Cold Spring Harb Perspect Med* **1**, (2011).
105. Betarbet, R. *et al.* Chronic systemic pesticide exposure reproduces features of Parkinson's disease. *Nat Neurosci* **3**, 1301–6 (2000).
106. Fuchs, J. *et al.* Phenotypic variation in a large Swedish pedigree due to *SNCA* duplication and triplication. *Neurology* **68**, (2007).
107. Giasson, B. I. *et al.* Neuronal α-Synucleinopathy with Severe Movement Disorder in Mice Expressing A53T Human α-Synuclein. *Neuron* **34**, (2002).
108. van der Putten, H. *et al.* Neuropathology in Mice Expressing Human α-Synuclein. *The Journal of Neuroscience* **20**, (2000).
109. Ostrerova-Golts, N. *et al.* The A53T α-Synuclein Mutation Increases Iron-Dependent Aggregation and Toxicity. *The Journal of Neuroscience* **20**, (2000).
110. Krüger, R. *et al.* AlaSOPro mutation in the gene encoding α-synuclein in Parkinson's disease. *Nat Genet* **18**, (1998).
111. Hansen, C. *et al.* A novel α-synuclein-GFP mouse model displays progressive motor impairment, olfactory dysfunction and accumulation of α-synuclein-GFP. *Neurobiol Dis* **56**, (2013).
112. Allen Institute for Brain Science. Allen Mouse Brain Atlas [dataset]. Available from mouse.brain-map.org.Allen Institute for Brain Science (2011 (2004).
113. Caputo, A. *et al.* Snca-GFP Knock-In Mice Reflect Patterns of Endogenous Expression and Pathological Seeding. *eNeuro* **7**, ENEURO.0007-20.2020 (2020).
114. Geertsma, H. M. *et al.* Constitutive nuclear accumulation of endogenous alpha-synuclein in mice causes motor dysfunction and cortical atrophy, independent of protein aggregation. *Human Molecular Genetics* (2022).
115. Ibáñez, P. *et al.* Causal relation between α-synuclein locus duplication as a cause of familial Parkinson's disease. *The Lancet* **364**, 1169–1171 (2004).
116. Chartier-Harlin, M.-C. *et al.* α-synuclein locus duplication as a cause of familial Parkinson's disease. *The Lancet* **364**, 1167–1169 (2004).
117. Doty, R. L. Olfaction in Parkinson's disease and related disorders. *Neurobiol Dis* **46**, 527–552 (2012).
118. Iravani, B., Arshamian, A., Schaefer, M., Svenningsson, P. & Lundström, J. N. A non-invasive olfactory bulb measure dissociates Parkinson's patients from healthy controls and discloses disease duration. *NPJ Parkinsons Dis* **7**, 75 (2021).
119. Villar-Conde, S. *et al.* The Human Hippocampus in Parkinson's Disease: An Integrative Stereological and Proteomic Study. *J Parkinsons Dis* **11**, 1345–1365 (2021).
120. Lenka, A. *et al.* Hippocampal subfield atrophy in patients with Parkinson's disease and psychosis. *J Neural Transm* **125**, 1361–1372 (2018).

121. Das, T., Hwang, J. J. & Poston, K. L. Episodic recognition memory and the hippocampus in Parkinson's disease: A review. *Cortex* **113**, 191–209 (2019).
122. Matsuda, W. *et al.* Single Nigrostriatal Dopaminergic Neurons Form Widely Spread and Highly Dense Axonal Arborizations in the Neostriatum. *Journal of Neuroscience* **29**, 444–453 (2009).
123. Alarcón-Arís, D. *et al.* Anti-α-synuclein ASO delivered to monoamine neurons prevents α-synuclein accumulation in a Parkinson's disease-like mouse model and in monkeys. *EBioMedicine* **59**, 102944 (2020).
124. Isaias, I. U. *et al.* A role for locus coeruleus in Parkinson tremor. *Front Hum Neurosci* **5**, (2012).
125. Gesi, M. *et al.* The role of the locus coeruleus in the development of Parkinson's disease. *Neurosci Biobehav Rev* **24**, 655–668 (2000).
126. Taguchi, K., Watanabe, Y., Tsujimura, A. & Tanaka, M. Brain region-dependent differential expression of alpha-synuclein. *Journal of Comparative Neurology* **524**, 1236–1258 (2016).
127. Pifl, C., Kish, S. J. & Hornykiewicz, O. Thalamic noradrenaline in Parkinson's disease: Deficits suggest role in motor and non-motor symptoms. *Movement Disorders* **27**, 1618–1624 (2012).
128. Seidel, K. *et al.* Involvement of the cerebellum in Parkinson disease and dementia with Lewy bodies. *Ann Neurol* **81**, 898–903 (2017).
129. Chen, L. *et al.* Synaptic location is a determinant of the detrimental effects of α-synuclein pathology to glutamatergic transmission in the basolateral amygdala. *Elife* **11**, (2022).
130. Kam, T.-I., Hinkle, J. T., Dawson, T. M. & Dawson, V. L. Microglia and astrocyte dysfunction in parkinson's disease. *Neurobiol Dis* **144**, 105028 (2020).
131. Loria, F. *et al.* α-Synuclein transfer between neurons and astrocytes indicates that astrocytes play a role in degradation rather than in spreading. *Acta Neuropathol* **134**, 789–808 (2017).
132. Booth, H. D. E., Hirst, W. D. & Wade-Martins, R. The Role of Astrocyte Dysfunction in Parkinson's Disease Pathogenesis. *Trends Neurosci* **40**, 358–370 (2017).
133. Zhang, Y. *et al.* An RNA-Sequencing Transcriptome and Splicing Database of Glia, Neurons, and Vascular Cells of the Cerebral Cortex. *Journal of Neuroscience* **34**, 11929–11947 (2014).
134. Wilhelm, I., Nyúl-Tóth, Á., Suciu, M., Hermenean, A. & Krizbai, I. A. Heterogeneity of the blood-brain barrier. *Tissue Barriers* **4**, e1143544 (2016).
135. George, S. *et al.* Microglia affect α-synuclein cell-to-cell transfer in a mouse model of Parkinson's disease. *Mol Neurodegener* **14**, 34 (2019).
136. Ferreira, S. A. & Romero-Ramos, M. Microglia Response During Parkinson's Disease: Alpha-Synuclein Intervention. *Front Cell Neurosci* **12**, (2018).
137. Lecours, C. *et al.* Microglial Implication in Parkinson's Disease: Loss of Beneficial Physiological Roles or Gain of Inflammatory Functions? *Front Cell Neurosci* **12**, (2018).
138. Choi, I. *et al.* Microglia clear neuron-released α-synuclein via selective autophagy and prevent neurodegeneration. *Nat Commun* **11**, 1386 (2020).
139. Williams, G. P. *et al.* CD4 T cells mediate brain inflammation and neurodegeneration in a mouse model of Parkinson's disease. *Brain* **144**, 2047–2059 (2021).
140. Xia, Y. *et al.* Reactive microglia enhance the transmission of exosomal α-synuclein via toll-like receptor 2. *Brain* **144**, 2024–2037 (2021).

141. Zhang, X., Zhang, R., Nisa Awan, M. U. & Bai, J. The Mechanism and Function of Glia in Parkinson's Disease. *Front Cell Neurosci* **16**, (2022).
142. Henderson, M. X. *et al.* Spread of α-synuclein pathology through the brain connectome is modulated by selective vulnerability and predicted by network analysis. *Nat Neurosci* **22**, 1248–1257 (2019).
143. Yang, Y. *et al.* Molecular comparison of GLT1+ and ALDH1L1+ astrocytes in vivo in astroglial reporter mice. *Glia* **59**, 200–207 (2011).
144. Zhang, Z. *et al.* The Appropriate Marker for Astrocytes: Comparing the Distribution and Expression of Three Astrocytic Markers in Different Mouse Cerebral Regions. *Biomed Res Int* **2019**, 1–15 (2019).

10. SUPPLIMENTARY FIGURES

A

B

C

D

E

F

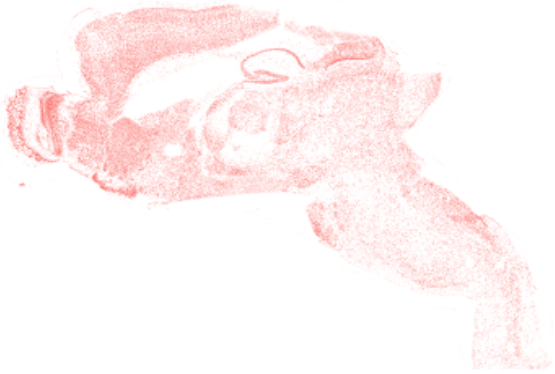

Supplementary Figure 1: Sagittal *Snca*^{NLS} Atlas. 6 representative images from *Snca*$^{NLS/NLS}$ mice stained for α-syn using IHC. Images are representative of *Snca* Atlas of approximately 50 sections per mouse. Images were aligned to the nearest ABA level and Bregma coordinate. Coordinates are as follows: A; Bregma +2.725 mm, ABA 7, B; Bregma +2.15 mm, ABA 10, C; Bregma +1.35 mm, ABA 14, D; Bregma +1.1 mm, ABA 15, E; Bregma +0.675 mm, ABA 17, F; Bregma +0.475 mm, ABA 18

A

B

C

D

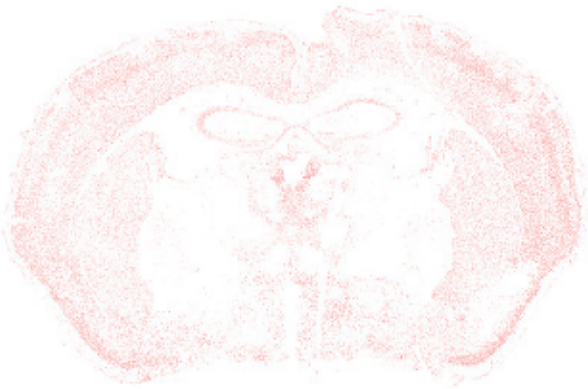

E

F

G

H

Supplementary Figure 2: *Snca*^{NLS} Coronal Atlas. 8 representative images from *Snca*$^{NLS/NLS}$ mice stained for α-syn using IHC. Images are representative of *Snca* Atlas of approximately 100 sections per mouse. Images were aligned to the nearest ABA level and Bregma coordinate. Coordinates are as follows: A; Bregma +3.045 mm, ABA 24, B; Bregma +1.645 mm, ABA 38, C; Bregma +1.045 mm, ABA 44, D; Bregma -1.255 mm, ABA 66, E; Bregma -2.48 mm, ABA 79, F; Bregma -3.18 mm, ABA 85, G; Bregma -6.055 mm, ABA 114, H; Bregma -7.255 mm, ABA 126.

11. TABLES

Table 1: Characteristics of the *Snca*$^{NLS/NLS}$ mouse cohort used in all analysis.

Orientation	Age	Sex	Mouse ID
Sagittal	P95	Male	SLF528
Sagittal	P96	Female	SLF549
Sagittal	P96	Female	SLF550
Sagittal	P140	Female	SLF702
Sagittal	P210	Female	SLF666
Sagittal	P210	Female	SLF668
Coronal	P96	Male	SLF537
Coronal	P96	Female	SLF554
Coronal	P96	Female	SLF650
Coronal	P126	Female	SLF524

Table 2: Antibody information for all cell-type and region-specific IF.

Antibody	Target	Host	Concentration	Manufacturer	Catalog #	Secondary
Syn1	A-syn	Mouse	1:1000	BD Biosciences	610787	AF 568
GFAP	astrocytes	Gineau Pig	1:1000	Synaptic Systems	172004(SY)	AF 488
ALDH1L	cortical astrocytes	Rabbit	1:400	Thermo Fisher Scientific	19H14L20	AF 488
IBA1	microglia	Rabbit	1:1000	WAKO Chemicals	019-19741	AF 647
NeuN	Neurons	Rabbit	1:2000	Thermo Fisher Scientific	26975-1-AP	AF 488
Olig2	Oligodendrocytes	Goat	1:200	R&D Systems	AF2418	AF 488
Th	DAs	Rabbit	1:1000	Millipore Sigma	AB152	AF 488

12. LITERATURE CONTRIBUTIONS

1. Geertsma, Haley M., Terry R. Suk, Konrad M. Ricke, Kyra Horsthuis, Jean-Louis A. Parmasad, **Zoe A. Fisk**, Steve M. Callaghan, and Maxime WC Rousseaux. "Constitutive nuclear accumulation of endogenous alpha-synuclein in mice causes motor impairment and cortical dysfunction, independent of protein aggregation." *Human Molecular Genetics* (2022).

   In this manuscript I assisted with collection of *Snca*$^{NLS/NLS}$ mouse tissue, behavioral experiments, and manuscript review.

2. Chen, Liqiang, Chetan Nagaraja, Samuel Daniels, **Zoe A. Fisk**, Rachel Dvorak, Lindsay Meyerdirk, Jennifer A. Steiner et al. "Synaptic location is a determinant of the detrimental effects of α-synuclein pathology to glutamatergic transmission in the basolateral amygdala." *Elife* 11 (2022): e78055.

   In this manuscript I analysed the distribution of α-synuclein in the cortex and thalamus using *Snca*$^{NLS/NLS}$ mice using immunofluorescence and confocal microscopy and determined the intensity and amount of α-syn positive cells in these regions. My contributions can be seen in Figure 2.

3. Suk, Terry R., Trina T. Nguyen, **Zoe A. Fisk**, Miso Mitkovski, Haley M. Geertsma, Jean-Louis A. Parmasad, Meghan M. Heer et al. "Characterizing the differential distribution and targets of Sumo paralogs in the mouse brain." *bioRxiv* (2022).

   In this manuscript I dissected, processed, stained, and imaged wt, S1T and S2T mouse tissue to determine the distribution and characteristics of HA-tagged sumo throughout key mouse brain regions. My contributions can be seen in Figure 2.

| *Human Molecular Genetics*, 2022, Vol. 00, No. 00

Human Molecular Genetics, 2022, Vol. 00, 00, 1–16

https://doi.org/10.1093/hmg/ddac035 Advance access publication date: 18 February 2022

Original Article

Constitutive nuclear accumulation of endogenous alpha-synuclein in mice causes motor impairment and cortical dysfunction, independent of protein aggregation

Haley M. Geertsma [1,2], Terry R. Suk [1,2], Konrad M. Ricke [1,2,3], Kyra Horsthuis[1,2], Jean-Louis A. Parmasad [1,2], Zoe A. Fisk [1,2,3], Steve M. Callaghan [1,2] and Maxime W.C. Rousseaux [1,2,3,4,5,*]

[1]Department of Cellular and Molecular Medicine, University of Ottawa, Ottawa, ON K1H8M5, Canada
[2]University of Ottawa Brain and Mind Research Institute, Ottawa, ON K1H8M5, Canada
[3]Aligning Science Across Parkinson's (ASAP) Collaborative Research Network, Chevy Chase, MD
[4]Ottawa Institute of Systems Biology, University of Ottawa, Ottawa, ON K1H8M5, Canada
[5]Eric Poulin Center for Neuromuscular Diseases, University of Ottawa Brain and Mind Research Institute, Ottawa, ON K1H8M5, Canada

*To whom correspondence should be addressed at: University of Ottawa, 451 Smyth Road, Ottawa, K1H8M5, Canada. Tel: +1 6138625800 ext. 8611;

Email: max.rousseaux@uottawa.ca

Abstract

A growing body of evidence suggests that nuclear alpha-synuclein (αSyn) plays a role in the pathogenesis of Parkinson's disease (PD). However, this question has been difficult to address as controlling the localization of αSyn in experimental systems often requiresproteinoverexpression,whichaffectsitsaggregationpropensity.Toovercomethis,weengineered*Snca*^{NLS} mice,whichlocalize endogenous αSyn to the nucleus. We characterized these mice on a behavioral, histological and biochemical level to determine whether the increase of nuclear αSyn is sufficient to elicit PD-like phenotypes. *Snca*^{NLS} mice exhibit age-dependent motor deficits and altered gastrointestinal function. We found that these phenotypes were not linked to αSyn aggregation or phosphorylation. Through histological analyses, we observed motor cortex atrophy in the absence of midbrain dopaminergic neurodegeneration. We sampled cortical proteomes of *Snca*^{NLS} mice and controls to determine the molecular underpinnings of these pathologies. Interestingly, we found several dysregulated proteins involved in dopaminergic signaling, including Darpp32, Pde10a and Gng7, which we further confirmed was decreased in cortical samples of the *Snca*^{NLS} mice compared with controls. These results suggest that chronic *endogenous* nuclear αSyn can elicit toxic phenotypes in mice, independent of its aggregation. This model raises key questions related to the mechanism of αSyn toxicity in PD and provides a new model to study an underappreciated aspect of PD pathogenesis.

Introduction

Alpha-synuclein (αSyn) is a protein notorious for its involvement in Parkinson's disease (PD) pathogenesis. For one, it is a primary constituent of Lewy bodies and Lewy neurites, pathological hallmarks of PD (1). Moreover, copy number variations and missense mutations in the αSyn gene, *SNCA*, cause genetic forms of PD, further reinforcing its involvement in disease etiology (2–8). αSyn was first described as a presynaptic and nuclear protein (9). However, nuclear αSyn has largely been overshadowed by a focus on its cytoplasmic/synaptic form, likely due to the cytoplasmic localization of Lewy bodies. Despite this, several studies have linked nuclear αSyn to PD on multiple levels: in cell (10–14) and animal (6,15–18) models of PD, as well as in brain tissue from individuals with αSyn pathologies [synucleinopathy; (19– 21)]. These studies examined the role of nuclear αSyn by overexpressing it together with mutations or a nuclear localization signal [NLS; (12,15,17,18,22,20)], or upon toxin exposure (16), hinting at a role for nuclear αSyn in disease pathogenesis by its involvement in DNA binding (23,24) or histone modification (17) to alter transcription, and in DNA repair (25). Although these studies support a link between nuclear αSyn and PD, its specific role in disease—whether deleterious or beneficial—remains clouded due to the reliance on its overexpression or exogenous stressors, making it difficult to parse out the driver of toxicity in the absence of αSyn aggregation.

To directly test the consequence of chronic αSyn mislocalization to the nucleus *in vivo,* without resorting to protein overexpression, we engineered a mouse model to endogenously express αSyn with a C-terminal NLS-Flag tag driving its mislocalization to the nucleus. We extensively characterized these mice at the behavioral, histological and biochemical level to assess whether chronic nuclear localization of αSyn causes age-dependent phenotypes resembling PD or related αSyn proteinopathies.

Results

Effective nuclear targeting of αSyn in *Snca*^{NLS} mice

To study if nuclear αSyn is sufficient to elicit age-related behavioral and pathological phenotypes, we generated a

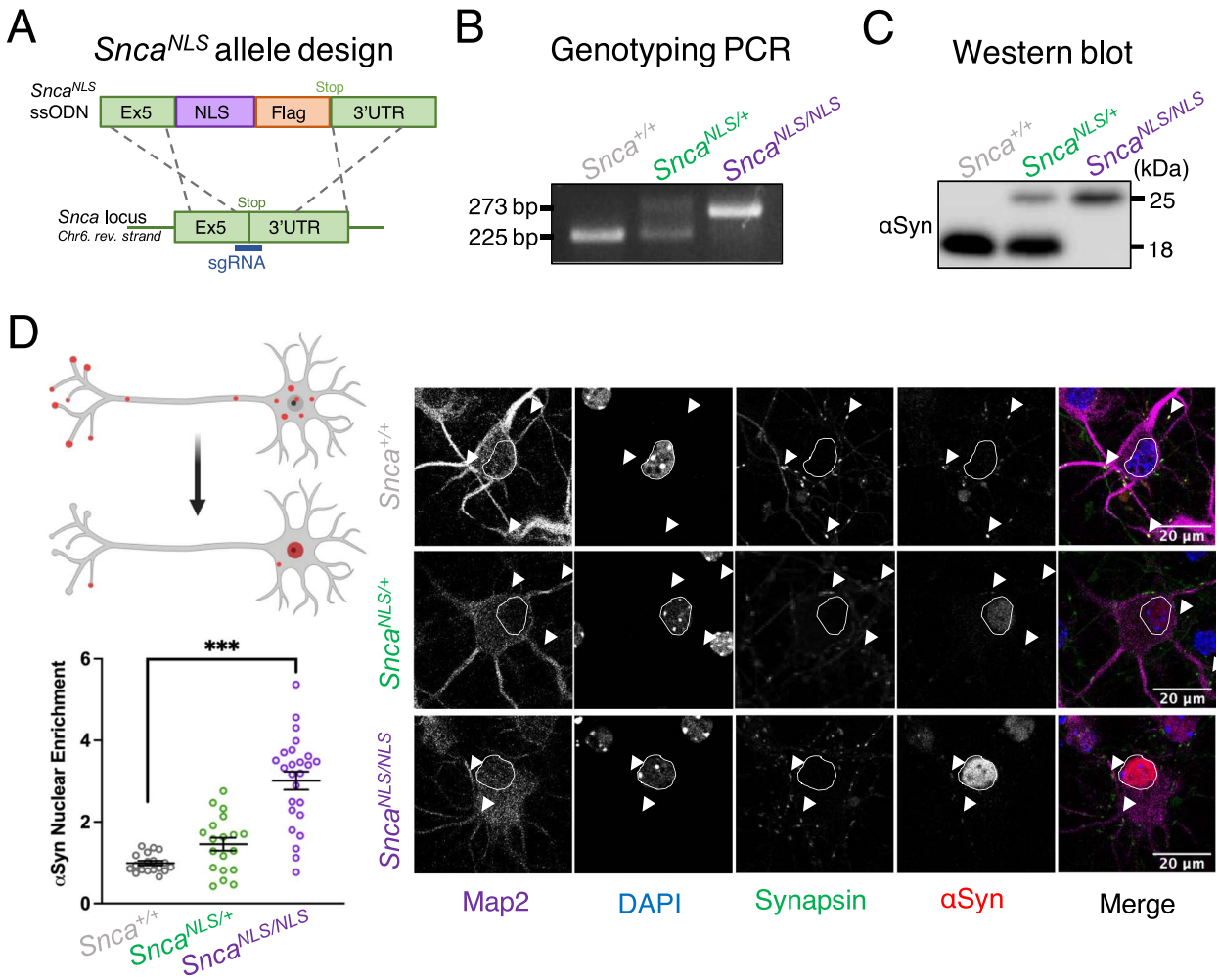

Figure 1. *Snca*^{NLS} mice effectively target αSyn to the nucleus *in vitro* and *in vivo*. (**A**) *Snca*$^{NLS\text{-}Flag}$ knock-in scheme with C-terminal NLS-Flag tag. Visualization of the knockin via (**B**) PCR and (**C**) western blot. (**D**) Illustration of nuclear localization of αSyn (upper left) with quantification (lower left) of nuclear αSyn from primary cortical neurons in wildtype (top right panels), *Snca*$^{NLS/+}$ (middle right panels) and *Snca*$^{NLS/NLS}$ (bottom right panels; $n = 3$). Protein quantification (lower left) depicts nested relative per-cell intensity of nuclear αSyn from three independent experiments. White arrows denote presynaptic αSyn and nuclei are circled in white. Nested one-way ANOVA with Bonferroni multiple comparison: **denotes $P < 0.001$.

mouse line that targets endogenous αSyn to the nucleus via the knockin of an NLS-Flag tag on αSyn (*Snca*^{NLS}). The NLS-Flag construct was targeted to the 3′ end of the *Snca* coding sequence with the modified *Snca-NLS-Flag* gene predicted to transcribe a fusion protein of wildtype αSyn with a C-terminal NLS-Flag tag (Fig. 1A). After generating and backcrossing mice (see Materials and Methods and Supplementary Material, Fig. S1), we confirmed the knockin via sequencing (Supplementary Material, Fig. S1B) and were able to distinguish between the genotypes via a PCR band shift (Fig. 1B) and a larger protein size via western blot (Fig. 1C). Mice were born at expected Mendelian ratios (Supplementary Material, Fig. S1C), confirming that insertion of this tag did not pose major developmental deficits.

To examine the efficiency of the NLS-Flag tag, we cultured primary cortical neurons for 7 days *in vitro* and quantified the level of nuclear αSyn through immunofluorescent microscopy. We observed a 3-fold increase in nuclear αSyn in *Snca*$^{NLS/NLS}$ and a 1.5-fold increase in *Snca*$^{NLS/+}$ compared with *Snca*$^{+/+}$ (wildtype) cells (Fig. 1D). This trend was consistent in stained adult mouse brain tissue at both 2- and 18-months where we found a 2–5-fold increase in nuclear αSyn in the cortex (Fig. 2A), dentate gyrus (Fig. 2B) and substantia nigra (Fig. 2C). Importantly, this roughly corresponds to the 2.5–3-fold increase of nuclear αSyn, which we and others have previously observed in post-mortem brain tissue from individuals with PD or other animal models of synucleinopathy, suggesting the model displays a disease-relevant increase of nuclear αSyn (6,15–19).

Increased nuclear αSyn leads to an age-dependent motor decline

To test whether chronic nuclear accumulation of αSyn is sufficient to elicit PD-like phenotypes over time, we subjected *Snca*$^{NLS/NLS}$ mice and littermates to a battery of behavior tests at 3-, 9- and 18-months of age. We found that the *Snca*$^{NLS/+}$ and *Snca*$^{NLS/NLS}$ mice performed similarly to wildtype at 3-months of age (Fig. 3A). By 9-months, however, the *Snca*$^{NLS/NLS}$ mice displayed a significant motor deficit in rotarod (Fig. 3B) as well as a delayed time to contact their forepaws in the adhesive

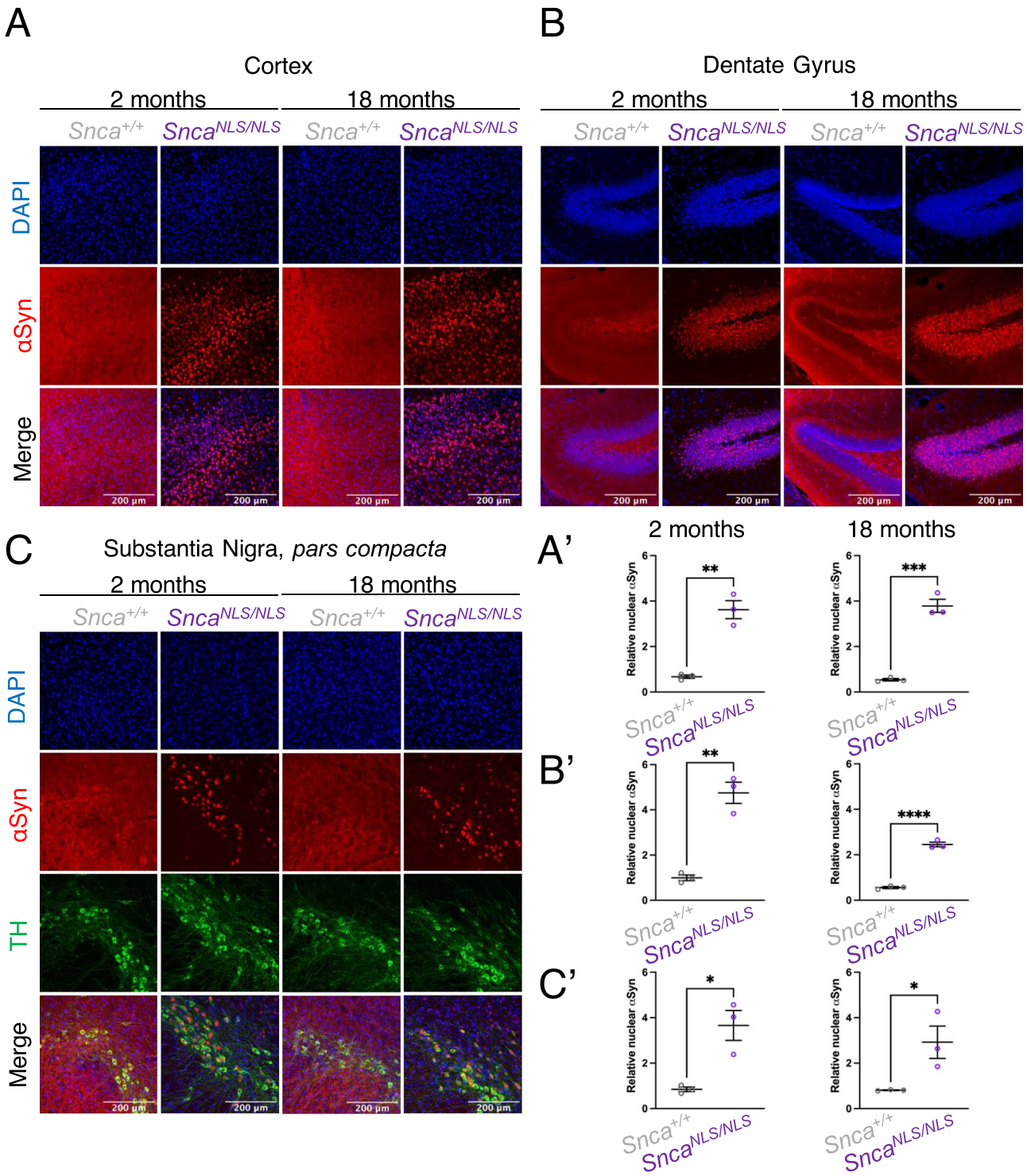

Figure 2. *Snca*^{NLS} mice exhibit a consistent 2–5-fold increase in nuclear αSyn with age. Immunofluorescent images of 2- (left) and 18-month (right) mouse (**A**) cortex, (**B**) dentate gyrus and (**C**) substantia nigra, *pars compacta*. Nuclear enrichment of αSyn was quantified for (A′–C′) all brain regions at both 2- (left) and 18-months (right). Unpaired, two-tailed *t*-test: *, **, ***, **** denote $P < 0.05$, < 0.01, < 0.001 and < 0.0001, respectively.

test (Fig. 3C). Interestingly, *Snca*$^{NLS/+}$ mice also exhibited a significant deficit on the rotarod test—suggestive of a dominant phenotype. This rotarod deficit was not observed when testing *Snca*$^{-/-}$ mice at 9 months (Supplementary Material, Fig. S2), suggesting it is due to the accumulation of nuclear αSyn and not a loss-of-function of pre-synaptic αSyn. Surprisingly, after aging the *Snca*^{NLS} mice to 18 months, we observed milder motor phenotypes relative to wildtype controls; likely due to the 18-month wildtype mice showing increased difficulty at performing these tasks when comparing their motor ability with that at 3- and 9-months of age (Supplementary Material, Fig. S3).

With increasing awareness around non-motor symptoms in PD, we also measured cognition, anxiety and overall wellness in the *Snca*^{NLS} line. We found that

motor phenotypes relative to wildtype controls; likely due to the 18-month wildtype mice showing increased difficulty at performing these tasks when comparing their motor ability with that at 3- and 9-months of age (Supplementary Material, Fig. S3).

With increasing awareness around non-motor symptoms in PD, we also measured cognition, anxiety and overall wellness in the *Snca*^{NLS} line. We found that *Snca*$^{NLS/NLS}$ and *Snca*$^{NLS/+}$ mice performed similarly to their wildtype littermates in non-motor behavior tests at all timepoints (Supplementary Material, Figs. S4– S6). In addition to motor decline, people living with PD often experience gastrointestinal difficulties such as constipation (26,27). To measure constipation in our mice, we examined fecal excretions in the span of an hour. We found that 18-month-old *Snca*$^{NLS/NLS}$ mice excretions contained significantly less water than their wildtype counterparts (Fig. 3D). Lastly, we observed a trend for early lethality in the *Snca*$^{NLS/NLS}$ mice, whereby 37% of *Snca*$^{NLS/NLS}$ mice died by 20 months of age, compared with 14% of wildtype littermates (P=0.1081, Fig. 3E). Taken together, the *Snca*$^{NLS/NLS}$ mice display age-dependent motor and gastrointestinal dysfunction reminiscent of PD.

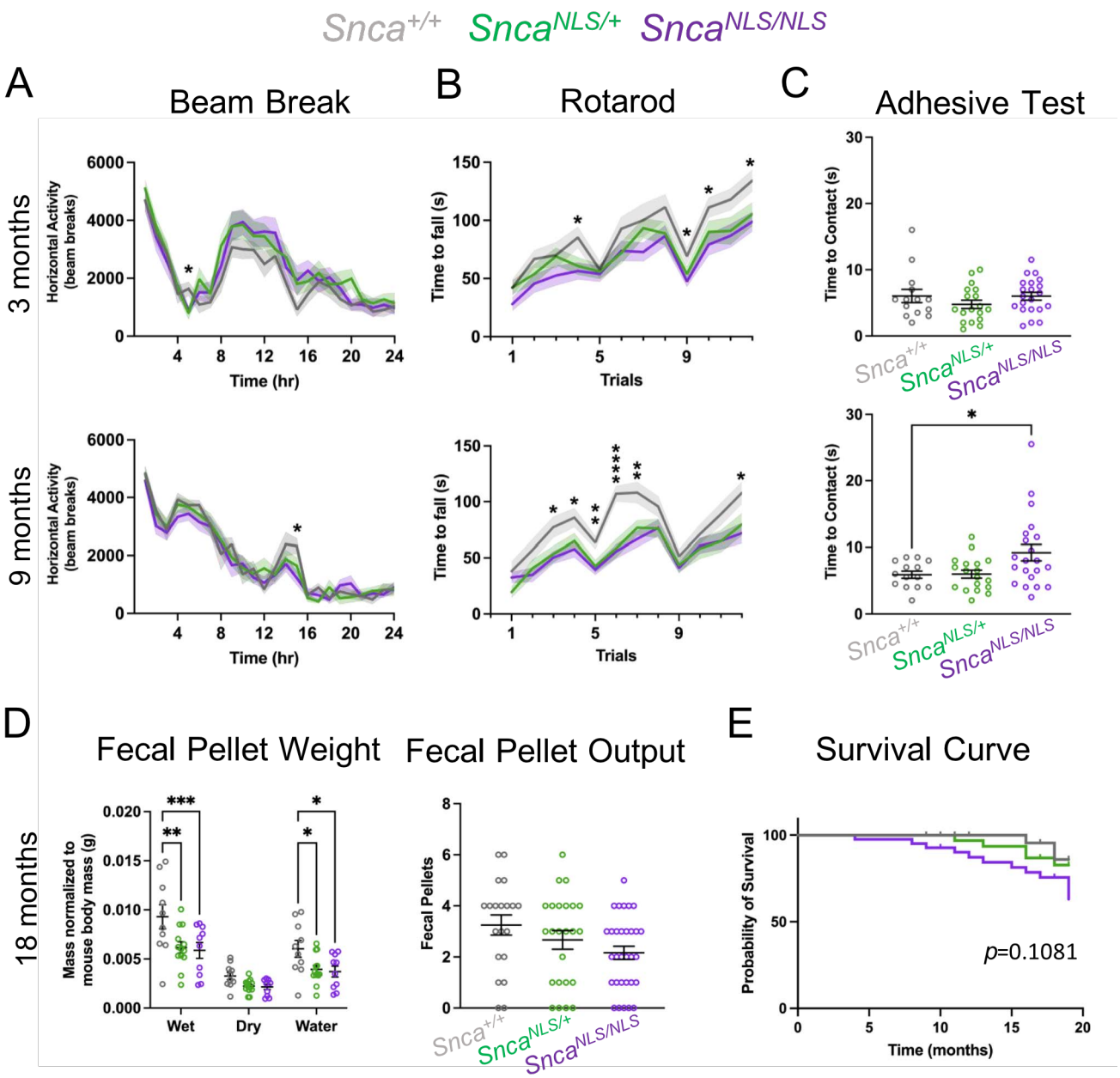

Figure 3. *Snca*^{NLS} mice exhibit significant motor and gastrointestinal dysfunction.Analysis of the 3- (top) and 9-month (bottom) mice for (**A**) Beam Break, (**B**) Rotarod and (**C**) Adhesive Test measuring time to contact their forepaws, (**D**) Fecal Pellet Weight measuring fecal weight and water content over 1 h (left), and Fecal Pellet Output measuring fecal pellets produced in 10 min (right), (n=10–21). (**E**) Survival curve from all mice in the behavior colony (n=42–58). One-way (C, D right), two-way ANOVA (A, D left), or mixed-effects analysis (B) with Bonferroni multiple comparison or Log-rank (Mantel Cox) test (**F**): ns, *, **, *** and **** denote P>0.05, <0.05, <0.01, <0.001 and <0.0001, respectively.

Snca$^{NLS/NLS}$ mice exhibit cortical atrophy, independent of αSyn aggregation or dopaminergic neurodegeneration

Many studies suggest that αSyn toxicity is intrinsically tied to its aggregation, as the two are often associated in humans with PD

and in animal models of the disease (1,28,29). However, models of αSyn toxicity often rely on the introduction of synthetically derived misfolded αSyn fibrils (30,31) or overexpression of αSyn (15,32), thereby potentiating its aggregation *in vivo*.Given that the *Snca*^{NLS} mice display age-dependent behavioral phenotypes, yet do not rely on αSyn overexpression, we asked whether accumulation of endogenous αSyn in the nucleus leads to its aggregation and thusly contributes to its toxicity. We examined both the solubility of αSyn as well as its pathologically linked phosphorylation at serine residue 129 (pS129) by biochemical fractionation of brain samples of *Snca*$^{NLS/NLS}$ mice compared with littermates. We used the *mThy1-SNCA* ('line 61') transgenic and *Snca* knockout (*Snca*$^{-/-}$) mouse lines as positive (32) and negative (33) controls, respectively. To our surprise, we found that the accumulation of nuclear αSyn does not lead to aggregation (Fig. 4A), nor does it become phosphorylated at S129 (Fig. 4A, B), and in fact total αSyn levels are reduced in these mice (Fig. 4A–C). These findings were further supported by histology,which showed no marked increase in pS129 in aged *Snca*$^{NLS/NLS}$ mice compared with their respective littermates (Fig. 4D). This suggests that nuclear accumulation of αSyn confers neuronal dysfunction independent of aggregation.

A hallmark of PD is nigrostriatal degeneration. Because of the relatively high expression of αSyn in dopaminergic neurons [Fig. 2C; (34)], we hypothesized nuclear αSyn could be acutely toxic to dopaminergic neurons, causing their death and ultimately leading to the observed behavioral deficits in *Snca*^{NLS} mice. To our surprise, we found that young and aged *Snca*$^{NLS/NLS}$ mice had intact nigrostriatal tracts, when evaluated by striatal tyrosine hydroxylase (TH) fiber density and stereological estimation of dopaminergic cell number in the SNc at 3- and 18-months of age (Fig. 5A and B,
Supplementary Material, Fig. S4E). Moreover, HPLC (high-performance liquid chromatography) analysis of mouse striata revealed that 18-month-old mice across genotypes exhibit similar levels of dopamine and its metabolites (DOPAC, HVA and 5-HIAA; Fig. 5C).

Since *Snca*$^{NLS/NLS}$ mice exhibit motor defects without nigrostriatal degeneration nor αSyn aggregation, we took a step back to ask whether nuclear αSyn may impact other areas of the brain, thus contributing to PD-like phenotypes. Cortical involvement has long been linked to several synucleinopathies including PD, dementia with Lewy bodies (DLB) and PD with dementia [PDD; (29,35–37)]. We therefore explored higher order cortical areas to determine whether *Snca*$^{NLS/NLS}$ mice exhibit neurodegenerative features outside of the SNc. We conducted gross anatomical studies using hematoxylin and eosin (H&E) and toluidine blue staining and found significant anterior cortical thinning in the motor cortex (Fig. 6A) and a marked increase in pyknotic cells (Fig. 6B) throughout the cortex of 18-month-old *Snca*$^{NLS/NLS}$ mice. We further stained cortical sections with NeuN [Neuronal nuclei antigen, a.k.a. RNA Binding Fox-1 Homolog 3 (Rbfox3)] and found a significant decrease in neurons in layers V/VI of 18-month-old *Snca*$^{NLS/NLS}$ mice compared withtheirlittermates(Fig. 6C).Thus,nuclearαSyncauses cortical dysfunction in the absence of its aggregation or nigrostriatal degeneration.

Unbiased proteomic analysis uncovers reduced Darpp-32, Pde10a and Gng7 levels in *Snca*$^{NLS/NLS}$ mice

We followed an unbiased strategy to uncover the molecular mechanisms underlying the behavioral and histological phenotypes of the *Snca*$^{NLS/NLS}$ mice via quantitative proteomic analysis on cortices from 9-monthold mice. At this age, *Snca*$^{NLS/NLS}$ mice exhibit behavioral abnormalities (Fig. 3), allowing identification of early molecular changes that drive the late-stage cortical atrophy exhibited in these mice and in PD. To quantify proteomic differences in wildtype and *Snca*$^{NLS/NLS}$ mice, we performed pooled TMT10plex labeling for 5 wildtype and 5 *Snca*$^{NLS/NLS}$ mouse cortices followed by mass spectrometry to identify differential proteomic changes (Fig. 7A). This approach yielded a list of nearly 1800 proteins, of which 114 had a Log_2 fold-change of ±1 relative to wildtype (Fig. 7B). Of these 114 hits, 66 were downregulated and 48 were upregulated (Supplementary Material,Table S2).Gene ontology term analysis revealed a significant enrichment for biological processes that are disturbed in PD, including regulation of GPCR signaling (Fig. 7C). To increase the stringency of our list, we filtered these hits using a statistical cut-off (Mann–Whitney *P*value <0.05).From this,we identified 10 high-confidence hits (Fig. 7D). Interestingly, among these 10 hits we noticed a few proteins of particular importance in DA signaling and have been associated with PD, such as Cacna1e, Darpp-32 [dopamine- and cAMP-regulated neuronal phosphoprotein a.k.a. protein phosphatase 1 regulator inhibitor subunit 1b (Ppp1r1b)], Fgf1, Gng7 (G Protein Subunit Gamma 7), Pde10a (Phosphodiesterase 10A) and SerpinA1a (38–45). We confirmed overall trends in reduction of Darpp-32, Pde10a and Gng7 in the 9month-old *Snca*$^{NLS/NLS}$ mice using western blot (Fig. 7E), thereby validating our proteomics approaches. Collectively, these data suggest that disrupted dopaminergic signaling pathways may be an early event of nuclear αSyn toxicity.

Discussion

The mechanisms underlying αSyn toxicity have been difficult to pin down. We and others have previously shown that nuclear αSyn is increased in the PD postmortem brain and in animal models harboring *SNCA* mutations (6,13,20,19,46). Nonetheless, previous studies examining the role of nuclear αSyn in PD pathogenesis have yielded conflicting results, ranging from neurodegenerative (13,15,17,46) to neuroprotective (20,25) phenotypes. This may be in part due to the degree of overexpression of αSyn or the choice of read-out in these models. Our study sought to overcome this by answering if the nuclear accumulation of *native* αSyn is sufficient

Figure 4.

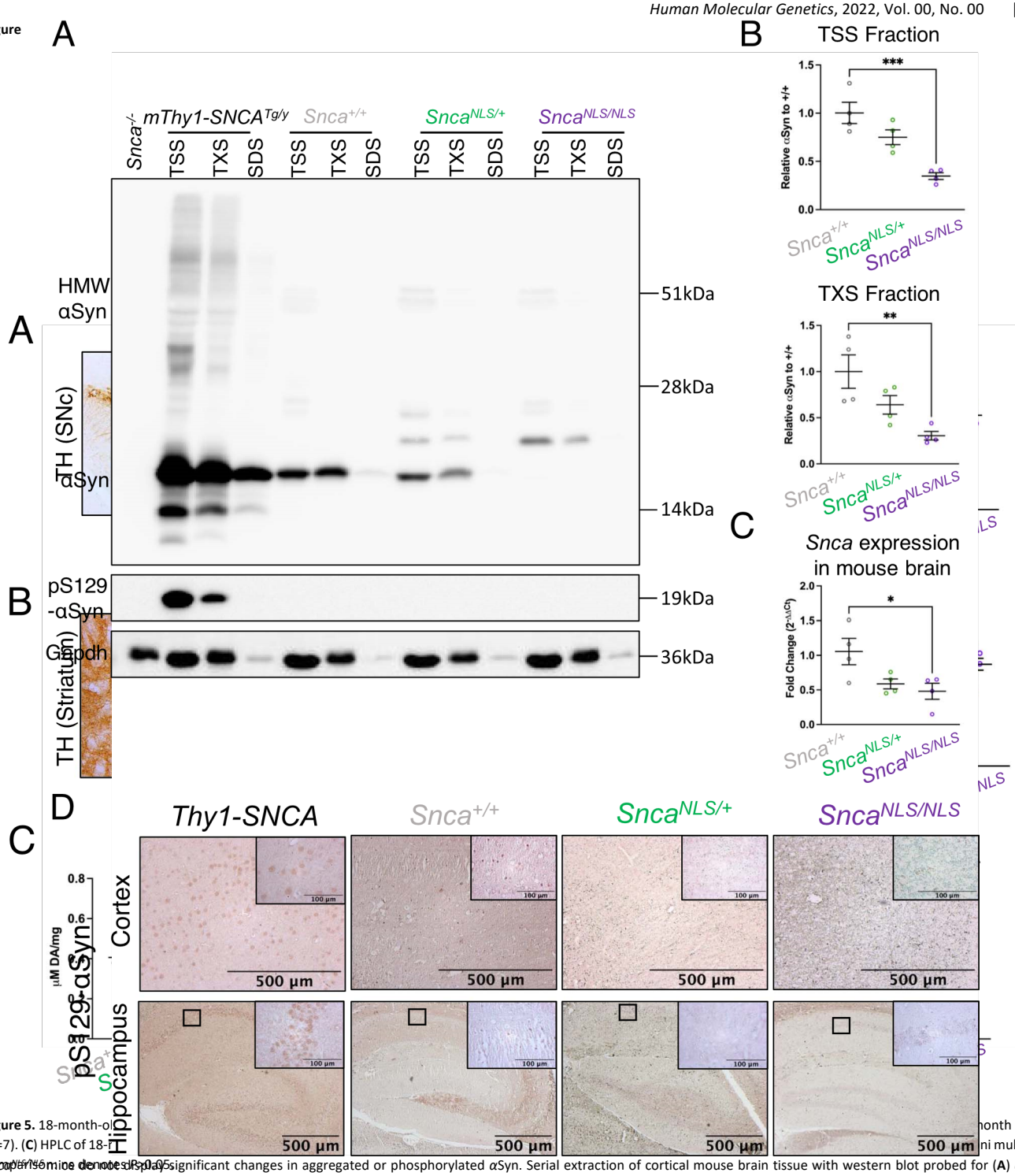

Figure 5. 18-month-old [illegible] month mice (n=7). (**C**) HPLC of 18-[illegible] ni multiple comparison test denoted as $p<0.05$, significant changes in aggregated or phosphorylated αSyn. Serial extraction of cortical mouse brain tissue with western blot probed for (**A**) αSyn (upper blot) and pS129-αSyn (middle blot) and Glyceraldehyde-3-Phosphate Dehydrogenase (Gapdh; bottom blot) comparing the level of αSyn in the (**B**) TSS (upper) and TXS (lower) fraction (n=4). (**C**) qPCR of *Snca* mRNA from 9-month mouse cortex (n=4). (**D**) pS129αSyn staining of the motor cortex (upper) and hippocampus (lower).One-way ANOVA with Bonferroni multiple comparison: *, ** and *** denotes $P<0.05$, <0.01 and <0.001, respectively.

to cause PD-like phenotypes in mice. We engineered a mouse model with an *NLS-Flag* knockin on *Snca* to characterize the effects of chronically increased nuclear αSyn. We found that *Snca*$^{NLS/NLS}$ mice reveal PD-like phenotypes including age-dependent motor decline, as well as cortical dysfunction.The cortical atrophy we observed draws parallels to the cell loss seen in synucleinopathies with cortical involvement like DLB and PDD (29,35–37). Moreover, the

anatomical location of this cell loss dovetails with the motor deficits seen in these mice and may shed light onto how nuclear αSyn in PD may be linked to cortical dysfunction and disease manifestation. When examining the proteomic profile of the *Snca*$^{NLS/NLS}$ mice, we found a few high-confidence hits that have been previously associated with PD. Among these, we identified Pde10a, Darpp-32 and Gng7. Although we found no significant decrease in striatal dopamine, it is interesting to note that these proteins are all involved in dopamine signaling, hinting at a potential mechanism by which nuclear αSyn causes dysfunction via perturbing intracellular signaling (38,42,47–55). Importantly, *Gng7* knockout mice exhibit significant age-dependent motor deficits, particularly in the rotarod test which was the motor assay with which the *Snca*^{NLS} mice exhibited the most difficulty(49).Inaddition,onestudylookingatpatientswith schizophrenia found reduced Pde10a and medial prefrontal cortex thinning, another aspect observed in the *Snca*^{NLS} mice (55). Together, these changes in protein levels hint at a possible mechanism whereby nuclear αSyn elicits dopaminergic signaling defects, in the absence of overt dopaminergic neurodegeneration.

Although characterizing *Snca*$^{NLS/NLS}$ mice, we consistently noted how this mouse line diverges from *Snca*$^{-/-}$ mouse phenotypes (Supplementary Material, Fig. S2), cementing that *Snca*$^{NLS/NLS}$ mouse phenotypes are likely gain-of-function. To wit, *Snca*$^{-/-}$ mice exhibit mild synaptic deficits in the absence of gross motor or non-motor deficits (33,56), likely due to compensation by β-synuclein and, to a lesser extent, γ-synuclein (57–59). Indeed, the motor phenotypes appear to be dependent on the local dose of nuclear αSyn as even the *Snca*$^{NLS/+}$ mice exhibit some motor behavior deficits— albeit to a lesser extent than their *Snca*$^{NLS/NLS}$ littermates, suggesting that they are due to a gain-of-function of nuclear αSyn and not a loss-of-function of synaptic αSyn. Nevertheless, we cannot exclude a model in which partial loss of synaptic αSyn combined with increased nuclear αSyn may drive the age-dependent behavioural and pathological phenotypes seen in *Snca*^{NLS} mice. Strikingly, behavioral and histological phenotypes in *Snca*^{NLS} mice occur independently from αSyn aggregation and pathogenic phosphorylation. Indeed, overall levels of αSyn are reduced in *Snca*^{NLS} mice—potentially by some regulatory mechanism or feedback loop—therefore suggesting that these αSyn-mediated phenotypes occur despite its aggregation or phosphorylation. This suggests

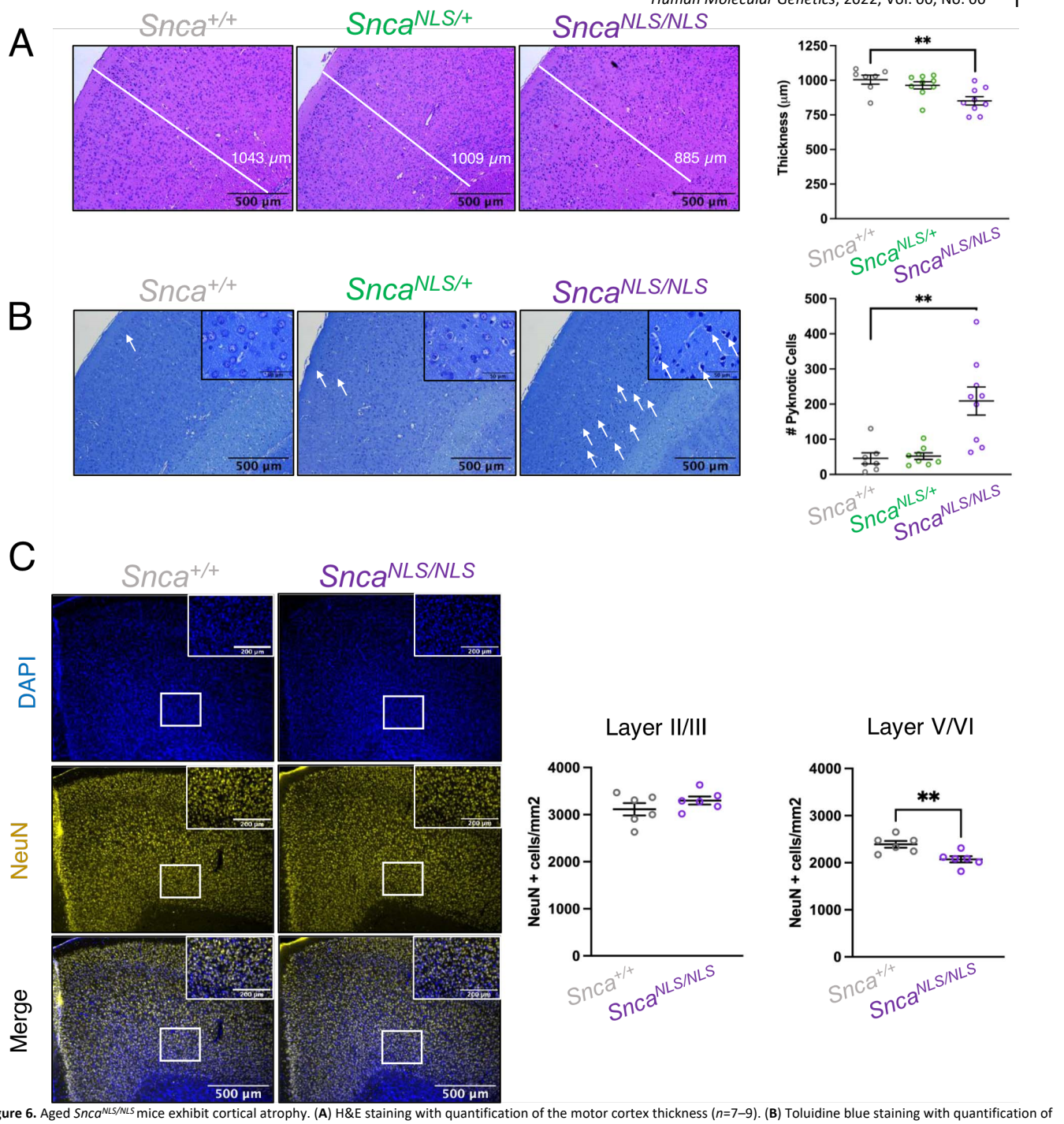

Figure 6. Aged *Snca*$^{NLS/NLS}$ mice exhibit cortical atrophy. (**A**) H&E staining with quantification of the motor cortex thickness (n=7–9). (**B**) Toluidine blue staining with quantification of pyknotic cells from the motor cortex (n=7–9). White arrows denote select pyknotic cells. (**C**) NeuN staining of wildtype (left) and *Snca*$^{NLS/NLS}$ (right) measuring NeuN+ cells in motor cortex layers II/III and V/VI. One-way ANOVA with Bonferroni multiple comparison (A, B) or unpaired, two-tailed t-test (C): ns, ** denote P>0.05 and <0.01, respectively.

a heretofore underappreciated role of *soluble*, nuclear αSyn in the pathogenesis of PD.

The cellular mechanisms that drive the nuclear accumulation of αSyn and its subsequent sequelae in PD remain elusive. Whether active or passive mechanisms bring αSyn to the nucleus is unknown. Native αSyn does not possess an NLS, therefore, it may be driven into the nucleus by passive mechanisms [it can traverse the nuclear pore complex due to its small size; (60)] and could be retained by interaction with nuclear components (e.g. histones or DNA) (16,17,20,24,25,61) or via uncharacterized modifications. Alternatively, active mechanisms such as its interaction with TRIM28 (19) or RAN (14) may be key in regulating its nuclear import. Moreover, αSyn likely has an important native role in the nucleus, particularly during

Human Molecular Genetics, 2022, Vol. 00, No. 00

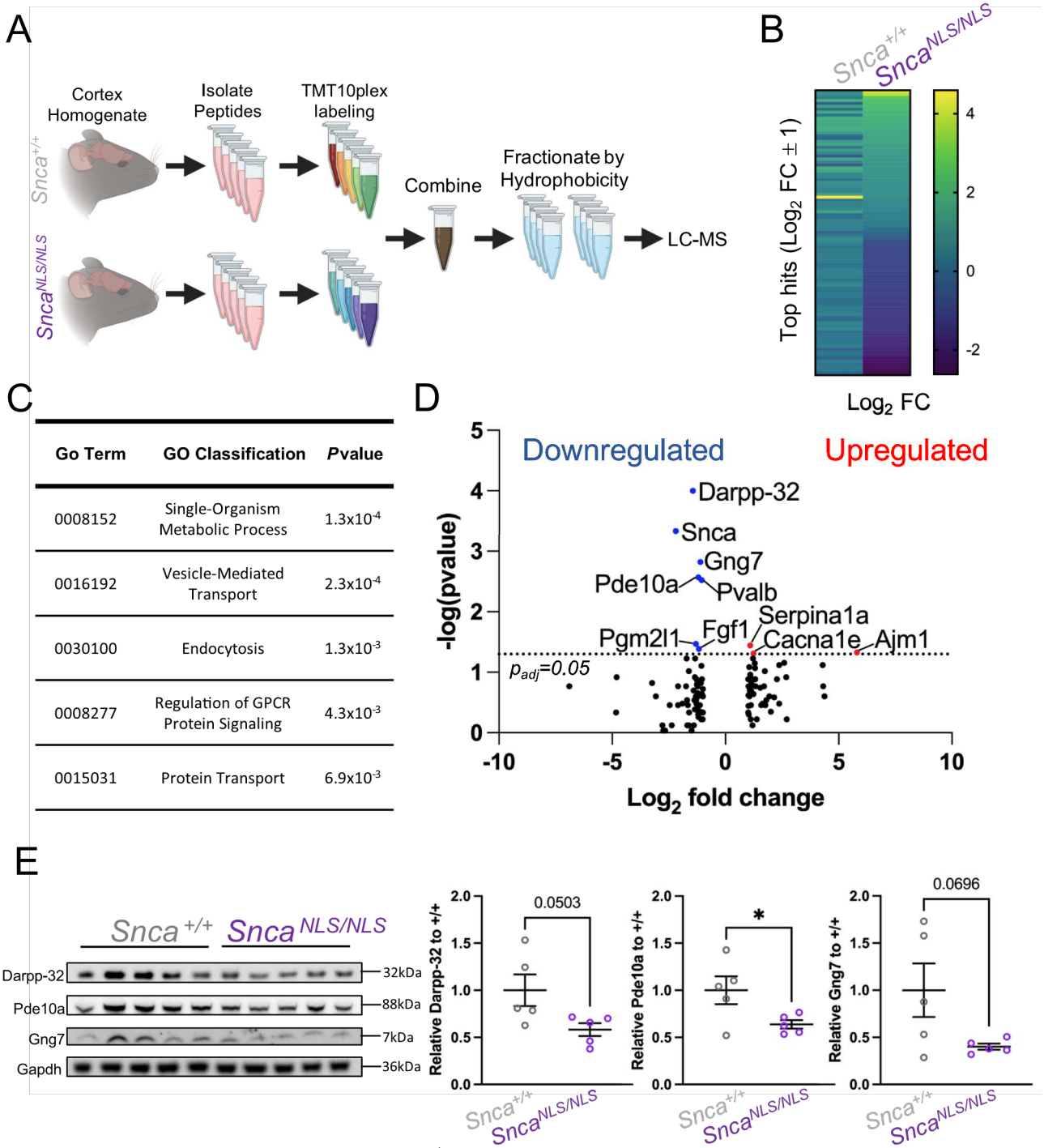

Figure 7. Mass spectrometry reveals proteomic alterations in the *Snca*$^{NLS/NLS}$ mice. (**A**) Mass spectrometry scheme for quantitative comparison of proteome between 9-month wildtype and *Snca*$^{NLS/NLS}$ cortices (n=5). (**B**) Heat map of all proteins identified through mass spectrometry with values results withwithin ±1 Log±21fold-change. (Log$_2$ fold-change highlighting significantly upregulated proteins in red and downregulated in blue. (**C**) Table of enriched gene ontology pathways among the ±1 Log^2 fold-change hits. (**D**) Volcano plot of mass spectrometry**E**) Western blot of cortical mouse brain tissue from 9-month mice probing for Darpp-32 (upper), Pde10a (upper middle), Gng7 (lower middle) and Gapdh (bottom) with quantification

(right). Unpaired, two-tailed t-test: ⁎ denotes P<0.05.

mouse embryonic development, where nuclear αSyn constitutes up to 40% of its total cellular distribution, compared with 3–15% of total cellular distribution in adult mice (20). There, αSyn is suggested to bind both DNA and histones to modulate gene expression (16,17,24,25,61–64). In wildtype mice, nuclear αSyn was shown to be neuroprotective by binding to DNA and colocalizing with DNA damage response elements to protect against DNA damage (25). Whether the increase in nuclear αSyn observed in PD—modeled in the *Snca*^{NLS} mice—causes a gain of this normal developmental function or a neomorphic function will be important to establish, to facilitate future therapeutic development.

Materials and Methods

Mouse design and engineering

Mouse engineering

To generate the *Snca*^{NLS} mice, Cas9 protein was complexed to a sgRNA targeting the 3′ locus of *Snca* (sgRNA target sequence: 5′-TTGGTAGCCTTCCTAATATC-3′); and, together with a single-stranded oligodeoxynucleotide (ssODN) repair template (sequence: 5′-CACTGTGAAGC-AGACAGTTGATATCTGTCACTTCACTGACAAGGCATGCTGTTATTATTTTCTTTTTCTGATATTAGGAAGGCTACCAAGACTATGAGCCTGAAGCCGACTACAAGGACGACGACGACC-AAGTAAGAATGTCATTGCACCCAATCTCCTAAGATCTGCCGGCTGCTCTTCCATGGCGTACAAGTGCTCAGT-3′; IDT Ultramer), were injected and implanted into pseudopregnant FVB female mice (65). Three founder mice were generated and backcrossed onto a ∼99.75% pure C57Bl6/J background (Taconic 1450 SNP analysis, sequencing and subsequent backcrossing; see Supplementary Material, Fig. S1A and B), before being expanded onto a mixed C57Bl6/J; C57Bl6/NCrl background. One line was selected for subsequent extensive characterization and is being made available through the Jackson Laboratory (RRID:IMSR_JAX:036763).

Genotyping

A small (∼1 mm) tail sample is digested prior to PCR amplification using primers outside of the sequence covered by the ssODN used for the initial mouse line. Forward: 5′-TTTTATCTGATTGAAATGATGAGC-3′; Reverse: 5′-ATGACTGGGCACATTGGAA-3′. PCR protocol: 95◦C for 2 min, (95◦C for 30 s, 56◦C for 30 s, 72◦C for 30 s) repeated for 35 cycles, 72◦C for 5 min. Mutant allele:
273 bp; Wildtype allele: 225 bp.

Mouse husbandry

All mice were housed with up to 5 mice per cage on a 12 h light–dark cycle. Mice were fed *ad libitum* and all husbandry was performed by the uOttawa Animal Care and Veterinary Services staff. All animal work was done under the approved breeding (CMMb-3009 and CMMb3654) and behavior (CMMe-3091) protocols approved under the uOttawa Animal Care Committee. All mice were handled daily for 1 week prior to all behavior testing and both male and female mice were used in all experiments.

Behavior

Open field

Lighting in the behavior room was set to 100 lux and mice were habituated for 60 min prior to testing. Mice were placed into the open field box (45 cm^3) for
10 min with their movement recorded/analyzed with Ethovision software (Noldus Information Technology).
dx.doi.org/10.17504/protocols.io.b5qzq5x6.

Fecal pellet output

Upon completion of the Open Field test, the number of fecal pellets excreted during the 10 min trial were quantified.

Beam break

Single mice were placed into a clean cage with access to food and water *ad libitum* for 24 h at the standard 12 h light–dark cycle with their movement recorded/analyzed via Fusion software.

Nesting: Directly following Beam Break testing, one square of nestlet (5 cm^2 cotton pad) was placed in each Beam Break cage for 17–19 h. Following this, the nestlets were scored on a scale of 1–5 as described in Deacon 2006 (66), with 1 and 5 representing minimal and maximal nest quality, respectively. dx.doi.org/10.17504/protocols. io.b5q2q5ye.

Y maze forced alternation

Mice were provided with extra-maze (irregular black cue with squared edges on right wall, black triangle on left wall) and intra-maze (Arm 1 has solid black rectangle, Arm 2 has horizontal bars and Arm 3 has diagonal stripes) cues. The room was set to 60 lux and mice were habituated for 60 min prior to testing. During the first 5 min trial, Arms 2 and 3 were alternately blocked. Following the 30 min inter-trial interval, the mice were placed back into the Y maze apparatus for 5 min without any blocked arms and their movements were recorded/analyzed with EthoVision software. dx.doi.org/10.17504/ protocols.io.b5smq6c6.

Adhesive test

After a 60 min habituation, the home cage of the mice was lightly wiped to remove all bedding material. The mice were individually placed back into the emptied home cage for a 1 min habituation. Next, a 1 cm^2 of medical adhesive was placed on each forepaw and the mice were placed back into the wiped home cage where the time to remove adhesive was measured up to a 2 min maximum. dx.doi.org/10.17504/protocols.io.b5snq6de.

Pole test

Following a 60 min habituation, mice were placed on a textured metal pole (8 mm diameter, 55 cm tall) ∼3 cm from the top facing upwards. The mice were given up to 1 min to turn around (facing downwards) and up to 1 min to descend the pole. dx.doi.org/10.17504/protocols.io.b5 sqq6dw.

Rotarod

Following a 60 min habituation, mice were placed on a rod (IITC Life Sciences) rotating from 4 to 40 revolutions per minute over 5 min for 4 trials per day with a 10 min inter-trial interval. This was repeated for 3 days total. dx. doi.org/10.17504/protocols.io.b5srq6d6.

DigiGait

Following a 60 min habituation, mice were placed in the DigiGait treadmill (Mouse Specifics Inc.). The treadmill ran at 22 cm/s (3- and 9-months timepoints) or 18 cm/s (18-month timepoint) with a 0◦ incline. 3 s of continuous movement was recorded using DigiGait Imager software and was then analyzed with DigiGait Analysis software. dx.doi.org/10.17504/protocols.io.b5stq6en.

Fear conditioning

Naïve age- and sex-matched mice were used to obtain the optimal intensity of foot shock. On Day 1 of testing, mice were placed into the Fear Conditioning apparatus (Noldus Information Technology) for 6 min during which time the mice experienced 3 tone-shock pairings (30 s tone co-terminated with a 2 s foot shock). On Day 2, mice were placed into the same Fear Conditioning apparatus for 6 min with no tone or foot shock. On Day 3, mice were placed into a different Fear Conditioning apparatus, now altered into a triangular shape with solid floor and a vanilla scent for 3 min with no tone then 3 min with the same 30 s tone but no foot shock. Freezing was measured/analyzed with EthoVision on all 3 testing days. dx.doi.org/10.17504/protocols.io.b5suq6ew.

Fecal pellet composition

Mice were placed in a clean cage and their fecal pellets were collected over a 1 h period. These pellets were weighed (wet weight) then desiccated at 65◦C for 19 h and reweighed (dry weight). The differences were calculated between these values to determine the water content.dx.doi.org/10.17504/protocols.io.b5svq6e6.

Histology

See Supplementary Material, Table S1 for a comprehensive list of antibodies used in this study.

Perfusion

Miceweresedatedwith120mg/kgEuthanyl(DIN00141704) then perfused with 1X phosphate buffered saline (PBS) then 4% paraformaldehyde (PFA). Brains were then extracted and incubated in 4% PFA for 72 h prior to a 3-step sucrose dehydration with 10, 20 and 30% sucrose (24 h each). Next, brains were flash frozen for 1 min in
−40◦C isopentane and cryosectioned at 40 μm. dx.doi.org/10.17504/protocols.io.b5swq6fe.

Immunofluorescent staining

Cryosectioned tissue was mounted on a slide then blocked with blocking buffer (0.5% Triton X-100, 10% normalhorseserumin1XPBS)thenincubatedinprimary antibody overnight at 4◦C. Next, the sections were incubated in secondary antibody before drying at room temperature for 2 min. The sections were then covered with #1.5 coverslips and fluorescent mounting medium (Dako cat# S3023). dx.doi.org/10.17504/protocols.io.b5s5 q6g6.

Quick decapitation, fixation

Mice were euthanized by isoflurane inhalation followed by decapitation and brains were quickly extracted.Brains were then submerged in 10% buffered formalin for 72 h prior to paraffin embedding and sectioning at 5 μm. dx.doi.org/10.17504/protocols.io.b5szq6f6.

Diaminobenzidine (DAB) staining

Paraffin-embedded sections were deparaffinized in serial baths of xylenes and ethanol prior to a sodium citrate (10 mm sodium citrate, 0.05% Tween-20, pH 6) antigen retrieval (20 min at 95◦C) and 0.9% H_2O_2 treatment (10 min). Next, sections were blocked in blocking buffer (0.1% Triton X-100, 10% normal horse serum in 1X PBS) then incubated in primary antibody overnight at 4◦C.The following day the sections were incubated in secondary and tertiary antibody solution before exposure to DAB, dehydrating in baths of ethanol and xylenes and covering the tissue with Permount (Fisher Scientific cat# SP15–100)and#1.5coverslips.dx.doi.org/10.17504/protocols.io.b5s9q6h6.

Toluidine Blue and H&E staining

Staining was performed by the Louise Pelletier Histology Core facility at the University of Ottawa on paraffinembedded 5 μm sectioned mouse brain tissue using the Leica Autostainer XL. Briefly, the sections were deparaffinized and exposed to Toluidine Blue for 10 min. For H&E, sections were deparaffinized, exposed to hematoxylin for 7 min and eosin for 30 s. Then, sections were dehydrated and covered with #1.5 coverslips. Two serial sections for each were analyzed by an investigator blinded to the genotypes.

Stereology

Stereology was performed as previously described (19). Briefly, for each mouse, 8 cryosections were stained for THandquantifiedusingStereoInvestigatorsoftware(version 11.06.2). The sections (40 μm) began at the outer limit of the substantia nigra (SNc) and every 6th section was used (Bregma −2.54 to −3.88 mm). Mean section thickness was determined during counting at a frequency of 10 frames (roughly three measurements per hemisphere). The SNc was sampled by randomly translating a grid with 150 μm × 150 μm squares in the outlined SNc and applying an optical fractionator consisting of a 75 μm × 75 μm square. All stereological analyses were performed by an investigator blinded to genotypes dx.doi.org/10.17504/protocols.io.b5ynq7ve.

TH densitometry

For each mouse, 4 cryosections were stained for TH and imaged with Zeiss Axio Imager M2 and analyzed in ImageJ (version 2.3.0/1.53f). The sections (40 μm) began at the outer limit of the striatum and every 12th section was used (Bregma 1.18 to −0.22 mm). Brightfield images were captured at 10X magnification and converted to greyscale. To analyze, an investigator blinded to genotypes averaged 20 intensity measurements within the dorsolateral striatum and normalized to the average of 5 intensity measurements in the corpus callosum (background staining control). All 4 cryosections per mouse were averaged and represent 1 datapoint on the graph dx.doi.org/10.17504/protocols.io.b5u4q6yw.

Primary cortical neurons

Micro Coverglass #1.5 (Electron Microscopy Sciences) coverslips were pre-coated with poly-d-lysine (50 μg/ml) for at least overnight at 37◦C, then washed with distilled water twice and air dried at

room temperatue for 2 h. Primary neurons were harvested from E13.5 to 15.5 pups and seeded at ∼1 × 10^5 cells per coverslip and cultured for 7 days *in vitro*. Cells were fixed in 4% PFA for 20 min, washed in 1X PBS, then blocked (10% serum +0.1% Triton X-100) for 1 h. Coverslips were stained overnight (see above immunofluorescent staining method) dx.doi.org/10.17504/protocols.io.b5u6q6ze.

Immunofluorescent imaging

Images for Figures 1 and 2 were obtained on a Zeiss AxioObserverZ1 LSM800 Confocal Microscope. Primary neuron images (Fig. 1) were obtained at 40X (oil) magnification at 8bit 1024 × 1024 resolution through a *Z* distance of ∼10 μm per image using optimal 0.27 μm spacing. Multichannel acquisition was performed using excitation/emissions: AF488 (Syn1) 493/517 nm (710V); DAPI353/465nm(750V);AF647(Map2)653/668nm(865V) and AF594 (αSyn) 280/618 nm (700V). Images from tissue sections (Fig. 2) were obtained at 20X magnification (0.8× zoom) at 16bit 1024 × 1024 resolution through a range of 10 μm per image using optimal 0.5 μm spacing. Multichannel acquisition was performed using excitation/emissions(laserintensity);AF488(αSyn)493/517nm (630V for Cortex and DG, 620V for SNc); DAPI 353/465 nm (650V for Cortex and DG, 630V for SNc); AF647 (TH) 653/668 nm (600V). All images were processed and analyzed in ImageJ2 (version 2.3.0/1.53f) using the 3D project and Maximum Z project functions for primary neuron and tissue sections, respectively. Images for Figure 6C were obtained on a Zeiss Axio Imager M2 at 5X magnification and were analyzed in ImageJ2 (version 2.3.0/1.53f).

Nuclear αSyn quantification

Primary cortical neurons were imaged using confocal imaging and all cells in the frame of view were used to quantify the extent of aSyn nuclear localization using ImageJ2 (version 2.3.0/1.53f). First, the nuclei were delineated with DAPI then aSyn intensity was measured within the delineation. This data is shown as the level of aSyn nuclear enrichment relative to wildtype littermates. Cortex, DG and SNc were analyzed in a similar manner. Briefly, 11–35 cells were sampled per animal using ImageJ2 (version 2.3.0/1.53f), nuclei were defined with DAPI and relative intensity of nuclear αSyn versus cytoplasmic αSyn (immediately adjacent to the nucleus) was measured.

NeuN analysis

Photomicrographs were analyzed using ImageJ2 (version 2.3.0/1.53f). Briefly, NeuN positive structures (neuronal nuclei) were counted in a 200 μM × 200 μM frame (Layer

II/III) or 350presented as NeuNμM × 350+ neuron #/mmμM frame (Layer V/VI) and then$_2$. Values represent the average from sampling three distinct sections per brain (n=6 per genotype) and were analyzed by an investigator blinded to the genotypes.

Biochemistry

See Supplementary Material, Table S1 for a comprehensive list of antibodies used in this study.

Serial extraction

A 0.79 mm^3 punch (1 mm thick slice, 1 mm i.d. punch) of cortical brain tissue from 18-month-old mice was homogenized and resuspended in a series of increasingly stringent buffers beginning with 100 μl of TSS Buffer (140 mm NaCl, 5 mm Tris–HCl), then 100 μl TXS Buffer (140 mm NaCl, 5 mm Tris–HCl, 0.5% Triton X-100), then 100 μl SDS Buffer (140 mm NaCl, 5 mm Tris–HCl, 1% SDS), as previously described (67). Total protein levels were measured using the Pierce™ BCA Assay Kit (Thermo Fisher cat# 23225). dx.doi.org/10.17504/protocols.io.b5 vvq666.

Western blot

Protein samples were loaded into a 12% polyacrylamide gel and subsequently transferred to a 0.2 μm nitrocellulose membrane. Membranes were blocked in a 10% milk solution then incubated in primary antibody (diluted in 2% bovine serum albumin) overnight at 4◦C. Next, the membrane was incubated in a horseradish peroxidaseconjugated secondary antibody diluted in 10% milk solution. Then, the membrane was rinsed with ECL Clarity solution (Bio-Rad cat# 1705061) and imaged with a GE ImageQuant LAS 4000. dx.doi.org/10.17504/protocols.io. b5wkq7cw.

RNA extraction and real-time quantitative PCR:

RNA was extracted from mouse brain homogenate using Trizol-Chloroform extraction (Invitrogen™ User Guide: TRIzol Reagent version B.0). Briefly, mouse brains were homogenized in 3 ml of PEPI Buffer [5 mm EDTA, 1X protease inhibitor (GenDEPOT cat# P3100-020),in 1X PBS] using a dounce homogenizer. 3% of homogenate was added to 1 ml of TRIzol Reagent (Fisher Scientific cat# 15-596-026) and RNA was isolated following the user guide referenced above. cDNA was synthesized using 5X All-in-One RT Master Mix Kit (Bio Basic cat# HRT025-10). Real-time quantitative PCR was performed using Green-2-Go qPCR Master Mix (Bio Basic cat# QPCR004S) with 25 ng cDNA per reaction and primers targeting mouse *Gapdh* (Forward: 5"-GGAGAGTGTTTCCTCGTCCC3", Reverse: 5"-ATGAAGGGGTCGTTGATGGC-3"), *Hprt1* (Forward: 5"- TGATAGATCCATTCCTATGACTGTAGA-3", Reverse: 5"-AAGACATTCTTTCCAGTTAAAGTTGAG-3"), and *Snca* (Forward: 5"-GAAGACAGTGGAGGGAGCTG-3", Reverse: 5"-CAGGCATGTCTTCCAGGATT-3"). Reactions were run on BioRad CFX96 thermocycler (protocol: 95◦C for 5 min, 40 cycles of 95◦C for 15 s and 60◦C for 60 s, then melting curve). *Snca* Ct values were standardized to the average of *Hprt1* and *Gapdh* dx.doi.org/10.17504/ protocols.io.b5wmq7c6.

Dopamine and metabolite measurement via liquid chromatography-mass spectrometry/mass spectrometry (LC–MS/MS)

Striatal punches (2 mm i.d., 3 mm thick section) were extracted from 18-month-old mouse brains and weighed prior to submitting to The Metabolomics Innovation Centre (TMIC). Fifty microliter of tissue extraction buffer was added to each sample tube followed by homogenization and centrifugation. Supernatant was used for LC– MS/MS analysis to get concentrations in the unit of μM. TMIC staff applied a targeted quantitative metabolomics approach to analyze the samples using a reverse-phase LC–MS/MS custom assay. This custom assay, in combination with an ABSciex 4000 QTrap (Applied Biosystems/MDS Sciex) mass spectrometer, can be used for the targetedidentificationandquantificationofdopamine(DA), homovanillic acid (HVA), 5-hydroxyindoleacetic acid (5HIAA) and 3,4-dihydroxyphenylacetic acid (DOPAC). The method combines the derivatization and extraction of analytes,and the selective mass-spectrometric detection using multiple reaction monitoring (MRM) pairs. Isotopelabeled internal standards and other internal standards are used for metabolite quantification.The custom assay contains a 96 deep-well plate with a filter plate attached with sealing tape, and reagents and solvents used to prepare the plate assay. First 14 wells were used for 1 blank, 3 zero samples, 7 standards and 3 quality control samples.For all metabolites except organic acid,samples were thawed on ice and were vortexed and centrifuged at 13000×*g*. Ten microliter of each sample was loaded onto the center of the filter on the upper 96-well plate and dried in a stream of nitrogen. Subsequently, phenylisothiocyanate was added for derivatization. After incubation, the filter spots were dried again using an evaporator. Extraction of the metabolites was then achieved by adding 300 μl of extraction solvent. The extracts were obtained by centrifugation into the lower 96-deep well plate, followed by a dilution step with MS running solvent.

For organic acid analysis, 150 μl of ice-cold methanol and 10 μl of isotope-labeled internal standard mixture was added to 50 μl of sample for overnight protein precipitation.Then it was centrifuged at 13000×*g* for 20 min. Fifty microliter of supernatant was loaded into the center of the wells of a 96-deep well plate, followed by the addition of 3-nitrophenylhydrazine (NPH) reagent. After incubation for 2 h, BHT stabilizer and water were added before LC–MS injection.

Mass spectrometric analysis was performed on an ABSciex 4000 Qtrap® tandem mass spectrometry instrument (Applied Biosystems/MDS Analytical Technologies, Foster City, CA) equipped with an Agilent 1260 series UHPLC system (Agilent Technologies, Palo Alto, CA). The samples were delivered to the mass spectrometer by a LC method followed by a direct injection (DI) method. Data analysis was done using Analyst 1.6.2.

TMT10plex™ proteomics via liquid chromatography-mass spectrometry

Whole mouse cortex was dissected from 9-monthold mouse brain and peptides were isolated using the EasyPep™ Mini MS Sample Prep Kit (Thermofisher cat# A40006) following manufacturer instructions. These samples were labelled with the TMT10plex™ Isobaric Label Reagent Set (Thermofisher cat# 90406) then combined into a single tube and fractionated into 12 samples using the Pierce™ High pH Reversed-Phase Peptide Fractionation Kit (Thermofisher cat# 84868). Fractions 2, 3, 9, 10, 11 and 12 were combined due to low protein concentration (combined to have a consistent protein concentration with other fractions) and the 6 final fractions were submitted for liquid chromatography-mass spectrometry (LC–MS) to the Ottawa Hospital Research Institute Proteomics Core Facility. LC–MS was performed using Orbitrap Fusion Lumos mass spectrometer with UltiMate 3000 RLSC nano HPLC (Thermo Scientific). Proteowizard MS-CONVERT was used to generate peak lists for preliminary qualitative analysis using MASCOT software version 2.7.0 (Matrix Science, UK). Protein identification and quantitative analysis was performed using MaxQuant (Tyanova, Nature Protocols 2016, 11:2301). The reference proteome for peptide spectrum matching was UniProt/*Mus musculus* (version 2020-1006). The MaxQuant results were exported to Scaffold Q+S (Proteome Software, USA) for further analysis and viewing. The mass spectrometry proteomics data have been deposited to the ProteomeXchange Consortium via the PRIDE (68) partner repository with the dataset identifier PXD032065 and 10.6019/PXD032065.

Statistical analyses

All statistical analyses were performed using GraphPad Prism (version 9.1.2) using the appropriate statistical test, either Student's *t*-test for simple comparisons or one- or two-way analysis of variance (ANOVA) followed by Bonferroni post-hoc analysis for multiple comparisons. The survival curve was analyzed using a log-rank Mantel–Cox test. The Mann–Whitney test with Benjamini–Hochberg correction was used with Scaffold (version 5.0.0) to analyze the TMT10plex™ mass spectrometry dataset. Chi squared test was used to compare actual and expected Mendelian ratios of the genotypes. Statistical tests used, sample sizes, and *P*values are delineated in each figure legend. All graphs plot the mean with the standard error of the mean (SEM). All figures and their quantification have been made public (doi.org/10.5281/zenodo.6082270).

Supplementary Material

Supplementary Material is available at *HMG* online.

Acknowledgements

The authors thank M.G.Schlossmacher and J.J.Tomlinson (Ottawa Hospital Research Institute, OHRI) and M. Farrer (University of Florida) for *Snca*$^{-/-}$ mice and R. Rissman and E. Masliah (University of California, San Diego) for the *mThy1-SNCA* ('line 61') mice. The authors thank H.Y. Zoghbi and J.P. Revelli (Baylor College of Medicine) for initial project discussions, reagent development and the freedom to explore new ideas and bring mice to the Rousseaux lab with no strings attached. The authors also thank all members of the Rousseaux, Schlossmacher and Zoghbi labs for important discussions and

critical feedback on the manuscript. The authors thank K. Ure for her guidance in conceptualizing and analyzing behaviour tests. The authors also thank the Schlossmacher, and M. Tiberi (OHRI) labs for their generous donation of antibodies. The authors thank S.X. Chen and K. Ure for providing critical feedback to the manuscript. The authors also thank the following Core facilities from the University of Ottawa and the Ottawa Hospital
Research Institute for use of their facility,equipment and expertise: Animal Behaviour and Physiology Core, Cell Biology and Imaging Acquisition Core, Louise Pelletier Histology Core and the OHRI Proteomics Core. The authors also thank the Genome Engineered Rodent Models Core at Baylor College of Medicine and Animal Care and Veterinary Service. Figures 1D and 7A, and Supplementary Figures S1A and C were generated in part with Biorender.com. All histograms were generated with Prism 9. The views expressed herein do not necessarily represent the views of the Minister of Health or the Government of Canada.

*Conflict of Interest statement.*The authors declare that they do not have any conflict of interest.

Funding

The Parkinson's Foundation Stanley Fahn Junior Faculty Award (PF-JFA-1762, M.W.C.R.), the Canadian Institutes of Health Research (PJT-169097), the Parkinson Canada New Investigator Award (2018-00016, M.W.C.R.), The
Michael J. Fox Foundation for Parkinson's Research/
Aligning Science Across Parkinson's Initiative–CollaborativeResearchNetwork(ASAP-020625,M.W.C.R.), the Parkinson's Research Consortium (PRC) Bonnie and Don Poole (H.M.G.), Dave and Jill Hogg (Z.A.F.), and Larry Haffner Fellowship (K.M.R.), the Ontario Graduate Scholarship (H.M.G.), the Queen Elizabeth II
Scholarship (H.M.G.), the Basic Research Fellowship from
Parkinson Canada (BRF-2021-0000000048, K.M.R.), the
ALS Society of Canada in partnership with the Brain
Canada Foundation through the Brain Canada Research Fund, with the financial support of Health Canada, for financial support through the ALS Trainee Award Program 2019 (T.R.S.).

Authors' contributions

H.M.G. and M.W.C.R. conceptualized the study. H.M.G. generated the studied mouse cohorts, performed all behavioral tasks (with the help of K.M.R., Z.A.F., J.L.A.P. and S.M.C), performed most of the histological and biochemical assays, and imaged and analyzed most figures included in this published article. T.R.S. obtained all confocal images, performed qPCR experiments and provided significant intellectual support. K.M.R. aided in tissue acquisition and processing and provided significant intellectual support.K.H.aided in the analysis of stained tissue. J.L.A.P. and T.R.S. harvested and maintained all primary cortical neurons. M.W.C.R. designed the knockin mice, and assisted in data collection and analysis. H.M.G. and M.W.C.R. wrote the manuscript and all authors provided edits.

References

1. Spillantini,M.G.,Schmidt,M.L.,Lee,V.M.,Trojanowski,J.Q.,Jakes, R.andGoedert,M.(1997)Alpha-synucleininLewybodies.*Nature*, **388**, 839–840.
2. Polymeropoulos, M.H., Lavedan, C., Leroy, E., Ide, S.E., Dehejia, A., Dutra, A., Pike, B., Root, H., Rubenstein, J., Boyer, R. *et al.* (1997) Mutation in the alpha-synuclein gene identified in families with Parkinson's disease. *Science*, **276**, 2045–2047.
3. Krüger,R.,Kuhn,W.,Müller,T.,Woitalla,D.,Graeber,M.,Kösel,S., Przuntek, H., Epplen, J.T., Schöls, L. and Riess, O. (1998) Ala30Pro mutation in the gene encoding alpha-synuclein in Parkinson's disease. *Nat. Genet.*, **18**, 106–108.
4. Zarranz, J.J., Alegre, J., Gómez-Esteban, J.C., Lezcano, E., Ros, R., Ampuero, I., Vidal, L., Hoenicka, J., Rodriguez, O., Atarés, B. *et al.* (2004) The new mutation,E46K,of α-synuclein causes parkinson and Lewy body dementia. *Ann. Neurol.*, **55**, 164–173.
5. Appel-Cresswell, S., Vilarino-Guell, C., Encarnacion, M., Sherman, H., Yu, I., Shah, B., Weir, D., Thompson, C., Szu-Tu, C., Trinh, J. *et al.* (2013) Alpha-synuclein p.H50Q, a novel pathogenic mutation for Parkinson's disease. *Mov. Disord. Off. J. Mov. Disord. Soc.*, **28**, 811–813.
6. Fares, M.-B., Ait-Bouziad, N., Dikiy, I., Mbefo, M.K., Jovicˇ c, A.,´

   Kiely, A., Holton, J.L., Lee, S.-J., Gitler, A.D., Eliezer, D. *et al.* (2014) The novel Parkinson's disease linked mutation G51D attenuates in vitro aggregation and membrane binding of α-synuclein, and enhances its secretion and nuclear localization in cells. *Hum. Mol. Genet.*, **23**, 4491–4509.
7. Ghosh, D., Sahay, S., Ranjan, P., Salot, S., Mohite, G.M., Singh, P.K., Dwivedi, S., Carvalho, E., Banerjee, R., Kumar, A. *et al.* (2014) The newly discovered Parkinson's disease associated finnish mutation (A53E) attenuates α-synuclein aggregation and membrane binding. *Biochemistry*, **53**, 6419–6421.
8. Konno,T.,Ross,O.A.,Puschmann,A.,Dickson,D.W.and Wszolek, Z.K. (2016) Autosomal dominant Parkinson's disease caused by SNCA duplications.*Parkinsonism Relat.Disord.*,**22**(Suppl 1),S1–S6.
9. Maroteaux, L., Campanelli, J.T. and Scheller, R.H. (1988) Synuclein: a neuron-specific protein localized to the nucleus and presynaptic nerve terminal. *J. Neurosci.*, **8**, 2804–2815.
10. Herman, S.A. and Coffin, J.M. (1986) Differential transcription from the long terminal repeats of integrated avian leukosis virus DNA. *J. Virol.*, **60**, 497–505.
11. Kahle, P.J., Neumann, M., Ozmen, L., Muller, V., Jacobsen, H., Schindzielorz, A., Okochi, M., Leimer, U., van Der Putten, H., Probst, A. *et al.* (2000) Subcellular localization of wild-type and Parkinson's disease-associated mutant alpha -synuclein in human and transgenic mouse brain. *J. Neurosci.*, **20**, 6365–6373.
12. Specht,C.G.,Tigaret,C.M.,Rast,G.F.,Thalhammer,A.,Rudhard,Y. and Schoepfer, R. (2005) Subcellular localisation of recombinant alpha- and gamma-synuclein. *Mol. Cell. Neurosci.*, **28**, 326–334.
13. Jiang, P., Gan, M., Yen, S.-H., Moussaud, S., McLean, P.J. and Dickson, D.W. (2016) Proaggregant nuclear factor(s) trigger rapid formation of α-synuclein aggregates in apoptotic neurons. *Acta Neuropathol. (Berl.)*, **132**, 77–91.
14. Chen, V., Moncalvo, M., Tringali, D., Tagliafierro, L., Shriskanda, A., Ilich, E., Dong, W., Kantor, B. and Chiba-Falek, O. (2020) The mechanistic role of alpha-synuclein in the nucleus: impaired nuclear function caused by familial Parkinson's disease SNCA mutations. *Hum. Mol. Genet.*, **29**, 3107–3121.
15. Masliah,E.,Rockenstein,E.,Veinbergs,I.,Mallory,M.,Hashimoto, M., Takeda, A., Sagara, Y., Sisk, A. and Mucke, L. (2000) Dopaminergic loss and inclusion body formation in α-synuclein mice: implications for neurodegenerative disorders. *Science*, **287**, 1265–1269.
16. Goers, J., Manning-Bog, A.B., McCormack, A.L., Millett, I.S., Doniach, S., Di Monte, D.A., Uversky, V.N. and Fink, A.L. (2003) Nuclear localization of

alpha-synuclein and its interaction with histones. *Biochemistry*, **42**, 8465–8471.

17. Kontopoulos, E., Parvin, J.D. and Feany, M.B. (2006) Alphasynuclein acts in the nucleus to inhibit histone acetylation and promote neurotoxicity. *Hum. Mol. Genet.*, **15**, 3012–3023.
18. Huang,Z.,Xu,Z.,Wu,Y.and Zhou,Y.(2011) Determining nuclear localization of alpha-synuclein in mouse brains. *Neuroscience*, **199**, 318–332.
19. Rousseaux, M.W., de Haro, M., Lasagna-Reeves, C.A., De Maio, A., Park, J., Jafar-Nejad, P., Al-Ramahi, I., Sharma, A., See, L., Lu, N. *et al.* (2016) TRIM28 regulates the nuclear accumulation and toxicity of both alpha-synuclein and tau. *elife*, **5**, e19809.
20. Pinho, R., Paiva, I., Jercic, K.G., Fonseca-Ornelas, L., Gerhardt, E., Fahlbusch, C., Garcia-Esparcia, P., Kerimoglu, C., Pavlou, M.A.S., Villar-Piqué, A. *et al.* (2019) Nuclear localization and phosphorylation modulate pathological effects of alpha-synuclein. *Hum. Mol. Genet.*, **28**, 31–50.
21. Koss, D.J., Erskine, D., Porter, A., Leite, M., Attems, J. and Outeiro, T.F. (2021) Alpha-synuclein is present in the nucleus in human brain tissue and is pathologically modified in dementia with Lewy bodies. *BioRxiv*, 2021.10.20.465125.
22. McLean, P.J., Ribich, S. and Hyman, B.T. (2000) Subcellular localization of alpha-synuclein in primary neuronal cultures: effect of missense mutations. *J. Neural Transm. Suppl.*, 53–63.
23. Ciron, C., Zheng, L., Bobela, W., Knott, G.W., Leone, T.C., Kelly, D.P. and Schneider, B.L. (2015) PGC-1*α* activity in nigral dopamine neurons determines vulnerability to *α*-synuclein. *Acta Neuropathol. Commun.*, **3**, 16.
24. Paiva, I., Jain, G., Lázaro, D.F., Jerci˘ c, K.G., Hentrich, T., Kerimoglu,´ C., Pinho, R., Szego, È.M., Burkhardt, S., Capece, V.˝ *et al.* (2018) Alpha-synuclein deregulates the expression of COL4A2 and impairs ER-Golgi function. *Neurobiol. Dis.*, **119**, 121–135.
25. Schaser, A.J., Osterberg, V.R., Dent, S.E., Stackhouse, T.L., Wakeham, C.M., Boutros, S.W., Weston, L.J., Owen, N., Weissman, T.A., Luna, E. *et al.* (2019) Alpha-synuclein is a DNA binding protein that modulates DNA repair with implications for Lewy body disorders. *Sci. Rep.*, **9**, 1–19.
26. Siddiqui, M.F., Rast, S., Lynn, M.J., Auchus, A.P. and Pfeiffer, R.F. (2002) Autonomic dysfunction in Parkinson's disease: a comprehensive symptom survey. *Parkinsonism Relat. Disord.*, **8**, 277–284.
27. Cheon, S.-M., Ha, M.-S., Park, M.J. and Kim, J.W. (2008) Nonmotor symptoms of Parkinson's disease: prevalence and awareness of patients and families. *Parkinsonism Relat. Disord.*, **14**, 286–290.
28. Baba, M., Nakajo, S., Tu, P.H., Tomita, T., Nakaya, K., Lee, V.M., Trojanowski, J.Q. and Iwatsubo, T. (1998) Aggregation of alphasynuclein in Lewy bodies of sporadic Parkinson's disease and dementia with Lewy bodies. *Am. J. Pathol.*, **152**, 879–884.
29. Braak, H., Tredici, K.D., Rüb, U., de Vos, R.A.I., Jansen Steur, E.N.H. and Braak, E. (2003) Staging of brain pathology related to sporadic Parkinson's disease. *Neurobiol. Aging*, **24**, 197–211.
30. Luk, K.C., Kehm, V.M., Zhang, B., O'Brien, P., Trojanowski, J.Q. and Lee, V.M.Y. (2012) Intracerebral inoculation of pathological *α*-synuclein initiates a rapidly progressive neurodegenerative *α*synucleinopathy in mice. *J. Exp. Med.*, **209**, 975–986.
31. Luk, K.C., Kehm, V., Carroll, J., Zhang, B., O'Brien, P., Trojanowski, J.Q.andLee,V.M.-Y.(2012)Pathological*α*-synucleintransmission initiates Parkinson-like neurodegeneration in non-transgenic mice. *Science*, **338**, 949–953.
32. Chesselet, Richter, F., Zhu, C., Magen, I., Watson, M.B. and Subramaniam, S.R. (2012) A progressive mouse model of Parkinson's disease: the Thy1-aSyn ("line 61") mice. *Neurotherapeutics*, **9**, 297–314.
33. Cabin, D.E., Shimazu, K., Murphy, D., Cole, N.B., Gottschalk, W., McIlwain, K.L., Orrison, B., Chen, A., Ellis, C.E., Paylor, R. *et al.* (2002) Synaptic vesicle depletion correlates with attenuated synaptic responses to prolonged repetitive stimulation in mice lacking alpha-synuclein. *J. Neurosci.*, **22**, 8797–8807.
34. Taguchi, K., Watanabe, Y., Tsujimura, A. and Tanaka, M. (2019) Expression of *α*-synuclein is regulated in a neuronal cell typedependent manner. *Anat. Sci. Int.*, **94**, 11–22.
35. Halliday, G.M., Holton, J.L., Revesz, T. and Dickson, D.W. (2011) Neuropathology underlying clinical variability in patients with synucleinopathies. *Acta Neuropathol. (Berl.)*, **122**, 187–204.
36. Giguère, N., Burke Nanni, S. and Trudeau, L.-E. (2018) On cell loss and selective vulnerability of neuronal populations in Parkinson's disease. *Front. Neurol.*, **9**, 455.
37. Foffani, G. and Obeso, J.A. (2018) A cortical pathogenic theory of Parkinson's disease. *Neuron*, **99**, 1116–1128.
38. Niccolini, F., Foltynie, T., Reis Marques, T., Muhlert, N., Tziortzi, A.C., Searle, G.E., Natesan, S., Kapur, S., Rabiner, E.A., Gunn, R.N. *et al.* (2015) Loss of phosphodiesterase 10A expression is associated with progression and severity in Parkinson's disease. *Brain J. Neurol.*, **138**, 3003–3015.
39. Halbgebauer, S., Nagl, M., Klafki, H., Haußmann, U., Steinacker, P., Oeckl, P., Kassubek, J., Pinkhardt, E., Ludolph, A.C., Soininen, H. *et al.* (2016) Modified serpinA1 as risk marker for Parkinson's disease dementia: analysis of baseline data. *Sci. Rep.*, **6**, 26145.
40. Benkert, J., Hess, S., Roy, S., Beccano-Kelly, D., Wiederspohn, N., Duda,J.,Simons,C.,Patil,K.,Gaifullina,A.,Mannal,N. *et al.* (2019) Cav2.3 channels contribute to dopaminergic neuron loss in a model of Parkinson's disease. *Nat. Commun.*, **10**, 5094.
41. Date, I., Notter, M.F.D., Felten, S.Y. and Felten, D.L. (1990) MPTPtreated young mice but not aging mice show partial recovery of the nigrostriatal dopaminergic system by stereotaxic injection of acidic fibroblast growth factor (aFGF). *Brain Res.*, **526**, 156–160.
42. Nishi, A. and Shuto, T. (2017) Potential for targeting dopamine/DARPP-32 signaling in neuropsychiatric and neurodegenerative disorders. *Expert Opin. Ther. Targets*, **21**, 259–272.
43. Schwarzschild, M.A., Agnati, L., Fuxe, K., Chen, J.-F. and Morelli, M. (2006) Targeting adenosine A2A receptors in Parkinson's disease. *Trends Neurosci.*, **29**, 647–654.
44. Schwindinger, W.F., Mihalcik, L.J.M., Giger, K.E., Betz, K.S., Stauffer, A.M., Linden, J., Herve, D. and Robishaw, J.D. (2010) Adenosine A2A receptor Signaling and golf assembly show a specific requirement for the*γ*7 subtype inthe striatum*J.Biol.Chem.*,**285**, 29787–29796.
45. Torres, E.R.S., Stanojlovic, M., Zelikowsky, M., Bonsberger, J., Hean, S., Mulligan, C., Baldauf, L., Fleming, S., Masliah, E., Chesselet, M.-F. *et al.* (2021) Alpha-synuclein pathology, microgliosis, and parvalbumin neuron loss in the amygdala associated with enhanced fear in the Thy1-aSyn model of Parkinson's disease. *Neurobiol. Dis.*, **158**, 105478.
46. Jiang, P., Gan, M., Yen, S.-H., McLean, P.J. and Dickson, D.W. (2017) Histones facilitate *α*-synuclein aggregation during neuronal apoptosis. *Acta Neuropathol. (Berl.)*, **133**, 547–558.
47. Nishi, A., Kuroiwa, M., Miller, D.B., O'Callaghan, J.P., Bateup, H.S., Shuto, T., Sotogaku, N., Fukuda, T., Heintz, N., Greengard, P. *et al.* (2008) Distinct roles of PDE4 and PDE10A in the regulation of cAMP/PKA signaling in the striatum.*J.Neurosci.*,**28**,10460–10471.
48. Fienberg, A.A., Hiroi, N., Mermelstein, P.G., Song, W.-J., Snyder, G.L.,Nishi,A.,Cheramy,A.,O'Callaghan,J.P.,Miller,D.B.,Cole,D.G. *et al.* (1998) DARPP-32: regulator of the efficacy of dopaminergic neurotransmission. *Science*, **281**, 838–842.
49. Sasaki, K., Yamasaki, T., Omotuyi, I.O., Mishina, M. and Ueda, H. (2013) Age-dependent dystonia in striatal G*γ*7 deficient mice is reversed by the dopamine D2 receptor agonist pramipexole. *J. Neurochem.*, **124**, 844–854.

50. Ma, S.-X., Seo, B.A., Kim, D., Xiong, Y., Kwon, S.-H., Brahmachari, S., Kim, S., Kam, T.-I., Nirujogi, R.S., Kwon, S.H. *et al.* (2021) Complement and coagulation cascades are potentially involved in dopaminergic neurodegeneration in α-synuclein-based mouse models of Parkinson's disease. *J. Proteome Res.*, **20**, 3428–3443.
51. Jung,S.Y.,Choi,J.M.,Rousseaux,M.W.C.,Malovannaya,A.,Kim,J.J., Kutzera, J., Wang, Y., Huang, Y., Zhu, W., Maity, S. *et al.* (2017) An anatomically resolved mouse brain proteome reveals Parkinson disease-relevant pathways*. *Mol. Cell. Proteomics*, **16**, 581–593.
52. Yger, M. and Girault, J.-A. (2011) DARPP-32, Jack of all trades... master of which? *Front. Behav. Neurosci.*, **5**, 56.
53. Santini, E., Valjent, E., Usiello, A., Carta, M., Borgkvist, A., Girault, J.-A.,Hervé,D.,Greengard,P.and Fisone,G.(2007)Criticalinvolvement of cAMP/DARPP-32 and extracellular signal-regulated protein kinase Signaling in l-DOPA-induced dyskinesia. *J. Neurosci.*, **27**, 6995–7005.
54. Dorsey, E.R., Sherer, T., Okun, M.S. and Bloem, B.R. The emerging evidence of the Parkinson pandemic. *J. Parkinsons Dis.*, **8**, S3–S8.
55. Bodén,R.,Persson,J.,Wall,A.,Lubberink,M.,Ekselius,L.,Larsson, E.-M. and Antoni, G. (2017) Striatal phosphodiesterase 10A and medial prefrontal cortical thickness in patients with schizophrenia: a PET and MRI study. *Transl. Psychiatry*, **7**, e1050–e1050.
56. Abeliovich, A., Schmitz, Y., Fariñas, I., Choi-Lundberg, D., Ho, W.H., Castillo, P.E., Shinsky, N., Verdugo, J.M., Armanini, M., Ryan, A. *et al.* (2000) Mice lacking alpha-synuclein display functional deficits in the nigrostriatal dopamine system. *Neuron*, **25**, 239–252.
57. Greten-Harrison, B., Polydoro, M., Morimoto-Tomita, M., Diao, L., Williams, A.M., Nie, E.H., Makani, S., Tian, N., Castillo, P.E., Buchman, V.L. *et al.* (2010) *αβγ*-Synuclein triple knockout mice reveal age-dependent neuronal dysfunction. *Proc. Natl. Acad. Sci. U. S. A.*, **107**, 19573–19578.
58. Burré, J., Sharma, M., Tsetsenis, T., Buchman, V., Etherton, M.R. and Südhof, T.C. (2010) α-Synuclein promotes SNARE-complex assembly in vivo and in vitro. *Science*, **329**, 1663–1667.
59. Anwar, S., Peters, O., Millership, S., Ninkina, N., Doig, N., ConnorRobson, N., Threlfell, S., Kooner, G., Deacon, R.M., Bannerman, D.M. *et al.* (2011) Functional alterations to the nigrostriatal system in mice lacking all three members of the synuclein family. *J. Neurosci.*, **31**, 7264–7274.
60. Timney,B.L.,Raveh,B.,Mironska,R.,Trivedi,J.M.,Kim,S.J.,Russel, D., Wente, S.R., Sali, A. and Rout, M.P. (2016) Simple rules for passive diffusion through the nuclear pore complex. *J. Cell Biol.*, **215**, 57–76.
61. Siddiqui, A., Chinta, S.J., Mallajosyula, J.K., Rajagopolan, S., Hanson, I., Rane, A. and Andersen, J.K. (2012) Selective binding of nuclear alpha-synuclein to the PGC1alpha promoter under conditions of oxidative stress may contribute to losses in mitochondrial function: implications for Parkinson's disease. *Free Radic. Biol. Med.*, **53**, 993–1003.
62. Jiang, K., Rocha, S., Westling, A., Kesarimangalam, S., Dorfman, K.D., Wittung-Stafshede, P. and Westerlund, F. (2018) Alphasynuclein modulates the physical properties of DNA. *Chem. Weinh. Bergstr. Ger.*, **24**, 15685–15690.
63. Vasudevaraju, P., Guerrero, E., Hegde, M.L., Collen, T.B., Britton, G.B. and Rao, K.S. (2012) New evidence on α-synuclein and tau binding to conformation and sequence specific GC* rich DNA: relevance to neurological disorders. *J. Pharm. Bioallied Sci.*, **4**, 112–117.
64. Ma,K.-L.,Song,L.-K.,Yuan,Y.-H.,Zhang,Y.,Yang,J.-L.,Zhu,P.and Chen, N.-H. (2014) α-Synuclein is prone to interaction with the GC-box-like sequence in vitro. *Cell. Mol. Neurobiol.*, **34**, 603–609.
65. Rousseaux, M.W., Revelli, J.-P., Vázquez-Vélez, G.E., Kim, J.-Y., Craigen, E., Gonzales, K., Beckinghausen, J. and Zoghbi, H.Y. (2018) Depleting Trim28 in adult mice is well tolerated and reduces levels of α-synuclein and tau. *eLife*, **7**, e36768.
66. Deacon,R.M.J.(2006) Assessing nest building in mice.*Nat.Protoc.*, **1**, 1117–1119.
67. Tokarew, J.M., El-Kodsi, D.N., Lengacher, N.A., Fehr, T.K., Nguyen, A.P., Shutinoski, B., O'Nuallain, B., Jin, M., Khan, J.M., Ng, A.C.H. *et al.* (2021) Age-associated insolubility of parkin in human midbrain is linked to redox balance and sequestration of reactive dopamine metabolites. *Acta Neuropathol. (Berl.)*, **141**, 725–754.
68. Perez-Riverol Y, Bai J, Bandla C, Hewapathirana S, GarcíaSeisdedos D, Kamatchinathan S, Kundu D, Prakash A, FrericksZipper A *et al.* (2022) The PRIDE database resources in 2022: A Hub for mass spectrometry-based proteomics evidences. *Nucleic Acids Res.*, **50**, D543–D552.

eLife

***For correspondence:** hongyuan.chu@vai.org
†These authors contributed equally to this work

Competing interest: See page 15

Funding: See page 15

Preprinted: 20 February 2022
Received: 20 February 2022
Accepted: 27 June 2022
Published: 01 July 2022

Reviewing Editor: Jun Ding, Stanford University, United States

SHORT REPORT

α-synuclein pathology to glutamatergic transmission in the basolateral amygdala

Liqiang Chen[1,2†], Chetan Nagaraja[1†], Samuel Daniels[1†], Zoe A Fisk[2,3,4,5], Rachel Dvorak[1], Lindsay Meyerdirk[1,2], Jennifer A Steiner[1], Martha L Escobar Galvis[1], Michael X Henderson[1,2], Maxime WC Rousseaux[2,3,4,5], Patrik Brundin[6], Hong-Yuan Chu[1,2*]

[1]Department of Neurodegenerative Science, Van Andel Institute, Grand Rapids, United States; [2]Aligning Science Across Parkinson's (ASAP) Collaborative Research Network, Chevy Chase, United States; [3]Department of Cellular and Molecular Medicine, University of Ottawa, Ottawa, Canada; [4]University of Ottawa Brain and Mind Research Institute, Ottawa, Canada; [5]Ottawa Institute of Systems Biology, Ottawa, Canada; [6]Pharma Research and Early Development (pRED), F. Hoffman- La Roche, Little Falls, United States

Abstract The presynaptic protein α-synuclein (αSyn) has been suggested to be involved in the pathogenesis of Parkinson's disease (PD). In PD, the amygdala is prone to develop insoluble αSyn aggregates, and it has been suggested that circuit dysfunction involving the amygdala contributes to the psychiatric symptoms. Yet, how αSyn aggregates affect amygdala function is unknown. In this study, we examined αSyn in glutamatergic axon terminals and the impact of its aggregation on glutamatergic transmission in the basolateral amygdala (BLA). We found that αSyn is primarily present in the vesicular glutamate transporter 1- expressing (vGluT1$^+$) terminals in the mouse BLA, which is consistent with higher levels of αSyn expression in vGluT1$^+$ glutamatergic neurons in the cerebral cortex relative to the vGluT2$^+$ glutamatergic neurons in the thalamus. We found that αSyn aggregation selectively decreased the cortico- BLA, but not the thalamo- BLA, transmission; and that cortico- BLA synapses displayed enhanced short- term depression upon repetitive stimulation. In addition, using confocal microscopy, we found that vGluT1$^+$ axon terminals exhibited decreased levels of soluble αSyn, which suggests that lower levels of soluble αSyn might underlie the enhanced short- term depression of cortico- BLA synapses. In agreement with this idea, we found that cortico- BLA synaptic depression was also enhanced in αSyn knockout mice. In conclusion, both basal and dynamic cortico- BLA transmission were disrupted by abnormal aggregation of αSyn and these changes might be relevant to the perturbed cortical control of the amygdala that has been suggested to play a role in psychiatric symptoms in PD.

Editor's evaluation

The manuscript by Chen et al., examines the synapse- specificity of α-synuclein aggregation and corresponding circuit dysfunction in the amygdala. Using confocal microscopy and slice electrophysiology, along with α-synuclein knockout mice and preformed fibrils, the authors demonstrate that cortico- amygdala, but not thalamo- amygdala, inputs are more vulnerable to α-synuclein aggregation and corresponding synaptic dysfunction. This has important implications for the etiology of psychiatric deficits that are common in Parkinson's disease.

Synaptic location is a determinant of the detrimental effects of

Introduction

α-synuclein (αSyn) is a soluble protein abundant at presynaptic axon terminals, where it regulates the dynamics of synaptic vesicles through interaction with synaptic proteins and presynaptic membranes (***Burré et al., 2010***; ***Runwal and Edwards, 2021***; ***Vargas et al., 2017***). αSyn is also prone to form insoluble cytoplasmic aggregates, which are the major protein component of Lewy pathology seen in synucleinopathies like Parkinson's disease (PD) (***Mezey et al., 1998***; ***Spillantini et al., 1997***). Increasing evidence supports the notion that pathologic αSyn propagates between synaptically interconnected brain regions and underlies PD progression (***Angot et al., 2010***; ***Luk et al., 2012***; ***Uemura et al., 2020***).

The amygdala is a key limbic structure for emotion regulation (***Janak and Tye, 2015***). Compelling clinical evidence indicates that cortical control of the amygdala activity is impaired in PD, leading to an inappropriate encoding of emotion valence or deficits in linking emotion to behavior (***Bowers et al., 2006***; ***Hu et al., 2015***; ***Yoshimura et al., 2005***). Moreover, the amygdala shows selective vulnerability to Lewy pathology (***Harding et al., 2002***; ***Nelson et al., 2018***; ***Sorrentino et al., 2019***), thus an impaired amygdala network function has been proposed to underlie the disrupted emotion processing in PD patients (***Harding et al., 2002***). Still, the normal function of αSyn and how its aggregation can impair amygdala circuit function remain poorly understood. Here, we show that αSyn is primarily present in vesicular glutamate transporter 1-expressing (vGluT1 $^{+}$) cortical axon terminals, and, by contrast, is barely detectable in vGluT2^{+} thalamic axon terminals in the basolateral amygdala (BLA). In an αSyn preformed fibrils (PFFs) model of synucleinopathies, αSyn pathology decreases vGluT1^{+} cortico- BLA glutamatergic transmission, without affecting the vGluT2^{+} thalamo- BLA neurotransmission. Furthermore, we demonstrate that a partial (secondary to αSyn aggregation) or complete (*Snca* KO mice) depletion of soluble αSyn from the axon boutons promotes short-term depression at corti co- BLA synapses in response to prolonged stimulation, leading to an impaired gain control of cortical inputs to the BLA. Therefore, we conclude that both gains of toxic properties and loss of normal function of αSyn contribute to the input- specific disruption of cortico- BLA synaptic connectivity and plasticity in synucleinopathies. Our data support clinical observations of an impaired cortical control of the amygdala activity that could contribute to psychiatric deficits in PD patients.

Results αSyn localizes preferentially in vGluT1^{+} axon terminals in mouse brain

Compelling evidence from PD patients suggests that the amygdala exhibits an impaired responsiveness to sensory stimuli, arising mainly from the cerebral cortex and the thalamus (***Bowers et al., 2006***; ***Hu et al., 2015***). Thus, we examined the presence of αSyn in vGluT1^{+} and vGluT2^{+} axon boutons in wild type (WT) mouse brains, which mainly come from cortical and thalamic regions, respectively (***Fremeau et al., 2001***; ***Kaneko and Fujiyama, 2002***; ***Vigneault et al., 2015***). ***Figure 1*** shows that αSyn immunoreactivity colocalizes with vGluT1^{+} puncta but is absent where there are vGluT2^{+} puncta, in the BLA, the cerebral cortex, and the striatum.

Earlier in situ hybridization studies showed higher αSyn mRNA expression in the cerebral cortex and the hippocampus than in the thalamus (***Abeliovich et al., 2000***; ***Ziolkowska et al., 2005***). Next, we used *Snca*$^{NLS/NLS}$ reporter mice to determine αSyn protein localization in the cortical and thalamic areas. These mice localize endogenous αSyn to the nucleus that allows the visualization of cellular topography (***Geertsma et al., 2022***), circumventing the diffused αSyn immunoreactivity in WT mice (***Figure 2A***). We observed that the αSyn was heavily expressed in cortical layer V/VI neurons, but only moderately or barely expressed in thalamic regions, particularly in the midline thalamus that provides major excitation to the BLA (***Ahmed et al., 2021***; ***Amir et al., 2019***; ***Hintiryan et al., 2021***; ***Figure 2B–D***). Together, our data show that αSyn is preferentially present at vGluT1^{+} cerebral cortical neurons and their axon terminals but is absent or expressed at very low levels at vGluT2^{+} thalamic neurons and their projections.

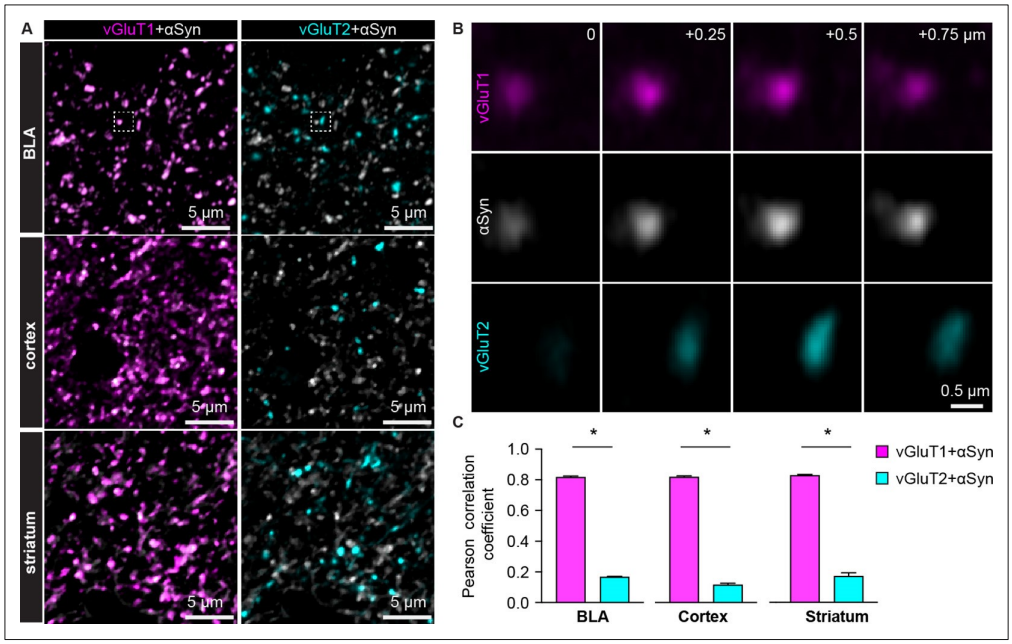

Figure 1. α-synuclein (αSyn) is selectively localized at vesicular glutamate transporter 1 (vGluT1⁺) axon terminals in mouse brain. (**A**) Representative confocal images showing colocalization of αSyn with vGluT1 (left), but not with vGluT2 (right) in the basolateral amygdala (BLA) (top), cerebral cortex (middle), and the striatum (bottom). Simultaneously collected confocal images from each brain region were split into vGluT1/αSyn and vGluT2/ αSyn channels for the purpose of illustration. (**B**) Zoomed z series of images of the boxed area from the BLA in (**A**) showing colocalization and correlated changes in the immunoreactive intensities of vGluT1 and αSyn. Such colocalization and correlation are absent between vGluT2 and αSyn within the same region. Images were taken and shown from a + µm z- depth with an inter- section interval of 0.25 µm. (**C**) Bar graphs showing Pearson correlation coefficient between vGluT1 and αSyn, as well as between vGluT2 and αSyn, in the BLA (αSyn/ vGluT1=0.82 ± 0.007, αSyn/vGluT2=0.17 ± 0.004; n=18 slices/4 mice; p<0.0001, MWU), cerebral cortex (αSyn/ vGluT1=0.82 ± 0.006, αSyn/vGluT2=0.12 ± 0.009; n=8 slices/3 mice; p=0.0002, MWU), and the striatum (αSyn/ vGluT1=0.83 ± 0.006, αSyn/vGluT2=0.17 ± 0.02; n=8 slices/3 mice; p=0.0002, MWU).

The online version of this article includes the following source data for figure 1: **Source data 1.** Source data for plot in ***Figure 1C***.

Glutamate release from vGluT1⁺ axon terminals is selectively disrupted by αSyn pathology

Considering that the endogenous levels of αSyn are determinants of the propensity to form αSyn aggregates, we hypothesize that vGluT1⁺ neurons and their terminals are more susceptible to αSyn pathology compared to those are vGluT2⁺ (***Erskine et al., 2018***; ***Vasili et al., 2022***). To test this hypothesis, we triggered widespread αSyn pathology in the brain using the intrastriatal PFFs seeding model (***Luk et al., 2012***). One- month post-injection, we detected robust αSyn pathology in vGluT1⁺ cerebral cortical regions (e.g. the temporal association cortex (TeA), the motor cortex, and the perirhinal cortex, ***Figure 3 and A1–A***) and the BLA (***Figure 3B–C***), but we barely observed any cytoplasmic aggregates in vGluT2⁺ thalamic regions (***Figure 3 and A4–A5***). This pattern of pathology is supported by differences in endogenous αSyn levels between the cerebral cortex and thalamus (***Figure 2B–D***) and is consistent with earlier reports (***Burtscher et al., 2019***; ***Henderson et al., 2019***; ***Luk et al., 2012***; ***Stoyka et al., 2020***). Importantly, neurons in the midline thalamus were retrogradely labeled when retrobeads were injected into the same location as for PFFs in the striatum (***Figure 3A6***). We concluded that the absence of cytoplasmic pS129 αSyn pathology in the thalamus was not due to technical issues (i.e. missing thalamostriatal axon terminals for PFFs internalization).

Next, we focused on the BLA to assess the functional impact of αSyn aggregation on glutamatergic transmission from the cerebral cortex and thalamus (***Abeliovich et al., 2000***; ***Ziolkowska et al., 2005***). We selectively activated cortical and thalamic inputs of the BLA by stimulating the external and internal capsules, respectively. One- month post-injection, the amplitude of electrically evoked

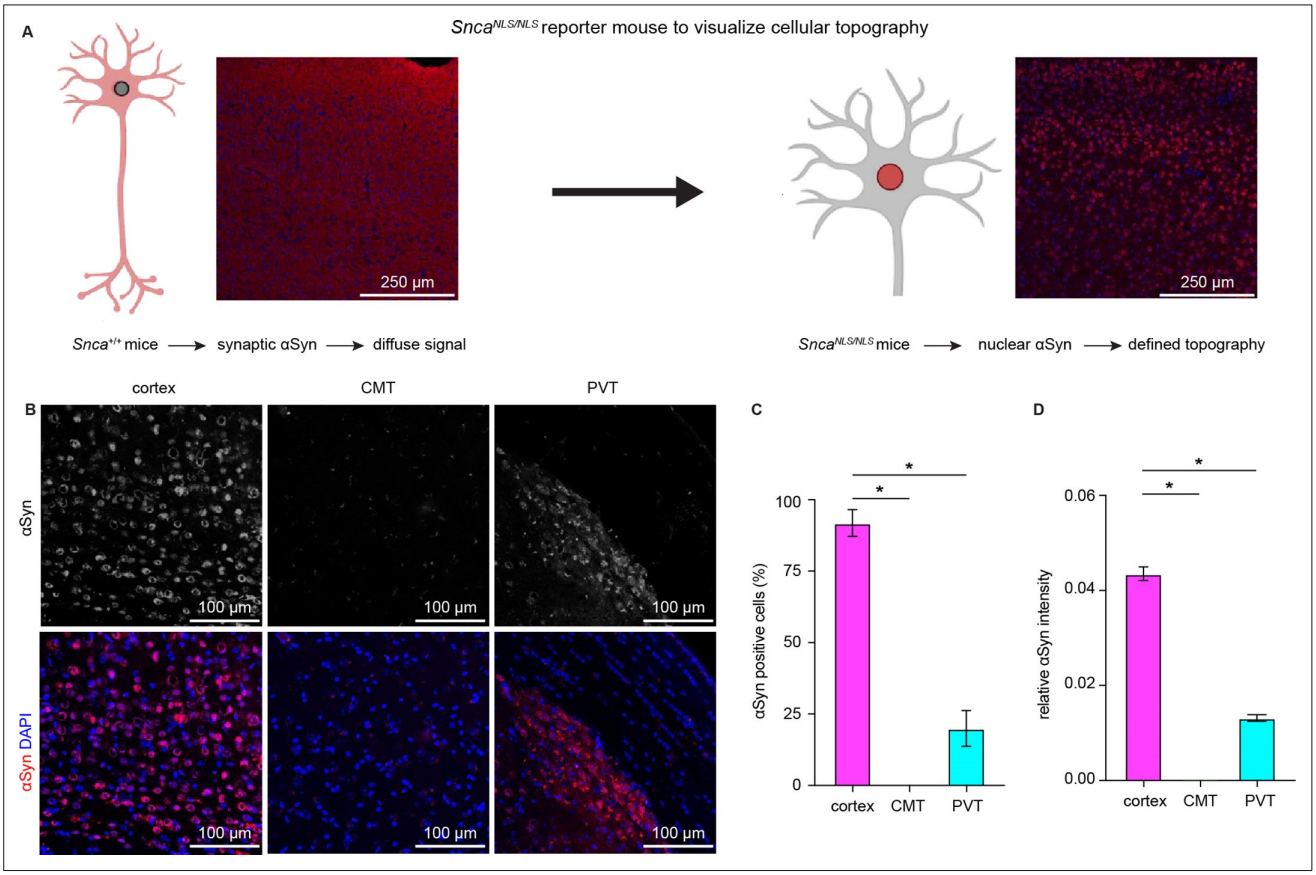

Figure 2. Cerebral cortical neurons express higher levels of endogenous α-synuclein (αSyn) than thalamic neurons. (**A**) Schematic of approach to determine cellular topography of αSyn in the *Snca*$^{NLS/NLS}$ reporter mouse line. (**B**) Representative photomicrographs in the different highlighted brain regions for either αSyn alone (top panels) or co- stained with DAPI as a nuclear marker. (**C–D**) Quantification of the proportion of αSyn- positive nuclei (C, % αSyn positive cells, cortex=91.9 ± 4.7%, CMT=0 ± 0%; PVT=19.9 ± 6.3%, n=3 mice) or average relative intensity of αSyn in the different regions (cerebral cortex=0.04 ± 0.001, n=742 cells/3 mice; CMT=0 ± 0, n=364 cells/3 mice; PVT=0.01 ± 0.0007, n=734 cells/3 mice). * p<0.05, one-way ANOVA followed by Sidak's multiple comparison tests. Abbreviations: CMT, centromedial thalamus; PVT, periventricular thalamus.

The online version of this article includes the following source data for figure 2: **Source data**

1. Source data for plots in ***Figure 2C and D***.

cortico- BLA excitatory postsynaptic currents (EPSCs) was greatly decreased in the slices from PFFs- injected WT mice relative to those from controls (***Figure 3D–E***). Consistently, prominent pS129 αSyn pathology can be detected along the external capsule where the cortical afferents enter the BLA (***Figure 3B–C***). In contrast, there was no difference in the amplitude of thalamo-BLA EPSCs between the PFFs- injected mice and controls (***Figure 3F–G***).

To avoid potential technical issues inherent to the use of electrical stimulation, we employed optogenetic approach to confirm the above results (***Figure 3H–O***). One- month post- injection, the amplitude of optogenetically- evoked cortico- BLA EPSCs in slices from PFFs- injected mice was decreased relative to those from PBS- injected controls (***Figure 3H–K***). By contrast, we did not detect the difference in the amplitude of optogenetically- evoked thalamo- BLA EPSCs between groups (***Figure 3L–O***). Altogether, we demonstrated that the presence of αSyn makes vGluT1^{+} cortical neurons and their axons more vulnerable to αSyn pathology and that this pathology is associated with detrimental effects on synaptic transmission.

Moreover, consistent with the development of αSyn pathology requiring the presence of endogenous αSyn in the PFFs model (***Luk et al., 2012***; ***Volpicelli- Daley et al., 2011***), we did not detect the difference in the cortico-BLA transmission between PFFs- versus PBS- injected αSyn KO mice (***Figure 3—figure supplement 1***).

Furthermore, because of the lack of detrimental effect in αSyn KO mice, we conclude that the impaired cortico-BLA transmission in the PFFs model is likely caused

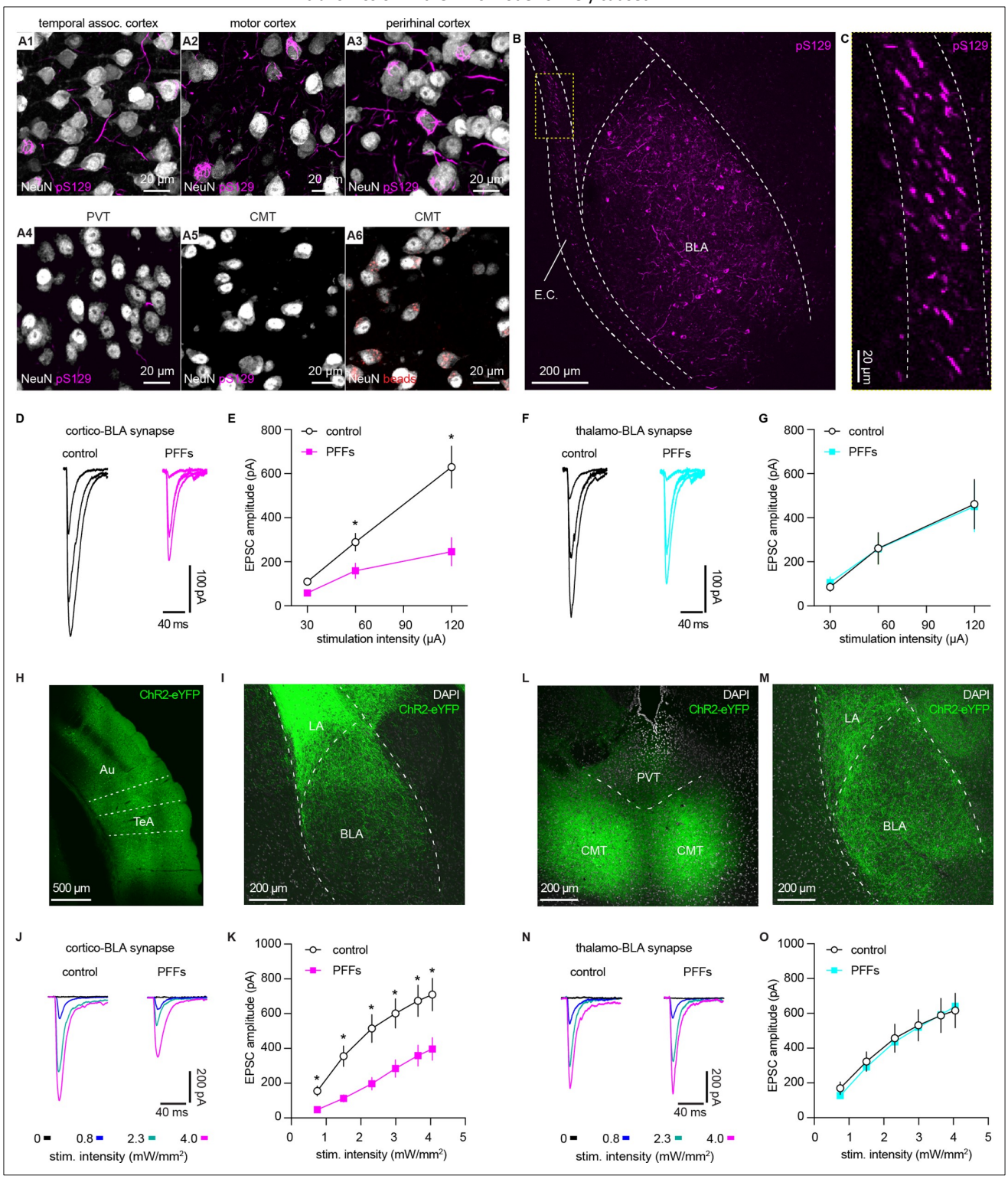

Figure 3. α-synuclein (αSyn) aggregates preferentially disrupt vesicular glutamate transporter 1 (vGluT1⁺) cortico- BLA transmission. (**A**) Representative images showing the presence of αSyn aggregates in the cortical regions (**A1–A3**), but largely absent in the midline thalamus (**A4–A5**). A6, representative images showing retrobeads labeled neurons in the centromedial thalamus. (**B–C**) Representative images showing pS129⁺ αSyn pathology in the basolateral amygdala (BLA) (**B**) and the external capsule (**C**). (**D–E**) Representative traces of excitatory postsynaptic currents (EPSCs) evoked by electrical stimulation of the external capsule (**D**) and summarized results (**E**) showing a reduced cortico-BLA transmission in slices from preformed fibrils (PFFs)- versus PBS-

injected mice. n=17 neurons/4 mice for each group. (**F–G**) Representative traces of EPSCs evoked by electrical stimulation of the internal capsule (**F**) and summarized results (**G**) showing unaltered thalamo- BLA transmission in slices from PFFs- versus PBS- injected wildtype mice. *Figure 3 continued on next page*

Figure 3 continued

n=17 cells/5 mice for controls, and 13 cells/4 PFF- injected mice. (**H–I**) Representative images showing viral infection site in the temporal association cortex (TeA) and nearby regions (**H**), and the axon terminal field in the BLA (**I**). (**J–K**) Representative traces of optogenetically-evoked EPSCs (**J**) and summarized results (**K**) showing a reduced amplitude of cortico- BLA EPSCs in slices from PFFs- versus PBS- injected mice. n=35–37 neurons/4 mice per group. (**L–M**) Representative images showing viral infection site in the midline thalamus (**L**), and the axon terminal field in the BLA (**M**). (**N– O**) Representative traces of optogenetically-evoked EPSCs (**N**) and summarized results (**O**) showing unaltered thalamo- BLA transmission in slices from PFFs- versus PBS- injected mice. n=28 neurons/4 mice per group. *, p<0.05, MWU followed by Bonferroni-Dunn correction for multiple comparisons. Abbreviations: CMT, centromedial thalamus; PVT, periventricular thalamus.

The online version of this article includes the following source data and figure supplement(s) for figure 3:

Source data 1. Source data for plots in ***Figure 3***.

Figure supplement 1. Intrastriatal preformed fibrils (PFFs) injection does not alter cortico-BLA transmission in synKO mice.

Figure supplement 1—source data 1. Source data for plot in ***Figure 3—figure supplement 1***.

by the gained toxic properties of αSyn as it aggregates, instead of intrastriatal PFFs injection per se (***Cookson and van der Brug, 2008***; ***Volpicelli-Daley et al., 2011***).

αSyn pathology decreases the number of functional cortico-BLA inputs

Several mechanisms can contribute to the decreased cortico-BLA synaptic strength as αSyn pathology develops, including the loss of synapses, decreased initial release probability, and/or postsynaptic adaptations. To determine the impact of αSyn aggregation on vGluT1^{+} cortico- BLA innervation, brain sections from control and PFFs-injected mice were processed for immunohistochemical assessment of vGluT1. The density of vGluT1-immunoreactive puncta in the BLA was then determined stereologically (***West, 1999***). The density of vGluT1-immunoreactive puncta was not altered between PFFs- and PBS-injected mice (***Figure 4A–C***). These results indicate that there is no loss of cortical axon terminals or cortico-BLA synapses in PFFs- injected mice at one-month post- injection.

Next, we assessed functional changes in cortico- BLA synaptic transmission using electrophysiology. The initial release probability was estimated by delivering paired-pulses of electric or optoge netic stimulation of cortico-BLA synapses in control and PFFs- injected mice. Using electric stimulation approach, the ratio of EPSC2 to EPSC1 (at a 50 ms inter- pulse interval) was not altered between groups (***Figure 4D–E***). Similarly, the ratio of EPSC2/EPSC1 at cortico-BLA synapses was not altered by αSyn pathology when assessed using optogenetics (at a 100 ms inter-pulse interval, ***Figure 4F–G***). Interestingly, in contrast to the short- term facilitation in response to electric stimulation (***Figure 4D–E***), paired- pulses of optogenetic stimulation always led to short- term depression of cortico- BLA transmission (***Figure 4F–G***), which might be due to the deactivation of ChR2 itself. Together, the above data suggest that the decreased cortico-BLA transmission was not caused by a lower initial release probability.

Further, we estimated the quantal properties of cortico-BLA synapses by measuring the frequency and amplitude of Sr^{2+}- induced, optogenetically- evoked asynchronous glutamate release from cortical terminals. The frequency of optogenetically-evoked cortico- BLA asynchronous EPSCs (Sr^{2+}-EPSCs) decreased significantly, but the amplitude of cortico-BLA Sr^{2+}- EPSCs was not altered in slices from PFFs- injected mice (***Figure 4H–J***). Given the unaltered number of vGluT1^{+} axon terminals and initial release probability of cortico- BLA synapses, fewer readily releasable synaptic vesicles and/or release sites can explain the observed reduction in cortico- BLA transmission.

αSyn pathology decreases AMPA receptor-mediated current at corticoBLA synapses

To determine whether the decreased cortico-BLA connection strength was associated with postsyn aptic adaptations, we measured the ratio of AMPA- and NMDA-mediated EPSCs (AMPA/NMDA ratio) from the cortico-BLA synapses. In response to optogenetic stimulation, cortico- BLA inputs showed a significant reduction of AMPA/NMDA ratio in slices from PFFs- injected mice relative to controls (***Figure 4K and L***). In addition, we also detected an enhanced inward rectification of AMPA-EPSCs at cortico- BLA synapses in slices

from PFFs-injected mice relative to controls (***Figure 4M***), indicating a relatively increased contribution of GluA2-lacking, Ca^{2+}-permeable AMPA receptors to cortico- BLA transmission in PFFs- injected mice. These data suggest that αSyn pathology also triggers postsynaptic

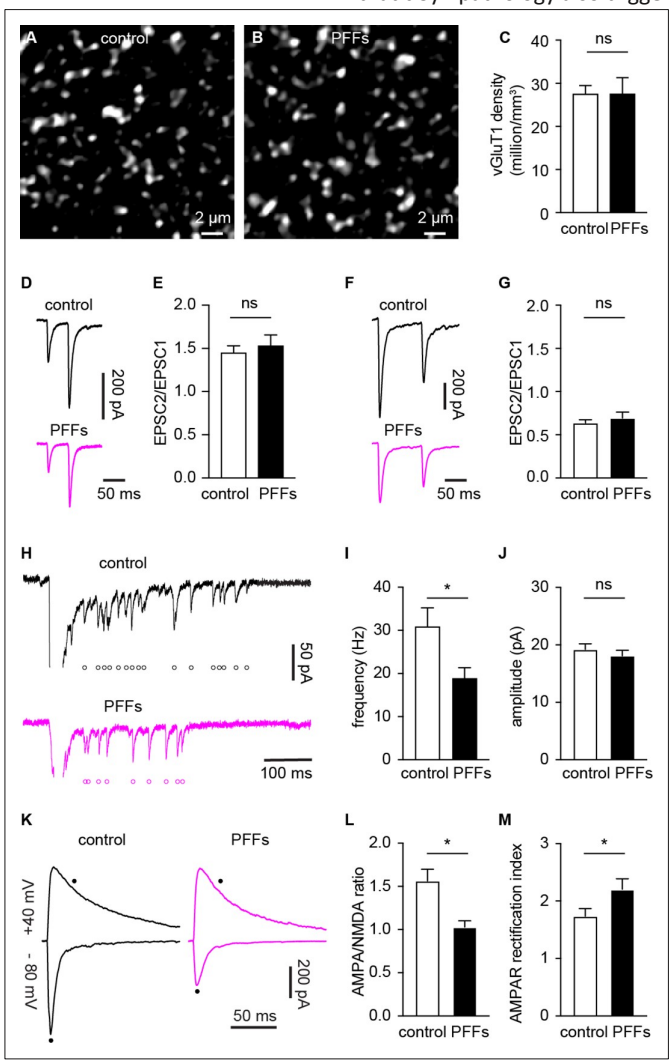

Figure 4. α-synuclein (αSyn) pathology decreases the number of functional cortico- BLA inputs. (**A–B**) Representative confocal images showing vesicular glutamate transporter 1 (vGluT1)- immunoreactivity in the basolateral amygdala (BLA) from control (**A**) and PFFs- injected (**B**) mice. (**C**) Summarized data showing no change in the vGluT1 density in the BLA between control and PFFs- injected mice (control=27.5 ± 2 million/ mm^3, n=11 slices/3 mice; preformed fibrils (PFFs)=27.5 ± 3.8 million/mm^3, n=12 slices/3 mice; p=0.98, MWU). (**D–E**) Representative traces of cortico- BLA excitatory postsynaptic currents (EPSCs) evoked by 20 Hz paired pulses of electric stimulation (**D**) and the summarized results of EPSC2/EPSC1 ratios (E, controls=1.45 ± 0.08, n=19 neurons/4 mice; PFFs=1.53 ± 0.13, n=18 neurons/4 mice; p=0.99, MWU). (**F–G**) Representative traces of cortico- BLA EPSCs evoked by 10 Hz paired pulses of optogenetic stimulation (**F**) and the summarized results of EPSC2/EPSC1 ratios (controls=0.64 ± 0.04, n=35 neurons/4 mice; PFFs=0.69 ± 0.07, n=31 neurons/4 mice; p=0.83, MWU). (**H**) Representative traces showing Sr^{2+} induced, optogenetically evoked EPSCs (Sr^{2+}- EPSCs) at cortico- BLA synapses from control and PFFs- injected mice. Each open circle indicates a single identified Sr^{2+}-EPSC. (**I–J**) Summarized result showing a reduction of the frequency (control=30.9 ± 4.3 Hz, n=24 neurons/3 mice; PFFs=18.9 ± 2.4 Hz, n=24 neurons/3 mice; p=0.012, MWU), but not the amplitude (control=19.2 ± 0.99 pA, n=24 neurons/3 mice; PFF=18.1 ± 0.98 pA, n=24 neurons/3 mice; p=0.31, MWU), of Sr^{2+}- EPSCs at cortico- BLA synapses. (**K**) Representative cortico- BLA EPSC traces recorded at –80 mV and +40 mV from control and PFF- injected mice. Black dots indicate the time at which AMPA- and NMDA- mediated components were measured. (**L**) Summarized results showing a decreased AMPA/NMDA ratio at cortico- BLA synapses from PFFs-injected mice relative to controls (control=1.56 ± 0.13, n=20 neurons/3 mice; PFFs=1.03 ± 0.07, n=18 neurons/3 mice, p=0.0012, MWU). (**M**) Summarized results showing an increased AMPA receptor rectification index at cortico-BLA synapses from PFFs- injected mice relative to controls (control=1.74 ± 0.13, n=20 neurons/3 mice; PFFs=2.21 ± 0.18, n=18 neurons/3 mice, p=0.035, MWU). ns, not significant. * p<0.05.

The online version of this article includes the following source data for figure 4:

Figure 4 continued on next page

Figure 4 continued

Source data 1. Source data for plots in ***Figure 4***.

adaptations at cortico-BLA synapses. Surprisingly, we did not detect changes in the AMPA/NMDA ratio (control=1.24 ± 0.11, PFFs=1.5 ± 0.12, n=16 neurons/ 3 mice per group, p=0.15, MWU) or AMPA receptor rectification (control=1.12 ± 0.1, PFFs=1.28 ± 0.08, n=16 neurons/ 3 mice per group, p=0.25, MWU) from thalamo- BLA synapse between groups. Thus, the above data suggest that αSyn pathology induces input- specific decrease of postsynaptic AMPA receptor-mediated cortico- BLA transmission, instead of a global reduction of AMPA receptor function in BLA neurons.

Taken together, the development of αSyn pathology selectively decreases the functional cortico- BLA connectivity by inducing both pre- and post-synaptic adaptations and such functional changes occur prior to overt degeneration of axon terminals.

Pathological aggregation decreases αSyn levels at axon terminals and impairs short-term synaptic plasticity

Formation of cytoplasmic aggregates is believed to move soluble αSyn away from the presynaptic boutons, affecting its role in regulating synaptic vesicle pools (***Benskey et al., 2016***; ***Luk et al., 2009***; ***Volpicelli- Daley et al., 2011***). Consistent with the earlier predictions, the intensity of αSyn immunoreactivity (Syn1 antibody from BD Biosciences) within vGluT1⁺ puncta decreased dramatically in slices from PFFs- injected mice, leading to an increased proportion of vGluT1⁺ boutons that lack a detectable level of αSyn (***Figure 5A–D***). To avoid technical issues associated with immunostaining (e.g. antigen mask due to αSyn aggregation), we assessed the αSyn immunoreactivity within vGluT1⁺ terminals using a different monoclonal antibody against mouse αSyn–Syn9027 (***Peng et al., 2018***). Consistently, both the αSyn immunoreactivity within vGluT1⁺ terminals and the proportion of vGluT1⁺ terminals that are αSyn- immunoreactive decreased significantly in slices from PFFs-injected mice relative to controls (***Figure 5E–H***). The percentage of αSyn- immunoreactive vGluT1⁺ terminals detected with Syn9027 in PFFs- injected mice was higher than those detected with Syn1, perhaps reflecting differences in the exposure of their epitopes (Syn1: aa 91–99; Syn9027: aa 130–140). These data suggest that αSyn pathology reduces the amount of soluble αSyn present at the cortical axon terminals in the BLA, and in that way could affect its physiological function.

αSyn modulates the dynamics of synapse vesicle pools (***Sulzer and Edwards, 2019***), which plays a key role in regulating synaptic plasticity and the computational function of neural circuits (***Abbott and Regehr, 2004***; ***Alabi and Tsien, 2012***). Thus, we stimulated cortico- BLA synapses repetitively to assess the impact of the observed reduction of αSyn levels on short- term synaptic plasticity. We detected a progressive depression of cortico-BLA EPSCs in control mice (***Figure 6A1 and A2***), reflecting mainly a progressive depletion of presynaptic vesicles (***Alabi and Tsien, 2012***; ***Cabin et al., 2002***). Interestingly, the cortico-BLA EPSCs in the slices from PFFs- injected mice showed a greater depression relative to those from controls (***Figure 6A1 and A2***). These results are in line with the key role of αSyn in sustaining and mobilizing synaptic vesicle pools (***Cabin et al., 2002***; ***Sulzer and Edwards, 2019***; ***Vargas et al., 2017***), and suggest the significant impact of the loss of αSyn function on synaptic plasticity and circuit computation.

Because both gains of toxic properties and loss of normal αSyn function are induced in the PFFs models, we employed the αSyn KO mice to further assess the impact of a loss of αSyn on the short- term synaptic plasticity of glutamatergic synapses. Consistently, the amplitude of cortico-BLA EPSCs from αSyn KO mice also exhibited greater depression in response to repetitive stimulation relative to littermate WT controls (***Figure 6B1–B2***), indicating an impaired mobilization of synaptic vesicle pools. It is worth noting that the earlier onset and greater magnitude of cortico-BLA EPSC depression in αSyn KO mice versus that in PFFs-injected mice (***Figure 6A, B***). Thus, it is plausible that the different temporal profiles of short- term synaptic dynamics are linked to the difference in the amount of αSyn present at presynaptic terminals between the PFFs model and KO mice. Last, we did not detect the difference in the temporal profiles of thalamo- BLA EPSCs in slices from αSyn KO mice and those from WT controls (***Figure 6—figure supplement 1***), which indicates a negligible impact of αSyn depletion on synaptic vesicle dynamics and is consistent with the lack of αSyn presence at vGluT2⁺ axon terminals (***Figure 1***). Together, these results suggest that pathological aggregation decreases the levels

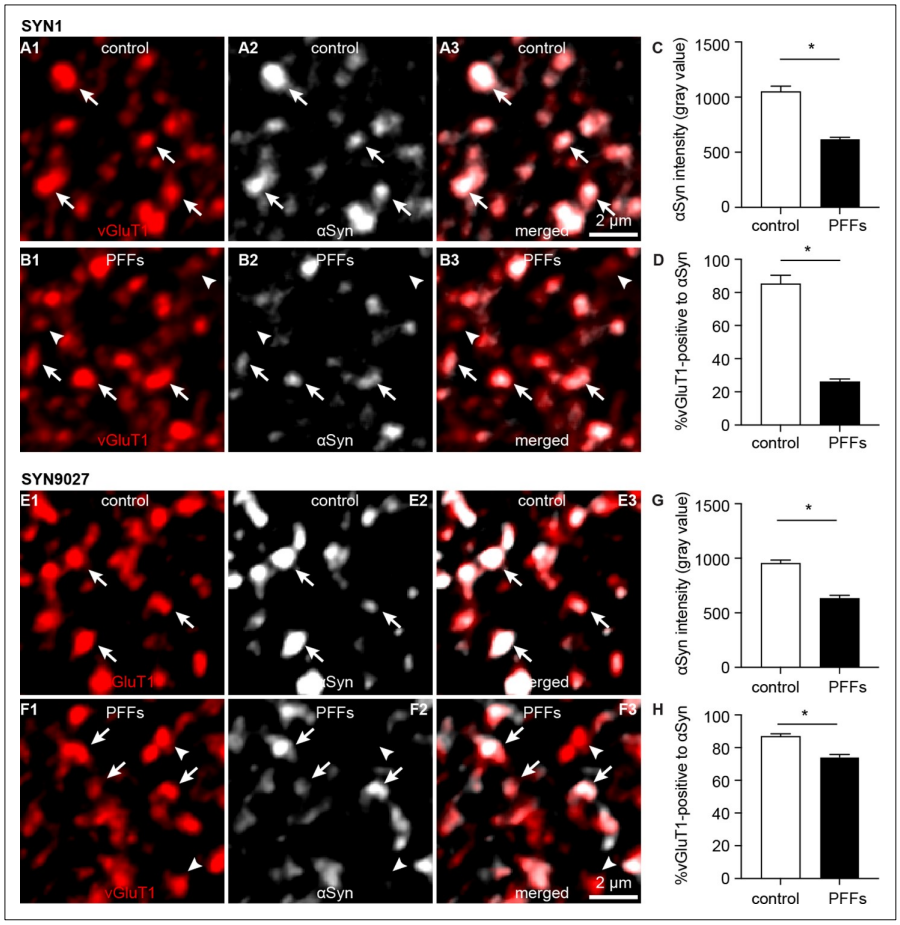

Figure 5. Decreased soluble α-synuclein (αSyn) at the axon terminals as pathology develops. (**A1–B3**) Representative confocal images showing αSyn immunoreactivity within vesicular glutamate transporter 1 (vGluT1⁺) puncta in the basolateral amygdala (BLA) using SYN1 antibody from control (**A1–A3**) and PFFs- injected mice (**B1–B3**).(**C**) Summarized graph showing a reduced αSyn immunoreactivity per vGluT1 immunoreactive puncta in PFFs-injected mice relative to controls (control=1049 ± 50; preformed fibrils (PFFs)= 617 ± 18, n=100 puncta/ group, p<0.0001, MWU). (**D**) Summarized graph showing a reduced percentage of vGluT1 immunoreactive puncta associated with detectable αSyn immunoreactivity in PFFs- injected mice relative to controls (controls=85 ± 5.2%; PFF=26 ± 1.7%, n=6 slices/group, p=0.002, MWU). (**E1–F3**) Representative confocal images showing αSyn immunoreactivity within vGluT1⁺ puncta in the BLA using SYN9027 antibody from control (**E1–E3**) and PFFs- injected mice (**F1–F3**). (**G**) Summarized graph showing a reduced αSyn immunoreactivity per vGluT1 immunoreactive puncta in PFFs- injected mice relative to controls (control=954 ± 29; PFFs=633 ± 27, n=241 puncta/ group, p<0.0001, MWU). (**D**) Summarized graph showing a reduced percentage of vGluT1 immunoreactive puncta associated with detectable αSyn immunoreactivity in PFFs- injected mice relative to controls (controls=87 ± 1.5%, n=12 slices; PFF=74 ± 1.6%, n=11 slices, p<0.0001, MWU).

The online version of this article includes the following source data for figure 5: **Source data 1.** Source data for plots in ***Figure 5***.

of soluble αSyn at the axon terminals, leading to a greater synaptic vesicle depletion and impaired short- term plasticity.

Discussion

Emerging evidence suggests that αSyn exhibits brain region- and cell type-specific expression in the brain. For example, while αSyn mRNA expression is high in glutamatergic and dopaminergic neurons, it is largely absent from GABAergic neurons across brain regions (***Taguchi et al., 2016***). To further explore such a cell subtype-selective αSyn expression among glutamatergic neurons and synapses, our study shows that αSyn is preferentially present at vGluT1⁺, but not vGluT2⁺, axon terminals across

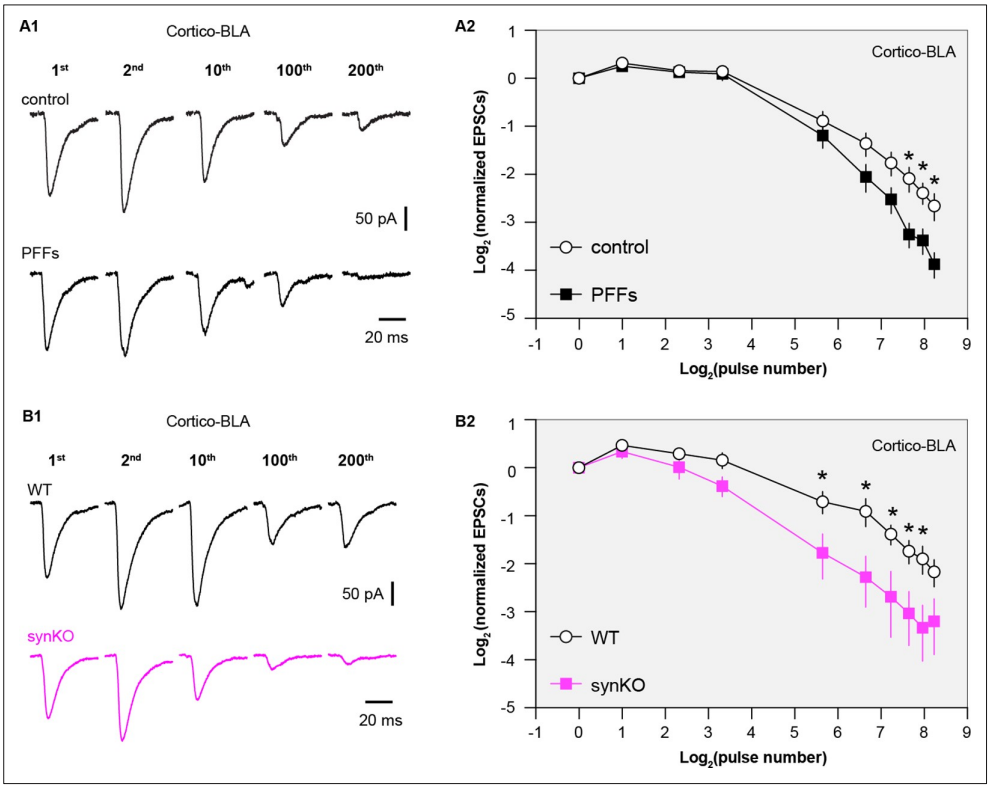

Figure 6. Loss of α-synuclein (αSyn) impairs short- term plasticity of the cortico- BLA inputs. (**A1**) Representative cortico- basolateral amygdala (BLA) excitatory postsynaptic currents (EPSCs) traces from control and preformed fibrils (PFF)- injected mice in response to repetitive stimulation (300 stimuli at 12.5 Hz). (**A2**) Summarized graph showing the temporal profiles of cortico- EPSCs depression in slices from control and PFFs- injected mice. The cortico- BLA EPSCs from PFFs- injected mice exhibited greater reduction in the amplitude toward the end of repetitive stimulation. n=13–15 neurons/ 3 mice. (**B1**) Representative cortico- BLA EPSCs traces from wild type (WT) control and αSyn KO mice in response to repetitive stimulation (300 stimuli at 12.5 Hz). (**B2**) Summarized graph showing the temporal profiles of cortico- EPSCs depression in slices from WT control and αSyn KO mice (n=8–9 neurons/3 mice. *, p<0.05, MWU followed by Bonferroni- Dunn correction for multiple comparisons).

The online version of this article includes the following source data and figure supplement(s) for figure 6:

Source data 1. Source data for plots in ***Figure 6***.

Figure supplement 1. α-synuclein (αSyn) KO does not affect short term plasticity profiles of thalamo-BLA inputs. **Figure supplement 1—source data 1.** Source data for plot in ***Figure 6—figure supplement 1***.

several brain regions, including the BLA and the striatum. Consistent with the observation from the axon terminals, we also detected higher amounts of αSyn in the cell bodies of cortical neurons relative to thalamic neurons using the recently generated *Snca*$^{NLS/NLS}$ reporter mice (***Geertsma et al., 2022***). Thus, our results support a cell- and synapse-subtype- selective αSyn protein expression among glutamatergic neurons in the mouse brain.

Endogenous levels of αSyn are determinants of neuronal vulnerability to αSyn pathology. As expected, we observed a decrease in cortical, but not thalamic, inputs to the BLA neurons in a PFF- seeding model of synucleinopathies. At a relatively early- stage (i.e. one- month post- injection), αSyn pathology decreases the number of functional cortical inputs to the BLA without loss of synapse or changes in presynaptic release probability. We posit that the disrupted cortico- BLA transmission can be caused by a reduced size of readily- releasable synaptic vesicle pool and/or a number of presynaptic release sites. This hypothesis was built on a wealth of evidence showing that αSyn aggregates decrease the expression of several synaptic vesicle-associated SNARE proteins (e.g. Snap25 and VAMP2) (***Volpicelli- Daley et al., 2011***). Moreover, our study also suggests a decreased AMPA receptor- mediated response can underlie the impaired cortico- BLA transmission in PFFs-injected mice. On the other hand, an increased relative contribution of GluA2-lacking AMPA receptors can be a compensatory mechanism for an overall reduction in AMPA- EPSCs at cortico- BLA synapses– a hypothesis that warrants further investigation. It is worth noting that such a decreased AMPA-EPSC of BLA neurons is input specific, which selectively occurs at cortico-BLA synapses. Thus, the molecular mechanisms that cooperate pre- and post- synaptic changes at the cortical inputs, but not the thalamic inputs, remain to be defined.

Our study further highlights the dependence of regional and cellular vulnerability on the endogenous αSyn, i.e., those neurons or axon terminals that express high levels of αSyn are prone to be functionally impacted by αSyn pathology relative to those that lack of or express low levels of αSyn (***Surmeier et al., 2017***; ***Thakur et al., 2019***; ***Vasili et al., 2022***). Of particular interest is that vGluT2^{+}/ TH^{+} midbrain dopamine neurons and their axon terminals in the striatum have been shown to be more resilient to neurodegeneration in postmortem PD brains and animal models studies (***Buck et al., 2021***; ***Steinkellner et al., 2022***). While several other mechanisms have been proposed (***Buck et al., 2021***), the absence of αSyn at vGluT2^{+} neurons/terminals could be critical for such resilience.

Loss of normal αSyn function has been thought to be an important but understudied aspect of αSyn pathology. Using an electrophysiological approach, we revealed that a partial or complete removal of αSyn from the axon terminals leads to an enhanced short-term depression in response to repetitive stimulation of cortico- BLA synapses (***Figure 6***). Short-term synaptic plasticity is an important 'gain control' mechanism for neurons to properly balance their responsiveness to distinct afferents in an input- specific manner (***Abbott et al., 1997***). Cortical and thalamic afferents of the BLA exhibit different short- term synaptic plasticity profiles in vivo, which could reflect their different contributions to the formation of emotion-related memory and behavior (***Sigur sson et al., 2010***). Physiologically, synapse- specific presence of αSyn could underlie such difference in the short-term plasticity profiles of the two inputs (***Figures 1 and 6***).

One can postulate that once aggregates form, a decreased synaptic strength associated with αSyn toxicity (***Figure 3***) and an enhanced synaptic depression due to the loss of αSyn normal function at presynaptic boutons (***Figures 5 and 6***) make the BLA neurons less likely to respond to sustained and repetitive sensory inputs from cortical regions. These circuit changes might explain studies showing a decreased functional connectivity of cortico-amygdala, but not the thalamo- amygdala network in PD patients, which further leads to a failed amygdala responsiveness to the aversive sensory inputs (***Hu et al., 2015***; ***Yoshimura et al., 2005***).

Materials and methods

Animals

Wild type (WT) C57Bl/6J mice (Jax stock#:000664, RRID: IMSR_JAX:000664) of both sexes (3–4 month- old) were obtained from the Van Andel Institute vivarium internal colony and used in the study. αSyn knockout (*Snca*$^{-/-}$) mice (RRID: IMSR_JAX:003692) were originally purchased from Jackson laboratories (Bar Harbor, ME) and then were backcrossed on a C57BL/6J background to generate heterozygous *Snca*$^{+/-}$ mice. Experimental *Snca*$^{-/-}$ mice and littermate WT controls were generated from heterozygous *Snca*$^{+/-}$ breeder pairs and were genotyped by Transnetyx (Cordova, TN, USA). *Snca*$^{NLS/NLS}$ mice (RRID: IMSR_JAX:036763) were generated and maintained on a C57Bl/6J background as described (***Geertsma et al., 2022***). Mice were housed up to four animals per cage under a 12/12 hr light/dark cycle with access to food and water ad libitum in accordance with NIH guidelines for care and use of animals. All animal studies were reviewed and approved by the Institutional Animal Care and Use Committee at Van Andel Institute (animal use protocol#: 22- 02-007).

Preparation and validation of αSyn preformed fibrils

Purification of recombinant mouse αSyn and generation of αSyn preformed fibrils (PFFs) was conducted as described elsewhere (***Luk et al., 2009***; ***Volpicelli- Daley et al., 2014***). The pRK172 plasmid (RRID: Addgene_166671) containing the gene of interest was transformed into BL21 (DE3) RIL-competent *E. coli* (230245, Agilent Technologies). A single colony from this transformation was expanded in Terrific Broth (12 g/L of Bacto-tryptone, 24 g/L of yeast extract 4% (v/v) glycerol, 17 mM KH_2PO_4, and 72 mM K_2HPO_4) with ampicillin. Bacterial pellets from the growth were sonicated and the sample was boiled to precipitate undesired proteins. The supernatant was dialyzed with 10 mM Tris, pH 7.6, 50 mM NaCl, 1 mM EDTA, 1 mM phenylmethylsulfonyl fluoride (PMSF) overnight. Protein was filtered with a 0.22 µm filter and concentrated using Vivaspin 15 R 10 K centrifugal filters (VS15RH01, Sartorius). Protein was then loaded onto a Superdex 200 column and 2 mL fractions were collected. Fractions were run on SDS-PAGE and stained with InstaBlue protein stain (50- 190- 5499 , Fisher Scientific) to select fractions that were highly enriched in αSyn. These fractions were combined and dialyzed in 10 mM Tris, pH 7.6, 50 mM NaCl, 1 mM EDTA, 1 mM PMSF overnight. Dialyzed fractions were applied to a MonoQ column (HiTrap Q HP 17115401, Cytiva) and run using a NaCl linear gradient (0.025–1 M). Collected fractions were run on SDS-PAGE and stained with InstaBlue protein stain. Fractions that were highly enriched in αSyn were collected and dialyzed into DPBS (Gibco). Protein was filtered through a 0.22 µm filter and concentrated to 7 mg/mL (αSyn) with Vivaspin 15 R 10 K centrifugal filters. Monomer was aliquoted and frozen at –80 °C. For preparation of αSyn PFFs, αSyn monomer was shaken at 1000 rpm for 7 days. Conversion to PFFs was validated by sedimentation at 100,000 x *g* for 60 min and by thioflavin S staining.

Stereotaxic surgery

Mice were placed in a stereotaxic frame (Kopf) under 2% isoflurane anesthesia and were supported by a thermostatic heating pad. Recombinant αSyn fibrils were diluted in phosphate-buffered saline (PBS) to a concentration of 5 mg/ml. Prior to stereotaxic injection, PFFs were pulse sonicated at medium intensity with 30 s on and 30 s off for 10 min using a sonicator (Biorupter Pico). To induce the formation of αSyn aggregation in mouse brain (***Luk et al., 2012***), sonicated PFFs (2.0 µl) were injected bilaterally into the dorsal striatum (anteroposterior,+0.2 mm from bregma;

mediolateral, ± 2.0 mm from the midline; dorsoventral, –2.6 mm from the brain surface) using a 10 µl syringe (Hamilton) driven by a motorized microinjector (Stoelting) at a rate of 0.2 µl/min. Given the neuronal heterogeneity of the BLA, retrobeads (Lumafluor Inc) were diluted 10 × into αSyn fibrils or PBS to label the projection neurons in the BLA for physiological studies. The final injection volume of PFFs with beads mixture was adjusted to keep a constant amount of αSyn injected across animals. Control mice received 2.0 µl PBS or PBS with retrobeads injections in the same location. For optogenetics studies, AAV vectors encoding ChR2(H134R)- eYFP (titer=1 × 10^{12} vg/ml, Addgene 26973, RRID: Addgene_127090) were stereotaxically injected into and centered at the TeA (anterioposterior –3.3 mm from the bregma, mediodorsal ± 4.1 mm, dorsoventral –1.5 mm from the brain surface) and the midline thalamus (anterioposterior –1.5 mm from the bregma, mediodorsal 0 mm, dorsoventral –3.3 mm from the brain surface) (***Ahmed et al., 2021***; ***Amir et al., 2019***). Animals were housed in their home cages before being euthanized for immunohistochemical or physiological studies at one-month post- injection. Details of this protocol can be found at: https://doi.org/10.17504/protocols.io.rm7vzye28l×1/v1.

Tissue collection – perfusion and sectioning

WT and *Snca*$^{-/-}$ mice received overdosage of avertin intraperitoneally (i.p.) and were subsequently subjected to transcardial perfusion with PBS and 4% paraformaldehyde (PFA, pH 7.4). Brains were removed and post-fixed in 4% PFA overnight, before being re- sectioned at 70 µm using a vibratome (VT1000s, Leica Biosystems, Buffalo Grove, IL). *Snca*$^{NLS/NLS}$ mice were anesthetized with 30 µl of 120 mg/kg Euthanyl (DIN00141704) before being perfused with 10 ml 1 x PBS and 10 ml 4% PFA. Brain tissue was collected and stored for 48 hr in 4% PFA. Brain tissue was then dehydrated in 10, 20, and 30% sucrose solutions for 48 hr each before being flash frozen in –40 °C isopentane for 1 min. Tissues were then cryosectioned at 20 µm and –21°C on the Thermo Scientific HM 525 NX cryostat at the Louise Pelletier Histology Core at the University of Ottawa and stored free floating in 1 × PBS +0.02% NaN3 at 4°C until use. Details of this protocol can be found here.

Immunofluorescent staining

Brain sections from WT and *Snca*$^{-/-}$ mice were rinsed using PBS and treated with 0.5% Triton X- 100% and 2% normal donkey serum (MilliporeSigma) in PBS for 60 min at room temperature, followed by incubation with primary antibodies overnight at room temperature or for 48 hr at 4°C. The concentrations of primary antibodies were rabbit anti- pS129 αSyn (1:10,000, Abcam Cat# 1536–1, RRID: AB_562180), mouse anti-αSyn (1:1000, BD Biosciences Cat# 610787, RRID: AB_398108), mouse anti- NeuN (1:2000, Millipore Cat# MAB377, RRID: AB_2298772), rabbit anti-vGlut1(1:1000, cat#: Milli pore Cat# ABN1647, RRID: AB_2814811) and guinea pig anti- vGluT2 (1:1000, Synaptic Systems Cat# 135404, RRID: AB_887884). After being thoroughly rinsed with PBS for 3 times, the sections were incubated with the secondary antibodies (1:500, AlexaFluor 594 donkey anti- mouse IgG, Jackson ImmunoResearch Labs Cat# 715-586- 150, RRID: AB_2340857; AlexaFluor 647 donkey anti-mouse IgG, Jackson ImmunoResearch Labs Cat# 715- 607- 003, RRID: AB_2340867; AlexaFluor 488 donkey anti- mouse IgG, Jackson ImmunoResearch Labs Cat# 711-546- 152 , RRID: AB_2340619; AlexaFluor 594 donkey anti-rabbit IgG, Jackson ImmunoResearch Labs Cat# 711- 585- 152, RRID: AB_2340621, or AlexaFluor 488 donkey anti- guinea pig IgG, Jackson ImmunoResearch Labs Cat# 706-545- 148, RRID: AB_2340472) for 90 min at room temperature. Brain sections were rinsed 3 times with PBS and mounted on glass slides using Vectorshield antifade mounting medium (H-1000 , Vector Laboratories) and cover slipped.

Brain sections from *Snca*$^{NLS/NLS}$ were incubated for 24 hr in blocking buffer (1.5% Triton X- 100, 10% cosmic calf serum in 1 × PBS), 24 hr in primary Syn1 antibody (1:1000, BD Biosciences Cat# 610787, RRID: AB_398108) and 1 hr in secondary antibody (1:500, Alexa Fluor 568 donkey anti- mouse antibody, (Thermo Fisher Scientific Cat# A10037, RRID: AB_2534013, Lot#: 1917938)) with DAPI at 1:1000 (Millipore Sigma, D9542-1 MG). Tissue was washed in 1 × PBS 5 times for 5 min each between each treatment and mounted on Fisherbrand Superfrost Plus slides. After drying for 24 hr, sections were covered with DAKO mounting medium (Cat#: S3023, Lot#: 11347938) and #1.5 coverslips.

Details of immunofluorescent staining can be found here.

Confocal imaging and analysis

Confocal images from WT and *SNCA*$^{-/-}$ were acquired using a Nikon A1R confocal microscopy. pS129 αSyn aggregates in different brain regions were imaged under a 40 × objective lens. For αSyn and vGluT1/vGluT2 colocalization analysis, three synaptic markers were immunostained simultaneously and z- stack images were acquired using an oil immersion 100 × objective (NA=1.45; x/y, 1024 × 1024 pixels; z step=150 nm). Images were acquired using identical settings between treatment groups, including laser power, pinhole size, gain, and pixel size. Intensity- based colocalization analysis was performed using Imaris software (RRID: SCR_007370, version 9.3, Oxford, UK, http://www.bitplane. com/imaris/imaris). Background subtraction on z- stack images was conducted using ImageJ (RRID: SCR_003070, NIH, https://imagej.net/) prior to importing files into Imaris. Once imported, two arbitrary regions of interest were created using the surface function (drawing mode: circle; radius=15 µm; number of vertices=30) and the three channels (vGluT2, vGluT1, and αSyn) were masked based on the surface reconstruction to isolate fluorescence within the ROIs. The Imaris 'Coloc' function was used to measure the colocalization between vGluT2/αSyn and vGluT1/αSyn for each ROI. Briefly, either vGluT1 or vGluT2 was selected as channel A and αSyn was selected as channel B. The automatic threshold feature within 'Coloc' was used to calculate the threshold values for each channel. Colocalization channels for vGluT1/ αSyn and vGluT2/αSyn for each ROI were created by using the 'Build Coloc Channel' function. Colocalization parameters were obtained for quantification from the colocalization channels. For quantification of the αSyn intensity within vGluT1^{+}

axon terminals, background subtraction on z- stack images was conducted using ImageJ (RRID: SCR_003070, NIH, https://imagej. net/). After background subtraction, vGluT1 immunoreactive puncta were manually identified as a set of regions of interest (ROI, n=20 puncta per image) from each BLA section and the mean gray values of αSyn immunoreactivity within the same ROI were then measured using ImageJ (RRID: SCR_003070, NIH, https://imagej.net/). Details of images analysis can be found at: dx.doi.org/10.17504/protocols. io.n2bvj61bblk5/v1.

Confocal images from *SNCA*$^{NLS/SNLS}$ mice were taken on the Zeiss AxioObserver Z1 LSM800 at the Cell Biology and Image Acquisition core at the University of Ottawa. Images were taken at 20 × (0.8 NA) objective with 8bit 1024 × 1024 resolution. The following multichannel acquisition was used to detect signal: DAPI 405 nm/561 nm (650 V); AF568 (αSyn) 405 nm/561 nm (750 V). Images were analyzed using FIJI (RRID: SCR_002285, http://fiji.sc), where Z projected images were separated by channel and the brightness was altered (DAPI: 0–200, αSyn: 0–175). Images were then merged and exported as .jpg files.

To determine cell counts and signal intensity per region, images were inputted into Fiji as 'colorized' images, then Z projected at average intensity. Images were exported as. tiff files and imported into CellProfiler Analyst 3.0 (RRID: SCR_007358, http://cellprofiler.org) (***Stirling et al., 2021***). Image metadata was extracted, and images with 'C' matching 0 were assigned as DAPI, 1 assigned as αSyn. DAPI and αSyn positive cells were counted individually using the 'IdentifyPrimaryObjects' feature (pixel size 20–50), and αSyn intensity was measured as 'αSyn' from 'DAPI' primary objected. Count and intensity data was analyzed in Prism 9 (RRID: SCR_002798, GraphPad Software, http://www. graphpad.com/). Details of this protocol can be found here.

Slice preparation for physiology

For physiological studies, mice were deeply anesthetized with avertin (300 mg/kg, i.p.) and then were perfused transcardially with ice- cold, sucrose-based artificial cerebrospinal fluid (aCSF) containing (in mM) 230 sucrose, 26 $NaHCO_3$, 10 glucose, 10 $MgSO_4$, 2.5 KCl, 1.25 NaH_2PO_4, and 0.5 $CaCl_2$, 1 sodium pyruvate, and 0.005 L-glutathione. Next, coronal brain slices (300 µm) containing BLA were prepared in the same sucrose-based aCSF solution using a vibratome (VT1200S; Leica Microsystems, Buffalo Grove, IL). Brain slices were kept in normal aCSF (in mM, 126 NaCl, 26 $NaHCO_3$, 10 glucose, 2.5 KCl, 2 $CaCl_2$, 2 $MgSO_4$, 1.25 NaH_2PO_4, 1 sodium pyruvate, and 0.005 L-glutathione) equilibrated with 95% O_2 and 5% CO_2 for 30 min at 35°C and then held at room temperature until use.

Ex vivo electrophysiology recording and optogenetics

Brain slices were transferred into a recording chamber perfused at a rate of 3–4 ml/min with synthetic interstitial fluid (in mM, 126 NaCl, 26 $NaHCO_3$,10 glucose, 3 KCl, 1.6 $CaCl_2$,1.5 $MgSO_4$, and 1.25 NaH_2PO_4) equilibrated with 95% O_2 and 5% CO_2 at 33–34°C via a feedback-controlled in- line heater (TC- 324C, Warner Instruments) (***Chen et al., 2021***). SR-95531 (GABAzine, 10 µM) was routinely added extracellularly to block $GABA_A$ receptor-mediated inhibitory synaptic transmission. Neurons were visu alized and recorded under gradient contrast SliceScope 1000 (Scientifica, Uckfield, UK) with infrared illumination using an IR- 2000 CCD camera (DAGE- MTI, USA) and motorized micromanipulators (Scientifica, Uckfield, UK). Individual BLA projection neurons labeled with retrobeads were identified using a 60 × water immersion objective lens (Olympus, Japan) and targeted for whole- cell patch- clamp recording. Data were collected using a MultiClamp 700B amplifier and a Digidata 1550B digitizer at a sampling rate of 50 kHz under the control of pClamp11 (RRID: SCR_011323, Molecular Devices, San Jose, USA). Borosilicate glass pipettes (O.D.=1.5 mm, I.D.=0.86 mm, item #BF150-86- 10, Sutter Instruments) for patch clamp recordings (4–6 MΩ) were pulled using a micropipette puller (P1000, Sutter Instruments, Novato, CA).

To assess glutamatergic transmission in the BLA, glass pipettes were filled with a cesium methanesulfonate based internal solution of (in mM): 120 CH_3O_3SCs, 2.8 NaCl, 10 HEPES, 0.4 Na_4- EGTA, 5 QX314- HBr, 5 phosphocreatine, 0.1 spermine, 4 ATP- Mg, and 0.4 GTP- Na (pH 7.3, 290 mOsm). BLA neurons were voltage clamped at –70 mV to assess the EPSCs in response to presynaptic electrical or optogenetic stimulations. Concentric bipolar electrodes (FHC, Bowdoin, ME) or glass pipettes (~2 MΩ) filled with the extracellular solution were used as stimulating electrodes and placed on the external and internal capsules to evoke glutamate release in the BLA from cortical and thalamic axon terminals, respectively (***Shin et al., 2010***). A range of electrical pulses (intensities=30–120 µA, duration=100 µs) were delivered through a stimulator (Digitimer, UK) to evoke glutamate release at either cortical or thalamic inputs. To study the process of synaptic vesicle pool mobilization during repetitive glutamatergic transmission, we delivered 300 electrical pulses (duration=100 µs) at 12.5 Hz and measured the amplitudes of EPSCs to quantify changes in the presynaptic glutamate release (***Cabin et al., 2002***). Only one neuron was recorded from each slice in the prolonged repetitive stimulation studies.

Optogenetic stimulation pulses (1 ms duration) were delivered through a 60 × objective lens (Olympus, Japan) using a 470 nm LED light source (CoolLED, UK). To isolate monosynaptic cortico-BLA and thalamo- BLA EPSCs, optogenetically evoked EPSCs were recorded in the presence of TTX (1 µM) and 4-AP (100 µM). Series resistance (Rs <20 MΩ) was regularly monitored throughout the recording to ensure Rs changes were less than 15%. Liquid junction potential (~9 mV) was not corrected. Details of the protocol can be found here.

Data analysis and statistics

Electrophysiology data were analyzed offline in Clampfit 11.1 (RRID: SCR_011323, Molecular Devices). The peak amplitude of monosynaptic EPSCs in response to electric stimulation was quantified from an average of three to five sweeps. Digital confocal images were analyzed using ImageJ (RRID: SCR_003070, NIH, https://imagej.net/) or Imaris (RRID: SCR_007370, Oxford, UK, http://www.bitplane. com/imaris/imaris). Statistics were performed using Prism9 (RRID: SCR_002798, GraphPad Software, http://www.graphpad.com/). Non- parametric, distribution- independent Mann–

Whiney U (MWU) test was used for non- paired data comparisons between groups, followed by Bonferroni- Dunn correction for multiple comparisons. Data from *Snca*$^{SNL/SNL}$ mice were compared using one- way AVOVA (Šídák's multiple comparisons test). All tests were two-tailed, and <i>p-value<0.05 was considered statistically significant. Summary results are reported as mean plus standard error of mean.

Acknowledgements

This work was supported by the NARSAD Young Investigator award from the Brain and Behavior
Research Foundation (HYC) and an investigator- initiated research award from the Department of Defense (W81XWH2110943, PI: HYC). Dr. Hong-Yuan Chu is a Frederick & Alice Coles and Thomas & Nancy Coles Investigator. This research was funded in part by Aligning Science Across Parkinson's [ASAP- 020625 for MWCR, ASAP- 020616 for MXH, ASAP- 020572 for HYC] through the Michael J Fox Foundation for Parkinson's Research (MJFF). For the purpose of open access, the author has applied a CC BY public copyright license to all Author Accepted Manuscripts arising from this submission. The authors thank the Van Andel Institute Optical Imaging Core for the advanced confocal microscopy as well as the Van Andel Institute Vivarium and Transgenics Core, especially Megan Tompkins, Alyssa Bradfield, Malista Powers, and William Weaver for animal husbandry and colony maintenance.

Additional information

Competing interests

Patrik Brundin: has received support as a consultant from AbbVie, Axial Therapeutics, Calico Life Sciences, CuraSen, Enterin Inc, Fujifilm-Cellular Dynamics International, Idorsia Pharmaceuticals, Lundbeck A/S. He has received commercial support for research from Lundbeck A/S and F. Hoffman- La Roche. He has ownership interests in Acousort AB, Axial Therapeutics, Enterin Inc and RYNE Biotechnology. During the time that this paper was undergoing revision he became an employee of F. Hoffman- La Roche, although none of the data were generated by this company. The other authors declare that no competing interests exist.

Funding

Funder	Grant reference number	Author
Brain and Behavior Research Foundation		Hong-Yuan Chu
Congressionally Directed Medical Research Programs		Hong-Yuan Chu
Aligning Science Across Parkinson's	ASAP-020616	Michael X Henderson Maxime WC Rousseaux Hong-Yuan Chu
Aligning Science Across Parkinson's	ASAP-020625	Maxime WC Rousseaux
Aligning Science Across Parkinson's	ASAP-020572	Hong-Yuan Chu

The funders had no role in study design, data collection and interpretation, or the decision to submit the work for publication.

Author contributions

Liqiang Chen, Chetan Nagaraja, Samuel Daniels, Data curation, Formal analysis, Investigation, Validation; Zoe A Fisk, Formal analysis, Investigation, Visualization; Rachel Dvorak, Formal analysis; Lindsay Meyerdirk, Jennifer A Steiner, Resources; Martha L Escobar Galvis, Patrik Brundin, Conceptualization, Visualization, Writing – review and editing; Michael X Henderson, Resources, Writing – review and editing; Maxime WC Rousseaux, Methodology, Resources, Writing – review and editing; Hong- Yuan Chu, Conceptualization, Data curation, Formal analysis, Funding acquisition, Investigation, Methodology, Project administration, Resources, Supervision, Validation, Visualization, Writing – original draft, Writing – review and editing

Author ORCIDs

Liqiang Chen http://orcid.org/0000-0003-3236-1129
Jennifer A Steiner http://orcid.org/0000-0003-0953-1310
Martha L Escobar Galvis http://orcid.org/0000-0001-8400-9392
Hong-Yuan Chu http://orcid.org/0000-0003-0923-683X

Ethics

All animal studies were reviewed and approved by the Institutional Animal Care and Use Committee at Van Andel Institute (animal use protocol#: 22- 02- 007).

Decision letter and Author response

Decision letter https://doi.org/10.7554/eLife.78055.sa1
Author response https://doi.org/10.7554/eLife.78055.sa2

Additional files

Supplementary files

- Transparent reporting form

Data availability

All source data associated with the revised manuscript have been deposited on Open Science Framework: https://doi.org/10.17605/OSF.IO/264SM. All data generated or analyzed during this study are included in the manuscript and source data have been provided for all main and supplementary figures.

The following dataset was generated:

Author(s)	Year	Dataset title	Dataset URL	Database and Identifier
Chu H- Y	2022	Synaptic Location Is Determinant of the Detrimental Effects of α-Synuclein Pathology to Glutamatergic Transmission in the Basolateral Amygdala	https://doi . org/ 10. 17605/ OSF. IO/ 264SM	Open Science Framework, a 10.17605/OSF.IO/264SM

References

Abbott LF, Varela JA, Sen K, Nelson SB. 1997. Synaptic depression and cortical gain control. *Science* **275**:220–224. DOI: https://doi.org/10.1126/science.275.5297.221, PMID: 8985017

Abbott LF, Regehr WG. 2004. Synaptic computation. *Nature* **431**:796–803. DOI: https://doi.org/10.1038/ nature03010, PMID: 15483601

Abeliovich A, Schmitz Y, Fariñas I, Choi- Lundberg D, Ho WH, Castillo PE, Shinsky N, Verdugo JM, Armanini M, Ryan A, Hynes M, Phillips H, Sulzer D, Rosenthal A. 2000. Mice lacking alpha- synuclein display functional deficits in the nigrostriatal dopamine system. *Neuron* **25**:239–252. DOI: https://doi.org/10.1016/s0896-6273(00)80886-7, PMID: 10707987

Ahmed N, Headley DB, Paré D. 2021. Optogenetic study of central medial and paraventricular thalamic projections to the basolateral amygdala. *Journal of Neurophysiology* **126**:1234–1247. DOI: https://doi.org/10. 1152/jn.00253.2021, PMID: 34469705

Alabi AA, Tsien RW. 2012. Synaptic vesicle pools and dynamics. *Cold Spring Harbor Perspectives in Biology* **4**:a013680. DOI: https://doi.org/10.1101/cshperspect.a013680, PMID: 22745285

Amir A, Paré J- F, Smith Y, Paré D. 2019. Midline thalamic inputs to the amygdala: Ultrastructure and synaptic targets. *The Journal of Comparative Neurology* **527**:942–956. DOI: https://doi.org/10.1002/cne.24557, PMID: 30311651

Angot E, Steiner JA, Hansen C, Li JY, Brundin P. 2010. Are synucleinopathies prion- like disorders? *The Lancet. Neurology* **9**:1128–1138. DOI: https://doi.org/10.1016/S1474-4422(10)70213-1, PMID: 20846907

Benskey MJ, Perez RG, Manfredsson FP. 2016. The contribution of alpha synuclein to neuronal survival and function - Implications for Parkinson's disease. *Journal of Neurochemistry* **137**:331–359. DOI: https://doi.org/ 10.1111/jnc.13570, PMID: 26852372

Bowers D, Miller K, Mikos A, Kirsch- Darrow L, Springer U, Fernandez H, Foote K, Okun M. 2006. Startling facts about emotion in Parkinson's disease: blunted reactivity to aversive stimuli. *Brain* **129**:3356–3365. DOI: https:// doi.org/10.1093/brain/awl301, PMID: 17095520

Buck SA, De Miranda BR, Logan RW, Fish KN, Greenamyre JT, Freyberg Z. 2021. VGLUT2 is a determinant of dopamine neuron resilience in a rotenone model of dopamine neurodegeneration. *The Journal of Neuroscience* **41**:4937–4947. DOI: https://doi.org/10.1523/JNEUROSCI.2770-20.2021, PMID: 33893220

Burré J, Sharma M, Tsetsenis T, Buchman V, Etherton MR, Südhof TC. 2010. Alpha- synuclein promotes SNARE- complex assembly in vivo and in vitro. *Science* **329**:1663–1667. DOI: https://doi.org/10.1126/science.1195227, PMID: 20798282

Burtscher J, Copin J- C, Rodrigues J, Kumar ST, Chiki A, Guillot de Suduiraut I, Sandi C, Lashuel HA. 2019. Chronic corticosterone aggravates behavioral and neuronal symptomatology in a mouse model of alpha- synuclein pathology. *Neurobiology of Aging* **83**:11–20. DOI: https://doi.org/10.1016/j.neurobiolaging.2019.08. 007, PMID: 31585362

Cabin DE, Shimazu K, Murphy D, Cole NB, Gottschalk W, McIlwain KL, Orrison B, Chen A, Ellis CE, Paylor R, Lu B, Nussbaum RL. 2002. Synaptic vesicle depletion correlates with attenuated synaptic responses to prolonged repetitive stimulation in mice lacking alpha- synuclein. *The Journal of Neuroscience* **22**:8797–8807. DOI: https://doi.org/10.1523/jneurosci.22-20-08797.2002, PMID: 12388586

Chen L, Daniels S, Kim Y, Chu H- Y. 2021. Cell type- specific decrease of the intrinsic excitability of motor cortical pyramidal neurons in parkinsonism. *The Journal of Neuroscience* **41**:5553–5565. DOI: https://doi.org/10.1523/ JNEUROSCI.2694-20.2021, PMID: 34006589

Cookson MR, van der Brug M. 2008. Cell systems and the toxic mechanism(s) of alpha- synuclein. *Experimental Neurology* **209**:5–11. DOI: https://doi.org/10.1016/j.expneurol.2007.05.022, PMID: 17603039

Erskine D, Patterson L, Alexandris A, Hanson PS, McKeith IG, Attems J, Morris CM. 2018. Regional levels of physiological α-synuclein are directly associated with Lewy body pathology. *Acta Neuropathologica* **135**:153–154. DOI: https://doi.org/10.1007/s00401-017-1787-6, PMID: 29134319

Fremeau RT, Troyer MD, Pahner I, Nygaard GO, Tran CH, Reimer RJ, Bellocchio EE, Fortin D, Storm- Mathisen J, Edwards RH. 2001. The expression of vesicular glutamate transporters defines two classes of excitatory synapse. *Neuron* **31**:247–260. DOI: https://doi.org/10.1016/s0896-6273(01)00344-0, PMID: 11502256

Geertsma HM, Suk TR, Ricke KM, Horsthuis K, Parmasad JLA, Fisk ZA, Callaghan SM, Rousseaux MWC. 2022. Constitutive nuclear accumulation of endogenous alpha-synuclein in mice causes motor impairment and cortical dysfunction, independent of protein aggregation. *Human Molecular Genetics*:ddac035. DOI: https://doi.org/10.1093/hmg/ddac035, PMID: 35179202

Harding AJ, Stimson E, Henderson JM, Halliday GM. 2002. Clinical correlates of selective pathology in the amygdala of patients with Parkinson's disease. *Brain* **125**:2431–2445. DOI: https://doi.org/10.1093/brain/ awf251, PMID: 12390970

Henderson MX, Cornblath EJ, Darwich A, Zhang B, Brown H, Gathagan RJ, Sandler RM, Bassett DS, Trojanowski JQ, Lee VMY. 2019. Spread of α-synuclein pathology through the brain connectome is modulated by selective vulnerability and predicted by network analysis. *Nature Neuroscience* **22**:1248–1257. DOI: https://doi.org/10.1038/s41593-019-0457-5, PMID: 31346295

Hintiryan H, Bowman I, Johnson DL, Korobkova L, Zhu M, Khanjani N, Gou L, Gao L, Yamashita S, Bienkowski MS, Garcia L, Foster NN, Benavidez NL, Song MY, Lo D, Cotter KR, Becerra M, Aquino S, Cao C, Cabeen RP, et al. 2021. Connectivity characterization of the mouse basolateral amygdalar complex. *Nature Communications* **12**:2859. DOI: https://doi.org/10.1038/s41467-021-22915-5, PMID: 34001873

Hu X, Song X, Yuan Y, Li E, Liu J, Liu W, Liu Y. 2015. Abnormal functional connectivity of the amygdala is associated with depression in Parkinson's disease. *Movement Disorders* **30**:238–244. DOI: https://doi.org/10. 1002/mds.26087, PMID: 25545969

Janak PH, Tye KM. 2015. From circuits to behaviour in the amygdala. *Nature* **517**:284–292. DOI: https://doi.org/10.1038/nature14188, PMID: 25592533

Kaneko T, Fujiyama F. 2002. Complementary distribution of vesicular glutamate transporters in the central nervous system. *Neuroscience Research* **42**:243–250. DOI: https://doi.org/10.1016/s0168-0102(02)00009-3, PMID: 11985876

Luk KC, Song C, O'Brien P, Stieber A, Branch JR, Brunden KR, Trojanowski JQ, Lee VMY. 2009. Exogenous alpha- synuclein fibrils seed the formation of Lewy body- like intracellular inclusions in cultured cells. *PNAS* **106**:20051–20056. DOI: https://doi.org/10.1073/pnas.0908005106, PMID: 19892735

Luk KC, Kehm V, Carroll J, Zhang B, O'Brien P, Trojanowski JQ, Lee VMY. 2012. Pathological α-synuclein transmission initiates Parkinson- like neurodegeneration in nontransgenic mice. *Science* **338**:949–953. DOI: https://doi.org/10.1126/science.1227157, PMID: 23161999

Mezey E, Dehejia AM, Harta G, Suchy SF, Nussbaum RL, Brownstein MJ, Polymeropoulos MH. 1998. Alpha synuclein is present in Lewy bodies in sporadic Parkinson's disease. *Molecular Psychiatry* **3**:493–499. DOI: https://doi.org/10.1038/sj.mp.4000446, PMID: 9857974

Nelson PT, Abner EL, Patel E, Anderson S, Wilcock DM, Kryscio RJ, Van Eldik LJ, Jicha GA, Gal Z, Nelson RS, Nelson BG, Gal J, Azam MdT, Fardo DW, Cykowski MD. 2018. The amygdala as a locus of pathologic misfolding in neurodegenerative diseases. *Journal of Neuropathology & Experimental Neurology* **77**:2–20. DOI: https://doi.org/10.1093/jnen/nlx099, PMID: 29186501

Peng C, Gathagan RJ, Covell DJ, Medellin C, Stieber A, Robinson JL, Zhang B, Pitkin RM, Olufemi MF, Luk KC, Trojanowski JQ, Lee VM- Y. 2018. Cellular milieu imparts distinct pathological α-synuclein strains in α-synucleinopathies. *Nature* **557**:558–563. DOI: https://doi.org/10.1038/s41586-018-0104-4, PMID: 29743672

Runwal G, Edwards RH. 2021. The membrane interactions of synuclein: physiology and pathology. *Annual Review of Pathology* **16**:465–485. DOI: https://doi.org/10.1146/annurev-pathol-031920-092547, PMID: 33497259

Shin RM, Tully K, Li Y, Cho JH, Higuchi M, Suhara T, Bolshakov VY. 2010. Hierarchical order of coexisting pre- and postsynaptic forms of long- term potentiation at synapses in amygdala. *PNAS* **107**:19073–19078. DOI: https:// doi.org/10.1073/pnas.1009803107, PMID: 20956319

Sigur sson T, Sigurdsson T, Cain CK, Doyère V, LeDoux JE. 2010. Asymmetries in long- term and short- term plasticity at thalamic and cortical inputs to the amygdala in vivo. *The European Journal of Neuroscience* **31**:250–262. DOI: https://doi.org/10.1111/j.1460-9568.2009.07056.x, PMID: 20074223

Sorrentino ZA, Goodwin MS, Riffe CJ, Dhillon JKS, Xia Y, Gorion KM, Vijayaraghavan N, McFarland KN, Golbe LI, Yachnis AT, Giasson BI. 2019. Unique α-synuclein pathology within the amygdala in Lewy body dementia: implications for disease initiation and progression. *Acta Neuropathologica Communications* **7**:142. DOI: https://doi.org/10.1186/s40478-019-0787-2, PMID: 31477175

Spillantini MG, Schmidt ML, Lee VMY, Trojanowski JQ, Jakes R, Goedert M. 1997. Alpha- synuclein in Lewy bodies. *Nature* **388**:839–840. DOI: https://doi.org/10.1038/42166, PMID: 9278044

Steinkellner T, Conrad WS, Kovacs I, Rissman RA, Lee EB, Trojanowski JQ, Freyberg Z, Roy S, Luk KC, Lee VM, Hnasko TS. 2022. Dopamine neurons exhibit emergent glutamatergic identity in Parkinson's disease. *Brain : A Journal of Neurology* **145**:879–886. DOI: https://doi.org/10.1093/brain/awab373, PMID: 35258081

Stirling DR, Carpenter AE, Cimini BA. 2021. CellProfiler Analyst 3.0: Accessible data exploration and machine learning for image analysis. *Bioinformatics* **37**:btab634. DOI: https://doi.org/10.1093/bioinformatics/btab634, PMID: 34478488

Stoyka LE, Arrant AE, Thrasher DR, Russell DL, Freire J, Mahoney CL, Narayanan A, Dib AG, Standaert DG, Volpicelli- Daley LA. 2020. Behavioral defects associated with amygdala and cortical dysfunction in mice with seeded α-synuclein inclusions. *Neurobiology of Disease* **134**:104708. DOI: https://doi.org/10.1016/j.nbd.2019.104708, PMID: 31837424

Sulzer D, Edwards RH. 2019. The physiological role of α-synuclein and its relationship to Parkinson's Disease. *Journal of Neurochemistry* **150**:475–486. DOI: https://doi.org/10.1111/jnc.14810, PMID: 31269263

Surmeier DJ, Obeso JA, Halliday GM. 2017. Selective neuronal vulnerability in Parkinson disease. *Nature Reviews. Neuroscience* **18**:101–113. DOI: https://doi.org/10.1038/nrn.2016.178, PMID: 28104909

Taguchi K, Watanabe Y, Tsujimura A, Tanaka M. 2016. Brain region- dependent differential expression of alpha- synuclein. *The Journal of Comparative Neurology* **524**:1236–1258. DOI: https://doi.org/10.1002/cne. 23901, PMID: 26358191

Thakur P, Chiu WH, Roeper J, Goldberg JA. 2019. α-SYNUCLEIN 2.0 - moving towards cell type specific pathophysiology. *Neuroscience* **412**:248–256. DOI: https://doi.org/10.1016/j.neuroscience.2019.06.005, PMID: 31202707

Uemura N, Uemura MT, Luk KC, Lee VMY, Trojanowski JQ. 2020. Cell- to- Cell Transmission of Tau and α-Synuclein. *Trends in Molecular Medicine* **26**:936–952. DOI: https://doi.org/10.1016/j.molmed.2020.03.012, PMID: 32371172

Vargas KJ, Schrod N, Davis T, Fernandez- Busnadiego R, Taguchi YV, Laugks U, Lucic V, Chandra SS. 2017. Synucleins have multiple effects on presynaptic architecture. *Cell Reports* **18**:161–173. DOI: https://doi.org/10. 1016/j.celrep.2016.12.023, PMID: 28052246

Vasili E, Dominguez- Meijide A, Flores- León M, Al- Azzani M, Kanellidi A, Melki R, Stefanis L, Outeiro TF. 2022. Endogenous levels of alpha- synuclein modulate seeding and aggregation in cultured cells. *Molecular Neurobiology* **59**:1273–1284. DOI: https://doi.org/10.1007/s12035-021-02713-2, PMID: 34984585

Vigneault É, Poirel O, Riad M, Prud'homme J, Dumas S, Turecki G, Fasano C, Mechawar N, El Mestikawy S. 2015. Distribution of vesicular glutamate transporters in the human brain. *Frontiers in Neuroanatomy* **9**:23. DOI: https://doi.org/10.3389/fnana.2015.00023, PMID: 25798091

Volpicelli- Daley LA, Luk KC, Patel TP, Tanik SA, Riddle DM, Stieber A, Meaney DF, Trojanowski JQ, Lee VMY. 2011. Exogenous α-synuclein fibrils induce Lewy body pathology leading to synaptic dysfunction and neuron death. *Neuron* **72**:57–71. DOI: https://doi.org/10.1016/j.neuron.2011.08.033, PMID: 21982369

Volpicelli- Daley LA, Luk KC, Lee VMY. 2014. Addition of exogenous α-synuclein preformed fibrils to primary neuronal cultures to seed recruitment of endogenous α-synuclein to Lewy body and Lewy neurite- like aggregates. *Nature Protocols* **9**:2135–2146. DOI: https://doi.org/10.1038/nprot.2014.143, PMID: 25122523

West MJ. 1999. Stereological methods for estimating the total number of neurons and synapses: issues of precision and bias. *Trends in Neurosciences* **22**:51–61. DOI: https://doi.org/10.1016/s0166-2236(98)01362-9, PMID: 10092043

Yoshimura N, Kawamura M, Masaoka Y, Homma I. 2005. The amygdala of patients with Parkinson's disease is silent in response to fearful facial expressions. *Neuroscience* **131**:523–534. DOI: https://doi.org/10.1016/j. neuroscience.2004.09.054, PMID: 15708493

Ziolkowska B, Gieryk A, Bilecki W, Wawrzczak- Bargiela A, Wedzony K, Chocyk A, Danielson PE, Thomas EA, Hilbush BS, Sutcliffe JG, Przewlocki R. 2005. Regulation of alpha- synuclein expression in limbic and motor brain regions of morphine- treated mice. *The Journal of Neuroscience* **25**:4996–5003. DOI: https://doi.org/10.1523/ JNEUROSCI.4376-04.2005, PMID: 15901780

Characterizing the differential distribution and targets of Sumo paralogs in the mouse brain

Terry R. Suk[1-4], Trina T. Nguyen[1-4], Zoe A. Fisk[1-4], Miso Mitkovski[5], Haley M. Geertsma[14], Jean-Louis A. Parmasad[1-4], Meghan M. Heer[1-4], Steve M. Callaghan[1-4], Nils Brose[6], Marilyn Tirard[6,*], and Maxime W.C. Rousseaux[1-4,*]

[1]University of Ottawa Brain and Mind Research Institute, Ottawa, Canada
[2]Department of Cellular and Molecular Medicine, University of Ottawa, Ottawa, Canada
[3]Eric Poulin Center for Neuromuscular Diseases, Ottawa, Canada
[4]Ottawa Institute of Systems Biology, Ottawa, Canada
[5]Imaging Facility, Max Planck Institute of Multidisciplinary Sciences, Göttingen, Germany
[6]Department of Molecular Neurobiology, Max Planck Institute of Multidisciplinary Sciences, Göttingen, Germany.
*Co-corresponding Authors: max.rousseaux@uottawa.ca or tirard@mpinat.mpg.de

Author Contributions

T.R.S., T.T.N., Z.A.F., M.M., H.M.G., J.L-A.P., M.M.H., S.M.C., M.T. investigation, formal analysis; M.W.C.R., M.T. and N.B., resources; M.W.C.R., M.T. and N.B., conceptualization; T.R.S., M.W.C.R., M.T. and N.B., writing original draft and editing; M.W.C.R., M.T. and N.B., supervision and funding acquisition. All authors reviewed and approved the manuscript.

ABSTRACT

SUMOylation is an evolutionarily conserved and essential mechanism whereby Small Ubiquitin Like Modifiers, or SUMO proteins (Sumo in mice), are covalently bound to protein substrates in a highly dynamic and reversible manner. SUMOylation is involved in a variety of basic neurological processes including learning and memory, and central nervous system development, but is also linked with neurological disorders. However, studying SUMOylation *in vivo* remains challenging due to limited tools to study Sumo proteins and their targets in their native context. More complexity arises from the fact that

Sumo1 and Sumo2 are ~50% homologous, whereas Sumo2 and Sumo3 are nearly identical and indistinguishable with antibodies. While Sumo paralogues can compensate for one another's loss, Sumo2 is highest expressed and only paralog essential for embryonic development making it critical to uncover roles specific to Sumo2 *in vivo*. To further examine the roles of Sumo2, and to begin to tease apart the redundancy and similarity between key Sumo paralogs, we generated (His_6-)HA epitope-tagged Sumo2 knock-in mouse alleles, expanding the current Sumo knock-in mouse tool-kit comprising of the previously generated His_6-HA-Sumo1 knock-in model. Using these HA-Sumo mouse lines, we performed whole brain imaging and mapping to the Allen Brain Atlas to analyze the relative distribution of the Sumo1 and Sumo2 paralogues in the adult mouse brain. We observed differential staining patterns between Sumo1 and Sumo2, including a partial localization of Sumo2 in nerve cell synapses of the hippocampus. Combining immunoprecipitation with mass spectrometry, we identified native substrates targeted by Sumo1 or Sumo2 in the mouse brain. We validated select hits using proximity ligation assays, further providing insight into the subcellular distribution of neuronal Sumo2conjugates. These mouse models thus serve as valuable tools to study the cellular and biochemical roles of SUMOylation in the central nervous system.

INTRODUCTION

Post translational modifications (PTMs) provide a dynamic mode of regulation over protein functions altering the secondary, tertiary, or quaternary structures of proteins. Although the most frequently characterized PTMs typically involve the covalent conjugation of small molecules, such as phosphate, glycosyl, or acetyl groups, protein function can also be modulated by the covalent conjugation of large molecules such as the protein Ubiquitin. Indeed, several Ubiquitin-like proteins have been identified to function as PTMs in eukaryotes including NEDD8, Atg8, Atg12, and Small Ubiquitin-like Modifiers (SUMOs) (Ilic et al., 2022; Mahajan et al., 1997; Matunis et al., 1996).

The covalent addition of SUMOs through SUMOylation is a dynamic and essential process that is highly conserved throughout eukaryote evolution(Celen and Sahin, 2020; Ilic et al., 2022). First, immature SUMO proteins are matured through Sentrin Specific

Protease (SENP) cleavage at a diglycine motif that is essential for covalent conjugation (Xu and Au, 2005). Next, SUMOs are activated in an ATP dependent manner and conjugated to the E1 ligase heterodimer complex consisting of SUMO Activating Enzyme 1 (SAE1) and Ubiquitin-Like Modifier Activating Enzyme 2 (UBA2)(Gong et al., 1999). SUMOs are then transferred to the sole E2 ligase, SUMO conjugating enzyme UBC9 (UBC9, encoded by *UBE2I*), which is essential for SUMOylation to occur(Desterro et al., 1997; Gong et al., 1997; Johnson and Blobel, 1997; Lee et al., 1998; Saitoh et al., 1998; Seufert et al., 1995). SUMOylation can then occur at a lysine residue of a target substrate, typically residing in a SUMO consensus motif (Ψ-K-x-D/E, Ψ=large hydrophobic amino acid), directly from UBC9 or upon facilitation by E3 ligases (Rodriguez et al., 2001; Sampson et al., 2001). Finally, SENPs can readily deSUMOylate the protein substrate, and SUMO is recycled for subsequent rounds of SUMOylation, allowing for highly dynamic regulation of substrate function (Nayak and Müller, 2014).

There are five known human SUMO paralogs (SUMO1 – SUMO5) with SUMO1 – SUMO3 being the most extensively studied as they are ubiquitously expressed and found in most vertebrates, whereas SUMO4 and SUMO5 are specific to humans and exhibit tissue-specific expression (Bouchard et al., 2021; Citro and Chiocca, 2013). SUMO1 shares around 50% homology with SUMO2 and SUMO3, whereas mature SUMO2 and SUMO3 share 97% homology leading to these proteins to be often referred together as SUMO2/3 (Bohren et al., 2004). While SUMO paralogs often play redundant roles and can exhibit some level of compensation, each paralog can also play unique roles in cells, localizing to different subcellular regions and targeting different protein substrates (Citro and Chiocca, 2013; Ilic et al., 2022). Additionally, *Sumo2*, but not *Sumo1* nor *Sumo3*, is the only essential paralog whereby knock-out in mice results in major developmental defects leading to embryonic lethality by E10.5 (Wang et al., 2014b). The essentiality of Sumo2 for proper development may be in part due to higher levels of Sumo2 in comparison to its paralogs, particularly Sumo3 (Wang et al., 2014b; Yu et al., 2020). Alternatively, it may also be the result of specific Sumo-conjugated proteomes between Sumo2 and its paralogs conferring different roles in cells. Thus, characterizing the specific roles of Sumo2 is crucial to not only help to uncover key mechanisms of cellular function

and advance our understanding of SUMOylation in basic biology, but to also provide insight into disease processes.

Several challenges currently limit the study of protein SUMOylation: 1) Differentiating between the Sumo paralogs using antibodies is limiting or not possible due to the high degree of homology(Garvin et al., 2022); 2) The highly dynamic nature of SUMOylation makes biological context such as tissue, cell type, and cell state, critical for capturing and characterizing SUMOylation events; and 3) Tools to study SUMOylation are limited and often rely on overexpression models, potentially confounding studies of protein function. Consequently, protein SUMOylation is heavily studied in highly proliferating cells where it is now well established that SUMOylation plays a key role in regulating nuclear and DNA-related mechanisms, but the role of this PTM remains unclear, and even debated, in more complex system, including post-mitotic cells such as neurons (Daniel et al., 2018; Daniel et al., 2017).

To overcome these limitations, we expanded the current Sumo mouse knock-in toolkit and generated and characterized in parallel two novel knock-in (KI) mouse models. Specifically, sequences encoding affinity tags are knocked into the endogenous *Sumo2* locus whereby an HA-Sumo2 or His_6-HA-Sumo2 fusion protein is generated, allowing for the characterization of Sumo2 and its substrates *in vivo.* Analogous to our work with a corresponding His_6-HA-Sumo1 KI allele (Daniel et al., 2018; Daniel et al., 2017; Tirard et al., 2012), this approach allows us to directly compare the localization patterns between Sumo1 and Sumo2 throughout the mouse central nervous system (CNS). We used whole brain imaging to map the relative abundance of Sumo1 and Sumo2 throughout the adult mouse brain and observed that, while Sumo levels are broadly distributed, they exhibit regional differences throughout the CNS. We found that, unlike Sumo1 (Daniel et al., 2018; Daniel et al., 2017; Tirard et al., 2012), Sumo2 is present in both nuclear and extranuclear compartments, including neuronal synapses. Based on this distinct subcellular distribution, we explored native Sumo1 and Sumo2 targets using immunoprecipitation and mass spectrometry. We identified genuine Sumo2-specific targets in the adult mouse brain, including a subset of non-nuclear proteins. Moreover, we observed dynamic changes between Sumo1- vs. Sumo2-selective substrates. Finally, we validated several hits using proximity ligations assays to detect protein-Sumo

interactions within primary cortical neurons. This approach did not only provide an additional mode of validating native interactors of Sumo2 in wild-type neurons, but also yielded spatial information, demonstrating both nuclear and cytoplasmic interactions between Sumo2 and its substrates. Together, these new mouse lines and our data provide an important new resource that lays the foundation of a "Sumo-code" which provides a new layer of complexity to brain function.

RESULTS

Generation of (His$_6$-)HA-Sumo2 mouse lines.

The use of epitope tags provides a versatile way to streamline the study of proteins by taking advantage of the highly selective nature of antibodies raised against these tags. In parallel institutions, we generated two independent alleles to facilitate the study of Sumo2 *in vivo*. We took advantage of a CRISPR/Cas9 approach to knock-in a 6xHishemagglutinin (*His$_6$-HA*) tag into the amino-terminus of *Sumo2* (*His$_6$-HA-Sumo2*) in C57BL/6J mice (Figure 1—figure supplement 1A) in one case, mirroring that of a previously generated mouse line to study Sumo1 *in vivo* (Tirard et al., 2012). Moreover, we also generated an HA-Sumo2 knock-in mouse that does not have the His$_6$ tag. We observed that knock-in of either *His$_6$-HA* or *HA* to *Sumo2* resulted in hydrocephaly and premature death in heterozygous mice, indicating a likely hypomorphic effect of the epitope tag on a C57BL/6J background. Interestingly, backcrossing the mice to an FVB/N background alleviated these effects, resulting in no overt differences between mutant and wild-type FVB/N (WT) littermates in either line. Nevertheless, given the importance of Sumo2 for life, and the robustness of the HA tag for visualization and biochemistry, we performed the bulk of our analyses on heterozygous His$_6$-HA-Sumo2 (and heterozygous His$_6$-HA-Sumo1; also crossed to an FVB/N background) knock-in mice.

His$_6$-HA-Sumo2 enables the comparison of endogenous Sumo2 levels in the CNS.

To determine whether the addition of the HA epitope tag affects native Sumo levels, we assessed the levels of Sumo2/3 conjugates by Western blot, comparing total levels of unconjugated Sumo ("Free Sumo") and Sumo-conjugated proteins from mouse brain lysates. We observed no change in the abundance of Sumo2/3 conjugates in the brains

of adult His_6-HA-Sumo2 mice compared to His_6-HA-Sumo1 or WT mice (Figure 1—figure supplement 1B). As decreased levels of Sumo1 conjugates were previously observed in homozygotes His_6-HA-Sumo1 mouse brain (Daniel et al., 2017), we thus measured whether there were any changes in the abundance of native Sumo1 conjugates in heterozygous His_6-HA-Sumo1 and His_6-HA-Sumo2 KI mice (Wang et al., 2014b). Again, no changes were observed between either Sumo KI line and their WT counterparts, indicating that the heterozygous His_6-HA-Sumo2 or His_6-HA-Sumo1 allele does not alter overall levels of Sumo conjugates in mouse brain (Figure 1—figure supplement 1C). Additionally, we did not observe a significant effect on the expression of *Sumo1* and *Sumo2* transcript levels in either of the His_6-HA-Sumo KI mice (Figure 1—figure supplement 1D). Thus, the novel His_6-HA-Sumo2 KI mice model enable the study of Sumo2 at endogenous levels *in vivo* without changes to the Sumo equilibrium.

The uniformity of the HA-tag epitope between the His_6-HA-Sumo1 and His_6-HASumo2 mice allows for a more direct comparison of endogenous Sumo1 and Sumo2 levels *in vivo*. We assessed the relative levels of Sumo1 and Sumo2 in the central nervous system, specifically the cortex (CTX), cerebellum (CBM), olfactory bulbs (OB), spinal cord (SC) and remainder of the brain (termed “striatum-thalamus-brainstem for simplicity [STh-B]”) from adult mice (Figure 1). Western blot analysis from CNS regional lysates shows that levels of unconjugated and conjugated Sumo2 are significantly higher than Sumo1 throughout the CNS (2-way ANOVA; Sumo effect: $P = 0.0046$ and $P = 0.0003$ for high molecular weight Sumo and free Sumo, respectively). The CTX, CBM, and OB are specifically enriched for Sumo2 whereas the S-Th-B and SC contains lower levels of Sumo2. Taken together, Sumo1 and Sumo2 are broadly distributed throughout the CNS, however regional differences in Sumo abundance and Sumo paralog predominance can be observed, indicating possible unique regional roles throughout the CNS.

Regional Analysis of Sumo1 and Sumo2 Throughout the Mouse Brain

As differences in Sumo levels are detectable from regional crude brain lysates, we leveraged the specificity of the HA-tag and performed whole brain clearing and mapping of Sumo1 and Sumo2 signals in the adult mouse brain. His_6-HA-Sumo1 and His_6-HASumo2 mouse brains were cleared and immunolabeled against the HA-tag and NeuN

before imaging using light sheet microscopy (Figure 2A; Figure 2—figure supplement videos 1 & 2). Images were then analyzed and aligned to the Allen Brain Atlas to determine the relative levels of the His_6-HA-Sumo signals in defined brain regions (Table 1). It is worth noting that due to the different absolute abundance of Sumo1 (low) versus Sumo2 (high) in the brain, only qualitative Sumo1 vs Sumo2 comparisons were made. To generate relative maps of HA-Sumo distribution, the mean regional HA signal intensity was first normalized to the regional density of NeuN to account for changes in cell density before being averaged across hemibrains to account for tissue variability. Generally, Sumo1 and Sumo2 showed similar distributions throughout the mouse brain (Figure 2BE) and we observed that both Sumo1 and Sumo2 were most abundant in cerebellar nuclei.

While Sumo levels were generally evenly distributed when characterizing gross anatomical regions, clear nuances in Sumo abundance were detectable at higher anatomical resolution. For example, in the hippocampus, Sumo levels were highest in the parasubiculum and presubiculum, and lowest in the *Fasciola cinerea* (Figure 2—figure supplement 1A & B). In the neocortex, we observed that Sumo levels were generally enriched in layers 2/3 (Figure 2B & D; Figure 2—figure supplement 1C), an area critical for integrative processing (Feldmeyer, 2012). Interestingly, while Sumo1 and Sumo2 often share similar distributions, we observed that Sumo2 is enriched in the anterior hypothalamus (Figure 2—figure supplement 1D), particularly in regions involved in the circadian rhythm, including the suprachiasmatic nucleus and subparaventricular zone (Drunen and Eckel-Mahan, 2021).

We investigated whether the brain-wide imaging findings could be validated by an orthogonal immunofluorescence assay (Figure 2—figure supplement 2). Looking at multiple brain regions, we found that Sumo1 and Sumo2 are broadly distributed through the somatosensory cortex. Interestingly, Sumo1 maintains a strictly nuclear localization, whereas Sumo2 is observed throughout the nucleus and in the cytoplasm and axons of cortical neurons. In the cerebellum, we found that Sumo2 is specifically enriched in granule cells, contrasting the strong Purkinje cell staining observed in His_6-HA-Sumo1 mice (Tirard *et al.* 2012). The hippocampus also displays characteristic nuclear staining for His_6-HA-Sumo1 in both the CA1 and CA3, whereas Sumo2 is seen throughout the nucleus and in the somata, and axons of hippocampal neurons. Thus, while Sumo1 and

Sumo2 may share regional expression in the brain, the distinct localizations of Sumo1 and Sumo2 *in vivo* indicate different targets of SUMOylation or different metabolism or conjugation dynamics of free Sumo likely play unique roles in neuronal regulation.

HA-Sumo2 localizes to synapses in vivo.

Consistent with our previous work, we observed that Sumo1 strictly localizes to neuronal nuclei (Figure 2–figure supplement 2) (Tirard et al., 2012). However, we noticed that Sumo2 signal can also be found outside the nuclear compartment (Figure 2–figure supplement 2). The role of Sumo in extra-nuclear compartments, specifically at synapses, remains a topic of debate, particularly in the context of Sumo1(Daniel et al., 2018; Daniel et al., 2017). Thus, we further characterized extra-nuclear Sumo2 signals using homozygous HA-Sumo2 mice. As in the His_6-HA-Sumo2 KI model, levels of Sumo2 conjugates were unaltered in total brain lysates from homozygous HA-Sumo2 mice as compared to WT littermates, ruling out an effect of the HA tag on overall Sumo2 expression and conjugation levels (Figure 3–figure supplement 1A) (Tirard et al., 2012). Western blot analysis of brain subcellular fractions using an anti-HA antibody highlighted not only the difference in global levels of Sumo1 and Sumo2 conjugates, but also revealed that Sumo2 conjugates are abundant in non-nuclear fractions, including synaptic cytosol fractions S2 and S3 (Figure 3–figure supplement 1B-C). A weak but specific signal was also observed in crude synaptosomes and other synaptic membrane fractions (Figure 3–figure supplement 1B-D).

Next, we used homozygous HA-Sumo2 mice to further characterize extra-nuclear Sumo2 by performing anti-HA immunolabeling of the hippocampal CA3 area, a region enriched in synapses (Figure 2–figure supplement 2). Brain sections from WT and HASumo2 mice were immunolabeled for HA and neuronal markers for dendrites and synaptic compartments, and anti-HA immunosignals were quantified in HA-Sumo2 mice as compared to WTs (Figure 3). Using confocal microscopy, we confirmed the presence of Sumo2 in extra-nuclear compartments, specifically along dendrites and in synapses (Figure 3A). Quantification of HA-Sumo2 immunosignals in DAPI positive area confirmed the strong enrichment of Sumo2 conjugates in neuronal nuclei, in agreement with the well-known role of Sumos as nuclear regulators (Figure 3A and B) (Hendriks and Vertegaal

2016, Hendriks and Vertegaal 2015). In addition, HA-Sumo2 immunosignal was also observed in MAP2-positive regions and, strikingly, in synapses positives for Synapsin1, Shank2, Gephyrin, and/or vGlut1 (Figure 3C and D). Higher magnification images confirmed the presence of Sumo2 along MAP2 dendrites and at synapses (Figure 4; Figure 4–figure supplement 1). Quantification of the 3D object-based co-localization between the anti-HA immunosignal with the various synaptic markers confirmed the presence of Sumo2 at synapses, with HA-Sumo2 signal being significantly co-localized with Shank2, Synapsin 1, vGlut1 and vGAT (Figure 4C and Figure 4–figure supplement 1, which shows a typical 3D reconstruction generated in Imaris). Co-localization of Sumo2 with Gephyrin was not obvious, most likely due to difficulties in immunolabeling inhibitory synapses with the method optimized for HA visualization. Altogether, our data demonstrate the presence of Sumo2 at synapses.

HA-Sumo mice reveal convergent and contrasting neuronal Sumo1 and Sumo2 substrates.

The observation that there are regional and subcellular differences between Sumo1 and Sumo2 indicate divergent roles for the Sumo paralogs in the mouse brain. To uncover such molecular differences between Sumo paralogs, we performed HA-tag immunoprecipitation, under denaturing conditions to break apart standard protein-protein interactions, from whole brain lysate of WT, His_6-HA-Sumo1, and His_6-HA-Sumo2 mice, followed by mass spectrometric analysis to identify candidate targets of Sumo1 and Sumo2 *in vivo* (Figure 5A; Table 2). To rank proteins identified from the mass spectrometry dataset, we summated the total peptides from 4 replicates per genotype and then filtered proteins with >2-fold enrichment over proteins identified in the WT condition. Next, to determine high-stringency candidates, proteins were further filtered based on peptide counts being identified in at least 2/4 replicates in the HA-Sumo conditions, and no more than 1/4 replicate in the respective WT condition. Using these criteria, we identified 131 proteins enriched in the HA-Sumo1 and 75 proteins enriched in the HA-Sumo2 immunoprecipitations (Table 2). Gene ontology and Reactome terms related to protein SUMOylation process (Figure 5B) were significantly enriched in both datasets (Figure 5C; Figure 5—figure supplement 1C; Table 3). Indeed, we identified critical

components of the SUMOylation pathway including E1 SUMO ligases Sae1 and Uba2, the E2 SUMO ligase Ube2i, and E3 ligases Ranbp2(Pichler et al., 2002), Trim28(Liang et al., 2011), and Pml(Chu and Yang, 2011), validating the use of our mouse model to identify molecular substrates involved with SUMOylation.

To determine whether we could identify specific interactors of Sumo2, we compared the relative fold change of peptides identified in the His_6-HA-Sumo2 immunoprecipitation to that of the His_6-HA-Sumo1 immunoprecipitation and found that there are shared, specific, and preferential interactors of Sumo2 vs. Sumo1 (Figure 5D; Figure 5—figure supplement 1D; Table 2). We selected several hits from our mass spectrometry screen for validation via Western blot (Figure 5D). Ranbp2 and Rangap1 are consistently identified amongst the most abundantly SUMOylated proteins (Gareau et al., 2012; Geiss-Friedlander and Melchior, 2007; Saitoh et al., 1998) and were indeed validated to be shared targets of Sumo1 and Sumo2 in the mouse brain. Additionally, both proteins displayed a preference for Sumo1 modification in the mouse brain as previously described (Gareau et al., 2012). Conversely, the E3 ligase and transcriptional repressor Trim28 displayed a preference for Sumo2 modification in the adult mouse brain. Interestingly, the transcription factor Prox1, involved in neurogenesis and a marker of granule cells in the dentate gyrus and cerebellum (Lavado et al., 2010), was one of the most abundantly SUMOylated proteins targeted specifically by Sumo2 in our screen. We further tested the sensitivity of the model to detect more modestly SUMOylated proteins targeted by Sumo2 in the mouse brain, as measured by relative abundance in our immunoprecipitation coupled with mass spectrometry experiment. We confirmed that both Histone Deacetylase 2 (Hdac2) and General Transcription Factor 2i (Gtf2i, also known as Tf2-i) were Sumo2-modified (Figure 5D). Because of the dynamic nature of SUMOylation and the fact that Sumo only targets a fraction of the total pool of most substrates, biologically meaningful interactions may be buried under strong, constitutively SUMOylated targets in our screen. As a proof of concept, we picked a hit with low enrichment in the His_6-HA-Sumo2 immunoprecipitation by expanding the filtering criteria to a >1.5 fold enrichment over wild-type: Matrin3 (Matr3). We found that Matr3 was selectively SUMOylated in the His_6-HA-Sumo2 pulldown (Figure 5D), indicating that even at milder cut-off thresholds, SUMOylated substrates identified by mass spectrometry can

be validated in an orthogonal assay. Taken together, these results show that the His_6HA-Sumo2 mouse model is effective to identify SUMOylated proteins, including proteins SUMOylated at relatively low levels *in vivo*, and can be used for targeted studies of protein substrates.

Subcellular Localization of Sumo Interaction in Neurons

Sumo1 and Sumo2 predominantly reside in the nucleus, and unsurprisingly, many of the interactors identified here and in other studies of protein SUMOylation are nuclear proteins. However, previous studies hinted at roles for SUMOylation outside of the nucleus(Hasegawa et al., 2014; Ilic et al., 2022; Wang et al., 2014a; Watanabe et al., 2008; Yang and Paschen, 2015). During the validation of whole brain imaging, we observed that His_6-HA-Sumo2, while extensively localized throughout the nucleus, could also be observed within the somata and synapses of neurons *in vivo*, contrasting the predominantly nuclear membrane staining of His_6-HA-Sumo1 (Figure 2—figure supplement 2; Figure 3). The cytoplasmic localization of His_6-HA-Sumo2 in neurons indicates unique extranuclear roles *in vivo.* Indeed, we identified several predominantly extranuclear proteins via mass spectrometry in the anti-HA affinity purification from the His_6-HA-Sumo2 knock-in mice. To better visualize the subcellular localization of Sumo, we cultured primary cortical neurons from heterozygous His_6-HA-Sumo1, His_6-HASumo2, and WT animals and co-stained them for HA and Map2 as a cytoplasmic marker. As previously observed, Sumo2 is predominantly distributed uniformly throughout the nucleus except for heterochromatic foci, but is also observed at low levels in the cytoplasm (Figure 6—figure supplement 1A), contrasting with the anti-HA immunosignal observed for Sumo1, which predominantly localizes at the nuclear membrane. This indicates that Sumo2 specifically may play a larger role in regulating proteins outside of the nucleus.

To better assess the subcellular localization of neuronal SUMOylated proteins targeted by Sumo2, and to provide an additional level of validation in an orthogonal system, we used proximity ligations assays (PLA) against endogenous Sumo2/3 and targets of Sumo2 identified from our mass spectrometry screen to visualize interactions within wild-type primary cortical neurons (Figure 6A) (Ristic et al., 2016; Sahin et al., 2016). In this

assay, proteins colocalizing within 40 nm will produce a PLA signal suggesting a potential interaction. We selected proteins expected to interact with Sumo2/3 in the nucleus, Gtf2i and Matr3, as well as expected cytoplasmic interactors Rangap1, Ctsd, Alix, and Kars1 for additional validation (Figure 6B & C). Gtf2i is distributed almost exclusively throughout the nucleus and interactions between Sumo2/3 and Gtf2i, inferred by the presence of PLA foci, are seen throughout the nucleoplasm. Interestingly, PLA foci were often observed to cluster around constitutive heterochromatin (Figure 6C, inset), indicating a potential role for Sumo2 in regulating Gtf2i at the periphery of heterochromatin in neurons. Matr3 is also localized throughout the nucleus and to a lesser extent in the cytoplasm, consistent with its identification in cytoplasmic processing bodies (Rajgor et al., 2016). Interestingly, PLA signals for Matr3 and Sumo2/3 are robust, indicating extensive interactions between the two proteins. Immunofluorescence staining of Rangap1, Ctsd, Alix, and Kars1 demonstrate these proteins predominantly reside outside of the nucleus (Figure 6C). PLA between these hits and Sumo2/3 display an increase in the proportion of cytoplasmic foci relative to nuclear foci (Figure 6B), in addition to a substantial decrease in total nuclear PLA foci compared to nuclear localized proteins Gtf2i and Matr3 (Figure 6—figure supplement 1B). Importantly, for all PLA assays conducted, negative controls did not elicit a PLA signal (Figure 6—figure supplement 1C). Taken together, our PLA analyses of wild-type neurons provide an additional layer of validation of Sumo2-substrate interactions. With the added benefit of providing spatial resolution to the interactions, PLA data support a role for neuronal

Sumo2 outside the nucleus.

DISCUSSION

Protein SUMOylation plays a variety of essential and conserved roles (Ilic et al., 2022). Increasing evidence indicates that SUMOylation plays roles in the brain, e.g. in neuronal development or learning and memory(Ripamonti et al., 2020). Furthermore, SUMOylation has been linked with various brain disorders, including Autism Spectrum Disorder,

Epilepsy, Schizophrenia, and neurodegenerative diseases such as Alzheimer's disease, Parkinson's disease, and Amyotrophic Lateral Sclerosis (Bernstock et al., 2018; Krumova and Weishaupt, 2013; Osmanovic et al., 2022; Rousseaux et al., 2016). However, despite a clear connection with neuronal function and dysfunction, SUMOylation has remained

enigmatic due to technical challenges and limitations for studying this modification (Daniel et al., 2017). We generated His_6-HA-Sumo2 and HA-Sumo2 KI mouse alleles to overcome these technical limitations and to provide insight into the role of native SUMOylation *in vivo.* These mice complement the previously generated His_6-HA-Sumo1 mouse line (Tirard et al., 2012), which together enable direct comparisons of Sumo1 and Sumo2 *in vivo* to further understand the specific roles conferred by Sumo2 and native roles of SUMOylation.

Using whole brain imaging against the HA epitope in His_6-HA-Sumo1 and His_6HA-Sumo2 mice, we found that Sumo1 and Sumo2 are broadly distributed throughout the mouse brain. Deeper anatomical analysis revealed clear patterns of Sumo differences across brain structures as well as some divergence of Sumo1 and Sumo2 levels in the brain. Indeed, we observed that levels of His_6-HA-Sumo1 was generally evenly distributed amongst cortical layers, whereas His_6-HA-Sumo2 levels were higher in layers 2/3 (Figure 2—figure supplement 1D). In the hypothalamus, we found that Sumo levels vary across anatomical regions (Figure 2—figure supplement 1E). Interestingly, regions involved in circadian rhythm including the subparaventricular zone (SBPV) and suprachiasmatic nucleus (SCH) show high levels of Sumo2. These findings are consistent with previous reports that have linked both Sumo1 and Sumo2 differentially affecting circadian clock related proteins such as PER2 and CLOCK, ultimately supporting a role for SUMOylation in regulating circadian rhythm processes (Chen et al., 2021; Drunen and Eckel-Mahan, 2021; Lee et al., 2015).

We observed differential subcellular distribution patterns between Sumo1 and Sumo2. Western blot analysis of brain subcellular fractions showed that Sumo2 is more abundantly expressed than Sumo1 (Figure 1), and that Sumo2 conjugates are present outside of the nuclear compartment, including synaptic fractions (Figure 3–figure supplement 1B & C). This is of importance, as the role of Sumo proteins at synapses has been debated, particularly in the context of Sumo1(Daniel et al., 2018; Daniel et al., 2017). We previously showed that Sumo1 conjugates are not present in synaptic compartments, in contrast to several other reports. Here, we used anti-HA immunolabeling of brain material from HA-Sumo2 mouse brains, and used WT littermates as negative controls to assess non-specific anti-HA immunolabeling (Figures 3, 4 and Figure 4–figure

Supplement 1). Strikingly, the quantification of anti-HA immunosignal intensity confirmed a co-localization of Sumo2 with pre- and post-synaptic markers, at both excitatory and inhibitory synapses (Figures 3A-B, 4A-C). This comparative and quantitative approach of investigating the HA-Sumo mouse models allows for the specific assessment of Sumo2 immunosignals within various neuronal sub-compartments, and we provide here the first robust dataset identifying the presence of a Sumo paralog, Sumo2, at synapses in the mammalian brain. These data suggest that Sumo1 and Sumo2 do not only have divergent patterns of expression in mouse brain, but also show differential distributions in the various subcellular compartments, with only Sumo2 present in synapses.

Sumo2 is the only essential Sumo paralog, and has key roles in neurodevelopment, nerve cell function, and neurological diseases(Krumova and Weishaupt, 2013; Ripamonti et al., 2020; Stankova et al., 2018; Wang et al., 2014b). To uncover some of the unique clientele targeted by Sumo2, we performed HA tag immunoprecipitation paired with mass spectrometry. As SUMOylation results in the covalent interaction between Sumo and the target substrate, mouse brains were lysed under denaturing conditions to promote the dissociation of protein complexes prior to immunoprecipitation to help identify bona fide SUMOylation substrates. Using stringent criteria, 75 proteins were identified to potentially interact with Sumo2, ~1/2 of which were selective to Sumo2. Conversely, using the same criteria, we identified 131 proteins that interact with Sumo1, 98 of which were selective to Sumo1. Pathway analysis of the Sumo2 dataset revealed that gene ontology terms related to SUMOylation were significantly enriched in the dataset, validating this method to identify potentially SUMOylated substrates. Moreover, pathway analysis of the Sumo1 dataset revealed enrichment of proteins involved in protein transport consistent with roles for Sumo1 in nucleocytoplasmic shuttling (Pichler et al., 2002; Salinas et al., 2004; Westman et al., 2010). Prox1 was validated via Western blot as one of the strongest interactors specific to Sumo2 in the mouse brain. Interestingly, previous studies demonstrated that SUMOylation of Prox1 by Sumo1 occurs *in vitro* and in cancer cell lines (Pan et al., 2009; Shan et al., 2008). During development, Prox1 was found to be SUMOylated by Sumo1, and this interaction is critical for neurogenesis in the neural tube development. However, the role of Prox1 in the mature brain remains unclear, although some data indicate an

involvement in adult neurogenesis (Correa-Vázquez et al., 2021). Due to the extent of the Prox1 and Sumo2 interaction observed in this study, further analysis may uncover key roles of SUMOylated Prox1 in the adult mouse brain. We further found that the RNA binding protein Matr3 interacts with Sumo2 *in vivo*, indicating that even a mild enrichment over wild-type in our dataset may identify *bona fide* biological interactors. Interestingly, many of the enriched computationally-predicted SUMOylation sites in Matr3 (K588 and K843) reside within a structurally disordered region of the protein that also happens to be enriched for mutations causing Amyotrophic Lateral Sclerosis (ALS) (Johnson et al., 2014). Structurally disordered regions are thought to be critically involved in the formation of protein aggregates in neurodegenerative diseases, and given the key role of SUMO in controlling protein solubility and the recent links between SUMOylation and ALS, SUMOylation of Matr3 may provide key insights into Matr3 biology related to this disease. SUMOylation occurs in a context-specific manner and can regulate protein localization within cells. One of the best characterized examples concerns the regulation of nucleocytoplasmic shuttling across nuclear pore complexes (Pichler et al., 2002; Salinas et al., 2004; Westman et al., 2010). However, SUMOylation can also regulate sub-compartmental localizations, such as protein targeting to the nucleolus or to heterochromatin (Andreev et al., 2022; Mo et al., 2002; Rawat et al., 2021). As Sumo2 was observed throughout the nucleus and outside the nucleus *in vivo* and in cultured neurons, we sought to determine the subcellular localization of Sumo2 interactions with hits identified via IP-MS using a PLA-based approach (Figure 6). Gtf2i was SUMOylated almost exclusively in the nucleus but interestingly appeared to cluster around heterochromatin. Gtf2i can function as both a transcriptional activator and repressor in response to various signals. For example, the specific splice isoforms β and Δ undergo changes in subcellular localization to differentially regulate the immediate early gene *cFos* in response to growth factor signaling(Hakre et al., 2006). However, roles for Gtf2i in regulating heterochromatin remain elusive. SUMOylation may provide a dynamic mechanism in response to neuronal activity to regulate both targeted expression at the gene level and global transcriptional changes(Niskanen et al., 2015). Finally, interactions between Matr3 and Sumo2/3 occurred broadly throughout the nucleus. However, interactions between Matr3 and Sumo2 in mouse brain occurred at relatively low levels

based on immunoprecipitation assays. This discrepancy observed in the nucleus may be explained via non-covalent interactions with Sumo2 through larger protein complexes as Matr3 typically functions in complex with other DNA and RNA binding proteins (Banani et al., 2016; Keiten-Schmitz et al., 2021, Keiten-Schmitz et al., 2020). Extranuclear proteins Rangap1, Ctsd, Alix, and Kars1, despite having a certain level of PLA signal within the nucleus, displayed an increase in the proportion of cytoplasmic PLA foci relative to nuclear PLA foci implying increased interactions with Sumo2/3 outside the nucleus. Indeed, Rangap1 plays roles in nuclear import, but can also be found to some extent within the nucleus (Cha et al., 2015). PLA foci between Rangap1 and Sumo2/3 were often found near the nuclear membrane, likely at nuclear pore complexes (Figure 6C, inset). Ctsd is a lysosomal protease predominantly localizing to lysosomes, thus interactions between Sumo2/3 and Ctsd may suggest that its SUMOylation may play a role in lysosomal metabolism(Nakanishi, 2003). Previous reports have linked Sumo with the apoptosis pathway(Basu-Shrivastava et al., 2022; Besnault-Mascard et al., 2005; Mojsa et al., 2015); here, we observe potential interactions between Sumo and the apoptotic protein Alix further inferring a role for Sumo in the apoptotic process. Finally extranuclear PLA foci could be observed for the lysyl-tRNA Synthetase Kars1, consistent with reports of Sumo interacting with tRNA-related proteins(Chymkowitch et al., 2017; Chymkowitch and Enserink, 2018; Rohira et al., 2013). Together these results suggest that Sumo2 may play a variety of roles outside the nucleus in various subcellular compartments. While PLA assays provide spatial information of putative protein interactions (i.e. interactions occurring within 40 nm), this does not discount indirect interactions (e.g. protein complexes) (Ristic et al., 2016; Sahin et al., 2016). Thus, differentiating between covalent SUMOylation, interactions with SUMO interacting motifs (SIMs), and protein complexes containing Sumo are not possible using this approach. Extensive localization and biochemical analyses, including arginine to lysine mutagenesis to block covalent SUMOylation, should be performed to properly assess how Sumo confers regulation on a specific target throughout the cell.

In sum, the novel (His_6-)HA-Sumo2 knock-in mouse lines described here represent powerful tools to facilitate the study of protein SUMOylation via Sumo2 *in vivo*. The HA epitope tag allows for specific yet versatile modes to detect and capture Sumo2 in its

native context, without altering its function. Furthermore, these mouse models add to the previously generated His_6-HA-Sumo1 allele, and thus expand the Sumo knock-in mouse toolkit to begin exploring differential SUMOylation in parallel systems. The versatility of these models extends to all other tissue systems, as Sumo proteins are broadly distributed beyond the brain (Hendriks et al., 2018; Uhlén et al., 2015). Beyond basic biology, these alleles can be used to explore disease processes, e.g. by crossing these mouse lines into disease models, thus enabling the study of the Sumo-linked disease proteome (Stankova et al., 2018). Ultimately, these tools will advance our understanding of the essential biological processes and potential disease targets regulated by SUMOylation.

MATERIALS AND METHODS

Mouse Husbandry

His_6-HA-Sumo1 and His_6-HA-Sumo2 mice, kept on an FVB/N background, were housed with up to 5 mice per cage on a 12 h light–dark cycle. Mice were fed *ad libitum* and all husbandry was performed by the uOttawa Animal Care and Veterinary Services staff. All animal work for the His_6-HA-Sumo1 and His_6-HA-Sumo2 mouse lines were done under the breeding (CMMb-3009 and CMMb-3904) protocols approved under the uOttawa Animal Care Committee.

All experiments regarding the HA-Sumo2 KI mice were performed in accordance with the guidelines for the welfare of experimental animals issued by the State Government of Lower Saxony, Germany (LAVES). Animals were hosted in a pathogen free facility at the Max Planck Institute of experimental Medicine and were maintained in groups in accordance with European Union Directive 63/2010/EU and ETS 123 (individually ventilated cages, specific pathogen-free conditions, 21 ± 1°C, 55% relative humidity, 12 h/12 h light/dark cycle). Mice received food and tap water *ad libitum* and were provided with bedding and nesting material. Cages were changed once a week. Animal health was controlled daily by caretakers and by a veterinarian. Health monitoring (serological analyses; microbiological, parasitological, and pathological examinations) was done quarterly according to FELASA recommendations with either NMRI sentinel mice or

animals from the colony. The mouse colony used for experiments did not show signs of pathogens. All experiments were performed during a light cycle.

Mouse Genotyping

Genomic DNA (gDNA)was isolated from small tail samples collected from mouse embryos (primary cortical neuron experiments), pups (pre-weaning), or adult mice (endpoint). His_6-HA-Sumo2 mice were genotyped using parallel reactions with primers targeting the *His_6-HA* knock-in tag and corresponding genomic loci upstream (Forward: 5′-AGGAAGAGAGCGAGAGAGGAA-3′, Reverse: 5′-CACCACCACTACCCATACGA-3′, 224bp product) and downstream (Forward: 5′-TCGTATGGGTAGTGGTGGTG-3′, Reverse: 5′-AGGAGGAGGGGTGGTTATGT-3′, 276bp product) of the knock-in. 25µL reactions were prepared using <10ng gDNA, primers (400nM final), 1.25µL DMSO (5% final), and 2X GoTaq (Promega). Thermocycler parameters: 95°C for 2 min, (95°C for 30 s, 57.6°C for 30 s, 72°C for 40 s) repeated for 35 cycles, final denature at 72°C for 5 min. HA-Sumo2 mice were genotyped with primers flanking the *HA* knock-in tag (Forward: 5′-GCCCTCTGCCTCGTCCAC-3′, Reverse: 5′-CCGCCGCGAGCTCACCTTG-3′, WT Allele: 160bp product, KI Allele: 187bp product). 20µL reactions were prepared using 1µL clean gDNA, primers (4 pmol final), and 5X Biozym Hot-Start Taq DNA Polymerase plus extra Mg^{2+} (Biozym 331620XL). Thermocycler parameters: 96°C for 3 min, (94°C for 30 s, 62°C for 60 s, 72°C for 60 s) repeated for 32 cycles, final denature at 72°C for 7 min. His_6-HA-Sumo1 mice were genotyped as previously described (Tirard et al., 2012).

Biochemical Analysis of Adult Mouse Brain and Spinal Cord

Mice were anesthetized using isoflurane inhalation and sacrificed via decapitation. Brains were quickly isolated, dissected for regional protein analysis, and flash frozen on dry ice. Analysis of total Sumo1 and Sumo2/3 levels were performed on whole brain lysates. Spinal cords were removed using hydraulic extrusion(Richner et al., 2017). Samples were thawed and immediately lysed using a dounce homogenizer in RIPA buffer (9.1 mM dibasic sodium phosphate, 1.7 mM monobasic sodium phosphate, 150 mM sodium chloride, 1 % NP-40, 0.5 % sodium deoxycholate, 0.1 % SDS) containing 50 mM freshly

prepared N-Ethylmaleimide (Sigma), 0.25 % β-mercaptoethanol, and Xpert Protease (GenDEPOT) and Xpert Phosphatase (GenDEPOT) inhibitor cocktails. Whole brain lysates were lysed in 11 mL of RIPA buffer described above and centrifuged at 125,000 x g for 2 hours at 4 °C. Regional lysates were centrifuged at 21,000 x *g* for 20 minutes at 4 °C and the supernatant was removed and suspended in 4X laemmli buffer (BioRad) with 2-mercaptaethanol (BioRad) and boiled at 95 °C for 5 minutes. Samples were run on 8 % polyacrylamide gels and transferred onto 0.45µm nitrocellulose membranes at 340 mA for 90 minutes and stained with ponceau to normalize protein levels between lysates. Normalized lysates were run on a 4-15 % GTx Mini-PROTEAN gel (BioRad) and transferred onto a 0.45 µm nitrocellulose membrane at 340 mA for 2 hours for western blot analysis. Densitometry was performed using BioRad Image Lab software and FiJi/ImageJ by normalizing the HA intensity to ponceau for High Molecular Weight (>70 kDa) and free Sumo levels.

Real Time Quantitative PCR (RT-qPCR) analysis

RNA was extracted from mouse brain homogenate using Trizol-Chloroform extraction (Invitrogen™ User Guide: TRIzol Reagent version B.0). Briefly, mouse brains were homogenized in 3 ml of PEPI Buffer [5 mM EDTA, 1X protease inhibitor (GenDEPOT cat# P3100-020), in 1X PBS] using a dounce homogenizer. 3 % of homogenate was added to 1 ml of TRIzol Reagent (Fisher Scientific cat# 15-596-026) and RNA was isolated as per the user guide referenced above. cDNA was synthesized using 5X All-in-One RT Master Mix (Bio Basic cat# HRT025-10) following manufacturer's instructions. RT-qPCR was performed using Green-2-Go qPCR Master Mix (Bio Basic cat# QPCR004-S) with 25 ng cDNA per reaction and primers targeting mouse *Sumo1* (NM_009460.2) (Forward: 5′GCTGATAATCATACTCCGAAAGAAC-3′, Reverse: 5′-CCCCGTTTGTTCCTGATAAA3′), *Sumo2*(NM_133354.2) (Forward: 5′-GGACAGGATGGTTCTGTGGTGC-3′, Reverse: 5′-CCCATCAAACCGGAATCTGATCTGC-3′), and *Hprt1*(NM_013556.2) (Forward: 5′-TGATAGATCCATTCCTATGACTGTAGA-3′, Reverse: 5′-

AAGACATTCTTTCCAGTTAAAGTTGAG-3′). Reactions were run on BioRad CFX96 thermocycler (protocol: 95°C for 5 min, 40 cycles of 95°C for 15 s and 60°C for 60 s, then melting curve). *Sumo1* and *Sumo2* Ct values were standardized to the Ct values of *Hprt1*.

Brain preparation for whole brain clearing and HA immunolabeling.

Mice were sedated via intraperitoneal injection of 16.25 mg sodium pentobarbital (Euthanyl, DIN 00141704). Once sedated, mice were perfused using 10 mL 1X PBS + 10 U/mL heparin (Millipore Sigma, H3393-50KU) followed by 10 mL of freshly prepared 4 % paraformaldehyde. Brains were carefully isolated and stored in 13 mL of 4 % paraformaldehyde at 4 °C overnight with gentle shaking. Brains were rinsed with 1X PBS then shipped to LifeCanvas Technologies (MA) in 1X PBS + 0.02 % sodium azide.

Whole mouse brain processing, staining, and imaging

Whole mouse brains were processed using the SHIELD protocol (LifeCanvas Technologies (Park et al., 2018)). Samples were cleared for 1 day at 42 °C then actively immunolabeled using SmartBatch+ (LifeCanvas Technologies) based on eFLASH technology integrating stochastic electrotransport (Kim et al., 2015) and SWITCH (Murray et al., 2015). Each sample was labeled with 60 µg anti-NeuN (Encor, MCA-1B7) and 36 µg rabbit anti-HA-tag (Cell Signalling Technology #3724) followed by fluorescently conjugated secondary antibodies in a 3:2 primary:secondary molar ratio (Jackson ImmunoResearch). Samples were incubated in EasyIndex (LifeCanvas Technologies) for refractive index of RI = 1.52 and imaged at 3.6X using a SmartSPIM axially-swept light sheet microscope (LifeCanvas Technologies). Images were tile corrected, de-striped, and registered to the Allen Brain Atlas (Allen Institute: https://portal.brain-map.org/). NeuN channels for each brain were registered to 8-20 atlas-aligned reference samples using successive rigid, affine, and b-spline warping (SimpleElastix: https://simpleelastix.github.io/). Average alignment to the atlas was generated across all intermediate reference sample alignments to serve as the final atlas alignment value per sample. Fluorescent measurements from the acquired images were projected onto the Allen Brain Atlas to quantify the total fluorescence intensity per region defined by the Allen

Brain Atlas. These values were then divided by the volume of the corresponding regional volume to calculate the intensity per voxel measurements.

HA Immunoprecipitation from mouse brain lysates

Immunoprecipitation was performed based on the previously established protocol(Tirard et al., 2012; Tirard and Brose, 2016). Briefly, mice aged 9-16 weeks old were anesthetized and sacrificed via decapitation and the brain was quickly removed and homogenized using a dounce homogenizer in RIPA buffer (9.1 mM dibasic sodium phosphate, 1.7 mM monobasic sodium phosphate, 150 mM sodium chloride, 1 % NP-40, 0.5 % sodium deoxycholate, 0.1 % SDS) containing 50 mM freshly prepared N-Ethylmalamide (Sigma), 0.25 % β-mercaptoethanol, and Xpert Protease (GenDEPOT) and Xpert Phosphatase (GenDEPOT) inhibitor cocktails. Samples were lysed on ice for 20 minutes with vigorous vortexing every 5 minutes before ultracentrifugation at an average of 100,000 x *g* for 30 minutes at 4 □C. Supernatants were removed and spiked with 50 mM N-ethylmalamide before being added to 50 µL of magnetic protein G Dynabeads (Invitrogen) preconjugated with 10 µg mouse HA antibody (in house) per sample. Samples were then placed on rotator at 4 □C for 1 hour. Beads were washed three times in 10 mL of RIPA buffer containing 20 mM N-Ethylmalamide, protease, and phosphatase inhibitors. Wash buffer was thoroughly removed, and beads were eluted using 75 µg synthetic HA peptide (Sino Biological Inc.).

Sample Preparation for Mass Spectrometry

Two thirds of eluted protein sample from HA Immunoprecipitation were run on a 4-15% Mini-PROTEAN (Bio-Rad) gel to separate proteins and remove synthetic HA peptide. Samples were stained using Silver Stain for Mass Spectrometry Kit (Thermo Scientific, 24600). Lanes were cut into 6-7 gel slices per sample and stored in 1% acetic acid until analysis via LC-MS/MS.

643 ***Protein Identification by LC-MS/MS***

644 Proteomics analysis was performed at the Ottawa Hospital Research Institute Proteomics
645 Core Facility (Ottawa, Canada). Proteins were digested in-gel using trypsin (Promega)
646 according to the method of Shevchenko (Shevchenko et al., 2006), but without the use of
647 iodoacetamide for cysteine alkylation due to the treatment of 50 mM N-ethylmaleimide
648 (Sigma) during the sample immunoprecipitation. Peptide extracts were concentrated by
649 Vacufuge (Eppendorf). LC-MS/MS was performed using a Dionex Ultimate 3000 RLSC
650 nano HPLC (Thermo Scientific) and Orbitrap Fusion Lumos mass spectrometer (Thermo
651 Scientific). MASCOT software version 2.7.0 (Matrix Science, UK) was used to infer
652 peptide and protein identities from the mass spectra. The observed spectra were matched
653 against *Mus musculus* sequences from SwissProt (version 2021-02) and against an
654 inhouse database of common contaminants. The results were exported to Scaffold
655 (Proteome Software, USA) for further validation and viewing and will be uploaded to the
656 ProteomXchange Consortium.
657

658 ***Gene Ontology analysis***

659 Top His_6-HA-Sumo1 and His_6-HA-Sumo2 interactors were analyzed using gProfiler2 web
660 tool (https://biit.cs.ut.ee/gprofiler/gost)(Peterson et al., 2020). Lists were arranged in
661 descending order based on relative peptide abundance and analyzed as an ordered query
662 for *Mus musculus* proteins using Benjamini-Hochberg FDR significance threshold with an
663 alpha of 0.05.
664
665

666 ***Immunohistochemistry of Mouse Brain***

667 Mice were anesthetized with 30 µl of 120 mg/kg Euthanyl (DIN00141704) and then
668 perfused with 10 ml 1x phosphate buffered saline (PBS) and 10 ml 4 % paraformaldehyde
669 (PFA). Brain and spinal cord tissue were collected and stored for 48 hours in 4 % PFA.
670 Brain and spinal cord tissue were then dehydrated in 10 %, 20 % and 30 % sucrose
671 solutions for 48 hours each before being flash frozen in -40 °C isopentane for 1 minute.
672 Tissues were then sectioned at 20 µm and -21 °C on the Thermo Scientific HM 525 NX
673 cryostat at the Louise Pelletier Histology Core at the University of Ottawa and stored free

floating in 1x PBS + 0.02 % NaN_3 at 4 ^oC until use in staining. Brains tissue were incubated for 24 hours in blocking buffer (1.5 % Triton X-100, 5 % cosmic calf serum in 1X PBS), 24 hours in primary antibody (1:500 HA-Tag C29F4 rabbit monoclonal antibody (Cat: 3724S, Cell Signaling Technology), and 1 hour in secondary antibody (1:500 Alexa Fluor 568 donkey anti mouse antibody, Cat: A10037, Lot: 1917938)) with DAPI (1:1,000 Millipore Sigma, D9542-1MG). Tissue was washed 5 times for 5 minutes each in 1x PBS between each treatment and mounted on Fisherbrand Superfrost Plus slides. Slides were left to dry for 24 hours and covered with DAKO mounting medium (Cat: S3023, Lot: 11347938) and #1.5 coverslips.

For the analysis of the synaptic localization of Sumo2, HA-Sumo2 KI brains were used (Figure 1—figure supplement 1B). Mice were anaesthetized (250 mg/Kg Avertin i.p.) and transcardially perfused with PBS and then with 4 % (w/v) paraformaldehyde (PFA) in 0.1 M phosphate buffer (PB), pH 7.4 at 4 °C for 10 min. Brains were removed and postfixed for 1 h at 4 °C. The tissue was cryoprotected in 30 % (w/v) sucrose in phosphatebuffered saline (PBS). Brains were frozen in the cryostat and sagittal 35 □m sections were prepared with a cryostat and collected free-floating in PBS. For immunohistochemistry, sections were pre-incubated for 24 h in PB containing 3 % horse serum (HS), 3 % fish skin gelatin (FSG), and 0.3 % Triton X-100, and were then incubated for 3 days at 4 °C in primary antibodies diluted in PBS containing 3 % HS, 3 % FSG and 0.3 % Triton X100. After washing repeatedly in PBS and overnight, sections were incubated overnight in dye coupled secondary antibodies, repeatedly washed, and mounted on slides with Aquapolymount (Polysciences). The antibodies used are listed in Table 4.

Primary Cortical Neuron Cultures

Pregnant mice were euthanized between at gestation E14.5-15.5 with 48 mg Pentobarbital Sodium (Bimeda-MTC, 8015E) delivered via intraperitoneal injection. Embryos were removed, washed in chilled PBS (Wisent Bioproducts, 311-010-CL), and cortices were isolated in chilled HBSS (Sigma Aldrich, H9394). Cortices were dissociated for 20 minutes with trypsin (Thermo Scientific, 90305) at 37 □C before adding trypsin inhibitor and DNase solution to quench reaction. Cells were pelleted at 2,500 x *g* for 5

minutes at 4 □C and washed with trypsin inhibitor with DNase solution. Cortical neurons were pelleted at 2,500 x *g* for 5 minutes at 4 □C and resuspended in 1 mL Neurobasal outgrowth media (Thermo Scientific, 21103049), supplemented with B-27 (Thermo Scientific, 17504044), N-2 (Thermo Scientific, 21103049), 500 µM L-Glutamine (Wisent Bioproducts, 609-065-EL), and 0.5 % penicillin/streptomycin (GE Healthcare Life Sciences, SV30010) before plating. Cultures were maintained for 7 days in vitro with a half media change after 3-4 days.

Immunofluorescence in Primary Cortical Neurons

Micro Coverglass #1.5 coverslips (Electron Microscopy Sciences) coverslips were precoated with poly-D-lysine (50 µg/ml) overnight at 37 □C, then washed with distilled water three times and air-dried at room temperature for at least two hours. Primary mouse cortical neurons were seeded at 75,000 cells per coverslip were seeded and cultured as described in Primary Cortical Neuron Cultures. On day 7, neurons were fixed using 10 % phosphate buffered formalin for (Fisher Chemical, SF100-4) for 10 minutes followed by 3 x 5-minute washes in 1 mL of 1X PBS. Neurons were blocked in 500 µL of blocking buffer (1.5 % Triton X-100, 10 % cosmic calf serum in 1X PBS) for 1 hour, then incubated in 300 µL of primary antibody diluted in blocking buffer overnight at 4 °C. The following day, the neurons were washed for 4 x 5-minute washes in 1 mL of 1X PBS then incubated in 300 µL of secondary antibody diluted in blocking buffer for 2 hours at room temperature. Next, the neurons were washed for 4 x 5-minute washes in 1 mL of 1X PBS, dried, and then placed on slides with Vectashield Antifade Mounting Medium with DAPI (MJS Biolynx Inc., H-1200). Z-Stack images were obtained on a Zeiss AxioObserverZ1 LSM800 Confocal Microscope at 63X magnification through a Z distance of 10 µm per image using optimal 0.27 µm spacing per slice. The dimensions were set to 1,024 x 1,024 pixels.

Proximity Ligation Assay in Primary Cortical Neurons

Primary mouse cortical neurons were cultured and fixed as described for immunofluorescence experiments. Individual coverslips for Proximity Ligation Assay experiments (PLA) were transferred to 12-well plates and outlined with a hydrophobic

pen. Neurons were blocked using 40 µL of Duolink blocking buffer (Sigma Aldrich, DUO82007) at 37 °C for 1 hour and were then washed for 3 x 5 minutes washes in 1 mL 1X PBS. Next, the neurons were incubated in 300 µL of primary antibody diluted in blocking buffer (1.5 % Triton X-100, 10 % cosmic calf serum in 1X PBS) overnight at 4 °C. The following day, the neurons were washed for 3 x 5 minutes washes in 1 mL of Duolink Wash Buffer A (0.01 M Tris-Base, 0.15 M NaCl, 0.05 % Tween-20, pH 7.4) followed by incubation in 40 µL of Duolink PLA MINUS (Sigma Aldrich, DUO82004) and PLUS probes (Sigma Aldrich, DUO82002) at 37 °C for 1 hour. Duolink PLA probes were diluted in antibody diluent (Sigma Aldrich, DUO82008) at a 1:5 dilution. Neurons were washed for 3 x 5 minutes washes in Duolink Wash Buffer A and then incubated in 40 µL of ligase (Sigma Aldrich, DUO82027) at 37 °C for 30 minutes. Ligase was diluted in 1X ligation buffer (Sigma Aldrich, DUO82009) at a 1:40 dilution. Neurons were washed for 3 x 5-minute washes in Duolink Wash Buffer A and then incubated in 40 µL of polymerase (Sigma Aldrich, DUO82028) at 37 °C for 90 minutes. Polymerase was diluted in 1X amplification buffer (Sigma Aldrich, DUO82011) at a 1:80 dilution. Then, neurons were washed 2 x 10 minutes in Duolink Wash Buffer B (0.2 M Tris-Base, 0.1 M NaCl, pH 7.5) and then again in 1 mL of Duolink Wash Buffer B diluted at 1:100 for 1 minute. Coverslips were briefly air dried and then mounted on slides using Vectashield Antifade Mounting Medium with DAPI. Z-Stack images were obtained on a Zeiss AxioObserverZ1 LSM800 Confocal Microscope at 63X magnification with a 5X digital zoom through a Z distance of 10 µm per image using optimal 0.27 µm spacing per slice with dimensions set to 512 x 512 pixels. Images were analyzed and quantified using the Spots function on the Imaris (ver. 9.9.1 Bitplane, Switzerland) software. Localization of the foci (nuclear versus cytoplasmic) was determined using the Orthogonal Views function for colocalization with DAPI signal.

Tissue Lysis

Dissected mouse organs were lysed in 1X RIPA buffer (9.1 mM Na_2HPO_4, 1.7 mM NaH_2PO_4, 150 mM NaCl, 1 % NP-40, 0.5 % sodium deoxycholate, 0.1 % SDS, 1X protease inhibitor (GenDEPOT, P3100), 1X phosphatase inhibitor (GenDEPOT, P3200) and 50 mM N-ethylmaleimide (Sigma-Aldrich, E3876-5G) using a Dounce homogenizer.

Tissue lysates were centrifuged at ~21,000 x *g* for 15 minutes at 4°C and the resulting supernatant was transferred into a fresh microcentrifuge tube.

Subcellular fractionation

Western blot analysis of brain subcellular fraction was performed as described previously(Jones and Matus, 1974; Tirard et al., 2012).

Western blot analysis

SDS-PAGE was performed with standard discontinuous gels or with commercially available 4%-12% Bis-Tris gradient gels (Invitrogen). Western blots were probed using primary and secondary antibodies as indicated in Table 4. Blots were routinely developed using enhanced chemiluminescence (GE Healthcare) and imaged using an INTAS ECL Chemostar PLUS Imager HR 6.0. For quantitative Western blotting, transferred proteins were visualized using the total protein stain MemCode (Invitrogen). Western blot signals were visualized using an INTAS ECL Chemostar PLUS Imager HR 6.0 apparatus and quantified using ImageJ, and a ratio of the antibody signal relative to the total protein stain as revealed by the MemCode was performed.

Confocal Imaging and Image analysis

MAP2, HA-Sumo2, DAPI and the respective synaptic marker fluorescence intensities were acquired from the hippocampal CA3 pyramidal layer and the *stratum radiatum*. In particular, multi-channel z-stacks of 354 x 354 µm-sized fields of view were acquired with a 40x oil immersion objective (1.4 NA) of a Nikon Ti, Yokogawa W1 spinning disk microscope with Andor iXon Ultra 888 EMCCD camera. A custom macro written within the FIJI software package (Schindelin et al., 2012) automatically identified the z-plane of highest HA-Sumo2 intensity, out of which all channels were extracted. The DAPI, MAP2 and synaptic marker channel of this z-plane were segmented with the Trainable WEKA Segmentation FIJI plugin (Arganda-Carreras et al., 2017), resulting in binary masks (Figure 3A, bottom row) that were subsequently used to extract the respective HA-Sumo2 mean intensity.

To more closely investigate HA-Sumo2 colocalization with the respective synaptic markers, high-resolution, multi-channel fields of view (x, y: 30, 30 µm) of the respective

stains within the Mossy fiber region were acquired using 63x oil-immersed objective (NA=1.4) on a Leica SP8 confocal laser scanning microscope. Oversampled (x, y, z: 30, 30, 100 nm), 1.2 µm-sized z-stacks within the mossy fiber region were acquired for each fluorescent channel. Signal to noise ratio and resolution were subsequently enhanced and sample geometry was corrected with the SVI Huygens deconvolution software package (ver. 22.04, Hilversum, Netherlands). To obtain object-based colocalization information, an Imaris (ver. 9.9.1 Bitplane, Switzerland) batch process was created to automatically process all three-dimensional fields-of-view identically. All HA-Sumo2 and the respective synaptic marker objects were created, yielding the total object number for the respective stain. Synaptic marker objects were designated as collocating with the HASumo2 objects only if they overlapped with HA-Sumo2 objects and if they contained a minimum HA-Sumo2 average intensity. Data resulting from both analysis workflows was assembled and quantified with the KNIME software package (ver. 4.5.2, Zurich, Switzerland).

Statistical Analysis

Statistical tests were performed using PRISM 9.4. Test type was picked based on the number of comparisons made. Levels of statistical significance are indicated in figure legends.

Figure Legends

Figure 1: HA-epitope knock-in enables direct comparisons of differential levels of Sumo1 and Sumo2 and their conjugates in the murine central nervous system.

Western blot analysis of various regions of His_6-HA-Sumo1 and His_6-HA-Sumo2 mouse central nervous system. Brain regions highlighted in the schematic (Top Left) were dissected for protein extraction and analyzed by Western blot using anti-HA antibody. HA signal corresponding to SUMOylated protein (bracket on the left side of the top left panel, HMW: High Molecular Weight) was normalized to ponceau (right top panel) and quantified via densitometry (bottom panels), N=3.

Figure 1—figure supplement 1: Heterozygous His_6-HA-Sumo2 and His_6-HA-Sumo1 mice exhibit normal Sumo levels.

(A). Schematic of His_6-HA-Sumo2 and HA-Sumo2 knock in mice. (B). Anti-Sumo2/3 Western blot analysis of total brain homogenates from heterozygous His_6-HA-Sumo1, His_6-HA-Sumo2 mice and WT controls. Anti-Sumo2/3 signal (bracket on the right side of the top left panel) was analyzed by densitometry. Signal from either heterozygous His_6HA-Sumo1 or His_6-HA-Sumo2 mice was normalized to the Gapdh signal and is relative to WT controls (right panel), N=4. (C). Anti-Sumo1 Western blot analysis of total brain homogenates from heterozygous His_6-HA-Sumo1, His_6-HA-Sumo2 mice and WT controls. Anti-Sumo1 signal (bracket on the right side of the top left panel) was analyzed by densitometry. Signal from heterozygous His_6-HA-Sumo1 and His_6-HA-Sumo2 mice was normalized to the Gapdh signal (bottom left panel) and is relative to WT controls (right panel), N=4. (D). RT-qPCR analysis of *Sumo1* and *Sumo2* transcript levels in whole brain from heterozygous His_6-HA-Sumo1, His_6-HA-Sumo2 mice and WT controls. *Sumo1* and *Sumo2* transcript levels were normalized to *Hprt1* as a housekeeping control. All statistical tests were analyzed using an ordinary One Way ANOVA with Tukeys multiple comparisons tests.

Figure 2: Whole brain imaging reveals the topographical distribution of Sumo paralogs. (A). Schematic of brain clearing and light sheet microscopy for whole brain imaging with a 3D Imaris render of a His_6-HA-Sumo2 brain. (B). Heatmaps of anti-HA immunosignal intensity normalized to regional density quantified by NeuN staining and alignment to the Allen Brain Atlas across the His_6-HA-Sumo2 KI depicted brain region, averaged between hemibrains and biological replicates (N=2, two hemispheres). (C). Bar plot depicting the relative levels of anti-HA immunosignal per voxel averaged across across His_6-HASumo2 brain regions defined by the Allen Brain Atlas. (D). Heatmaps of anti-HA immunosignal intensity normalized to regional density quantified by NeuN staining and alignment to the Allen Brain Atlas across the His_6-HA-Sumo1 KI depicted brain region, averaged between hemibrains and biological replicates (N=2, two hemispheres). (E). Bar plot depicting the relative levels of anti-HA immunosignal intensity normalized to regional density across

857 His_6-HA-Sumo1 brain regions defined by the Allen Brain Atlas. Each datapoint in (C) and
858 (D) is from the mean intensity from a single hemisphere (N=2, two hemispheres).
859
860 Figure 2—figure supplement 1: Detailed examination of regional anatomical Sumo
861 paralog distribution.
862 (A). Bar plot depicting the relative levels of anti-HA immunosignal in the regions of His_6HA-
863 Sumo2 hippocampus. Each datapoint is the mean intensity from a single hemisphere
864 (N=2, two hemispheres). Middle and Left panels depict a representative image and zoom
865 of the hippocampal formation overlayed with a mask depicting anatomical regions defined
866 by the Allen Brain Atlas. Scale Bar: 1000 μm. (B). Bar plot depicting the relative levels of
867 anti-HA immunosignal across His_6-HA-Sumo1brain regions. Middle and Left panels depict
868 a representative image and zoom of the hippocampal formation overlayed with a mask
869 depicting anatomical regions defined by the Allen Brain Atlas. Scale Bar: 1000 μm. (C).
870 Bar plot depicting relative anti-HA immunosignal levels in the primary somatosensory
871 area–mouth (SSp-m) layers of His_6-HA-Sumo1 (Top) and His_6-HA-Sumo2 (Bottom) brain
872 (D). Bar plot depicting relative anti-HA immunosignal levels in regions of the
873 hypothalamus of His_6-HA-Sumo1 (Top) and His_6-HA-Sumo2 (Bottom). Each datapoint
874 from the brain atlases depict the mean intensity from a single hemisphere (N=2, two
875 hemispheres). For each abbreviated brain region, refer to Table 1 for legend.
876
877 Figure 2—figure supplement 2: Sumo1 and Sumo2 share similar and distinct anatomical
878 locations and subcellular compartments.
879 Confocal microscopy analysis of anti-HA (red) and DAPI (blue) nuclear labeling of
880 wildtype (untagged, top lane), His_6-HA-Sumo1 (middle lane) and His_6-HA-Sumo2 KI
881 (bottom lane) cortex layer 2/3, cerebellum, and hippocampal CA1 and CA3 regions. Z-
882 projection images are representative of three independent replicates. Scale bar: 50 μm
883
884 Figure 2—figure supplement video 1: Imaris 3D render of anti-HA immunosignal in whole
885 His_6-HA-Sumo1 brain. Scale bar: 3000 μm
886

Figure 2—figure supplement video 2: Imaris 3D render of anti-HA immunosignal in whole His_6-HA-Sumo2 brain. Scale bar: 3000 µm

Figure 3: Extra-nuclear localization of Sumo2 in neurons of the hippocampal CA3 region. (A). Anti-HA (purple), DAPI (blue), MAP2 (red), and anti-Shank2 (green) immunostaining of wild-type (left) and HA-Sumo2 KI (right) hippocampal CA3 region. Scale bar: 50 □m. (B) Anti-HA signal in masked regions for each marker (exemplified for Shank2 in the bottom panel A) was quantified in both wild-type (WT) and HA-Sumo2 KI, and average intensity was calculated. N=3, *p<0.05, **p<0.005, ***p<0,0005, ****p<0,0001.

Figure 3–figure supplement 1: Differential levels and sub-cellular distribution of Sumo1 and Sumo2 conjugates in whole mouse brain fractions.
(A). Total Protein stain (left panel) and anti-HA Western blot (right panel) analysis of whole brain lysates from homozygous HA-Sumo2 and corresponding WT littermates. The black bar on the right indicates Sumo2 signal used for the quantification shown by the dot plot (right panel).
(B and C). Total protein stain (right panel) and anti-HA (left panel) Western blot analysis of subcellular fractions from homozygous His_6-HA-Sumo1 (B) and HA-Sumo2 KI (C). Western blot analysis using anti-Synaptophysin and PSD95 (bottom panels) validates the subcellular fractionation procedure. The black line between the HA panel indicates that different exposure times are depicted, as the HA signal in the P1 fraction saturates faster than in the other fractions. The black line on the right of the HA panels indicate the Sumo signal used for quantification in E. H, homogenate; P1, nuclear pellet S1; supernatant after P1 sedimentation; P2, crude synaptosomal pellet; S2, supernatant after P2 sedimentantion; P3, pellet after ultracentrifugation of the S2, cytosolic pellet; S3, supernatant after P3 sedimentation; LP1, lysed synaptosomal membranes; LS1, supernatant after LP1 sedimentation; LP2, pellet after sedimentation of the LS1; LS2, supernatant after LP2 sedimentation; SPM, synaptic plasma membranes. (D). Bar plot depicting the quantification of anti-HA signal as indicated by the black line on the right side of each anti-HA Western blot in C and D, relative to the total protein stain.

Figure 4: Sumo2 localizes at synapses *in vivo*.

(A). High magnification images of wild-type (left) and HA-Sumo2 KI (right) hippocampal CA3 region labelled with anti-HA (purple), DAPI (blue), MAP2 (red), and synaptic markers (green) Shank2, Gephyrin, Synapsin1, vGlut1 and vGAT1. Scale bar, 10 □m. (B). High magnification images with equally scaled anti-HA intensity corresponding to the insets (white boxes) in A showing anti-HA (purple) immunostaining of wild-type (left) and HASumo2 KI (right) hippocampal CA3 region immunolabelled with the synaptic markers (green) Shank2, Gephyrin, Synapsin1, vGLUT1 and vGAT1. Scale bar: 5 □m. N=3. (C). The percentage of co-localization between each synaptic marker and the anti-HA signal was quantified in both wild-type (WT) and HA-Sumo2 KI. N=3, *p<0.05, **p<0.005, ****p<0,0001.

Figure 4–figure supplement 1: Imaris-based representation of the synaptic Sumo2 colocalization with Shank2 and Synapsin1.

Blended representation generated in Imaris using images from Figure 4B and depicting the colocalization between HA-Sumo2 and Shank2 (top panels) and Synapsin 1 (bottom panels). The right panels include the MAP2 (grey) immunolabeling. Scale bar: 5 □m.

Figure 5: Neuronal Sumo2 has shared and distinct substrates compared to Sumo1 *in vivo.*

(A). Schematic of approach to identify His_6-HA-Sumo interactors from the adult mouse brain via anti-HA affinity immunoprecipitation and mass spectrometry (N=4). (B). Heat map depicting the relative peptide abundance of His_6-HA-Sumo2 interactors relative to levels in His_6-HA-Sumo1 immunoprecipitation. (C). gProfiler2 Gene Ontology analysis for His_6-HA-Sumo2 interactors. (D). Anti-HA affinity Immunoprecipitation followed by Western Blot analysis of His_6-HA-Sumo1 and His_6-HA-Sumo2 interactors as listed on the left side (N=3-6). Black arrowheads indicate protein SUMOylation inferred by shift in molecular weight.

Figure 5—figure supplement 1: Neuronal Sumo1 has shared and distinct substrates compared to Sumo2 *in vivo.*

(A). Anti-HA Western blot analysis of eluates from anti-HA affinity immunoprecipitation (IP: HA) from WT, His_6-HA-Sumo1, and His_6-HA-Sumo2 mouse brain lysates demonstrating HA signal patterns of Sumo1 and Sumo2 and their corresponding conjugates (B). Heat map depicting the relative peptide abundance of His_6-HA-Sumo1 interactors relative to levels in His_6-HA-Sumo2 immunoprecipitation. (C). gProfiler2 Gene Ontology analysis for His_6-HA-Sumo1 interactors. (D). Venn diagram depicting unique and common His_6-HA-Sumo1 and His_6-HA-Sumo2 interactors.

Figure 6: Established and newly identified Sumo2 substrates are present both in nuclear and extranuclear compartments in neurons.
(A). Schematic of the proximity ligation assay (PLA) strategy for native Sumo2/3 and target proteins in WT primary cortical neurons. (B). The relative proportion of PLA foci between the selected target proteins and Sumo2/3 was quantified and normalized within the nucleus (grey) versus outside of the nucleus (red) (N=3). (C) Representative Zprojected immunofluorescent images and PLA assays for selected target proteins identified from the mass spectrometry screen (N=3). White arrowheads indicate cytoplasmic PLA foci. Scale bar: 10 μm.

Figure 6—figure supplement 1: Localization of Sumo2 to extranuclear compartments and proof of PLA assay specificity.
(A). Confocal microscopy analysis of anti-Map2 (purple) and anti-HA (grey) immunolabeling of WT (top lanes), His_6-HA-Sumo1 (middle lanes), and His_6-HA-Sumo2 primary cortical neurons (bottom lanes). Scale bar: 10 μm. N=3 (B). Bar plot depicting the total number of nuclear (left plot) and cytoplasmic (right plot) PLA foci for the indicated antibody (N=3). Data are presented as a mean ± S.E.M. (C). Representative Z-projected images of proximity ligation assays performed with only a single antibody (indicated on top, top lanes) merged with DAPI (bottom panels). Scale bar: 10 μm.

ACKNOWLEDGEMENTS

This research was supported in part by an NSERC Discovery Grant and Discovery

Launch Supplement to M.W.C.R. (RGPIN-2019-04133 and DGECR-2019-00369); the Canada Research Chairs program to M.W.C.R; Quantitative Synaptology SFB1286/A09 to N.B. and M.T.; the ALS Society of Canada in partnership with the Brain Canada Foundation through the Brain Canada Research Fund, with the financial support of Health Canada, for financial support through the ALS Trainee Award Program 2019 (T.R.S.); an NSERC Undergraduates Student Research Award to T.T.N.; the Ontario Graduate Scholarship (H.M.G.), the Queen Elizabeth II Scholarship (H.M.G.) and a CIHR Canadian Graduate Scholarship (H.M.G.). M.W.C.R. thanks H.Y. Zoghbi (Baylor College of Medicine, HHMI) for initial project discussions, reagent development and the freedom to explore new ideas. The authors also thank all members of the Rousseaux, Brose, and Zoghbi labs for important discussions and critical feedback on the manuscript. The authors also thank the following Core facilities from the University of Ottawa and the Ottawa Hospital Research Institute (OHRI) for use of their facility, equipment, and expertise: the Cell Biology and Imaging Acquisition Core and the OHRI Proteomics Core. The authors also thank the Genome Engineered Rodent Models Core at Baylor College of Medicine and Animal Care and Veterinary Service. Figures 1, 2, 5 and 6 were generated in part with Biorender.com. The views expressed herein do not necessarily represent the views of the Minister of Health or the Government of Canada.

COMPETING INTERESTS

The authors have no competing interests to declare.

REFERENCES

Andreev VI, Yu C, Wang J, Schnabl J, Tirian L, Gehre M, Handler D, Duchek P, Novatchkova M, Baumgartner L, Meixner K, Sienski G, Patel DJ, Brennecke J. 2022. Panoramix SUMOylation on chromatin connects the piRNA pathway to the cellular heterochromatin machinery. *Nat Struct Mol Biol* **29**:130–142. doi:10.1038/S41594-022-00721-X

Banani SF, Rice AM, Peeples WB, Lin Y, Jain S, Parker R, Rosen MK. 2016. Compositional Control of Phase-Separated Cellular Bodies. *Cell* **166**:651–663. doi:10.1016/J.CELL.2016.06.010

Basu-Shrivastava M, Mojsa B, Mora S, Robbins I, Bossis G, Lassot I, Desagher S. 2022. Trim39 regulates neuronal apoptosis by acting as a SUMO-targeted E3 ubiquitin-ligase for the transcription factor NFATc3. *Cell Death Differ*.

doi:10.1038/S41418-022-01002-2
Bernstock JD, Yang W, Ye DG, Shen Y, Pluchino S, Lee YJ, Hallenbeck JM, Paschen W. 2018. SUMOylation in brain ischemia: Patterns, targets, and translational implications. *J Cereb Blood Flow Metab* **38**:5–16. doi:10.1177/0271678X17742260
Besnault-Mascard L, Leprince C, Auffredou MT, Meunier B, Bourgeade MF, Camonis J, Lorenzo HK, Vazquez A. 2005. Caspase-8 sumoylation is associated with nuclear localization. *Oncogene* **24**:3268–3273. doi:10.1038/SJ.ONC.1208448
Bohren KM, Nadkarni V, Song JH, Gabbay KH, Owerbach D. 2004. A M55V polymorphism in a novel SUMO gene (SUMO-4) differentially activates heat shock transcription factors and is associated with susceptibility to type I diabetes mellitus. *Journal of Biological Chemistry* **279**:27233–27238. doi:10.1074/jbc.M402273200
Bouchard D, Wang W, Yang WC, He S, Garcia A, Matunis MJ. 2021. SUMO paralogue–specific functions revealed through systematic analysis of human knockout cell lines and gene expression data. *Mol Biol Cell* **32**:1849. doi:10.1091/MBC.E21-01-0031
Celen AB, Sahin U. 2020. Sumoylation on its 25th anniversary: mechanisms, pathology, and emerging concepts. *FEBS Journal*. doi:10.1111/febs.15319
Cha K, Sen P, Raghunayakula S, Zhang XD. 2015. The Cellular Distribution of RanGAP1 Is Regulated by CRM1-Mediated Nuclear Export in Mammalian Cells. *PLoS One* **10**. doi:10.1371/JOURNAL.PONE.0141309
Chen LC, Hsieh YL, Tan GYT, Kuo TY, Chou YC, Hsu PH, Hwang-Verslues WW. 2021. Differential effects of SUMO1 and SUMO2 on circadian protein PER2 stability and function. *Sci Rep* **11**. doi:10.1038/S41598-021-93933-Y
Chu Y, Yang X. 2011. SUMO E3 ligase activity of TRIM proteins. *Oncogene* **30**:1108–1116. doi:10.1038/onc.2010.462
Chymkowitch P, Enserink JM. 2018. Regulation of tRNA synthesis by posttranslational modifications of RNA polymerase III subunits. *Biochim Biophys Acta Gene Regul Mech* **1861**:310–319. doi:10.1016/J.BBAGRM.2017.11.001
Chymkowitch P, Nguéa P A, Aanes H, Robertson J, Klungland A, Enserink JM. 2017. TORC1-dependent sumoylation of Rpc82 promotes RNA polymerase III assembly and activity. *Proc Natl Acad Sci U S A* **114**:1039–1044. doi:10.1073/PNAS.1615093114
Citro S, Chiocca S. 2013. Sumo paralogs: Redundancy and divergencies. *Frontiers in Bioscience - Scholar* **5 S**:544–553. doi:10.2741/S388/PDF
Correa-Vázquez JF, Juárez-Vicente F, García-Gutiérrez P, Barysch S v., Melchior F, García-Domínguez M. 2021. The Sumo proteome of proliferating and neuronaldifferentiating cells reveals Utf1 among key Sumo targets involved in neurogenesis. *Cell Death & Disease 2021 12:4* **12**:1–14. doi:10.1038/s41419-021-03590-2
Daniel JA, Cooper BH, Palvimo JJ, Zhang FP, Brose N, Tirard M. 2018. Response: Commentary: Analysis of SUMO1-conjugation at synapses. *Front Cell Neurosci* **12**:117. doi:10.3389/FNCEL.2018.00117/BIBTEX
Daniel James A., Cooper BH, Palvimo JJ, Zhang FP, Brose N, Tirard M. 2017. Analysis of SUMO1-conjugation at synapses. *Elife* **6**. doi:10.7554/ELIFE.26338

Daniel James A, Cooper BH, Palvimo JJ, Zhang F-P, Brose N, Tirard M. 2017. Analysis of SUMO1-conjugation at synapses. *Elife* **6**. doi:10.7554/eLife.26338

Desterro JMP, Thomson J, Hay RT. 1997. Ubch9 conjugates SUMO but not ubiquitin. *FEBS Lett* **417**:297–300. doi:10.1016/S0014-5793(97)01305-7

Drunen R van, Eckel-Mahan K. 2021. Circadian Rhythms of the Hypothalamus: From Function to Physiology. doi:10.3390/clockssleep3010012

Feldmeyer D. 2012. Excitatory neuronal connectivity in the barrel cortex. *Front Neuroanat* **0**:24. doi:10.3389/FNANA.2012.00024/BIBTEX

Gareau JR, Reverter D, Lima CD. 2012. Determinants of small ubiquitin-like modifier 1 (SUMO1) protein specificity, E3 ligase, and SUMO-RanGAP1 binding activities of nucleoporin RanBP2. *J Biol Chem* **287**:4740–4751. doi:10.1074/JBC.M111.321141

Garvin AJ, Lanz AJ, Morris JR. 2022. SUMO monoclonal antibodies vary in sensitivity, specificity, and ability to detect SUMO conjugate types. *bioRxiv*. doi:10.1101/2022.03.19.484974

Geiss-Friedlander R, Melchior F. 2007. Concepts in sumoylation: a decade on. *Nat Rev Mol Cell Biol* **8**:947–956. doi:10.1038/NRM2293

Gong L, Kamitani T, Fujise K, Caskey LS, Yeh ETH. 1997. Preferential interaction of sentrin with a ubiquitin-conjugating enzyme, Ubc9. *Journal of Biological Chemistry* **272**:28198–28201. doi:10.1074/jbc.272.45.28198

Gong L, Li B, Millas S, Yeh ETH. 1999. Molecular cloning and characterization of human AOS1 and UBA2, components of the sentrin-activating enzyme complex. *FEBS Lett* **448**:185–189. doi:10.1016/S0014-5793(99)00367-1

Hakre S, Tussie-Luna MI, Ashworth T, Novina CD, Settleman J, Sharp PA, Roy AL. 2006. Opposing functions of TFII-I spliced isoforms in growth factor-induced gene expression. *Mol Cell* **24**:301–308. doi:10.1016/J.MOLCEL.2006.09.005

Hasegawa Y, Yoshida D, Nakamura Y, Sakakibara SI. 2014. Spatiotemporal distribution of SUMOylation components during mouse brain development. *Journal of Comparative Neurology* **522**:3020–3036. doi:10.1002/CNE.23563

Hendriks IA, Lyon D, Su D, Skotte NH, Daniel JA, Jensen LJ, Nielsen ML. 2018. Sitespecific characterization of endogenous SUMOylation across species and organs. *Nature Communications 2018 9:1* **9**:1–17. doi:10.1038/s41467-018-04957-4

Hendriks IA, Vertegaal ACO. 2016. A comprehensive compilation of SUMO proteomics. *Nat Rev Mol Cell Biol* **17**:581–595. doi:10.1038/nrm.2016.81

Hendriks IA, Vertegaal ACO. 2015. SUMO in the DNA damage response. *Oncotarget* **6**:15734–15735. doi:10.18632/ONCOTARGET.4605

Ilic D, Magnussen HM, Tirard M. 2022. Stress - Regulation of SUMO conjugation and of other Ubiquitin-Like Modifiers. *Semin Cell Dev Biol*. doi:10.1016/j.semcdb.2021.12.010

Johnson ES, Blobel G. 1997. Ubc9p is the conjugating enzyme for the ubiquitin-like protein Smt3p. *Journal of Biological Chemistry* **272**:26799–26802. doi:10.1074/jbc.272.43.26799

Johnson JO, Pioro EP, Boehringer A, Chia R, Feit H, Renton AE, Pliner HA, Abramzon Y, Marangi G, Winborn BJ, Gibbs JR, Nalls MA, Morgan S, Shoai M, Hardy J,

Pittman A, Orrell RW, Malaspina A, Sidle KC, Fratta P, Harms MB, Baloh RH, Pestronk A, Weihl CC, Rogaeva E, Zinman L, Drory VE, Borghero G, Mora G, Calvo A, Rothstein JD, Drepper C, Sendtner M, Singleton AB, Taylor JP, Cookson MR, Restagno G, Sabatelli M, Bowser R, Chio` A, Traynor BJ, Moglia C, Cammarosano S, Canosa A, Gallo S, Brunetti M, Ossola I, Marinou K, Papetti L, Pisano F, Pinter GL, Conte A, Luigetti M, Zollino M, Lattante S, Marangi G, la Bella V, Spataro R, Colletti T, Battistini S, Ricci C, Caponnetto C, Mancardi G, Mandich P, Salvi F, Bartolomei I, Mandrioli J, Sola P, Lunetta C, Penco S, Monsurr MR, Conforti FL, Tedeschi G, Gambardella A, Quattrone A, Volanti P, Floris G, Cannas A, Piras V, Marrosu F, Marrosu MG, Murru MR, Pugliatti M, Parish LD, Sotgiu A, Solinas G, Ulgheri L, Ticca A, Simone I, Logroscino G, Pirisi A. 2014. Mutations in the Matrin 3 gene cause familial amyotrophic lateral sclerosis. *Nat Neurosci* **17**:664–666. doi:10.1038/NN.3688

Jones DH, Matus AI. 1974. Isolation of synaptic plasma membrane from brain by combined flotation-sedimentation density gradient centrifugation. *Biochim Biophys Acta* **356**:276–87. doi:10.1016/0005-2736(74)90268-5

Keiten-Schmitz J, Röder L, Hornstein E, Müller-McNicoll M, Müller S. 2021. SUMO: Glue or Solvent for Phase-Separated Ribonucleoprotein Complexes and Molecular Condensates? *Front Mol Biosci* **8**. doi:10.3389/FMOLB.2021.673038

Keiten-Schmitz J, Wagner K, Piller T, Kaulich M, Alberti S, Müller S. 2020. The Nuclear SUMO-Targeted Ubiquitin Quality Control Network Regulates the Dynamics of Cytoplasmic Stress Granules. *Mol Cell* **79**:54-67.e7. doi:10.1016/J.MOLCEL.2020.05.017

Kim SY, Cho JH, Murray E, Bakh N, Choi H, Ohn K, Ruelas L, Hubbert A, McCue M, Vassallo SL, Keller PJ, Chung K. 2015. Stochastic electrotransport selectively enhances the transport of highly electromobile molecules. *Proc Natl Acad Sci U S A* **112**:E6274–E6283. doi:10.1073/PNAS.1510133112/SUPPL_FILE/PNAS.1510133112.SM05.AVI

Krumova P, Weishaupt JH. 2013. Sumoylation in neurodegenerative diseases. *Cell Mol Life Sci* **70**:2123–2138. doi:10.1007/S00018-012-1158-3

Lavado A, Lagutin O v., Chow LML, Baker SJ, Oliver G. 2010. Prox1 is required for granule cell maturation and intermediate progenitor maintenance during brain neurogenesis. *PLoS Biol* **8**:43–44. doi:10.1371/JOURNAL.PBIO.1000460

Lee GW, Melchior F, Matunis MJ, Mahajan R, Tian Q, Anderson P. 1998. Modification of Ran GTPpase-activating protein by the small ubiquitin- related modifier SUMO-1 requires Ubc9, an E2-type ubiquitin-conjugating enzyme homologue. *Journal of Biological Chemistry* **273**:6503–6507. doi:10.1074/jbc.273.11.6503

Lee Y, Chun SK, Kim K. 2015. Sumoylation controls CLOCK-BMAL1-mediated clock resetting via CBP recruitment in nuclear transcriptional foci. *Biochimica et Biophysica Acta (BBA) - Molecular Cell Research* **1853**:2697–2708. doi:10.1016/J.BBAMCR.2015.07.005

Liang Q, Deng H, Li X, Wu X, Tang Q, Chang T-H, Peng H, Rauscher FJ, Ozato K, Zhu F. 2011. Tripartite Motif-Containing Protein 28 Is a Small Ubiquitin-Related Modifier E3 Ligase and Negative Regulator of IFN Regulatory Factor 7. *The Journal of Immunology* **187**:4754–4763. doi:10.4049/jimmunol.1101704

Mahajan R, Delphin C, Guan T, Gerace L, Melchior F. 1997. A small ubiquitin-related polypeptide involved in targeting RanGAP1 to nuclear pore complex protein RanBP2. *Cell* **88**:97–107. doi:10.1016/S0092-8674(00)81862-0

Matunis MJ, Coutavas E, Blobel G. 1996. A novel ubiquitin-like modification modulates the partitioning of the Ran-GTPase-activating protein RanGAP1 between the cytosol and the nuclear pore complex. *Journal of Cell Biology* **135**:1457–1470. doi:10.1083/JCB.135.6.1457

Mo YY, Yu Y, Shen Z, Beck WT. 2002. Nucleolar delocalization of human topoisomerase I in response to topotecan correlates with sumoylation of the protein. *J Biol Chem* **277**:2958–2964. doi:10.1074/JBC.M108263200

Mojsa B, Mora S, Bossowski JP, Lassot I, Desagher S. 2015. Control of neuronal apoptosis by reciprocal regulation of NFATc3 and Trim17. *Cell Death Differ* **22**:274–286. doi:10.1038/CDD.2014.141

Murray E, Cho JH, Goodwin D, Ku T, Swaney J, Kim S-Y, Choi H, Park Y-G, Park J-Y, Hubbert A, McCue M, Vassallo S, Bakh N, Frosch MP, Wedeen VJ, Seung HS, Chung K. 2015. Simple, Scalable Proteomic Imaging for High-Dimensional Profiling of Intact Systems. *Cell* **163**:1500–1514. doi:10.1016/j.cell.2015.11.025

Nakanishi H. 2003. Neuronal and microglial cathepsins in aging and age-related diseases. *Ageing Res Rev* **2**:367–381. doi:10.1016/S1568-1637(03)00027-8

Nayak A, Müller S. 2014. SUMO-specific proteases/isopeptidases: SENPs and beyond 1–7. doi:10.1186/s13059-014-0422-2

Niskanen EA, Malinen M, Sutinen P, Toropainen S, Paakinaho V, Vihervaara A, Joutsen J, Kaikkonen MU, Sistonen L, Palvimo JJ. 2015. Global SUMOylation on active chromatin is an acute heat stress response restricting transcription. *Genome Biol* **16**:1–19. doi:10.1186/S13059-015-0717-Y/FIGURES/8

Osmanovic A, Förster A, Widjaja M, Auber B, Anibh ·, Das M, Christians A, Brand · Frank, Petri S, Weber RG. 2022. A SUMO4 initiator codon variant in amyotrophic lateral sclerosis reduces SUMO4 expression and alters stress granule dynamics. *Journal of Neurology 2022* **1**:1–9. doi:10.1007/S00415-022-11126-7

Pan MR, Chang TM, Chang HC, Su JL, Wang HW, Hung WC. 2009. Sumoylation of Prox1 controls its ability to induce VEGFR3 expression and lymphatic phenotypes in endothelial cells. *J Cell Sci* **122**:3358–3364. doi:10.1242/JCS.050005

Park YG, Sohn CH, Chen R, McCue M, Yun DH, Drummond GT, Ku T, Evans NB, Oak HC, Trieu W, Choi H, Jin X, Lilascharoen V, Wang J, Truttmann MC, Qi HW, Ploegh HL, Golub TR, Chen SC, Frosch MP, Kulik HJ, Lim BK, Chung K. 2018. Protection of tissue physicochemical properties using polyfunctional crosslinkers. *Nature Biotechnology 2018 37:1* **37**:73–83. doi:10.1038/nbt.4281

Peterson H, Kolberg L, Raudvere U, Kuzmin I, Vilo J. 2020. gprofiler2 -- an R package for gene list functional enrichment analysis and namespace conversion toolset g: Profiler. *F1000Res* **9**. doi:10.12688/F1000RESEARCH.24956.2/DOI

Pichler A, Gast A, Seeler JS, Dejean A, Melchior F. 2002. The nucleoporin RanBP2 has SUMO1 E3 ligase activity. *Cell* **108**:109–120. doi:10.1016/S0092-8674(01)00633-X

Rajgor D, Hanley JG, Shanahan CM. 2016. Identification of novel nesprin-1 binding partners and cytoplasmic matrin-3 in processing bodies. *Mol Biol Cell* **27**:3894–3902. doi:10.1091/MBC.E16-06-0346

Rawat P, Boehning M, Hummel B, Aprile-Garcia F, Pandit AS, Eisenhardt N, Khavaran A, Niskanen E, Vos SM, Palvimo JJ, Pichler A, Cramer P, Sawarkar R. 2021. Stress-induced nuclear condensation of NELF drives transcriptional downregulation. *Mol Cell* **81**:1013-1026.e11. doi:10.1016/J.MOLCEL.2021.01.016

Richner M, Jager SB, Siupka P, Vaegter CB. 2017. Hydraulic Extrusion of the Spinal Cord and Isolation of Dorsal Root Ganglia in Rodents. *J Vis Exp* **2017**. doi:10.3791/55226

Ripamonti S, Shomroni O, Rhee JS, Chowdhury K, Jahn O, Hellmann KP, Bonn S, Brose N, Tirard M. 2020. SUMOylation controls the neurodevelopmental function of the transcription factor Zbtb20. *J Neurochem* **154**:647–661. doi:10.1111/JNC.15008

Ristic M, Brockly F, Piechaczyk M, Bossis G. 2016. Detection of protein–protein interactions and posttranslational modifications using the proximity ligation assay: Application to the study of the SUMO pathwayMethods in Molecular Biology. Humana Press Inc. pp. 279–290. doi:10.1007/978-1-4939-3756-1_17

Rodriguez MS, Dargemont C, Hay RT. 2001. SUMO-1 Conjugation in Vivo Requires Both a Consensus Modification Motif and Nuclear Targeting. *Journal of Biological Chemistry* **276**:12654–12659. doi:10.1074/jbc.M009476200

Rohira AD, Chen CY, Allen JR, Johnson DL. 2013. Covalent small ubiquitin-like modifier (SUMO) modification of Maf1 protein controls RNA polymerase III-dependent transcription repression. *J Biol Chem* **288**:19288–19295. doi:10.1074/JBC.M113.473744

Rousseaux MWC, de Haro M, Lasagna-Reeves CA, de Maio A, Park J, Jafar-Nejad P, Al-Ramahi I, Sharma A, See L, Lu N, Vilanova-Velez L, Klisch TJ, Westbrook TF, Troncoso JC, Botas J, Zoghbi HY. 2016. TRIM28 regulates the nuclear accumulation and toxicity of both alpha-synuclein and tau. *Elife* **5**:e19809. doi:10.7554/eLife.19809

Sahin U, Jollivet F, Berthier C, de Thé H, Lallemand-Breitenbach V. 2016. Detection of protein SUMOylation in situ by proximity ligation assays. *Methods in Molecular Biology* **1475**:139–150. doi:10.1007/978-1-4939-6358-4_10/FIGURES/3

Saitoh H, Sparrow DB, Shiomi T, Pu RT, Nishimoto T, Mohun TJ, Dasso M. 1998. Ubc9p and the conjugation of SUMO-1 to RanGAP1 and RanBP2. *Current Biology* **8**:121–124. doi:10.1016/S0960-9822(98)70044-2

Salinas S, Briançon-Marjollet A, Bossis G, Lopez MA, Piechaczyk M, Jariel-Encontre I, Debant A, Hipskind RA. 2004. SUMOylation regulates nucleo-cytoplasmic shuttling of Elk-1. *J Cell Biol* **165**:767–773. doi:10.1083/JCB.200310136

Sampson DA, Wang M, Matunis MJ. 2001. The Small Ubiquitin-like Modifier-1 (SUMO-1) Consensus Sequence Mediates Ubc9 Binding and is Essential for SUMO-1 Modification. *Journal of Biological Chemistry* **276**:21664–21669. doi:10.1074/jbc.M100006200

Seufert W, Futcher B, Jentsch S. 1995. Role of a ubiquitin-conjugating enzyme in degradation of S- and M-phase cyclins. *Nature 1995 373:6509* **373**:78–81. doi:10.1038/373078a0

Shan S fang, Wang L fang, Zhai J wei, Qin Y, Ouyang H fang, Kong Y ying, Liu J, Wang Y, Xie Y hua. 2008. Modulation of transcriptional corepressor activity of

prosperorelated homeobox protein (Prox1) by SUMO modification. *FEBS Lett* **582**:3723–3728. doi:10.1016/J.FEBSLET.2008.09.057

Shevchenko A, Tomas H, Havliš J, Olsen J v., Mann M. 2006. In-gel digestion for mass spectrometric characterization of proteins and proteomes. *Nat Protoc* **1**:2856–2860. doi:10.1038/NPROT.2006.468

Stankova T, Piepkorn L, Bayer TA, Jahn O, Tirard M. 2018. SUMO1-conjugation is altered during normal aging but not by increased amyloid burden. *Aging Cell* **17**. doi:10.1111/ACEL.12760

Tirard M, Brose N. 2016. Systematic Localization and Identification of SUMOylation Substrates in Knock-In Mice Expressing Affinity-Tagged SUMO1. *Methods Mol Biol* **1475**:291–301. doi:10.1007/978-1-4939-6358-4_20

Tirard M, Hsiao H-H, Nikolov M, Urlaub H, Melchior F, Brose N. 2012. In vivo localization and identification of SUMOylated proteins in the brain of His6-HASUMO1 knock-in mice. *Proc Natl Acad Sci U S A* **109**:21122–7. doi:10.1073/pnas.1215366110

Uhlén M, Fagerberg L, Hallström BM, Lindskog C, Oksvold P, Mardinoglu A, Sivertsson Å, Kampf C, Sjöstedt E, Asplund A, Olsson IM, Edlund K, Lundberg E, Navani S, Szigyarto CAK, Odeberg J, Djureinovic D, Takanen JO, Hober S, Alm T, Edqvist PH, Berling H, Tegel H, Mulder J, Rockberg J, Nilsson P, Schwenk JM, Hamsten M, von Feilitzen K, Forsberg M, Persson L, Johansson F, Zwahlen M, von Heijne G, Nielsen J, Pontén F. 2015. Proteomics. Tissue-based map of the human proteome. *Science* **347**. doi:10.1126/SCIENCE.1260419

Wang L, Rodriguiz RM, Wetsel WC, Sheng H, Zhao S, Liu X, Paschen W, Yang W. 2014a. Neuron-specific Sumo1-3 knockdown in mice impairs episodic and fear memories. *J Psychiatry Neurosci* **39**:259–266. doi:10.1503/JPN.130148

Wang L, Wansleeben C, Zhao S, Miao P, Paschen W, Yang W. 2014b. SUMO 2 is essential while SUMO 3 is dispensable for mouse embryonic development . *EMBO Rep* **15**:878–885. doi:10.15252/embr.201438534

Watanabe M, Takahashi K, Tomizawa K, Mizusawa H, Takahashi H. 2008. Developmental regulation of Ubc9 in the rat nervous system.

Westman BJ, Verheggen C, Hutten S, Lam YW, Bertrand E, Lamond AI. 2010. A proteomic screen for nucleolar SUMO targets shows SUMOylation modulates the function of Nop5/Nop58. *Mol Cell* **39**:618–631. doi:10.1016/J.MOLCEL.2010.07.025

Xu Z, Au SWN. 2005. Mapping residues of SUMO precursors essential in differential maturation by SUMO-specific protease, SENP1. *Biochem J* **386**:325–330.

Yang W, Paschen W. 2015. SUMO proteomics to decipher the SUMO-modified proteome regulated by various diseases. *Proteomics* **15**:1181–1191. doi:10.1002/PMIC.201400298

1272 Yu S, Galeffi F, Rodriguiz RM, Wang Z, Shen Y, Lyu J, Li R, Bernstock JD, Johnson 1273 KR, Liu S, Sheng H, Turner DA, Wetsel WC, Paschen W, Yang W. 2020. Small
1274 ubiquitin-like modifier 2 (SUMO2) is critical for memory processes in mice. *FASEB*
1275 *J* **34**:14750–14767. doi:10.1096/FJ.202000850RR 1276

Figure 1

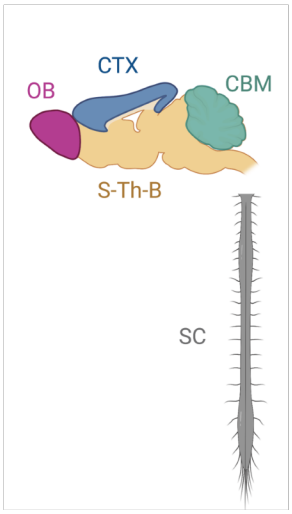

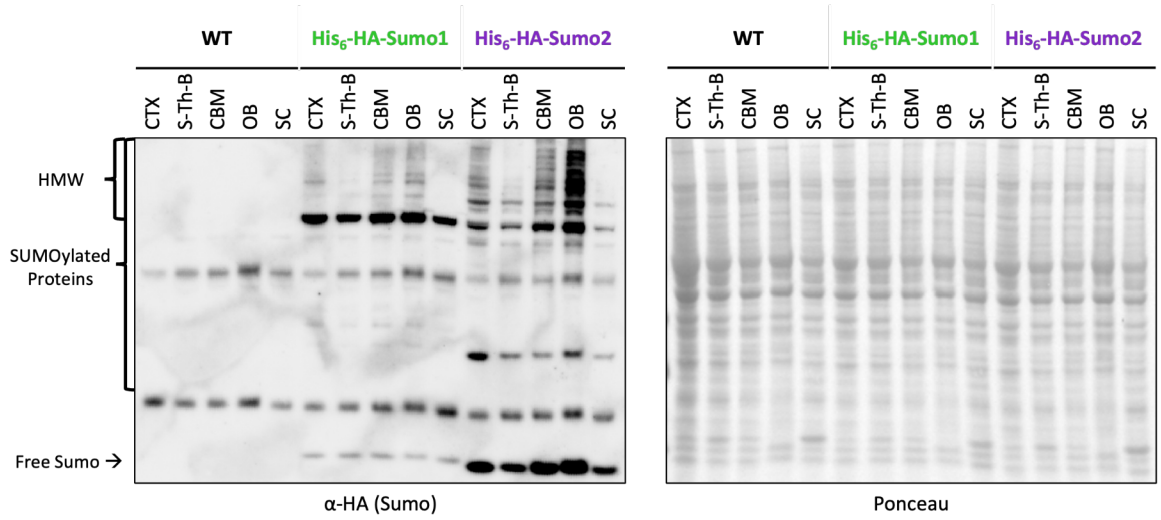

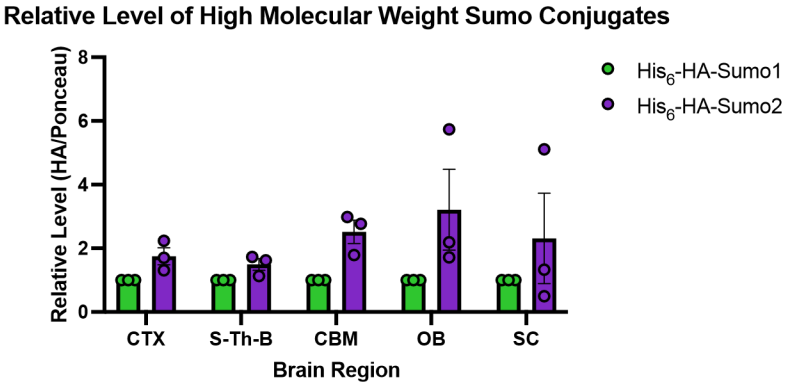

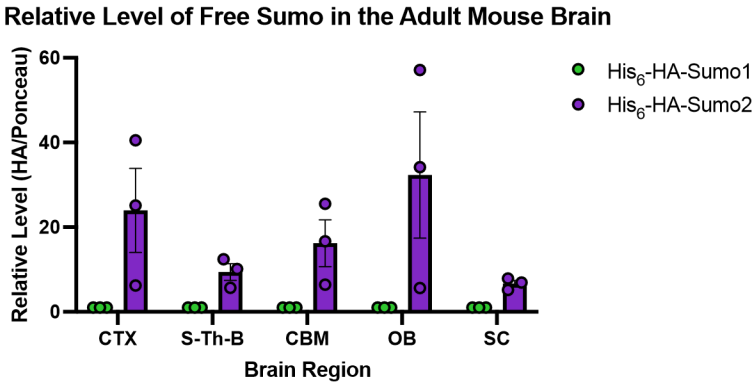

Figure 1–figure supplement 1

A

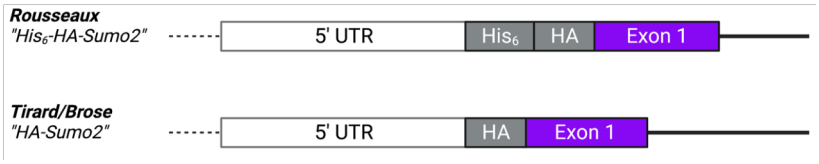

B

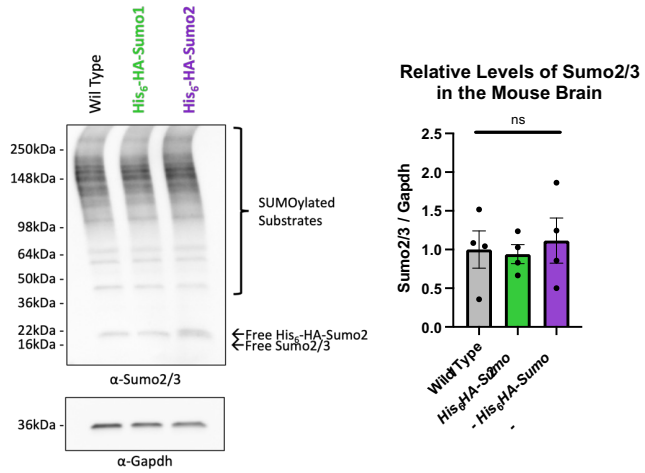

C

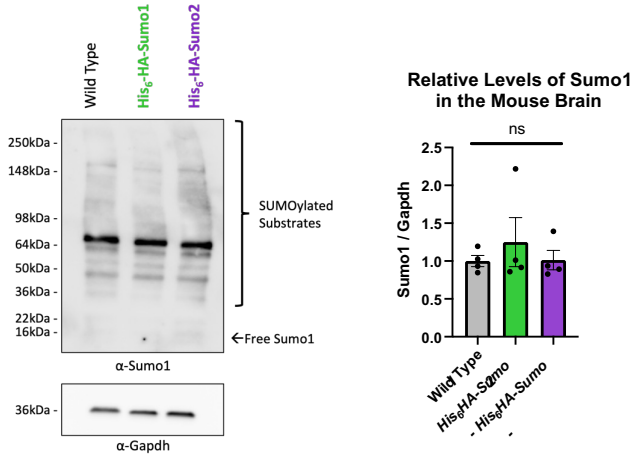

D

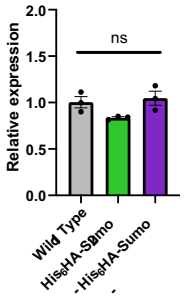

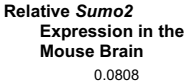

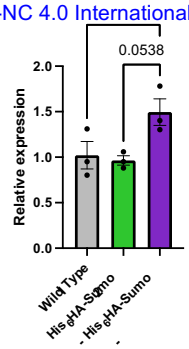

Figure 2

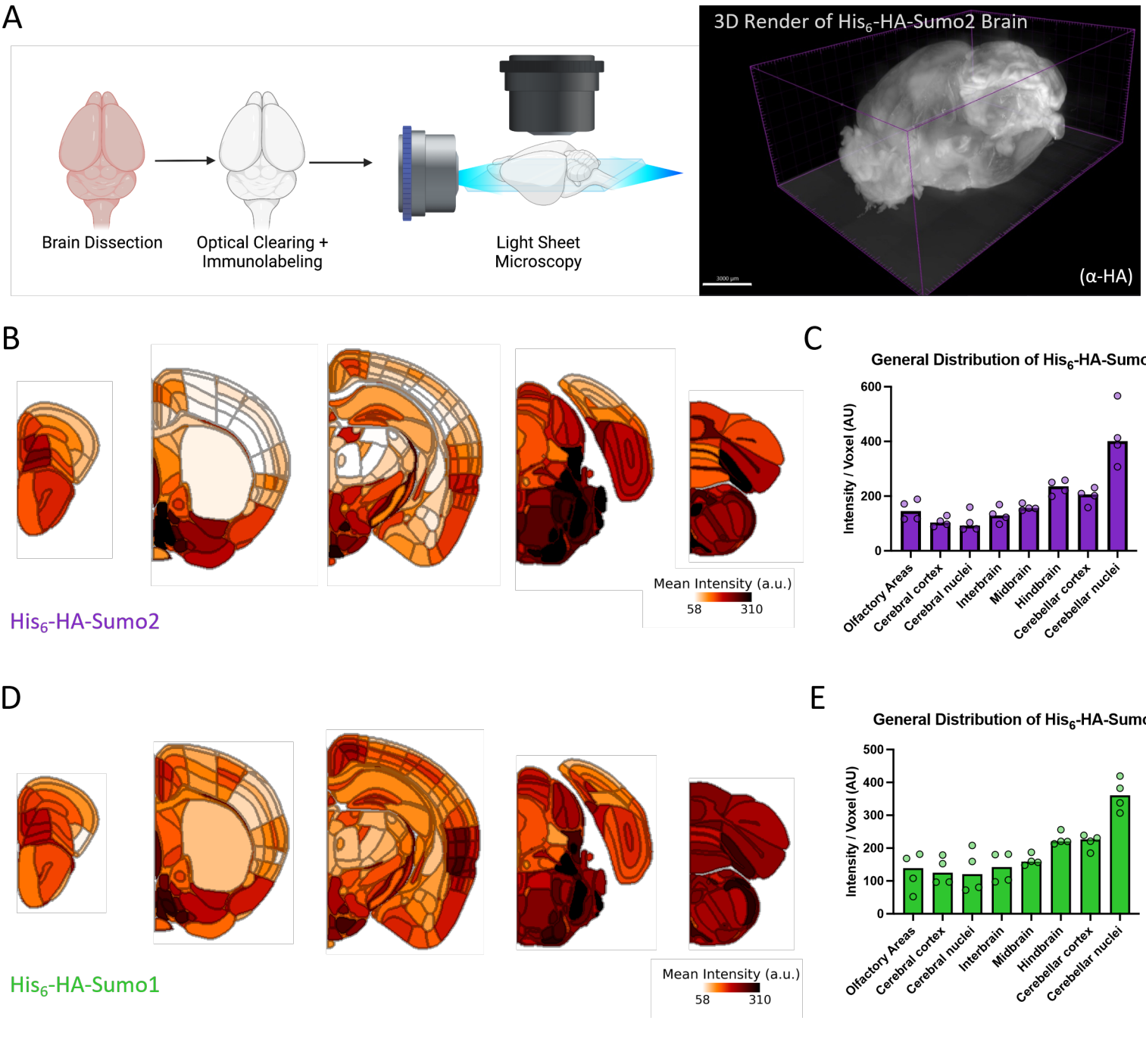

https://doi.org/10.1101/2022.09.09.507035; Figure 2–figure supplement 1

A

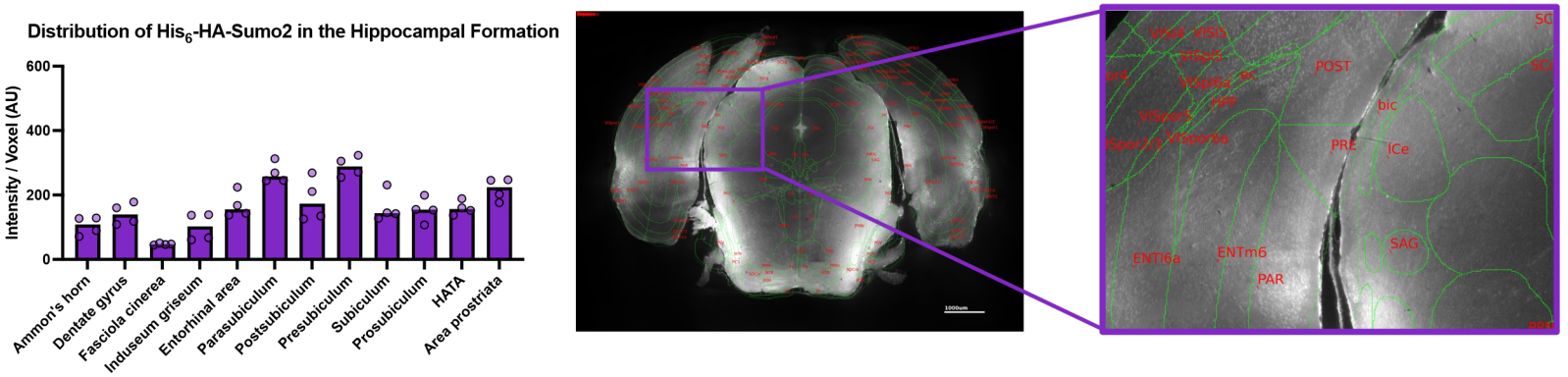

B

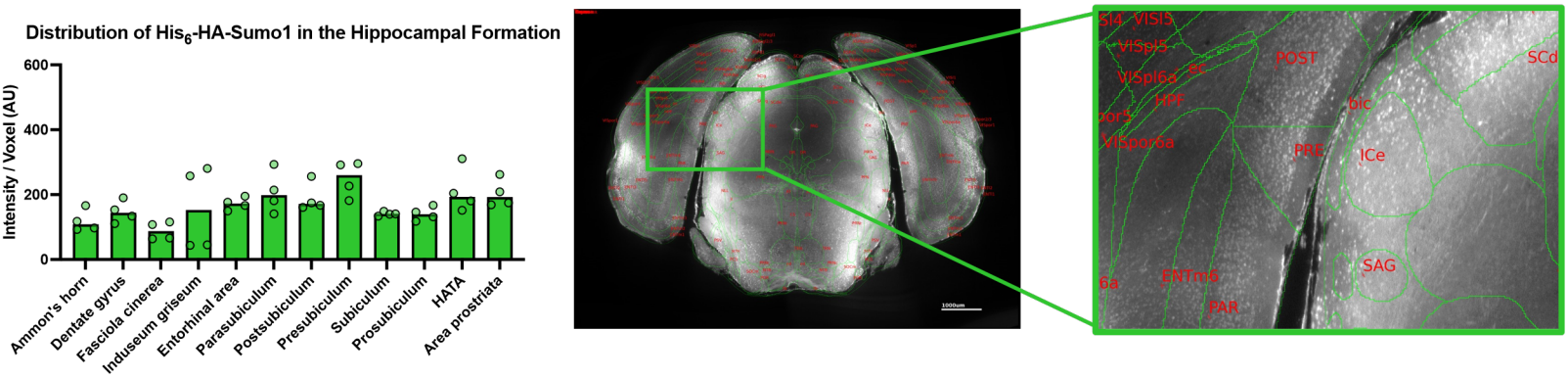

C

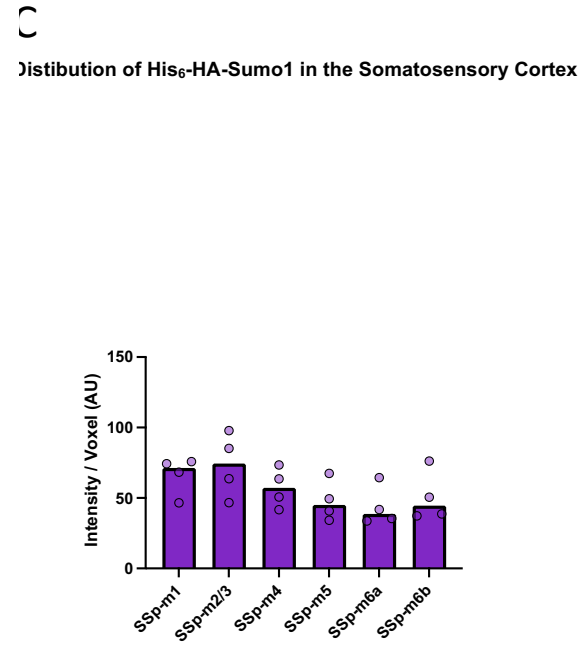

D

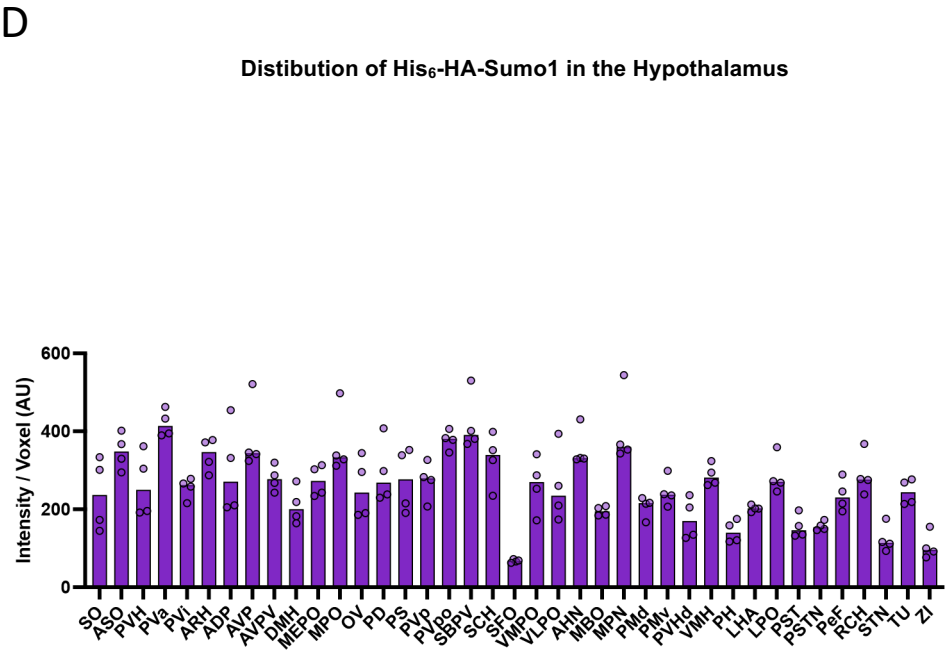

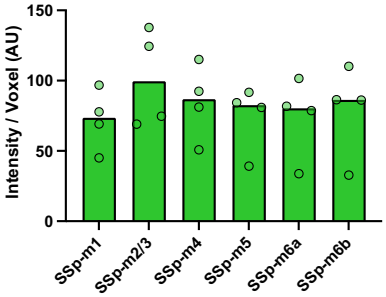

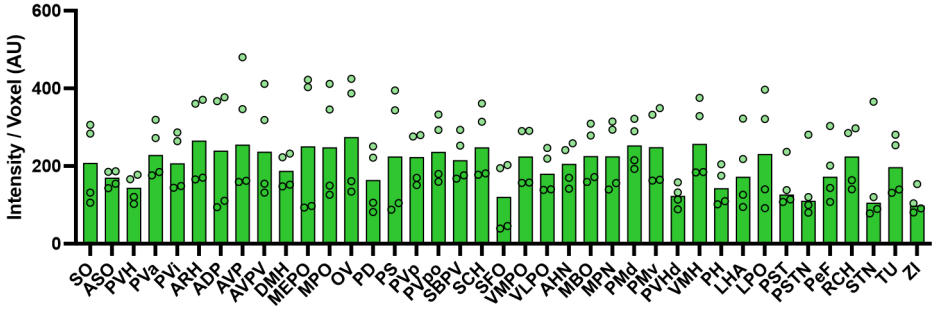

Distribution of His_6-HA-Sumo2 in the Somatosensory Cortex

Distibution of His_6-HA-Sumo2 in the Hypothalamus

https://doi.org/10.1101/2022.09.09.507035;

Figure 2—figure supplement 2

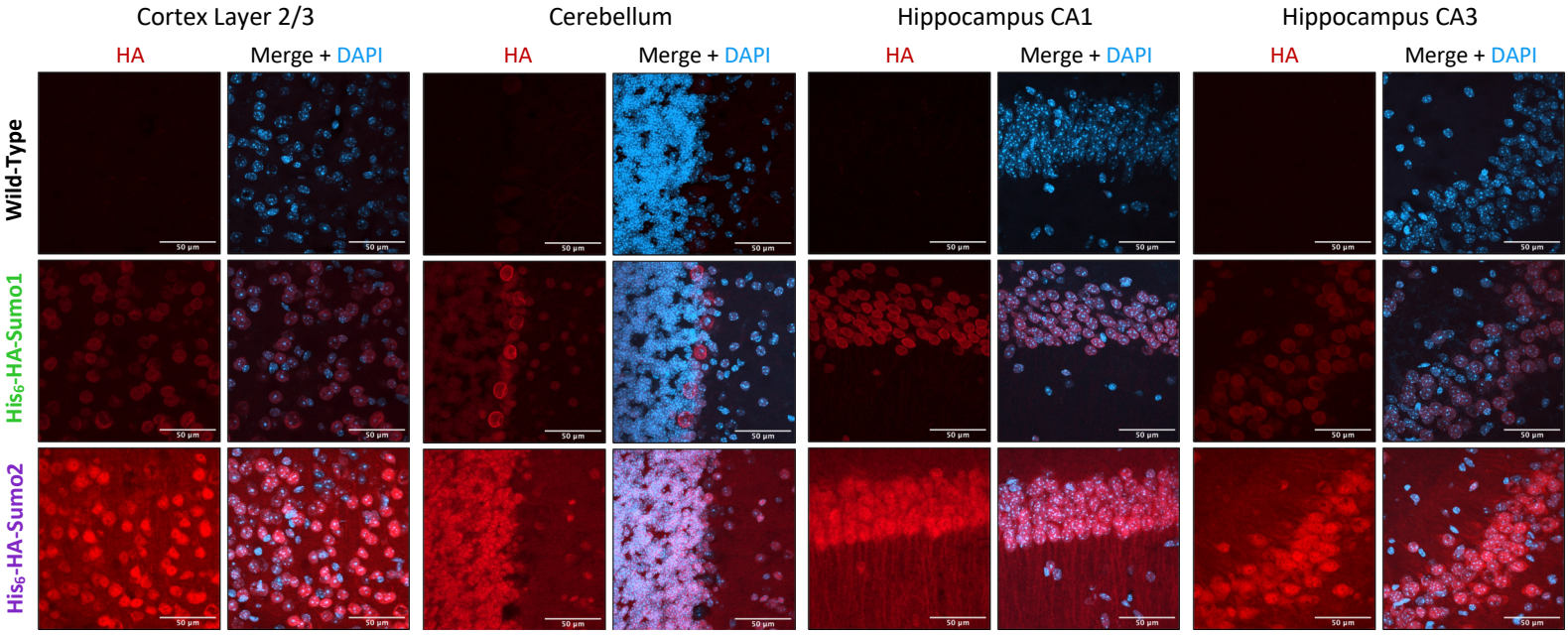

Figure 3

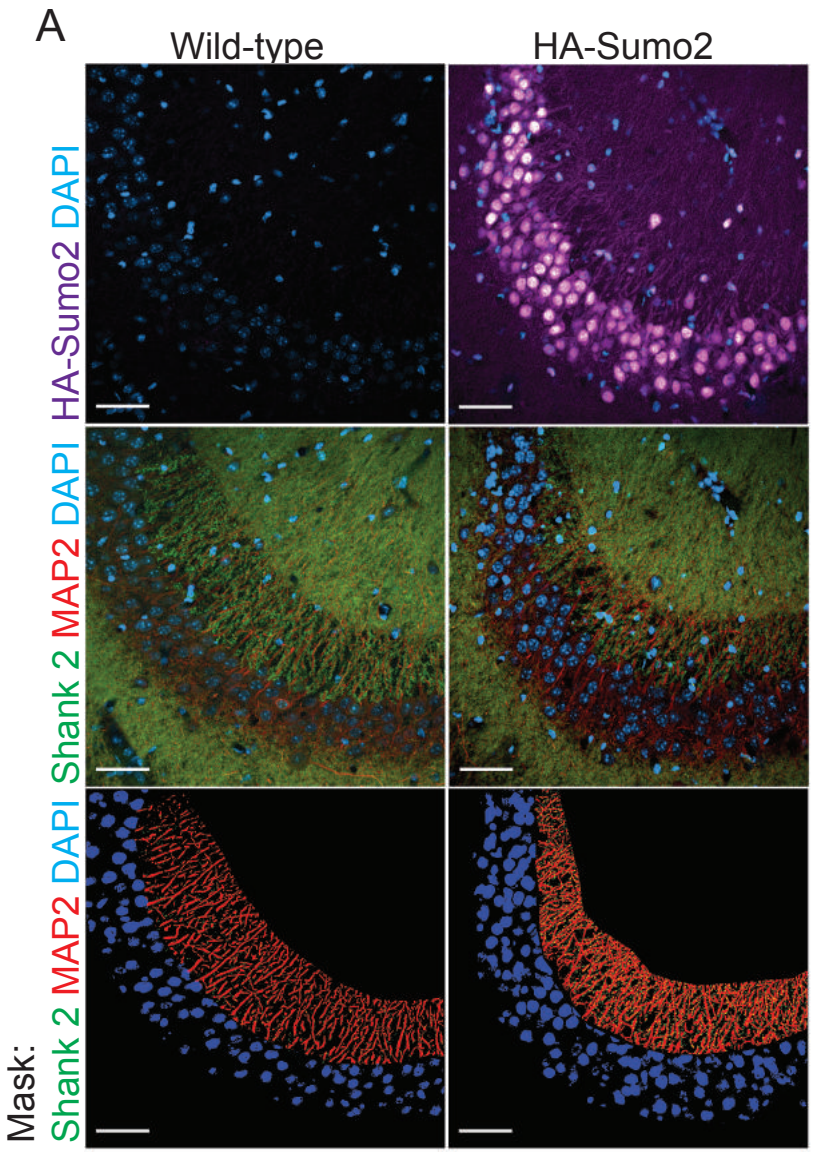
A
Wild-type
HA-Sumo2
HA-Sumo2 DAPI
Shank 2 MAP2 DAPI
Mask:
Shank 2 MAP2 DAPI

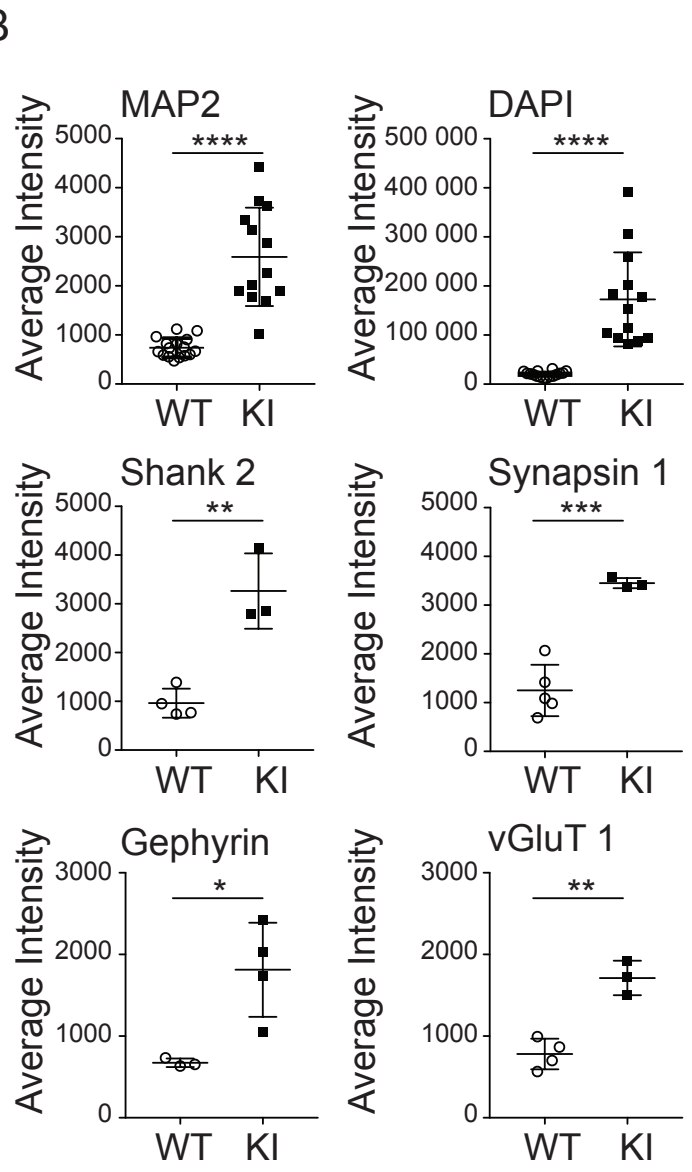
B
MAP2
DAPI
Shank 2
Synapsin 1
Gephyrin
vGluT 1
Average Intensity
WT
KI
****
**
***
*

Figure 3—figure supplement 1

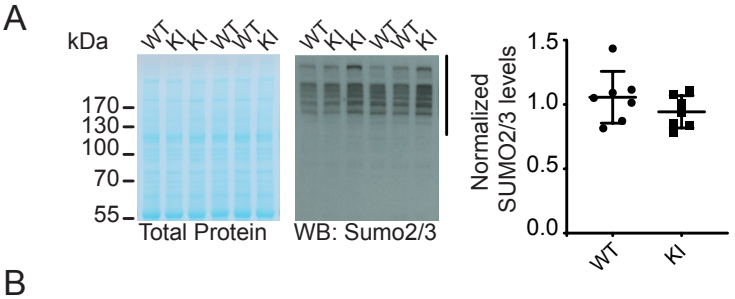

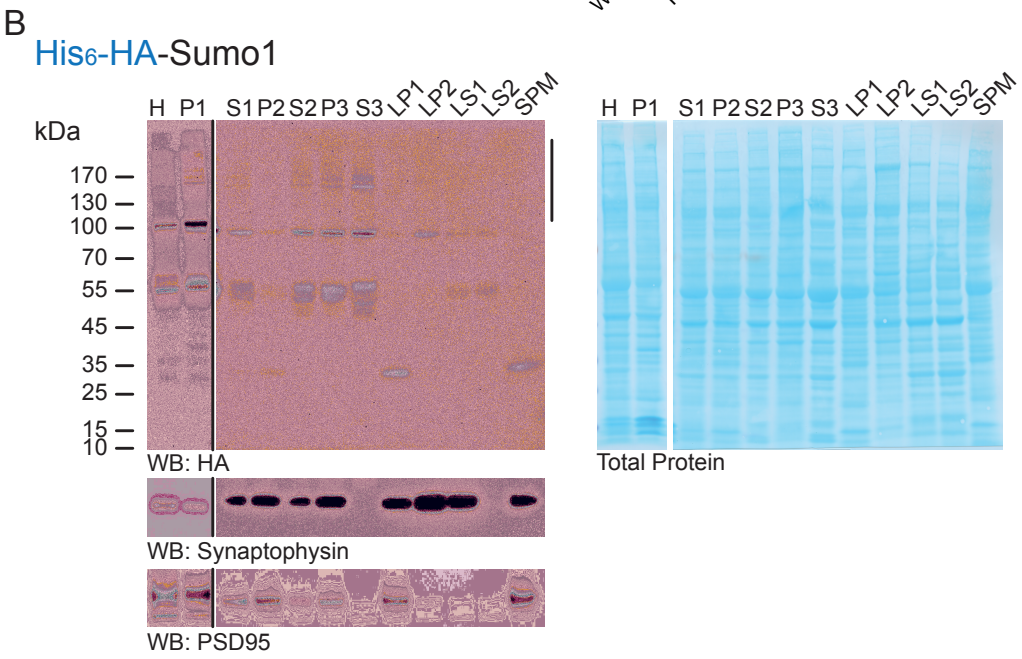

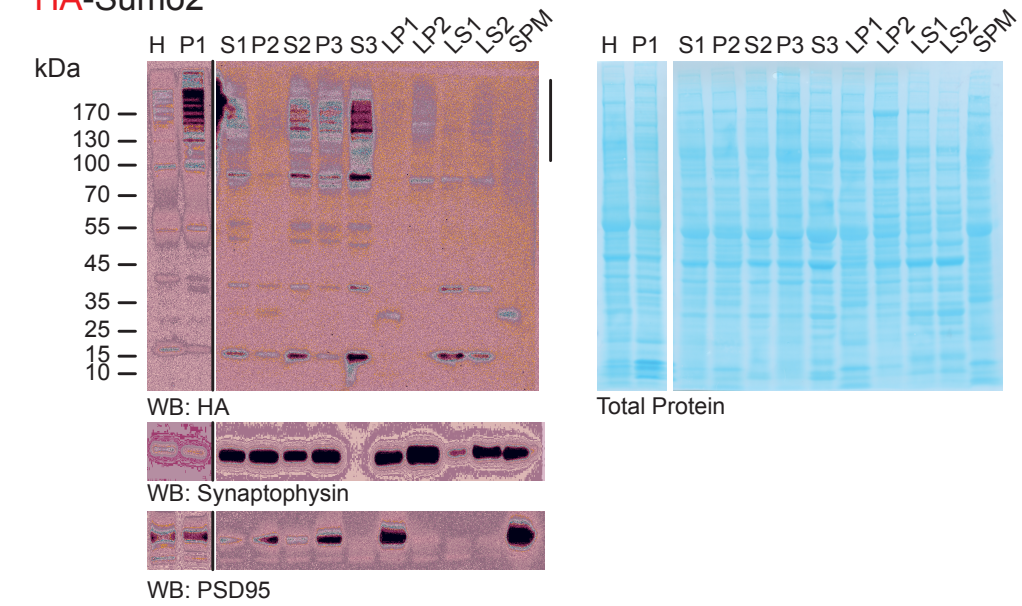

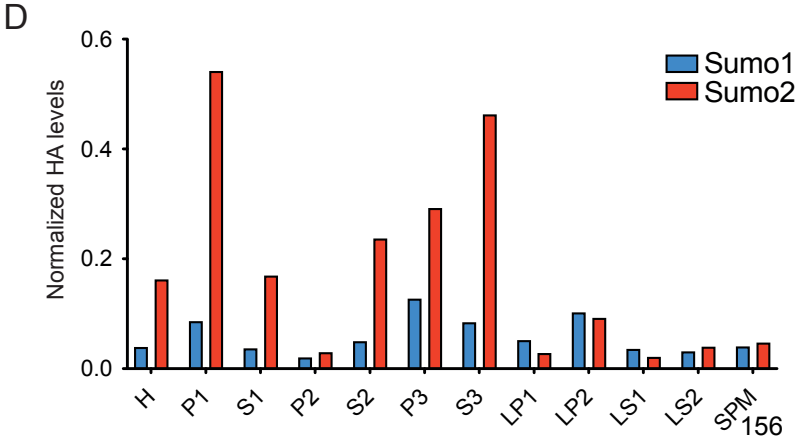

Figure 4

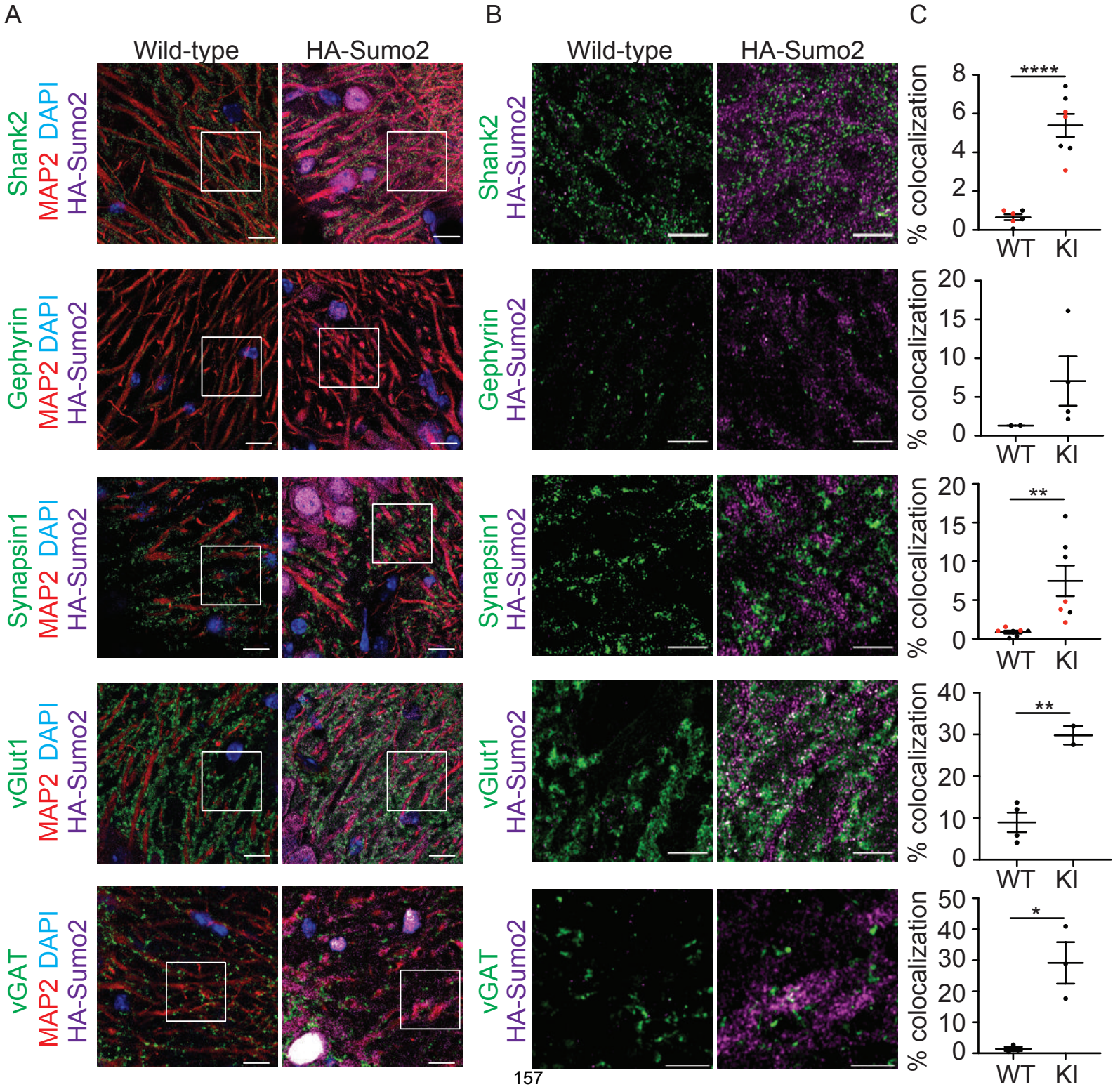
A
Wild-type
HA-Sumo2
Shank2 MAP2 DAPI HA-Sumo2
Gephyrin MAP2 DAPI HA-Sumo2
Synapsin1 MAP2 DAPI HA-Sumo2
vGlut1 MAP2 DAPI HA-Sumo2
vGAT MAP2 DAPI HA-Sumo2
B
Wild-type
HA-Sumo2
Shank2 HA-Sumo2
Gephyrin HA-Sumo2
Synapsin1 HA-Sumo2
vGlut1 HA-Sumo2
vGAT HA-Sumo2
C
% colocalization
****
**
**
*
WT
KI

Figure 4—figure supplement 1

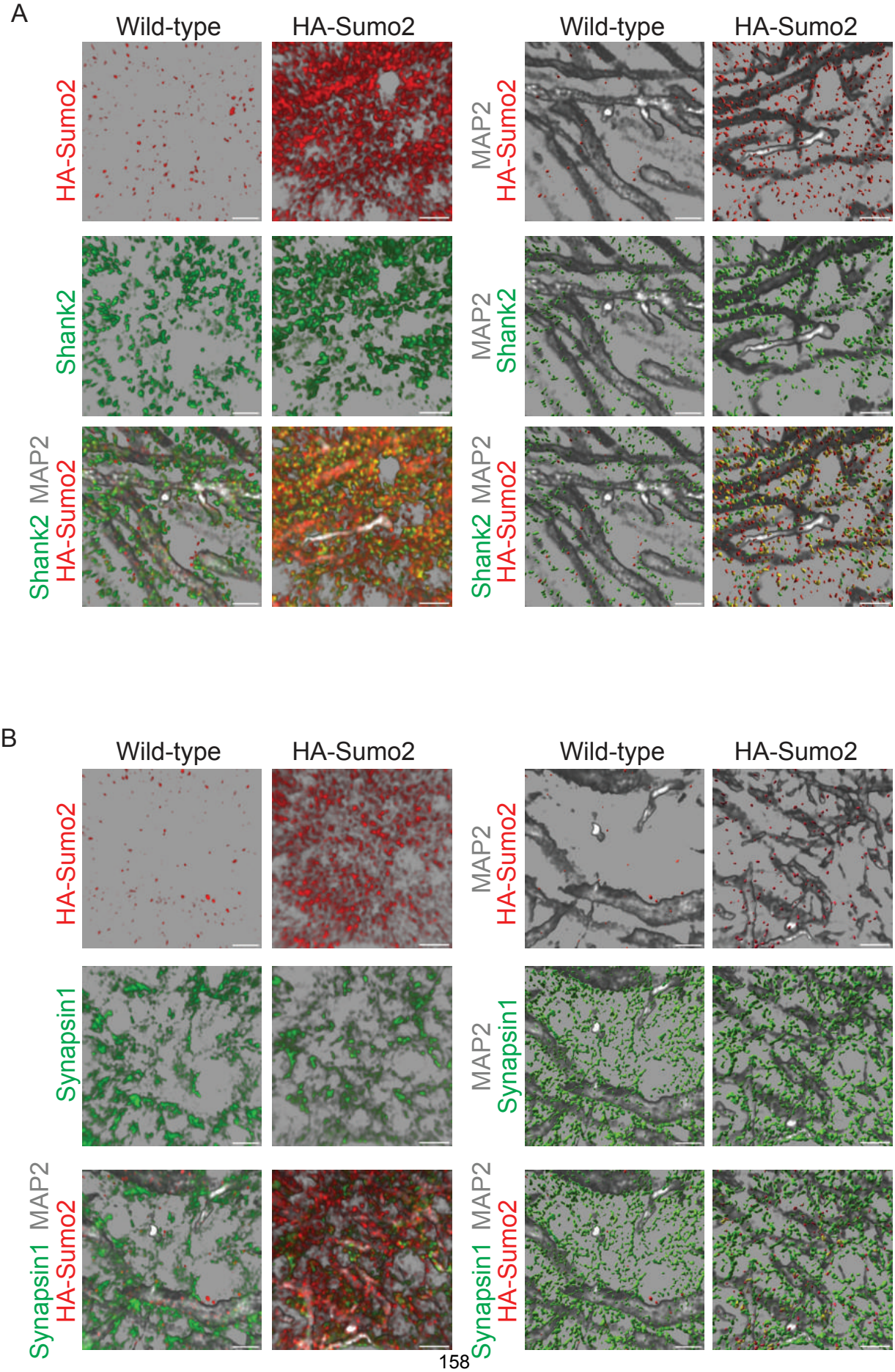

Figure 5

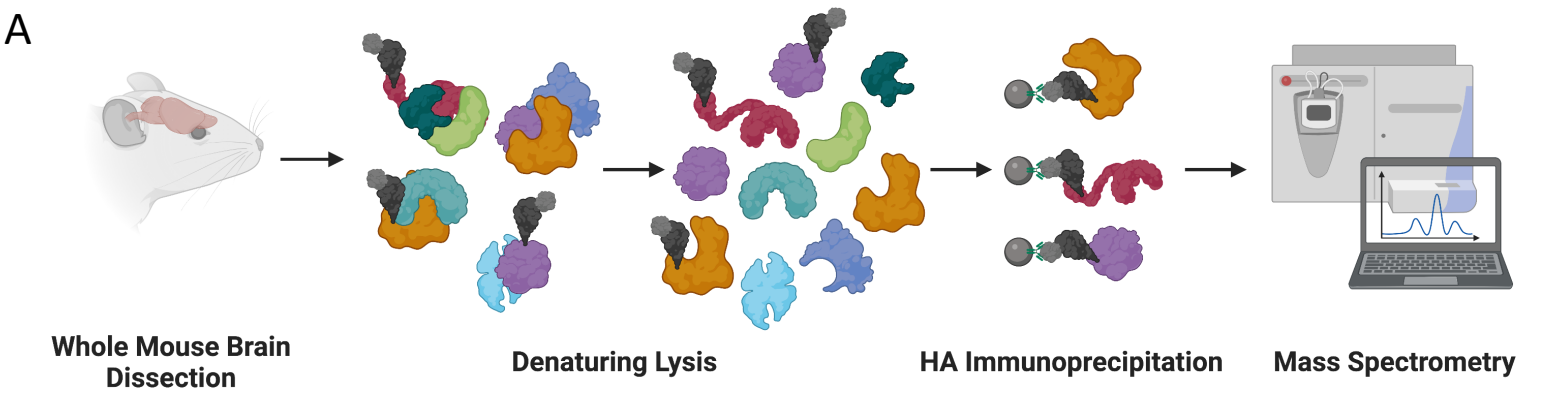

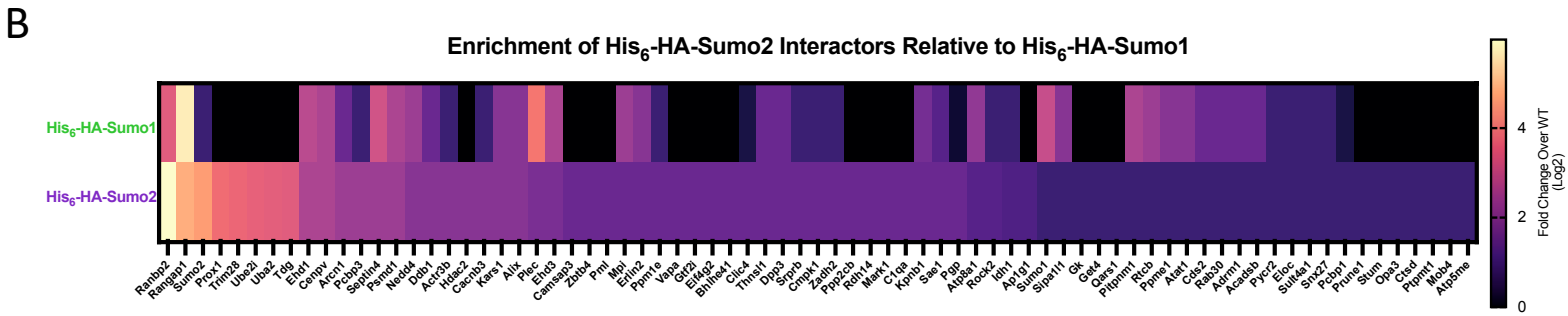

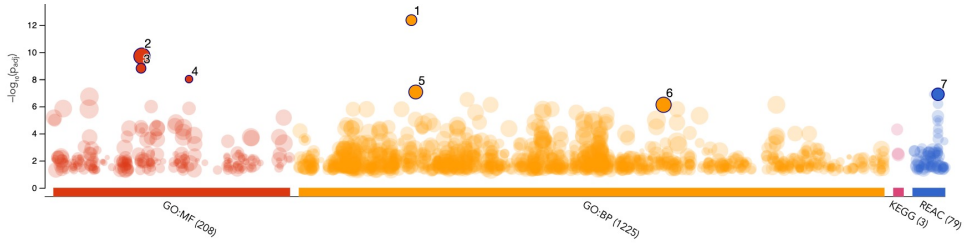

ID	Source	Term ID	Term Name	p_{adj} (query_1)
1	GO:BP	GO:0016925	protein sumoylation	4.392×10^{-13}
2	GO:MF	GO:0019899	enzyme binding	1.977×10^{-10}
3	GO:MF	GO:0019789	SUMO transferase activity	1.550×10^{-9}
4	GO:MF	GO:0044388	small protein activating enzyme binding	9.720×10^{-9}
5	GO:BP	GO:0018205	peptidyl-lysine modification	8.689×10^{-8}
6	GO:BP	GO:0070647	protein modification by small protein conjugati...	7.630×10^{-7}
7	REAC	REAC:R-MMU-2990846	SUMOylation	1.279×10^{-7}

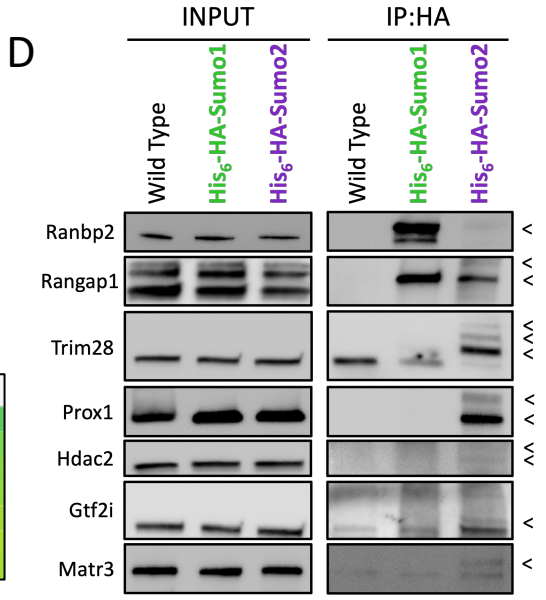

Figure 5—figure supplement 1

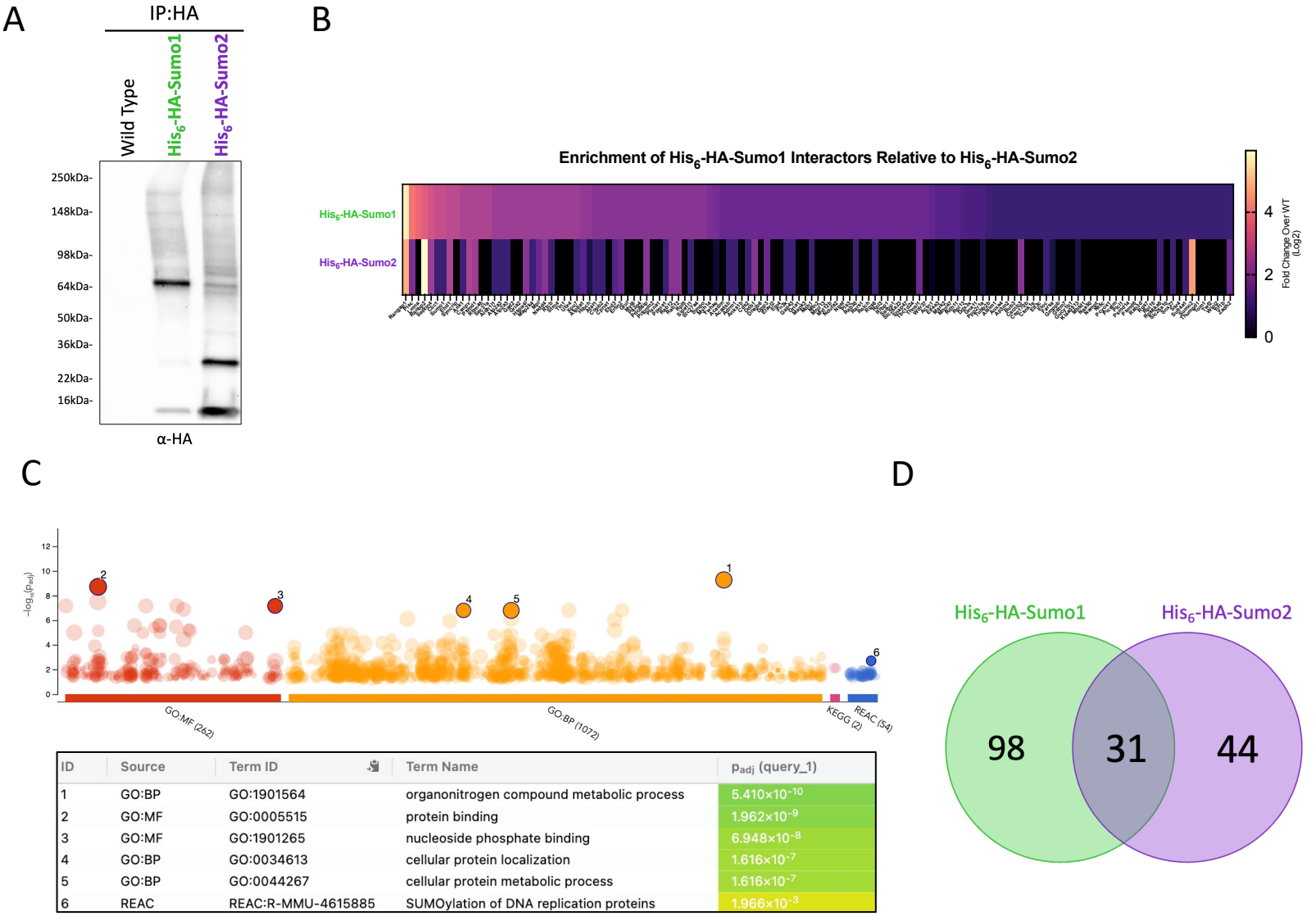

ID	Source	Term ID	Term Name	p_{adj} (query_1)
1	GO:BP	GO:1901564	organonitrogen compound metabolic process	5.410×10^{-10}
2	GO:MF	GO:0005515	protein binding	1.962×10^{-9}
3	GO:MF	GO:1901265	nucleoside phosphate binding	6.948×10^{-8}
4	GO:BP	GO:0034613	cellular protein localization	1.616×10^{-7}
5	GO:BP	GO:0044267	cellular protein metabolic process	1.616×10^{-7}
6	REAC	REAC:R-MMU-4615885	SUMOylation of DNA replication proteins	1.966×10^{-3}

Figure 6

A

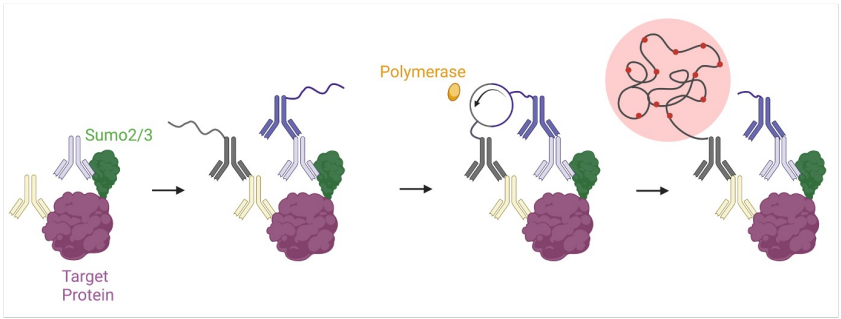

B

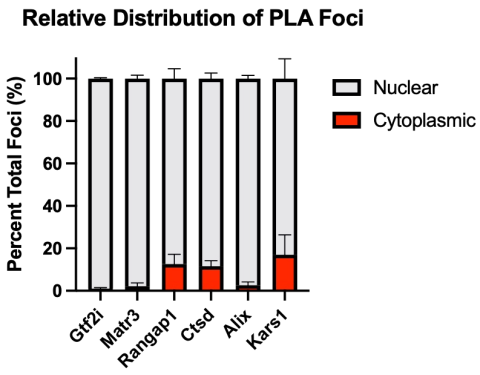

C

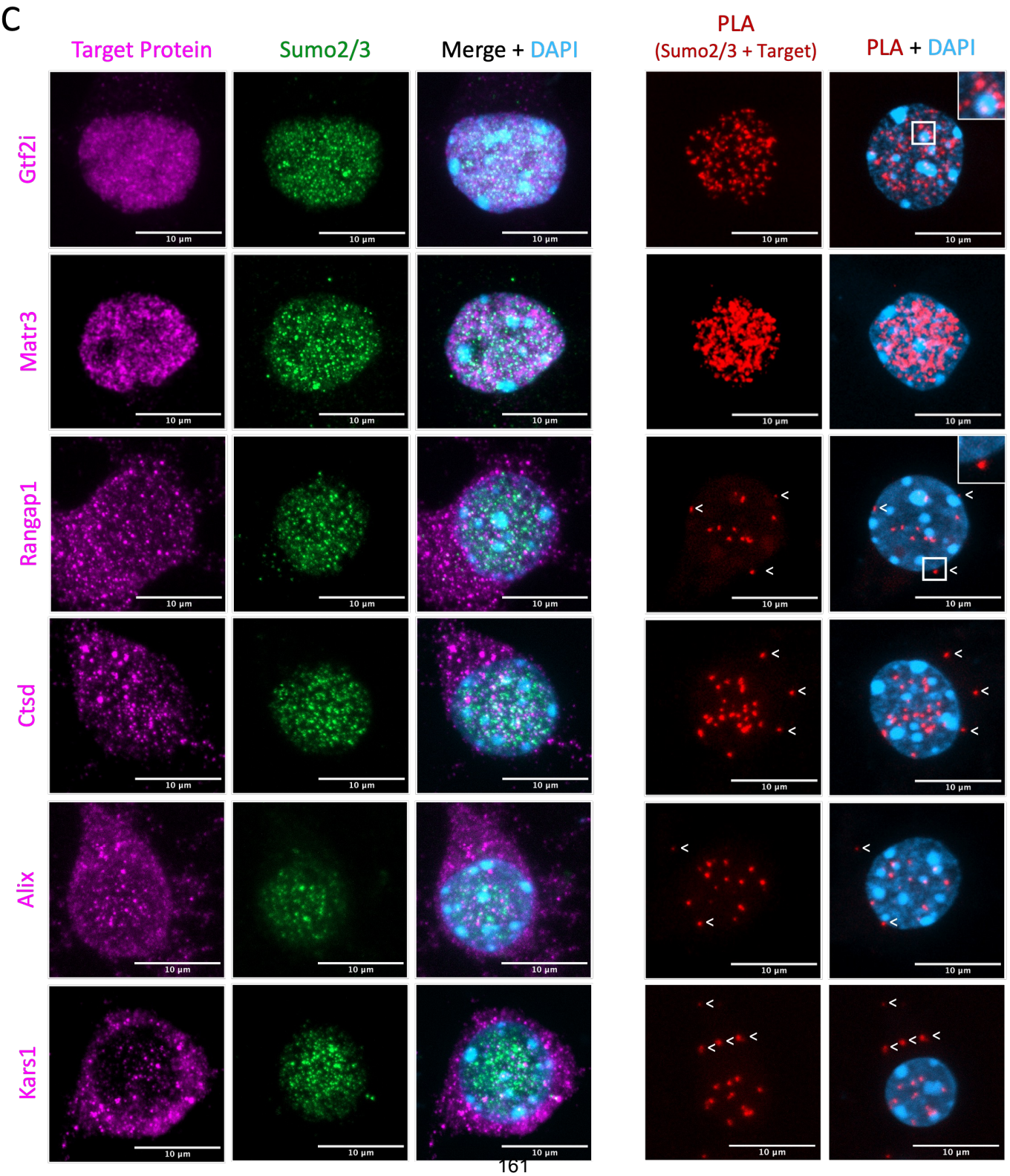

Figure 6—figure supplement 1